TECHNISCHE UNIVERSITÄT MÜNCHEN

Fakultät für Physik

SODIUM ION BATTERIES – FROM FUNDAMENTALS TO APPLICATION

Lukas Seidl

Vollständiger Abdruck der von der Fakultät für Physik der Technischen Universität München zur Erlangung des akademischen Grades eines

Doktors der Naturwissenschaften (Dr. rer. nat.)

genehmigten Dissertation.

Vorsitzende(r):	apl. Prof. Dr. Norbert Kaiser
Prüfer der Dissertation:	1. Prof. Dr. Ulrich Stimming
	2. Prof. Dr. Aliaksandr Bandarenka

Die Dissertation wurde am 11.04.2018 bei der Technischen Universität München eingereicht und durch die Fakultät für Physik am 26.11.2018 angenommen.

Table of contents

Abstract

Energy storage is one of the key challenges on the way to sustainable, CO_2-neutral or even -free renewable energies. Often, there is a mismatch between the availability of energy produced by renewable sources and the energy demand of consumers, which can be balanced by the use of energy storage devices. One option to store electric energy is the use of large scale batteries, which have to fulfill numerous requirements, such as high energy and power densities, high round trip efficiencies, high level of safety, long lifetime, low costs and use of abundant raw materials. Battery technologies currently available do not meet all these requirements yet. Li-ion batteries are the most advanced technology to date, however, their costs due to the limited Li-resources are too high for large scale deployment. One strategy to tackle this issue is to exchange the Li-ion by its neighbor in the periodic table, the Na-ion. Na is about three orders of magnitude more abundant than Li and homogeneously distributed in the earth´s crust, significantly reducing the raw material costs. Moreover, Na-ion batteries further benefit in terms of cost and weight by the use of Al current collectors instead of those made from Cu, which need to be used in Li-ion batteries at the negative electrode.

In the new field of Na-ion batteries, many fundamental challenges need to be tackled to bring the Na-ion battery technology closer to commercialization. Those concern the discovery of new electrode materials suitable for Na-ion insertion with properties such as high energy and power densities, lifetime, low costs and minimized hazards. In order to promote the development of new materials, a fundamental understanding of the electrode processes and about the interplay between different battery components is required, such as the electrode and the electrolyte. The more familiar Li-ion batteries can serve as a starting point and valuable reference system for such studies. In the present case, fundamental studies on the formation of a solid electrolyte interphase (SEI) on a graphite single crystal model electrode are shown, giving a mechanistic insight into the formation of the SEI precipitation on a molecular level. The multistage nature of the SEI-formation is studied by *in-situ* and *in-operando* scanning tunneling microscopy (STM), revealing the film morphology as well as the formation mechanism, including an initially still reversible SEI. A profound understanding of the SEI helps to benefit from its benign influence on the battery lifetime, safety and coulombic efficiency.

The concept of *in-operando* STM is also applied to image phase transitions of graphite model electrodes, a candidate material for the negative electrode in Na-ion batteries, when intercalating solvated Na-ions as $Na^+(G_x)_y$-complexes, where G_x are linear ethylene glycol dimethyl ether homologues, also known as glymes, with x+1 O-atoms. Before the discovery of co-intercalating Na-ions together with their solvation shell to form ternary graphite intercalation compounds, the reversible sodiation and de-sodiation of graphite was believed to be energetically impossible. Here, not only the reversible intercalation of Na-ions into graphite is demonstrated, but a deep understanding of the electrochemical phase transitions is gained by the combined use of *in-operando* techniques, besides STM also including X-ray diffraction and the electrochemical quartz crystal microbalance technique, which is operated as a novel *in-situ* hydrodynamic spectroscopy technique on graphite decorated quartzes. This leads to a precise description of the intercalation mechanism, based on the direct visualization and quantification of the graphite lattice expansion upon sodiation from the pristine 3.35 Å to more than 11 Å when sodiated, forming an intermediate ternary stage 2 Na-graphite intercalation compound. Moreover, the subsurface diffusion of the intercalated $Na^+(G_x)_y$-complexes can be directly visualized by STM, which shows that the under-coordinated $Na^+(G_3)_1$-complex diffuses significantly slower (5.9 nm s^{-1}) than the sufficiently coordinated $Na^+(G_4)_1$-complex (22.1 nm s^{-1}), because of the increased $Na^+(G_3)_1$-graphite interaction.

Ex-situ STM on an orthorhombic, layered V_2O_5 single crystal model electrode helps to gain a deeper understanding of the electrochemical insertion of Na-ions into a V_2O_5 positive electrode. The insertion

of the first Na-ion to form the $Na_1V_2O_5$ phase occurs irreversibly, while a second Na-ion can be reversibly inserted/extracted to form the bilayered $Na_2V_2O_5$. A detailed morphological study on the battery performance in Na-ion batteries is conducted by synthesizing and testing materials covering the entire range from microstructures, such as yolk-shell V_2O_5 microspheres, to nanostructures, as V_2O_5 nanobundles. The latter shows a superior battery performance, since the nanostructure increases the electrode capacity (209.2 mAh g^{-1}, 2nd cycle), the energy density (453 mWh g^{-1}, 2nd cycle) and efficiency (77.2 %, 100th cycle), the operating voltage (2.38 V, 100th cycle), the lifetime as well as the rate capability.

Finally, having understood the fundamental electrochemistry and interplay of each battery component, a fully operating prototype Na-ion battery employing a graphite negative electrode and a V_2O_5 positive electrode is presented. The graphite | V_2O_5 prototype battery has an energy density of 49.2 mWh g^{-1} (normalized to the total mass of active material), an averaged discharge voltage of 1.4 V and a round trip efficiency of 51.8 %. Thus, this thesis presents the full chain of development of a new technology, starting from very fundamental, mechanistic studies, followed by optimizing and adjusting each battery component and finally demonstrating a first, fully operative prototype.

1 Introduction

Life on earth depends on the atmosphere and its climate. Disturbing the equilibrium of the world´s climate directly affects life on earth. Due to this importance, the Intergovernmental Panel on Climate Change (IPCC) was established in 1988, an organization reporting on climate changes and exploring its consequences and origins. In 2014, the IPCC published their fifth report on the climate change,[1] in which the change of global surface temperature since 1850 is shown (Figure 1 (a)). Being constant until 1900, the temperature rose by around 0.8 °C in the past century. Parallel to the rise of temperature, a rise of the sea level by around 20 cm and of greenhouse gas concentrations (CO_2 ca. 100 ppm, CH_4 ca. 1 ppm and N_2O ca. 0.05 ppm) in the earth´s atmosphere is detected (Figure 1 (b) and (c)). In the IPCC report the human influence on the CO_2-content is categorized as *extremely likely*, which is also reflected in the rise of annual anthropogenic CO_2 emissions (Figure 1 (d)).

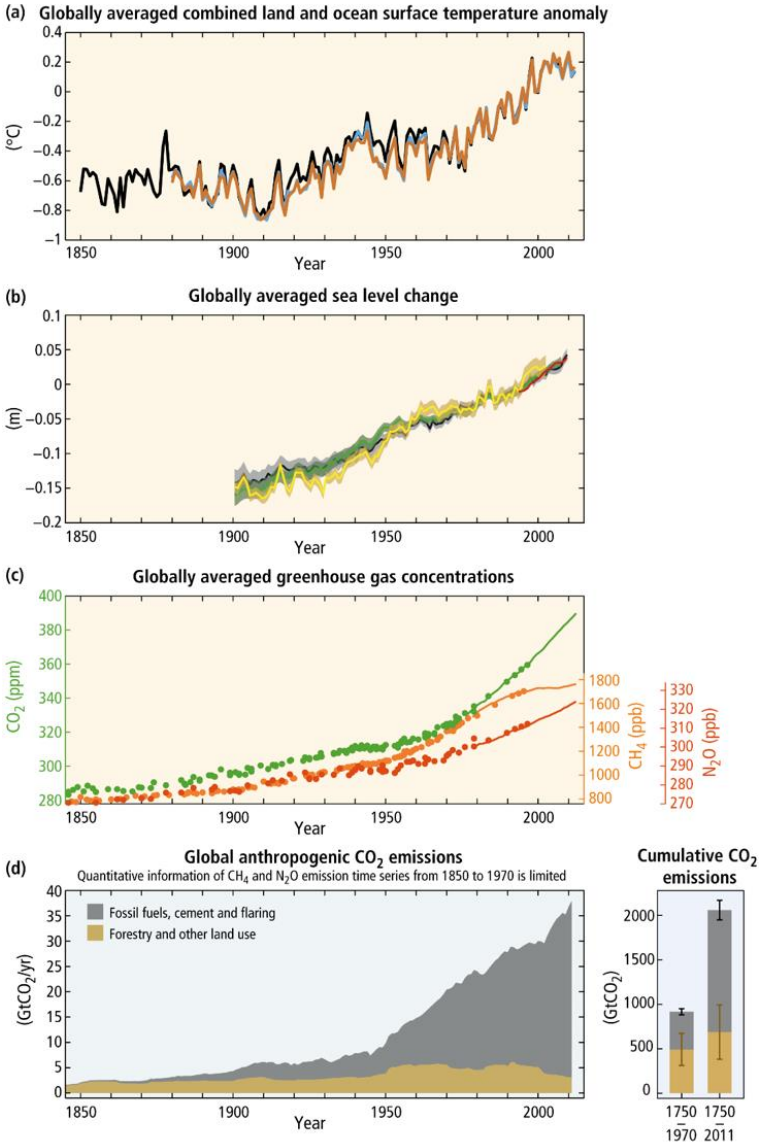

Figure 1: Development of (a) the earth´s surface temperature, (b) the sea level, (c) the greenhouse gas concentrations in the earth´s atmosphere and (d) the anthropogenic CO_2 emissions. Graphs are taken from the fifth assessment report of the IPCC published in 2014.[1]

The climate change affects ecological systems like the oceans, the arctic ice shields, forests, deserts and the global weather. The dissolution of CO_2 in the oceans results in a decrease of pH-value, the rise of temperature disturbs oceanic currents like the gulf-stream and leads to a volume expansion of the heated water. The polar ice disappears and weather extrema become more frequent. Everything has direct sociopolitical as well as geopolitical consequences.

In 2015, 78.3 % of the global energy demand was covered by fossil energy carriers contributing significantly to the global CO_2 emissions. Nuclear power contributed by 2.5 % and 19.2 % were covered by CO_2-neutral or even -free renewable energies. 70 % of the global electricity produced by renewable sources was generated by hydro power, 15.6 % by wind power, 8.4 % by biomass, 5.1 % by solar energy and 1.7 % by other renewable energy sources.[2, 3] One core issue of renewable energies lies in daily and seasonal fluctuations of their availability and a mismatch with the actual energy demand. Large scale energy storage is inevitable to implement

renewable energies into smart grids and to peak shave these fluctuations. A variety of technologies can be used to store energy, for instance as mechanical energy in flywheels,[4–6] as pumped hydro power[4–6] or compressed air,[4–6] as thermal energy[5, 6] or chemical energy by producing solar fuels,[5] as electric energy in superconducting magnetic energy storage devices[5] or in electrochemical devices such as super capacitors[4–6] and rechargeable batteries.[4–11]

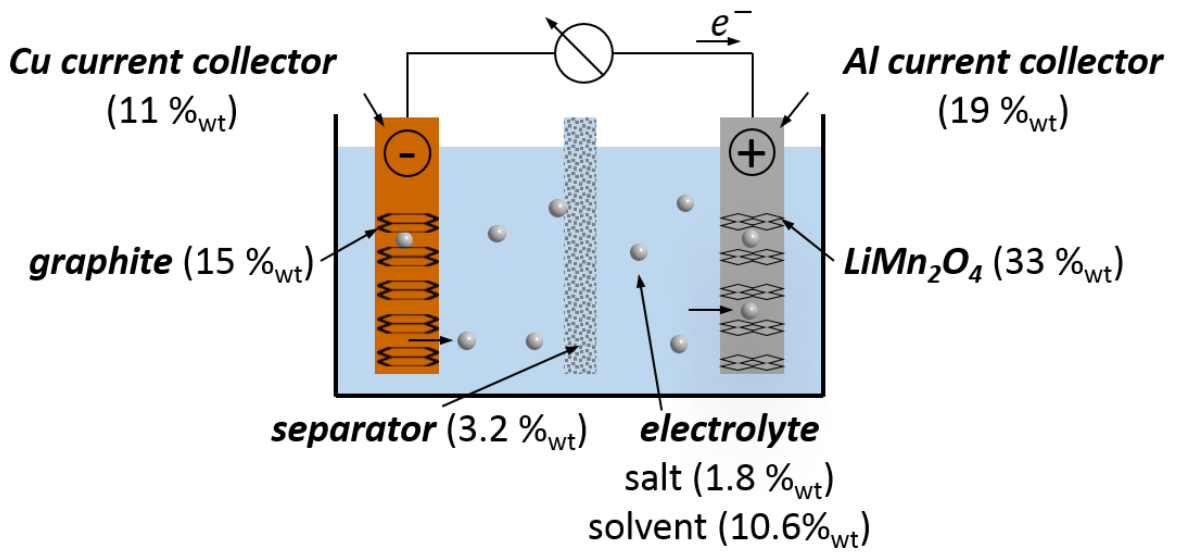

Figure 2: Mass distribution of the main battery components in a lithium-ion battery for electric vehicles with a graphite negative electrode, a $LiMn_2O_4$ positive electrode and a 1 M $LiPF_6$ in EC/DMC (1:1) electrolyte. Minor contributions to the battery mass also come from the electrode binder, thermal insulation, the casing and other electronic parts. The numbers are literature based.[12]

The frontrunners in battery technology today are lithium ion batteries (LIBs, Figure 2). The beneficial properties of the Li-ion made it the material of choice so far, since the Li/Li^+ redox couple has the lowest redox potential (-3.04 V *vs.* NHE) in the electrochemical potential series and in addition Li is one of the lightest elements in the periodic table (6.94 g mol^{-1}).[13] Both increase the gravimetric theoretical energy densities of the electrode materials used. In reality, however, Li also brings about a couple of issues negatively affecting the energy density of the entire battery: in LIBs the current collector of the negative electrode must be Cu (8.92 g cm^{-3}), since the cheaper and lighter Al (2.70 g cm^{-3}) cannot be used due to the formation of Li-Al alloys at low potentials. This problem can be solved when switching from the Li-ion to the Na-ion, which does not show this alloying behavior.[13–15] The Cu-current collector contributes by 11 % to the total battery mass, while the Al-current collector on the positive electrode is heavier, since the electrode capacities of both electrodes must be balanced, requiring larger positive electrodes (Figure 2).[12] Using Al instead of the Cu at same electrode thickness yields a 7.7 % weight saving of the total battery. Of course, the application of Na in a battery also results in a weight penalty at the electrodes and in the precursor used in the electrolyte. Considering the standard MnO_2 cathode material as an example, with an electrode mass for $LiMn_2O_4$ of 180.8 g mol^{-1} and the Na analogue $NaMn_2O_4$ with 196.9 g mol^{-1}, and assuming a 33 % weight contribution to the total battery weight,[12] the extra weight gained by the use of Na compared to the Li-case amounts to 2.9 %. Using a Na-salt $NaPF_6$ (167.9 g mol^{-1}) instead of the $LiPF_6$ (151.8 g mol^{-1}) the weight increase of the entire battery amounts to 0.2 %, considering a 1.8 % contribution of the salt to the total battery mass.[12] Thus, the argument of the weight benefit by using Li from purely gravimetric considerations does not hold true, since in an analogue Na-ion battery (NIB) the overall battery weight can be lowered by 4.6 % only by using a different current collector. The crucial parameter for mobile applications definitely is the energy density, which drops by 8.3 % by solely considering the voltage

loss caused by the less negative Na/Na^+ potential (-2.71 V *vs.* NHE)[13] and assuming a cathode potential of 4 V (a typical value, e.g. for $LiMn_2O_4$)[16]. Thus, the overall loss in gravimetric energy density of NIBs compared to LIBs amounts to only a few percent. One should bear in mind that these calculations are based on the assumption of Li^+ and Na^+ intercalating into the electrode materials equally well. In reality, electrode capacities of NIBs might differ to LIBs. One for instance can practically insert 350 mAh g^{-1} of Li^+ into graphite,[17] whereas less Na^+ can be reversibly intercalated (100 mAh g^{-1}, and that only by co-intercalating solvent).[18]

An advantage often used to motivate NIBs is the potentially lower costs and the availability and production capabilities of the raw materials needed to produce Li, respectively Na. Figure 3 illustrates the elemental abundance in the earth´s crust. Na is about three orders of magnitude more abundant than Li, directly reflecting in the crude material price of the Li (65 US$ kg^{-1}, battery grade, March 2017) and the Na (2.5 US$ kg^{-1}, battery grade, March 2017).[19] An estimation of the total Li-mass in a battery based on the numbers given by Dunn *et al.*[12] amounts to 1.35 % of the total battery weight, whereas for Na it is 4.8 %. Considering the metal prices, one ends up currently with approximately 76 US¢ price benefit per kg battery of a NIB compared to a LIB, based on the higher abundance of Na in the earth´s crust. Figure 3 also shows the abundance of Al and Cu. The metric ton of Al is traded with 1727.74 US$ (March 2017), while one ton of Cu costs 5660.35 US$ (March 2017).[20] The savings coming from the Al current collector amount to approximately 57 US¢ per kg battery, which is in the same order as the savings obtained from the cheaper Na.

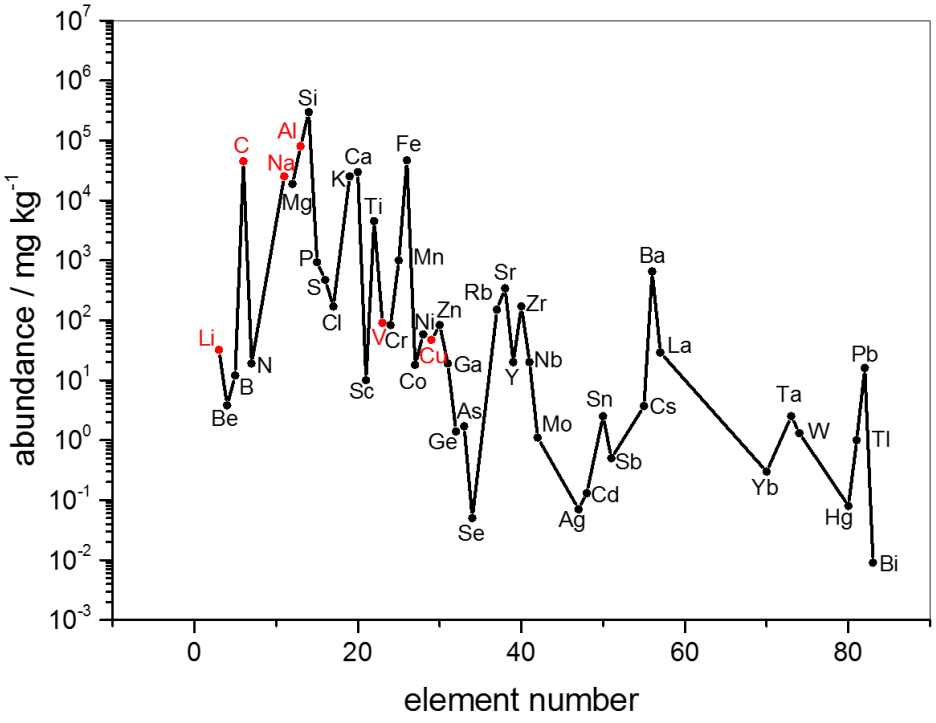

Figure 3: Elemental abundance in the earth´s crust. Numbers are based on a study of Alekseenko et al.[21]

The focus of electric mobility is to achieve high energy and power densities in batteries with secondary importance of battery price. Therefore, the lower battery costs of a NIB, which from the upper considerations for a 500 kg battery pack in an electric vehicle only amounts to a saving of roughly 700 US$, cannot outweigh the larger energy and power densities of LIBs, especially since energy- and power-densities in real LIBs are even larger than in real NIBs. In large scale energy storage devices for stationary application, as is needed for renewable energies, for instance to store the electricity

produced by a photovoltaic device or a wind turbine, weight is not such an issue. Instead, battery costs and especially the use of abundant materials permitting upscaling to large scale becomes important. Here, battery costs can be lowered by a suitable choice of electrode materials as well as a suitable electrolyte. Materials known from LIB-research cannot simply be transferred to NIBs, since their Li- respectively Na-electrochemistry can be fundamentally different. Hence, new materials need to be found, characterized and understood for application in NIBs. This challenge defines the task of this thesis.

Materials for negative electrodes in NIBs include metal oxides and sulfides, alloy based materials, organic composites as well as carbon based materials.[22, 23] Each material comes along with a variety of advantages and issues for application in a NIB, which will be illuminated in more detail in a section dedicated to the state of the art of battery research (chapter 3). Due to their high elemental abundance in the earth´s crust (Figure 3), carbon based materials, especially graphite, are of special interest as a negative electrode material for NIBs, as they are considered as an extremely low cost material. On the same time, the introduction of graphite anodes in LIBs in the early 1990ies paved the way to their commercialization. Graphite is a well understood low cost material with beneficial electrochemical properties and one of the most desired negative host materials for sodium ions, believed to be the missing step for NIB-commercialization.[24] Attempts to reversibly intercalate Na into graphite failed during the past twenty years.[25–27] With the discovery of a Na-co-intercalation from ether-based electrolytes in 2014 by Jache *et al.*,[18] reasonable amounts of Na^+ could be reversibly stored in graphite electrodes by partially screening the Na-ion charge and hence facilitating the intercalation processes. However, there is still a lack in understanding the fundamental co-intercalation mechanisms, especially when using the four shortest glymes (mono- to tetra-glyme) as solvents. Here, the tri-glyme shows an exceptional behavior, which is totally different from the other solvents and which is not understood. Moreover, the formation of a solid electrolyte interphase (SEI) in these glyme electrolytes is an open question.

These questions are subject of this thesis: The general SEI-formation on graphitic electrodes in organic electrolytes will be treated in section 5.1. A deeper mechanistic understanding of the co-intercalation processes of solvated Na-ions into graphite is gained in section 5.2. Detailed *in-operando* scanning tunneling microscopy studies on graphite single crystal model electrodes give further insight and an atomistic understanding into the SEI-formation mechanism as well as phase transitions of the graphite lattice upon sodiation/de-sodiation in a NIB. The SEI growth can be imaged in real time, not only permitting morphological studies, but also revealing potential dependent processes and time scales. The observation of graphite phase transitions upon sodiation visualizes the lattice expansion of the graphite on an atomic level, not only revealing the intercalation mechanism, but also providing a direct measure of diffusion rates of Na-species migrating within the graphene sheets of the graphite crystal – a unique observation so far. Complemented with other *in-operando* techniques, such as X-Ray diffraction and the electrochemical quartz crystal microbalance technique, the structural changes of the graphite crystal during operation in a NIB are further studied. Especially a proof of principle of the latter technique employing graphite coated quartzes is presented, demonstrating a similar sensitivity towards crystal lattice expansions/retractions as the X-Ray powder diffraction technique.

The studies on the negative electrodes are complemented by studies on materials for positive electrodes. Many compounds are known, which can reversibly intercalate Na-ions at high positive potential, making them the ideal counterpart to the above introduced low voltage materials for the negative electrode. One can categorize positive electrode materials in different classes: layered transition metal oxides, polyanionic compounds, Prussian blue analogues and organic materials.[28–30] Again, each material has some advantages and disadvantages as NIB positive electrode, being

described in more detail in chapter 3. An interesting positive electrode material for NIBs is the orthorhombic V_2O_5, as it is an intercalation host for a variety of mono- and multivalent ions,[31] it was successfully employed in NIBs,[32] and it possesses a wide range of powder morphologies on the micro- and nanoscale.

Besides gaining a fundamental understanding of the V_2O_5 electrochemistry in a NIB, the scope of this thesis also is to study the influence of the V_2O_5-morphology on the battery performance in NIBs to develop strategies for further improvements (section 5.3). The starting point again is a scanning tunneling microscopy study on V_2O_5 single crystal model electrodes, permitting atomistic studies on the V_2O_5 phase transitions during operation in a NIB. This knowledge as well as the knowledge gained from a morphological study of different V_2O_5 electrodes, where micro-materials such as hollow or yolk-shell V_2O_5 microspheres are compared to nano-materials like V_2O_5 nanobundles or -belts, helps to optimize the V_2O_5 electrode. In view of developing a NIB prototype employing a graphite negative electrode and a V_2O_5 positive electrode, non-standard electrolytes are tested with V_2O_5 electrodes. Finally, the optimized V_2O_5 electrode and battery electrolyte are combined to a fully operating full cell NIB employing a graphite anode, the first prototype of its kind. The work on the full cell NIB will complete the thesis in section 5.4. Hence, this thesis represents the development of a NIB starting by answering and understanding the fundamental questions regarding the electrochemical behavior of the tested materials and to apply and transfer this knowledge to a fully operating NIB prototype. At the same time advanced experimental techniques, such as in-operando XRD, electrochemical STM, scanning electrochemical potential microscopy (SECPM) or the EQCM technique with coated quartzes are applied, modified and optimized for battery research.

2 Fundamentals and Materials

2.1 Batteries[33]

Before introducing the fundamental electrochemistry, a short overview over different battery types shall be given. In general, one discriminates between non-rechargeable (primary) and rechargeable batteries (secondary), where the latter are of major interest for energy storage applications in the mobile sector, in portable electronic devices or in large scale stationary applications. Different battery types exist, each having advantages and disadvantages for certain applications. Figure 4 gives an overview over the most common battery concepts, which in part are used in commercial products (lead-acid, nickel-metal hydride and rocking chair batteries) and which in part are still concepts and have only been realized in laboratories so far (metal-air and dual-ion batteries). Each concept shall be briefly discussed in the following sections.

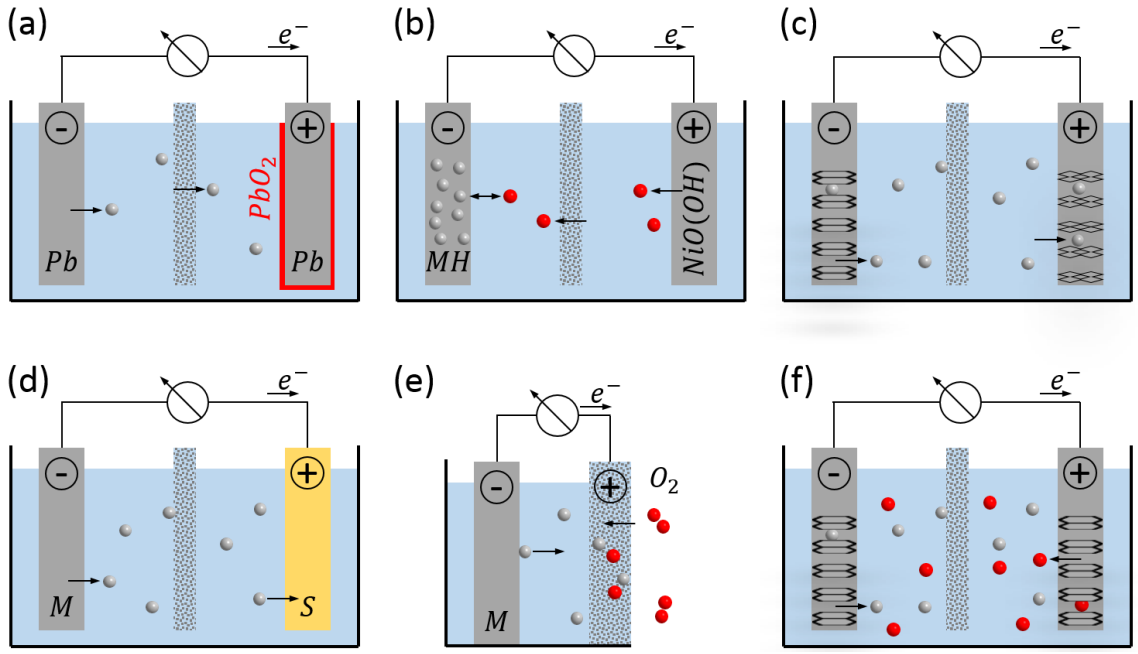

Figure 4: Different battery types during discharge in comparison: (a) lead-acid battery, (b) nickel-metal hydride battery, (c) rocking-chair battery, (d) metal-sulfur battery, (e) metal-air battery and (f) dual-ion battery. Grey symbols represent alkali-cations and red symbols represent OH^--, O^{2-}-anions, respectively other anions.

2.1.1 Lead-acid battery

Figure 4 (a) shows the setup of a lead-acid battery. It consists of a Pb and a PbO_2 electrode immersed in concentrated sulfuric acid (H_2SO_4). A proton conducting separator prevents an electrical short between the two electrodes and at the same time serves as transport medium for the exchanged ions. When discharging the battery, the Pb electrode is the negative electrode, *i.e.* the anode, and the PbO_2 electrode is the positive electrode, *i.e.* the cathode. For matters of convenience, in the following the negative electrode shall always also be called 'anode' and the positive electrode 'cathode', even though during charging the assignment would actually be reversed. The anode reaction is:

$$Pb + H_2SO_4 \rightleftharpoons PbSO_4 + 2H^+ + 2e^- \quad (1)$$

The discharge reaction occurs from left to right, while during charging it is opposite. At the same time, the reaction at the cathode is:

$$PbO_2 + H_2SO_4 + 2H^+ + 2e^- \rightleftharpoons PbSO_4 + 2H_2O \quad (2)$$

Thus, the overall cell reaction is:

$$Pb + PbO_2 + 2H_2SO_4 \rightleftharpoons 2PbSO_4 + 2H_2O \quad (3)$$

Even though the lead-acid technology was already developed in 1854, it is still present to date, also due to low cost. On the other hand, they have severe shortcomings in terms of energy and power density and great care has to be taken regarding the sulfuric acid. Thus, alternative battery concepts based on different electrochemistries have been developed, where some selected examples are introduced in the following sections.

2.1.2 Nickel-metal hydride battery

Another commercially available secondary battery is the nickel-metal hydride battery (Figure 4 (b)). As the lead acid battery, the nickel-hydride battery employs an aqueous electrolyte, with pH 14

however. The working principle is based on the hydrogenation of metals, where hydrogen ions are inserted into the metal M, followed by a reduction to a metal hydride MH and the implementation into the metal crystal lattice. This reaction occurs at the negative electrode:

$$MH + OH^- \rightleftharpoons M + H_2O + e^- \quad (4)$$

Most metals show this hydrogenation behavior. A material typically employed in commercial metal-hydride batteries is the $La_{0.8}Nd_{0.2}Ni_{2.5}Co_{2.4}Si_{0.1}$ electrode. Upon discharge, a proton is released from the MH electrode to form water with the hydroxide anion. This anion is produced at the positive electrode, from where it passes through the separator to the negative electrode. At the positive electrode, Ni(III)-hydroxide is reduced consuming the electron and converting water to the hydroxide anion:

$$NiO(OH) + H_2O + e^- \rightleftharpoons Ni(OH)_2 + OH^- \quad (5)$$

The total cell reaction hence is:

$$MH + NiO(OH) \rightleftharpoons M + Ni(OH)_2 \quad (6)$$

Nickel-metal hydride batteries have an enhanced energy as well as power density compared to the lead acid batteries, but suffer from an increased self-discharge, a weakness to over-charging/-discharging and a performance loss at low temperatures.

2.1.3 Rocking chair battery

Today, the most prominent battery is the lithium-ion battery, whose operation principle is based on an intercalation/insertion electrochemistry of Li-ions into a host material (Figure 4 (c)). Li^+ can intercalate in different materials at different electrochemical potentials. Choosing two different materials with a large voltage difference allows to store Li^+ at two different energy levels, which also explains the energy storage principle. In order to store/withdraw energy from the battery, the Li^+ must be shuttled between the two electrodes when charging/discharging, in analogy to a rocking chair. In commercial batteries graphite is used as anode material, as it offers low voltage levels to the Li^+. In most LIBs $LiCoO_2$ based compounds are the cathode material of choice.[34] Consequently, the anode half-cell reaction is:

$$LiC_6 \rightleftharpoons Li^+ + e^- + C_6 \quad (7)$$

At the cathode, it is:

$$CoO_2 + Li^+ + e^- \rightleftharpoons LiCoO_2 \quad (8)$$

The overall reaction finally is:

$$LiC_6 + CoO_2 \rightleftharpoons C_6 + LiCoO_2 \quad (9)$$

Since voltage differences between anode and cathode are reached, which exceed the electrochemical stability window of aqueous electrolytes, other, organic electrolytes need to be employed. Such electrolytes in part sustain voltages of more than 5 V. Mostly, they are made from mixtures of carbonate solvents, such as dimethyl carbonate (DMC), ethylene carbonate (EC), propylene carbonate (PC), *etc*. Again, the two electrodes are separated by an ion conducting separator or membrane, which prevents an electrical short circuit between the two electrodes.

Rocking chair batteries can be applied in manifold electrochemistries, not only making use of monovalent alkali metal ions, but also of bivalent and even trivalent ions. Each of these concepts again is linked with their own challenges, advantages and drawbacks.

Historically, the concept of a rocking chair battery was developed, since it solved a severe safety issue: Originally, Li-metal anodes were used in LIBs due to their high energy and power density. However, metallic Li is a highly reactive material and potentially dangerous. On the other hand, the repeated dissolution/deposition of Li from/on the Li-electrode leads to the formation of dendrites, which penetrate the separator and finally shorten the anode and cathode. This not only destroys the battery, but can also lead to thermal runaway and finally to ignition. Still, research is seeking for ways, how to build a safe version of Li-metal batteries, mainly by replacing the liquid electrolyte with solid, ion-conducting ceramics or glasses (solid-state battery).

$LiCoO_2$ positive electrodes in LIBs possess a high operating voltage and capacity, but suffer from some drawbacks, like a structural instability when too much Li^+ is removed upon discharge, or a spontaneous reaction with the electrolyte, leading to harmful gas evolution like CO_2, CO, CH_4, C_2H_4, C_2H_6, O_2 and H_2O and concomitant safety issues.[35, 36] Moreover, the Co is comparably expensive, which can be replaced by the more abundant Mn. Due to its economic and environmental benefits, $LiMn_2O_4$ is an attractive alternative to $LiCoO_2$, but has a lowered voltage and capacity. Another widely used electrode material is $LiFePO_4$, which is composed of earth abundant and environmentally friendly materials. At the same time its electronic conductivity is poor, resulting in voltage losses and low rate capabilities.[35, 36] The graphite negative electrode can also be replaced by a titanium oxide based $Li_4Ti_5O_{12}$ electrode. In contrast to the graphite electrode, the intercalation potential of Li-ions into the $Li_4Ti_5O_{12}$ lies within the stability window of the electrolyte solvents, preventing electrolyte decomposition and extending the battery lifetime. On the other hand, this also results in voltage losses and a lowered energy density.[37, 38]

Besides these materials based on an intercalation chemistry, other electrode concepts exist, such as alloying electrodes, where the alkali ions form an alloy with the electrode. Alloying electrodes can store huge amounts of charge, however, alloying is also accompanied by large volume changes between charged and discharged state, limiting the battery lifetime. A famous example are Si negative electrodes.[39] Another concept is the conversion type electrode, where a transition metal fluoride (*e.g.* FeF) and the alkali-ion (*e.g.* Li^+) exchange an anion (*e.g.* F^-) upon charge/discharge. Capacities obtained with conversion electrodes lie between the intercalation and the alloying electrodes, making them potentially interesting for application. The conversion reaction, however, is also accompanied by large volume changes, by a large voltage hysteresis between charge and discharge, which leads to a poor round trip efficiency, and by a large irreversible capacity loss in the first cycle.[39]

2.1.4 Metal-sulfur battery[40, 41]

Another approach to further increase the energy and power density of a battery is to combine an electropositive metal anode with an electronegative cathode material, such as sulfur (Figure 4 (d)). Room temperature metal-sulfur batteries, with the Li-S-battery as frontrunner are supposed to be the next big step in battery technology and at the moment are taking the step from research to commercialization. Molten Na-S-batteries operating at elevated temperatures above the melting points of Na and S and employing a solid electrolyte have already been commercialized and were used as load-leveling and emergency power devices.[42] The electrochemistry is based on a reversible Li-dissolution/-deposition at the Li-anode:

$$2Li \rightleftharpoons 2Li^+ + 2e^- \tag{10}$$

The Li^+ migrates to the S-cathode, where it reacts to Li_2S:

$$S + 2Li^+ + 2e^- \rightleftharpoons Li_2S \tag{11}$$

The full cell reaction is:

$$2Li + S \rightleftharpoons Li_2S \quad (12)$$

The charging/discharging process occurs via the formation of different lithium polysulfides Li_2S_x ranging from Li_2S (fully discharged) via Li_2S_2, Li_2S_4, Li_2S_6, Li_2S_8 finally to S_8 (fully charged). These polysulfides have the tendency to dissolve in the electrolyte, which results in a considerable capacity fading and limited battery lifetime. Moreover, the safety issue with the metallic Li anode still persists. The polysulfide dissolution is tried to be suppressed by embedding the S into a stabilizing matrix of materials, such as carbon, which at the same time also increases the electric conductivity of the electrode. Of course, the Li can also be replaced by cheaper materials, like Na or Mg. Besides the potentially higher energy density of Li-S-batteries, the low material costs of S are another benefit.

2.1.5 Metal-air battery[43, 44]

A battery concept aiming into the same direction of combining a highly electropositive metal with a highly electronegative element is presented in Figure 4 (e). This concept is called metal-air battery. The anode again is a metal, whereas the cathode reactant is oxygen/air, similar as in a polymer exchange membrane (PEM) fuel cell. This reaction occurs at the conductive, porous separator, which is connected to the external electric circuit. As in a PEM fuel cell, the O_2 must be reduced at the cathode during discharge. In this sense, one can think about metal air batteries as a hybrid of a battery and a fuel cell - a reversible fuel cell with the metal as fuel.

The rather extreme concept of metal-air batteries is still part of conceptual studies, where the Li-air system is the main focus of research. Again, a metallic Li-electrode is deployed as anode:

$$2Li \rightleftharpoons 2Li^+ + 2e^- \quad (13)$$

In an aprotic electrolyte, the cathode reaction is:

$$2Li^+ + 2e^- + O_2 \rightleftharpoons Li_2O_2 \quad (14)$$

In total, the reaction is:

$$2Li + O_2 \rightleftharpoons Li_2O_2 \quad (15)$$

The main motivation for Li-air batteries is the outstanding theoretical energy density, which is as high as for gasoline. The realization of a properly working non-aqueous metal-air battery is still lacking, since so far only few reversible cycles were achieved. The battery community is skeptical about whether metal-air batteries can ever be brought to commercialization, since they suffer from a widespread of problems, including safety issues regarding the metal anode, the reversibility of the chemistry and kinetic issues occurring in the oxygen reduction reaction. Approaches to solve these problems are to not operate the battery as open system in air, but to store the pure oxygen in a tank or to operate in aqueous electrolytes, where the Li-anode must be protected by a thick membrane. Both approaches are disadvantageous in terms of energy and power density. The metal-air battery concept will probably remain a concept and not find its way into a real battery.

2.1.6 Dual-ion battery[45, 46]

Another interesting battery concept is the so called dual-ion battery (Figure 4 (f)). The beauty of this concept is that it applies two electrodes of the same kind, which during discharge intercalate cations at the anode and anions at the cathode. This for example allows to use a graphite-graphite cell, where Li^+ intercalates into the graphite anode and an X^- anion into the graphite cathode. The anion can also be multivalent. The corresponding reaction at the anode is:

$$LiC_6 \rightleftharpoons Li^+ + e^- + C_6 \quad (16)$$

For a monovalent anion, the cathode reaction is:

$$XC_6 + e^- \rightleftharpoons X^- + C_6 \tag{17}$$

Finally, the overall cell reaction is:

$$XC_6 + LiC_6 \rightleftharpoons X^- + Li^+ + 2C_6 \tag{18}$$

In contrast to the above introduced battery technologies, equation (18) contains the ions on the right side. This is simply due to the fact that the LiX-salt dissociates into the Li^+ and X^- ions in solution, which is also where the charge is stored. Opposite to all the above introduced battery concepts, where the charge is stored in one of each electrodes, the charge in a dual-ion cell is stored in the electrode (charged) or in the electrolyte (discharged).

Compared to rocking chair batteries, dual-ion batteries have slightly lower capacities, however voltages of far above 5 V can be obtained, for example when intercalating PF_6^- or $TFSI^-$ ($N(SO_2CF_3)_2^-$, bis(trifuoromethylsulfonyl)imide). Additionally, a high reversibility as well as the application of the inexpensive graphite electrodes make this concept a candidate for large scale energy storage devices.

2.2 Electrochemistry[47]

The battery concepts presented in the previous section all represent electrochemical devices. In order to facilitate the understanding of the results, the fundamentals of electrochemistry will be discussed in the next sections. This discussion starts with non-faradaic processes, where the electrochemical double layer is introduced. Thereafter, faradaic processes and the basic electrochemical thermodynamics are treated.

2.2.1 Non-faradaic processes

Electrochemistry starts, when bringing an electronically conductive material, for example a metal, in contact with an (often liquid) electrolyte, typically an ion-containing liquid solvent. Even for the simple system of a metal immersed in an (nearly) ion-free solvent like water, electrochemical processes at the metal-solvent interface occur, since solvent molecules often possess an electric dipole moment due to an uneven charge-distribution throughout the molecule. Assuming the simplest case of an uncharged metal, *i.e.* the metal has the so called 'Potential of Zero Charge' (PZC), immersed into a polar solvent, the solvent molecules will have a randomly distributed orientation at the metal-solvent interface. As soon as the metal is charged by a potential change, the metal no longer is at PZC. The polar solvent molecules feel the charged surface of the metal, which attracts and orients them to the surface so that the dipoles can minimize their free energy. The solvent orientation depends on the sign of the metal charge. The oriented dipoles build a bi-layered structure with the metal surface charges at the metal-solvent interface. Due to its two components, *i.e.* metal surface charge and oriented solvent dipoles, this structure is also called electrochemical double layer (EDL).

The EDL-structure becomes significantly more complex when introducing ions into the electrolyte. In order to keep the solution neutral, positively charged (cations) and negatively charged ions (anions) are present in the electrolyte in equal amounts (symmetric electrolyte). Similar as with the charged metal surface, the solvent molecules are attracted by the charged ions and orient their dipole moment accordingly (Figure 5). One talks about solvation, while the regular arrangement of the solvent molecules around the ions is called solvation shell.

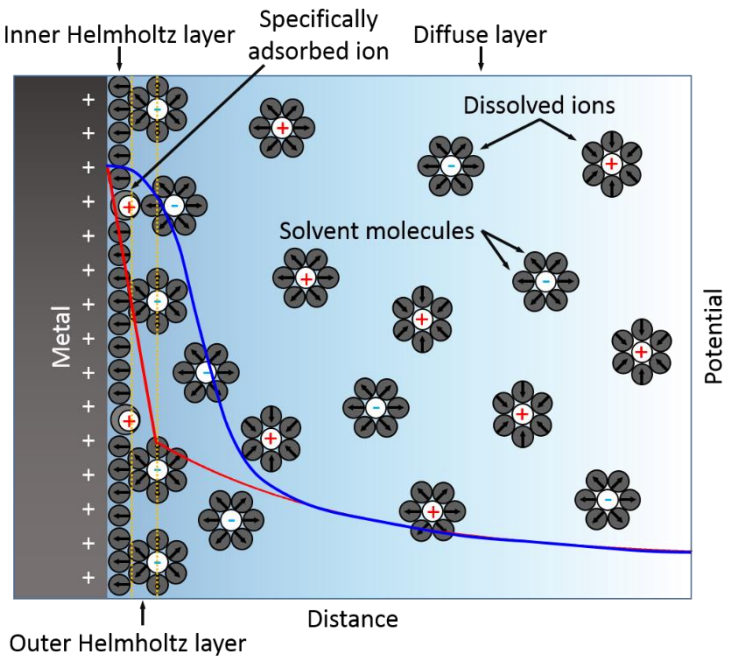

Figure 5: Structure of the EDL based on the Grahame[48] model. The red line illustrates the potential drop from the metal surface towards the bulk electrolyte according to the Gouy-Chapman-Stern model with the linear potential drop in the Helmholtz plane and the exponential potential drop in the diffuse layer (21). The blue line shows the sigmoidal potential decay, which was postulated and experimentally confirmed by Friedl et al.[49]

At PZC, the solvent molecules as well as the solvated ions again have a random distribution and orientation. In the absence of specific adsorption, there is no surface excess of one ionic species compared to the other. In 1853, Helmholtz[50] postulated the double layer for the first time and described it as the accumulation of ions at a metal surface charged with opposite sign, building up the outer Helmholtz plane (Figure 5). The geometry of the two adjacent charged layers reminds about a plate capacitor capable to store the double layer charge with a capacity C_{EDL}:

$$C_{EDL} = \frac{\varepsilon\varepsilon_0}{d_{EDL}} V_{EDL} \tag{19}$$

The two adjacent layers being separated by a dielectric with dielectric constant ε and vacuum permittivity ε_0 have a spacing d_{EDL} and a voltage difference V_{EDL} resulting in an approximately linear potential gradient $d\phi/dx = V_{EDL}/d_{EDL}$ in x-direction. No charge transfer across the metal-electrolyte interface occurs when charging/discharging the EDL. Hence, EDL-charging is a non-faradaic process.

The Helmholtz model neglects processes like electrode potential, ion-adsorption/-solvation, and thermal motion/diffusion of the solvated ions, which disturbs the planar bilayer structure of the EDL. Gouy[51] and Chapman[52] described the formation of a diffuse layer in order to refine Helmholtz´s model, however, their model fails for a strongly charged EDL, especially as the finite ion size is not considered. Stern[53] combined both models, the Helmholtz- and the Gouy-Chapman-model, where the double layer consists of a rigid inner and an outer diffuse layer.

So far, all models considered the ions as point charges. The EDL-scheme presented in Figure 5 is based on the Grahame[48] model, which also accounts for ionic radii plus their solvation shell. The inner Helmholtz plane is defined as the layer of specifically adsorbed ions to the electrode, while the outer

Helmholtz plane is determined by adsorbed solvated ions. Towards the bulk electrolyte an exponential ion concentration gradient C is observed:

$$C = C_0 \exp\left(\frac{-ze\phi}{k_B T}\right) \tag{20}$$

As written, equation (20) only holds true for symmetric electrolytes with the bulk ion concentration C_0, ion charge z and elementary charge e, the Boltzmann constant k_B and temperature T. Treating the diffuse EDL as a Poisson-Boltzmann problem and assuming a small potential drop across the diffuse layer, an exponential potential drop results from equation (20):

$$\phi = \phi_0 \exp\left(-\sqrt{\frac{2C_0 z^2 e^2}{\varepsilon\varepsilon_0 k_B T}}\, x\right) \tag{21}$$

Thus, within the Helmholtz planes one observes a linear potential drop, whereas the potential decays exponentially in the diffuse layer. The potential drop is also illustrated in Figure 5 (red line).

Of course, the Grahame model is still oversimplified. The EDL model was advanced by gaining a deeper understanding of redox reactions of specifically adsorbed ions, which is also known as pseudo capacitance, the fundamental principle of supercapacitors (Bockris-Müller-Devanthan[54], Trasatti[55], Conway[56], Marcus[57, 58]). Schmickler and Henderson[59, 60] also considered the influence of electrode material on the EDL by treating the metal electrode as electron Fermi-gas, which is known as jellium model. In the jellium model, the metal atoms of the electrode are treated as a positive charge background, which abruptly stops at the electrode electrolyte interface, while a negatively charged electron cloud reaches into the electrolyte. With the recently increased use of ionic liquids in electrochemistry, additional EDL structures were found. At a charged electrode the ionic liquid anions and cations form a layered structure of alternating anion- and cation-layers, which becomes more and more diffuse with increasing distance to the surface.[61]

2.2.2 Faradaic processes

2.2.2.1 Electrochemical equilibrium

In the discussion about the EDL electrochemistry only non-faradaic processes in the electrode-electrolyte interface were considered. With the introduction of a redox couple into the electrode-electrolyte system, also faradaic processes can occur according to:

$$Ox + ne^- \rightleftharpoons Red \tag{22}$$

In a faradaic process an oxidized chemical species Ox is reduced to a species Red by the uptake of n electrons and vice versa. At electrochemical equilibrium the oxidation and the reduction reaction occur at the same rate resulting in a zero net current. Moreover, the redox reaction establishes an equilibrium potential U^0, which can be derived from a thermodynamic treatment:

$$U^0 = U^{00} + \frac{RT}{nF} \ln \frac{a_{ox}^{\nu_{ox}}}{a_{red}^{\nu_{red}}} \tag{23}$$

This equation is the famous Nernst equation, where a_{ox} and a_{red} are the activities of the oxidized, respectively reduced species with stoichiometric coefficients ν_{ox} and ν_{red}. For dilute solutions, the activities a_{ox} and a_{red} can be substituted by concentrations of the reactants (C_{ox} and C_{red}), while in gaseous systems they can be approximated by partial pressures. In practical cells, however, a 1 M solution might no longer be at unit activity, since the solution is not dilute anymore. The Nernst equation describes the concentration dependence of the equilibrium potential of a redox reaction.

It is inconvenient to evaluate half-cell potentials when dealing with activities, which usually are unknown. A more handy way to report potentials is to make use of the formal potential $U^{00'}$. Equation (23) can also be written as a function of the dimensionless activity coefficients γ_{ox} and γ_{red}:

$$U^0 = U^{00} + \frac{RT}{nF} \ln \frac{\gamma_{ox}^{\nu_{ox}} C_{ox}^{\nu_{ox}}}{\gamma_{red}^{\nu_{red}} C_{red}^{\nu_{red}}} \tag{24}$$

Splitting the natural logarithm into two terms, equation (24) turns into:

$$U^0 = U^{00'} + \frac{RT}{nF} \ln \frac{C_{ox}^{\nu_{ox}}}{C_{red}^{\nu_{red}}} \tag{25}$$

where the formal potential is:

$$U^{00'} = U^{00} + \frac{RT}{nF} \ln \frac{\gamma_{ox}^{\nu_{ox}}}{\gamma_{red}^{\nu_{red}}} \tag{26}$$

The activity coefficient γ_i of species i can be approximately calculated according the Debye-Hückel theory,[62] where the electrostatic interaction between ions in solutions is described. The activity coefficient is calculated by:

$$\ln \gamma_i = -\frac{z_i^2 e^2}{8\pi\varepsilon\varepsilon_0 k_B T} \frac{\kappa}{1 + \kappa r_i} \tag{27}$$

The parameter κ contains the ionic strength $\mathrm{I} = \sum_i C_i z_i^2$ with the concentration C_i and ionic charge z_i of ions i:

$$\kappa = \sqrt{\frac{2N_A e^2 \mathrm{I}}{\varepsilon\varepsilon_0 k_B T}} \tag{28}$$

N_A is the Avogadro constant.

In aqueous electrolytes U^{00} is tabulated for the most important redox couples. As absolute electrode potentials cannot be measured, the standard cell voltage measured against a second electrode with another redox couple at defined and constant activities is reported in these tables. The usual reference system is the standard hydrogen electrode consisting of a Pt electrode in contact with the redox couple H_2/H^+ at pH = 0 and at a hydrogen pressure of 1 bar. The potential of this reference electrode is arbitrarily defined as 0 V. Important relevant standard potentials in this work are Li/Li^+ (-3.04 V *vs.* H_2/H^+) and Na/Na^+ (-2.71 V *vs.* H_2/H^+). If not explicitly mentioned, the electrode potentials of the latter two metal/metal-ion redox couples serve as reference potentials in this thesis in corresponding electrochemical systems.

2.2.2.2 Electrochemical non-equilibrium

Up to here, the discussion was limited to thermodynamic equilibrium, thus the reduction and oxidation in the redox reaction in equation (22) proceeded at the same rate. Disturbing the equilibrium, for example by applying/drawing an external current, a deviation of the electrode potential U from the equilibrium potential is observed - the so called overpotential η:

$$\eta = U - U^0 \tag{29}$$

n electrons are participating in the general redox reaction in equation (22). A multi-electron reaction therefore can be separated into n one-electron, one-step reactions according to:

$$Ox' + e^- \underset{j_a,\ k_{ox}}{\overset{j_c,\ k_{red}}{\rightleftharpoons}} Red' \tag{30}$$

The reduction has a reaction rate constant k_{red} and delivers a cathodic partial current (density) j_c, whereas the oxidation rate is k_{ox}, which results in an anodic partial current j_a. The total current density j of the reaction is the sum of both, anodic and cathodic current density:

$$j = j_a + j_c \tag{31}$$

After a theoretical treatment, where the forward and the backward reaction in equation (30) are treated as reactions following an Arrhenius type behavior, one obtains a relation between the overpotential and the current density of the reaction:

$$j = j_0 \left\{ \frac{C_{red}(0)}{C^*_{red}} \exp\left[\frac{(1-\alpha)F}{RT}\eta\right] - \frac{C_{ox}(0)}{C^*_{ox}} \exp\left[\frac{-\alpha F}{RT}\eta\right] \right\} \tag{32}$$

Equation (32) is also known as Butler-Volmer equation and describes the current response j of a redox reaction with transfer of a single electron as a function of overpotential η. At equilibrium $\eta = 0$ and the oxidation as well as reduction occur at the same rate j_0, the exchange current density, which yields a total current of zero. $C_{red}(0)$ and $C_{ox}(0)$ are the concentrations of the reduced, respectively oxidized species at the electrode surface, whereas C^*_{red} and C^*_{ox} are the concentrations in the bulk electrolyte. α is the so called transfer coefficient, which has a value between zero and one and which results from the shape of the energy barrier between the oxidized and the reduced state of the redox couple.

For large overpotentials, equation (32) increases exponentially and grows to infinity, which certainly has no physical meaning. Thus, the Butler-Volmer equation is only valid for small overpotentials, where the current density j is sufficiently small. At larger currents, the reactants are consumed at the electrode and the concentrations $C_{red}(0)$ and $C_{ox}(0)$ in equation (32) are no longer constant, but deviate from the bulk electrolyte concentration C^*_{red} and C^*_{ox} and also become a function of time ($C_{red}(0,t)$ and $C_{ox}(0,t)$). With the varying concentrations, the Butler-Volmer equation can be refined to:

$$j = j_0 \left\{ \frac{c_{red}(0,t)}{c^*_{red}} \exp\left[\frac{(1-\alpha)F}{RT}\eta\right] - \frac{c_{ox}(0,t)}{c^*_{ox}} \exp\left[\frac{-\alpha F}{RT}\eta\right] \right\} \tag{33}$$

This equation is capable to predict the current response of an electrode as a function of electrode potential, however, the concentration at the electrode surface itself is a complicated function and depends on processes like electrolyte diffusion or convection.

Electrochemical methods make use of the current-voltage dependence. Thus, one distinguishes two types of methods: potentiostatic and galvanostatic methods. In potentiostatic methods a constant potential is applied to the electrode and the resulting current response I is recorded with time t, while in a galvanostatic measurement a constant current is applied to the electrode and the voltage response is recorded.

Performing a potential step at an electrode initially in equilibrium, one disturbs the equilibrium resulting in an electrochemical current. This current will flow, until the system is in equilibrium again. Typically, the current exponentially decays with time for capacitive currents, like charging the EDL, or with a $t^{-1/2}$ behavior for Cottrell semi-infinite diffusion processes, which can be fast electrolyte or slow solid state ion-diffusion. Thus, when performing a potential step of a certain step size, one can

get information about the underlying processes by recording the current signal. This technique is called chronoamperometry. The galvanostatic analogue is called chronopotentiometry.

Measuring a series of chronoamperograms or chronopotentiograms, where relatively small potential respectively current steps are performed, one cannot only get insight into the potential dependence of electrochemical processes, but one can also measure diffusion coefficients. As mentioned above, electrochemical processes occur in parallel and superimpose, when performing a potential step. Each process, however, proceeds at a different rate, which is why they are dominant in certain time regimes, depending on the corresponding diffusion coefficient D_0. Solid state diffusion of ions in the electrode for instance is a Cottrell diffusion process, which is described by the so called Cottrell equation:[63]

$$It^{1/2} = D_0^{1/2}\,\Delta Q / l\pi^{1/2} \tag{34}$$

A certain amount of charge ΔQ is 'consumed' at the electrode during the potential step, while the charge carriers have to diffuse a path of characteristic length l. The Cottrell equation shows an $It^{1/2}$ *vs.* t dependence, which can be used to determine the diffusion coefficient D_0. Knowing about ΔQ and l, one can either directly read out D_0 from the Cottrell plateau in a $It^{1/2}$ *vs.* t plot or from the slope of the linear plot of the I *vs.* $t^{-1/2}$ plot in the Cottrell region. From a series of chronoamperograms/chronopotentiograms one can determine the potential dependency of diffusion coefficients and link it to processes like adsorption, absorption, intercalation, etc. This method is called the potentiostatic intermittent titration technique (PITT), respectively galvanostatic intermittent titration technique (GITT).

PITT and GITT are often used to deepen the understanding about phase transitions and to quantify diffusion in battery electrodes. In PITT, which is the potentiostatic analogous to GITT, the electrode is kept at a specific potential and the current is recorded with time. Afterwards, a small potential step (PITT) respectively current step (GITT) is performed and the resulting current- (PITT)/voltage-transient (GITT) is measured. This procedure is repeated until the potential region of interest is scanned. The charge of the individual transients plotted against the electrode potential reveal highly resolved charge peaks whenever a phase transition occurs. Moreover, one obtains the diffusion coefficient as a potential dependent parameter.

Changing the electrode potential continuously, one can record a current-voltage curve, which gives insight into electrochemical processes, since it always shows a current increase according to equation (33), when the electrode potential is in a region of the redox potential of a redox active species in the electrode-electrolyte interface. Performing a linear potential sweep between two potentials at a potential sweep rate $\nu = dU/dt$ is also called linear sweep voltammetry (LSV). A potential sweep between two potential vertexes followed by switching to a backward potential sweep (*i.e.* sweeping from second to first potential vertex) is called cyclic voltammetry (CV).

Non-faradaic processes, such as EDL charging show up as a constant current background in the CV, with a current:

$$|I| = AC_{EDL}\nu \tag{35}$$

The current I caused by the EDL charging linearly scales with the potential sweep rate ν, often also called potential scan rate, and with the electrode surface area A. Thus, a systematic variation of ν can be used to determine C_{EDL} when A is known, or A when C_{EDL} is known. Diffusion limited, faradaic processes cause a peak in the LSV, respectively CV, which has a peak current I_p of:

$$I_p \propto n^{3/2} A D_0^{1/2} C \nu^{1/2} \tag{36}$$

The peak current is proportional to $n^{3/2}$, the number of transmitted electrons, the reactant concentration C, the square root of the sweep rate ν and the diffusion coefficient D_0. The latter can also be determined by measuring CVs at different sweep rates and analyzing the peak current density. This method can also be used to countercheck the D_0 determination from GITT and PITT for reversible reactions with semi-infinite diffusion.

Cyclic voltammetry is a potentiodynamic method, whereas the galvanostatic charging/discharging is often applied in battery research. Here, a constant current is applied to a battery electrode and the voltage response is analyzed. Whenever a faradaic process is triggered by the current, a voltage plateau is observed. Once that process no longer can supply the current, the voltage changes in order to maintain the current. Deriving the voltage-current profile, one obtains a so called dQ/dV-plot, which shows electrochemical processes in a similar way as CV, *i.e.* peaks can be observed at the characteristic potentials for the redox system. A notation often used in battery research is the so called 'C-rate', which indicates the current density used to charge/discharge an electrode/battery. The C-rate is noted as C/t, with the charging/discharging time t in hours. Thus, a rate of C/10 corresponds to a charging/discharging time of 10 h.

2.3 Electrochemical Cell

Three-electrode electrochemical measurements were performed in a so-called Swagelok® cell, which is sketched in Figure 6. The analyzed electrode, the working electrode (WE), is the sample. Its electrochemical behavior is characterized by measuring the current via a counter electrode (CE) and the potential via a reference electrode (RE), which is coupled to the system via a high input impedance in order to minimize a flow of current and to maintain a stable potential.

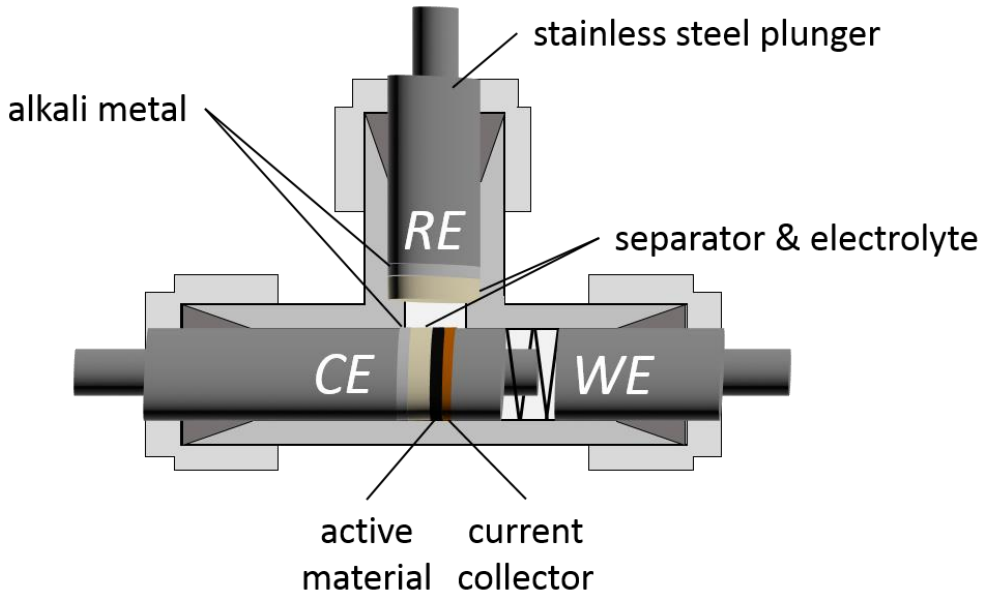

Figure 6: Setup of an electrochemical three electrode Swagelok® cell.

The WE consists of a current collector, which either is a Cu-foil for operation of anodes in LIBs or an Al-foil, and an active material. The electrode preparation is described in a separate section. A glass fiber separator (VWR collection, particle retention: 1.6 µm) between WE and CE/RE is soaked with an electrolyte and prevents a direct short circuit between the electrodes. CE and RE are composed of an alkali metal, depending on the battery type built. In LIBs Li (99.9 %, Alfa Aesar) is used, in NIBs Na

(99.9 %, Sigma Aldrich). All electrodes are contacted by stainless steel plungers, which are connected to a potentiostat. The Swagelok® cell is assembled airtight in an Ar-filled (Westfalen, 5.0) glovebox (MBRAUN, MB 200B glovebox and MB 20G LMF gas purifier) with O_2- and H_2O-levels not exceeding 1 ppm. After cell assembly, the cell can be operated outside the glovebox in air atmosphere.

A majority of the standard electrochemical measurements were performed in the three-electrode configuration in the Swagelok®-type cells. A couple of experiments on the other hand were also conducted in a two-electrode configuration in 2016-type coin cells (20 mm diameter, 1.6 mm height) with a stainless steel casing. The WE (16 mm) was separated by a glass fiber separator from a metallic Na-metal CE. Finally there were special cells for STM, EQCM and *in-operando* XRD measurements.

Electrochemical cells were either operated in a 'half-cell' or a 'full-cell' configuration. The term 'half-cell' in the following denotes a cell, where the WE was operated in combination with a Li-/Na-CE, which represents an 'infinite' ion-source. A 'full-cell' in contrast was a battery operated with a powder positive and negative electrode, resembling a full battery. Whenever a Li-/Na-CE was employed in combination with a powder-WE, *i.e.* the half-cell configuration, the operating voltage of the Li-/Na-electrode was less positive than for the powder electrode. Consequently, in this thesis the powder electrode in a half-cell was always operated as the positive electrode, even the low voltage graphite electrodes. This is important to keep in mind, as the terminology 'charge' and 'discharge' then is reversed compared to a full-cell.

2.3.1 Electrode Preparation and Active Material Syntheses

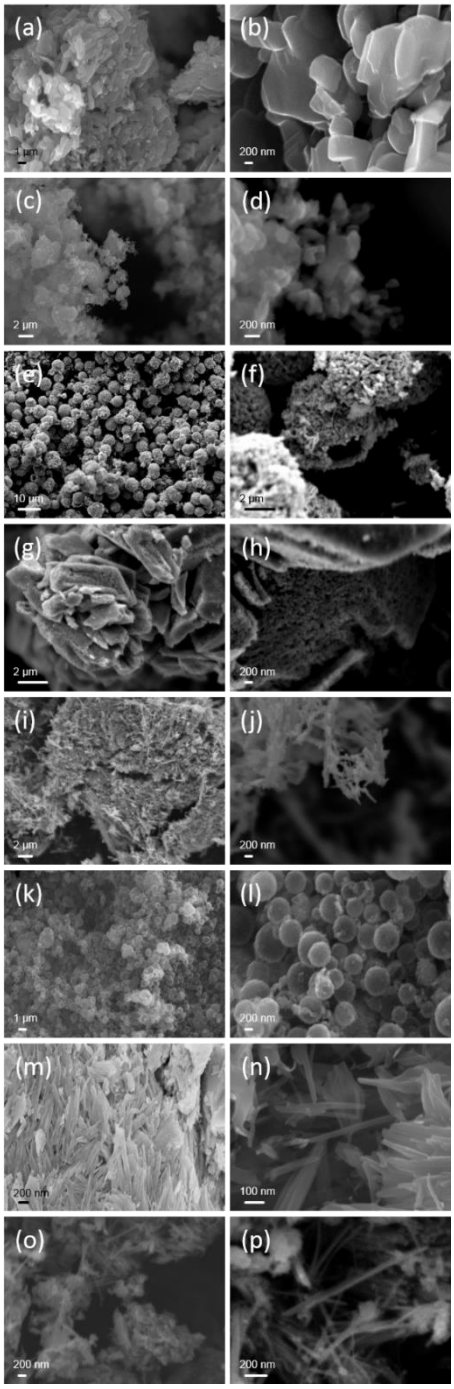

Figure 7: Secondary electron SEM micrographs of the different V_2O_5 powders: (a), (b) commercial V_2O_5 micro grains, (c), (d) V_2O_5 micro particles, (e), (f) hollow layered V_2O_5 microspheres, (g), (h) porous V_2O_5 micro grains, (i), (j), V_2O_5 nano rods (k), (l) yolk-shell V_2O_5 microspheres, (m), (n) sonicated V_2O_5 nanobundles and (o), (p) sonicated V_2O_5-TiO_2 nanobundles.

2.3.1.1 Battery electrodes

The preparation of electrodes for battery cells includes several fabrication steps. The process starts with coating an ink of active material, conductive carbon (Timical SuperC65 and SuperP), binder and solvent onto the current collector foil. The current collector foil was either Cu (9 µm, PI-KEM Limited, United Kingdom) or Al (15 µm, PI-KEM Limited, United Kingdom). For the use of conductive active materials like graphite, the conductive carbon was not used. Graphite (mesocarbon microbeads (MCMB, TB-17)) was mixed with a polyvinylidene fluoride binder (PVDF, Kynar 900 HSV) in a 9:1 ratio. The less conductive V_2O_5-slurries were prepared as an 8:1:1 mixture of V_2O_5, conductive carbon and PVDF-binder. The solvent N-Methyl-2-pyrrolidone (NMP, 99.5 %, anhydrous, Sigma Aldrich) was added to the mixtures and equally distributed the binder on the electrode particles. The obtained slurry was coated by an automatic coater (RK K CONTROL COATER) onto the current collector as a 100 µm to 250 µm thick film. After coating, the NMP solvent was evaporated at 50 °C from the coating. Afterwards, electrodes fitting into the cell were punched from the coated current collector (circular with 10 mm (Swagelok®) and 16 mm (coin-cell) diameter). In order to have a more homogeneous material distribution and a better contact to the current collector, the electrodes were mechanically pressed between two polished steel stamps with a pressure of 1 bar (Mauthe Maschinenbau, KBr-press PE-011). Before use in a battery, the electrodes as well as the glass fiber separators were vacuum dried at 120 ° for 2 h (Büchi Glass Oven B585 or in a Schlenk tube).

2.3.1.2 V_2O_5 Electrode Syntheses

Different V_2O_5 electrode materials were synthesized. The synthesized samples cover a wide morphological range reaching from different microstructures, such as solid and hollow microspheres, down to various nanomaterials. Figure 7 gives an overview of SEM micrographs showing the powder morphologies investigated in this study. The following sections shortly describes the syntheses of each sample.

2.3.1.2.1 Commercial V_2O_5 Micro Grains

A commercially available, high purity V_2O_5 powder was used for benchmark as well as gauging tests for sample characterizations (Figure 7 (a), (b)). It was used as purchased (99.99 %, Alfa Aesar Puratronic®).

2.3.1.2.2 V_2O_5 Micro Particles

From an 18 mM vanadium-(III)-acetylacetonate (97 %, Sigma Aldrich) and 0.14 mM polyvinyl-pyrrolidone (PVP) (96.1 %, Alfa Aesar, A14315) solution in ethylene glycol (99.8 %, Sigma Aldrich, anhydrous), which was stirred for 2 h at 140 °C and calcined for 2 h at 500 °C in air, hollow microspheres were supposed to be obtained.[64] Instead, V_2O_5 micro particles were obtained (Figure 7 (c), (d)).

2.3.1.2.3 Hollow Layered V_2O_5 Microspheres

Hollow layered V_2O_5 microspheres (Figure 7 (e), (f)) were synthesized by a solvothermal process following a recipe of Uchacker *et al.*[65]. A 75 mM NH_4VO_3 (99.0 %, Eastern chemical works) in ethylene glycol (AR, Beijing chemical works) solution was heated to 180 °C for 24 h in a homebuilt Teflon autoclave, followed by a 2 h calcination step in air atmosphere at 450 °C.

2.3.1.2.4 Porous V_2O_5 Micro Grains

A simple chemical synthesis yielded porous V_2O_5 micro grains (Figure 7 (g), (h)): An aqueous solution of 6.6 mM V_2O_5 and 19.8 mM $H_2C_2O_4 \times 2H_2O$ (≥ 99.0 %, Sigma Aldrich) was stirred at 80 °C until a clear blue VOC_2O_4 solution was obtained. 3 ml of that solution were mixed with 30 ml isopropanol (99.5 %, Sigma Aldrich, anhydrous) and were autoclaved (Berghof BR-100) for 2.5 h at 200 °C, followed by centrifugation (Eppendorf Centrifuge 5810 R) and calcination (Carbolite HST Horizontal Split Tube Furnace 1200) in air at 350 °C for 2 h. The obtained morphology was different to the morphology suggested by literature, where hollow microspheres were supposed to be synthesized.[66] Nevertheless, the obtained morphology was still considered worth to be studied in further detail.

2.3.1.2.5 V_2O_5 Nano Rods

V_2O_5 nano rods (Figure 7 (i), (j)) were synthesized in an autoclave from a solution of 0.36 g V_2O_5 and 5 ml H_2O_2 (VWR BDH Prolabo, AnalaR NORMAPUR® analytical reagent) in 60 ml H_2O for 48 h at 180 °C, which was centrifuged afterwards. The recipe can be found in literature.[67]

2.3.1.2.6 Yolk-Shell V_2O_5 Microspheres

For the synthesis of the yolk-shell V_2O_5 microspheres (Figure 7 (k), (l)), vanadium-(IV)-acetylacetonate (99.98 %, Sigma Aldrich) was slowly added to N,N-dimethylformamide (DMF) (99.8 %, Sigma Aldrich, anhydrous) under stirring until a transparent, yellowish solution was obtained. Subsequently, the solution was autoclaved for 24 h at 220 °C and finally calcined for 2 h at 400 °C in air.[68]

2.3.1.2.7 V_2O_5 Nanobundles

V_2O_5 nanobundles (Figure 7 (m), (n)) were synthesized via a sonochemical route described in Mao´s *et al.* publication.[69] An aqueous 50 mM solution of commercial V_2O_5 (99.99 %, Alfa Aesar Puratronic®) and 100 mM NaF (99.99 %, Alfa Aesar) was sonicated at 50 °C for 2 h at 100 % ultrasound intensity (Bandelin Sonopuls homogenizer, Bandelin UW3200 generator, Bandelin VS70/T sonotrode). After synthesis, the solution was washed three times by MilliQ water (Millipore Integral 3, > 18.2 MΩ, 3 ppb TOC) in a centrifuge in order to remove the residual NaF.

2.3.1.2.8 V_2O_5-TiO_2 Nanobundles

The V_2O_5-TiO_2 nanobundles (Figure 7 (o), (p)) were synthesized the same way as the above described V_2O_5 nanobundles, with the difference that 10 $\%_{wt}$ (80 mM) of TiO_2 (99 %, Alfa Aesar) are added to the solution.

2.3.2 Electrolytes

The electrolyte employed for studies on LIBs was a standard electrolyte, which can be purchased (Solvionics, H_2O < 20 ppm) as a ready 1 M $LiPF_6$ in a 1:1 mixture (by volume) of ethylene carbonate (EC) and dimethyl carbonate (DMC). All other electrolytes were self-synthesized by mixing salts

($NaClO_4$ (≥ 98.0 %, Sigma Aldrich ACS reagent) with solvents (EC (99 %, Sigma Aldrich, anhydrous), DMC (≥ 99 %, Sigma Aldrich, anhydrous), propylene carbonate (PC, 99.7 %, Sigma Aldrich, anhydrous), ethylene glycol dimethyl ether (G_1, 99.5 %, Sigma Aldrich, anhydrous), diethylene glycol dimethyl ether (G_2, 99.5 %, Sigma Aldrich, anhydrous), triethylene glycol dimethyl ether (G_3, 99 %, Alfa Aesar), tetraethylene glycol dimethyl ether (G_4, ≥ 99 %, Sigma Aldrich)). Not all electrolyte components can be purchased as anhydrous, which requires further drying with 3 Å molecular sieves (Merck Millipore). This way, the water content of all electrolytes can be lowered to well below 40 ppm (checked via Karl-Fischer titration measurements, Metrohm).

2.4 Scanning Electron Microscopy[70]

In contrast to STM (section 4.1.1), scanning electron microscopy (SEM) can be classified as optical microscope making use of the small electron-wavelength ($\lambda_{De\ Broglie} = \frac{2\pi\hbar}{\sqrt{2m_e eV_a}} = 12.3$ pm for a 10 keV electron)[71] in order to increase the resolution compared to an optical light microscope. The spatial resolution of a SEM usually is smaller than the STM-resolution, but there are fewer sample requirements than for a STM-sample: as for STM, the sample must be conductive/semi-conductive, but it does not need to be a flat, single crystalline surface and can also be a porous powder.

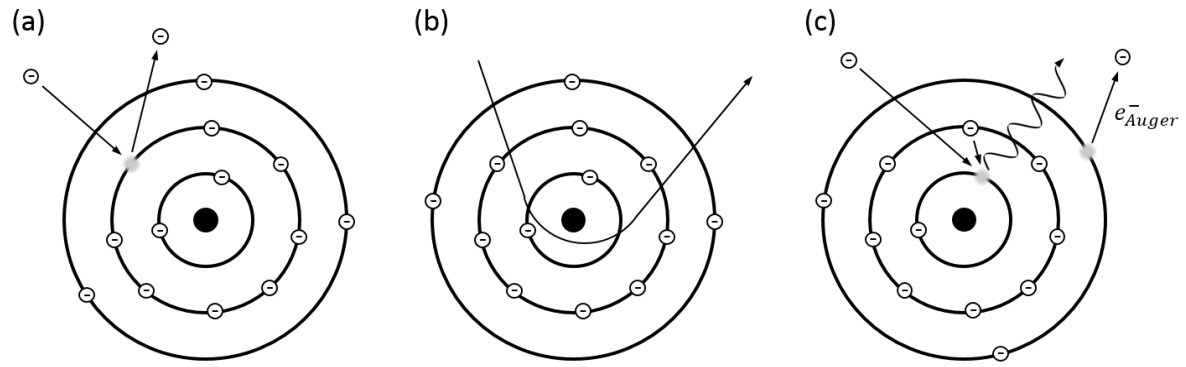

Figure 8: Scattering modes of incident electrons with the electron shell of an atom, either resulting in (a) secondary, (b) backscattered or (c) Auger electrons.[70]

SEM microscopes can be operated in two different modes, the secondary and the backscattered electron mode (Figure 8 (a) and (b), respectively). In both cases, an electron beam with typical energies of 10 keV to 100 keV is scanned over the sample surface in a defined raster. When interacting with the electron shell of the sample atoms, the accelerated electrons in the electron beam can in-elastically collide with an electron in the shell, creating an electron vacancy in the atom orbital. The ejected electron, the so called secondary electron, can be detected by a detector, which measures the intensity of this electron flux pixel by pixel, resulting in a microscopic image. For an incident electron being elastically scattered, the scattering strength scales with the atomic number Z of the sample atom. Heavy elements scatter electrons stronger, which leads to an additional, element specific contrast in the SEM images. The thus backscattered electrons again are detected by a detector assigning each pixel an electron intensity. Secondary and backscattered electrons are detected by different detectors. The data presented in this thesis were measured with devices from Zeiss (EVO MA10) and Hitachi (S 5500).

2.5 Energy Dispersive X-Ray Spectroscopy and X-Ray Photoelectron Spectroscopy[72]

The elastic scattering of incident electrons with the core electrons of an atom as sketched in Figure 8 (a) results in the formation of an electron vacancy in the atom orbital. If the vacancy is not in the outermost electron shell, an electron from an outer shell can jump into the vacancy and lower the

energy of the excited atom by emitting an X-ray photon of a material specific wavelength, depending on the energy difference between the two electron orbitals (Figure 9).

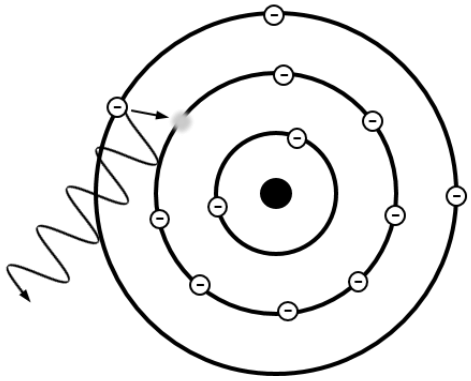

Figure 9: Relaxation of an excited atom via an electron orbital transition and the emission of an X-ray photon of characteristic wavelength.

This effect is used in energy dispersive X-ray spectroscopy (EDS), where every element emits its own characteristic X-ray radiation when externally stimulated, for instance by the electron beam of the SEM. The observed energy spectrum serves as fingerprint of every element. In combination with SEM, the SEM topology can be coupled to EDS and an elemental distribution within the sample is obtained. EDS measurements were conducted with a Hitachi (S 5500) device.

A closely related spectroscopic technique is the X-ray photoelectron spectroscopy (XPS), where an atom is ionized by monochromatic X-ray photons of energy $h\nu$. When the energy is sufficiently high, the atom is ionized and an electron of kinetic energy $E_{kinetic}$ is emitted (Figure 10). Knowing the X-ray photon frequency ν, one can measure the energy spectrum of the emitted electrons and obtains the element specific binding energy $E_{binding}$:

$$E_{binding} = h\nu - E_{kinetic} \tag{37}$$

XPS not only allows to detect the elements in a sample, but also allows to quantify the elemental composition of the sample from the signal intensities. In addition, the binding energy is not only element specific, but orbital specific. Thus, energy differences stemming from different electron spins, different oxidation states of an atom or different chemical environments can be analyzed.

In XPS a monochromatic X-ray beam excites the atoms of the sample, whereas an electron beam with some *keV* energy is used in EDS. The penetration depth of X-ray photons into the sample is in the range of a few nanometers, while the electrons can penetrate the sample by several micrometers. Thus, the information depth of both techniques is different, making XPS a highly surface sensitive technique. XPS measurements were done with a PHI Quantera SXM™ (Scanning X-ray Microprobe™, ULVAC-PHI).

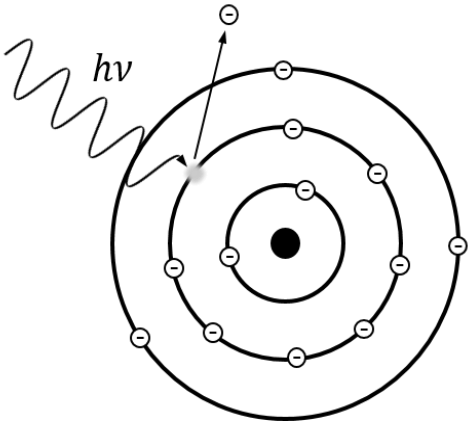

Figure 10: Scheme of the photoelectric effect as basis for XPS.

2.6 X-Ray Diffraction[73]

X-rays can be created in many ways; Figure 8 shows some examples. Accelerated electrons for instance can ionize atoms by inelastic scattering with the electron shell of the atom and ejecting an electron from a core shell (Figure 8 (a)). The excited atom relaxes by filling the created vacancy with an electron from an outer, *i.e.* higher energy orbital (Figure 9). The electron transition, if possible, lowers the energy of the atom by a quantified amount of energy, being the energy difference between both orbitals. Since energy must be conserved, a photon with this energy is emitted, having a transition characteristic wavelength.

Irradiating matter with electrons also results in another type of X-rays, the so called Bremsstrahlung. Bremsstrahlung is created by elastic scattering of electrons in the electron shell of an atom (Figure 8 (b)). When the trajectory of electrons is deflected, X-rays are emitted. Since the elastic scattering does not occur on quantified energy levels, but rather is continuous, the Bremsstrahlung spectrum is continuous, too.

Figure 8 (c) shows another electron scattering mode, where the inelastic electron collision creates a vacancy in a lower energy shell, which is filled by an electron from an outer shell. Simultaneously, the released energy from this transition is transferred to an electron in an outer shell, which besides X-rays is also emitted from the atom. The ejected electron is called Auger electron.

In X-ray diffraction (XRD) only the first two effects are of importance. In an XRD-diffractometer electrons are accelerated towards a Cu-target, where the continuous Bremsstrahlung and the characteristic Cu-radiation is created. For XRD studies, the X-rays for instance pass a graphite single crystal monochromator, which is optimized for the Cu-K_α transition and which filters out the Bremsstrahlung. The Cu-K_α transition results from an electron transition from the $2p_{3/2}$, respectively $2p_{1/2}$ orbital to the 1s orbital.

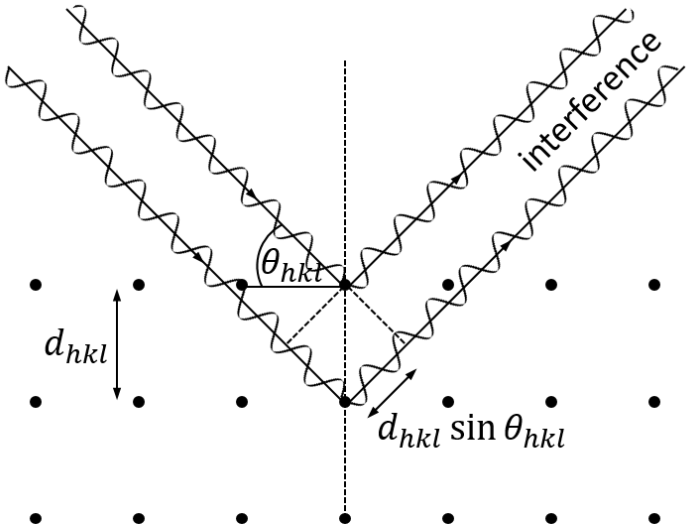

Figure 11: Bragg reflection of incident X-rays diffracted at a crystallographic surface at an angle θ and lattice constant d_{hkl}.

Considering a monochromatic wave front of X-rays inciding a crystal surface with different, parallel reflection planes, the total path travelled by the respective photons depends on the crystal plane they are reflected from (Figure 11). For a photon reflected at the outermost plane and a photon reflected at the first inner plane (or in general two neighboring planes), the difference in optical path amounts to $2d_{hkl} \sin \theta_{hkl}$.

The reflected photons thus interfere depending on the angle of reflection θ_{hkl}. If one varies θ_{hkl} and analyzes the interference pattern, one can find a positive interference whenever the optical path is an integer of $n \cdot \lambda$, with a natural number n and the photon wavelength λ. Thus, the formula

$$n \cdot \lambda = 2d_{hkl} \cdot \sin \theta_{hkl} = 2\frac{c}{l} \sin \theta_{hkl} \tag{38}$$

sets the crystal lattice parameter d_{hkl} in relation to the X-ray wavelength λ and the reflection angle θ. Equation (38) is Bragg´s famous law,[74] and describes the operation principle of XRD. Thus, from the angle θ_{hkl} with a maximum reflected XRD intensity, the lattice parameter d_{hkl} of a crystal can be calculated. In a polycrystalline sample or a powder sample composed of statistically oriented small single crystalline grains, a certain number of grains has a crystal orientation parallel to the surface, causing the diffraction signal.

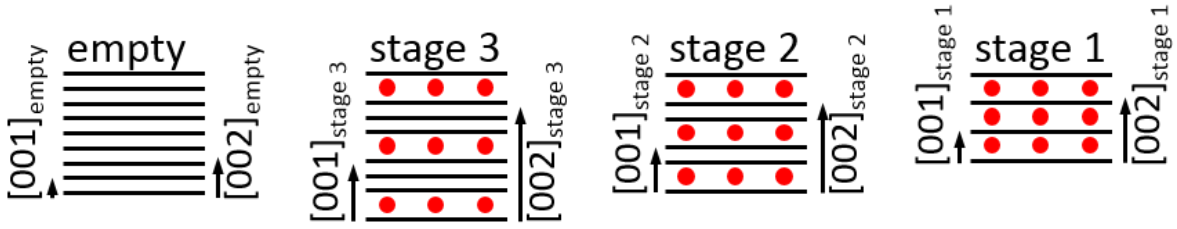

Figure 12: Schematic presentations of different staging in an intercalation compound with the corresponding lattice vectors of the [001] and [002] vectors. Black lines represent atomic layers and red symbols show intercalated species.

In battery research, a frequently observed intercalation mechanism of ions into an electrode is the so-called staging (Figure 12). Staging describes an intercalation process, where layered electrode materials are partially filled in subsequent steps, while in each step only very specific layers are filled.

Thus, only every x-th crystal layer is filled with ions for a stage-x compound. For graphite, the staging number x of the basal plane (002) can be determined by XRD, when analyzing the Miller indices l from the peak positions of the (00l)- and (00l+1)-peak. Using the fact

$$d_{00l} = \frac{c}{l} = \frac{\lambda}{2\sin\theta_{00l}} \text{ and } d_{00l+1} = \frac{c}{l+1} = \frac{\lambda}{2\sin\theta_{00l+1}}, \tag{39}$$

where c is the magnitude of the crystal vector (lattice constant) perpendicular to the graphite basal plane, one obtains the Miller index of the intercalated graphite according to:

$$l = \frac{1}{\left[\frac{\sin\theta_{00l+1}}{\sin\theta_{00l}} - 1\right]} \tag{40}$$

The miller index l is closely linked to the staging number x, since $l = x + i$, with an unknown integer $i = 0, 1, 2, ect.$[75] In order to determine the integer i, one needs to know the staging number of the fully intercalated electrode crystal. It can be found by a separate experiment, for instance by tracking the lattice expansion of the crystal in [00l] direction from an empty to a fully intercalated crystal and by comparing it to the theoretically expected lattice expansion found by the (00l) XRD-peak. One for instance can calculate the relative expansion, *i.e.* the ratio of interlayer spacing of the fully intercalated and the empty lattice, and compare it to the theoretically expected relative lattice expansion for different staging numbers and different values of i. As an example, one can consider the different models sketched in (Figure 12): for a stage 1 electrode, one would calculate the ratio of $[001]_{\text{stage 1}}$ / 1·$[001]_{\text{empty}}$, for a stage 2 electrode $[001]_{\text{stage 2}}$ / 2·$[001]_{\text{empty}}$ and for a stage 3 electrode $[001]_{\text{stage 2}}$ / 3·$[001]_{\text{empty}}$. These values must be compared to the ratio $[001]_{\text{full}}$ / $[001]_{\text{empty}}$, which for example is obtained by measuring the volume expansion of a macroscopic crystal upon full intercalation. This way, one finds the staging number x for the fully loaded electrode. At the same time, one knows the miller index l from XRD for this stage and this way one can calculate the integer i. Knowing i, one can determine the staging number for any miller index found by XRD.

Sample characterization of the synthesized V_2O_5-powders was performed with *Bragg-Brentano* geometry using a Bruker AXS D8 Advance instrument (Bruker, Karlsruhe/Germany) with a Cu K_α source (35 mA, 30 kV). The *in-operando* XRD measurements were measured with a Rigaku SmartLab X-ray diffractometer (200 mA, 45 kV) in reflection mode (*Bragg-Brentano*), also with a Cu K_α source. A specifically designed electrochemical cell was used for *in-operando* measurement, which is described in further detail in Hartung´s *et al.* publication.[76] Electrodes were prepared by mixing MCMB powder with 10 to 20 $\%_{wt}$ teflonized acetylene black (TAB). The mixture was pressed onto a stainless steel grid with a pressure of 2 t. Before the electrode was introduced into the cell, where it was separated by a glass fiber separator (Whatman) from the Na-metal CE, it was vacuum dried at 120 °C. For galvanostatic charging/discharging the electrochemical cell was operated as two-electrode setup. Illumination of the sample occurred via a 6 µm thin Al-foil XRD window (Goodfellow, light tight). The cell was assembled under Ar-atmosphere in a glovebox and can be operated in air atmosphere when assembled.

3 State of the Art

The following chapter reviews the state of the art of battery research, starting with LIBs and the SEI-formation on graphite electrodes. Then, an overview over the current understanding of the graphite electrochemistry in NIBs is presented, followed by an introduction to NIB positive electrodes with emphasis on V_2O_5. Finally, a short paragraph reviews full cell NIBs with graphite negative electrodes.

The studies on the negative graphite electrode in a LIB and the SEI-formation are treated in section 5.1, and have been published in an article in the journal 'Nanoscale' in 2016 to a large part.[77] The SEI was first discovered in 1979[78], a long time before the first LIB was commercialized in 1991 (Figure 13). The SEI is a thin surface film forming on the battery electrode when the electrolyte is reduced/oxidized at the anode/cathode during first discharge/charge and is of major importance in a battery. In the following, the SEI formation on the anode is of interest. A proper SEI is beneficial for the cycle life, lifetime, power capability and safety of a battery.[79] It is a compact surface film acting as a Li-ion conductive membrane, which at the same time is an electronic insulator.[79, 80] The life time and cycle life of a battery are extended by the SEI, because the compact surface film stabilizes the electrodes against exfoliation and prevents the remaining electrolyte from further decomposition.[81–83]

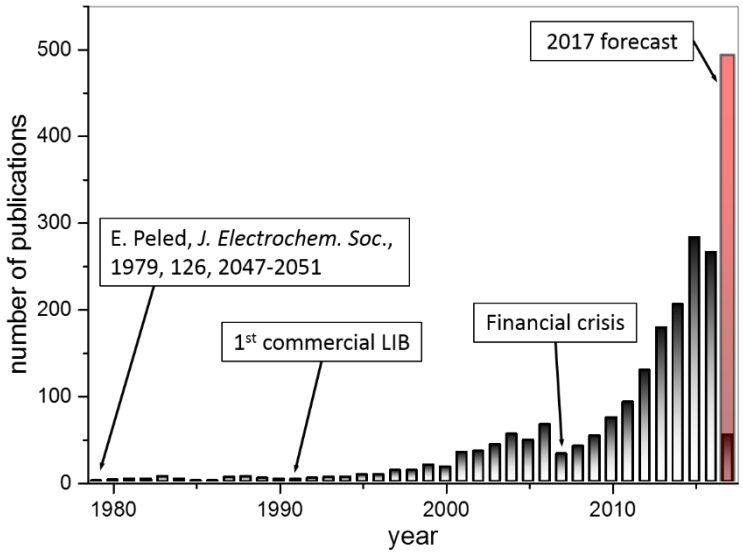

Figure 13: Timeline of publications related to the SEI-formation. The numbers are based on the SciFinder database using the tags 'solid electrolyte interphase Li' (February 2017). The 2017 forecast is a linear extrapolation of the number of publications measured until February 2017.

Due to its importance for batteries, the number of publications related to the SEI formation in the past few years exponentially increased, *cf.* Figure 13. Many different aspects regarding the SEI formation on graphite electrodes are illuminated in recent literature. Fundamental questions related to the chemical composition and structure are addressed by a variety of methods like TOF SIMS[84] (time of flight secondary ion mass spectrometry), SECM[85–87] (scanning electrochemical microscopy), SEM, TEM (transmission electron microscopy), NMR (nuclear magnetic resonance spectroscopy), XPS, FTIR[88, 89] (Fourier transformed infrared spectroscopy), NSOM[90] (near-field scanning optical microscopy) to AFM[91–93] (atomic force microscopy) and theoretical Molecular Dynamics studies[94, 95] on the SEI formation mechanism. Besides gaining a fundamental understanding, efforts on improving the SEI operating properties aim at tailoring the chemical composition of the SEI taking advantage of electrolyte additives,[96–98] or by graphite electrode pretreatment before cell assembly to avoid exfoliation.[99, 100]

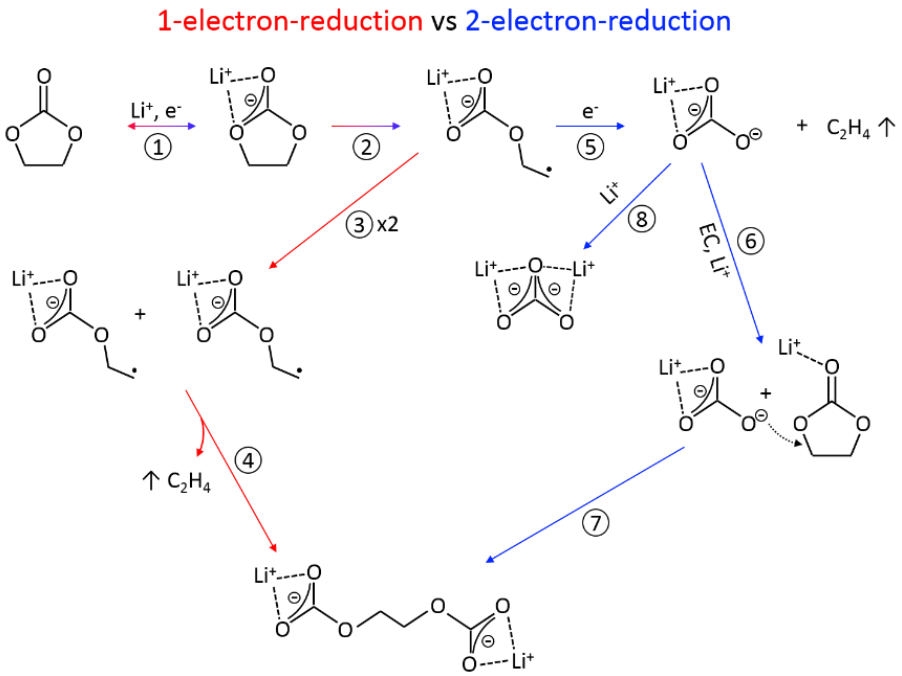

Figure 14: Reduction scheme of EC occurring via a 1-electron-reduction (steps (1) - (4)) and a 2-electron-reduction pathway (steps (1), (2), (5) - (7) and (8)) as proposed in literature.[101–106]

The SEI formation on a graphite anode in a LIB is described as a result of the electrochemical reduction of electrolyte components, such as the organic solvents and the Li-salts. A typical LIB electrolyte consists of a 1 M $LiPF_6$ solution in EC/DMC. The cyclic carbonate EC is reduced by accepting an electron and a Li-ion (Figure 14 step (1)), followed by a ring opening[79, 101, 107–110] and the formation of a radical anion[101] (Figure 14 step (2)). Now, several subsequent reduction pathways are possible: two of these radical anions can combine, resulting in the formation of a dialkyl carbonate molecule and ethylene gas (Figure 14 step (4)). This pathway is a 1-electron-reduction, but requires sufficiently low potentials. At more positive potentials, a 2-electron-reduction occurs, first leading to a $LiCO_3^-$ ion formation and ethylene gas evolution (Figure 14 step (5)), followed by a reaction of the $LiCO_3^-$ ion with a Li-ion and a EC molecule (Figure 14 step (6)), which takes the excess electron of the $LiCO_3^-$ opening the ring and which finally again leads to the formation of a dialkyl carbonate (Figure 14 step (7)).[102] In parallel, Li_2CO_3 can be formed by a Li-ion uptake of the intermediate $LiCO_3^-$ ion (Figure 14 step (8)).

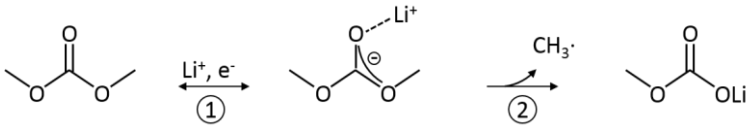

Figure 15: Reduction scheme of DMC as proposed in literature.[103, 104]

Linear carbonate reduction, for instance DMC-reduction, occurs via a 1-electron-reduction associated with the substitution of a methyl-group by a Li-ion and the concomitant lithium methyl carbonate and ethane gas formation by recombination of methyl radicals (Figure 15).[103, 104] As the intermediate radicals formed according to both mechanisms shown in Figure 14 and Figure 15 are highly reactive species, further reactions are possible. At low electrode potentials $LiPF_6$ is known to decompose to LiF and to PF_5,[79, 111–114] which can react to HF in contact with trace water, or with the upper formed Li_2CO_3 to inorganic species such as POF_3 and CO_2:

$$LiPF_6 \rightleftharpoons PF_5 + LiF_{(s)} \xrightarrow{H_2O} LiF_{(s)} + POF_3 + 2HF \quad (41)$$

$$PF_5 + Li_2CO_3 \rightleftharpoons 2LiF_{(s)} + POF_3 + CO_2 \quad (42)$$

At low potentials, all chemical species can react with each other, making the SEI a complex mixture of different fluorides, oxides, phosphates, oligomers and lithium carbonates.[79, 101–110]

All those species precipitate on the electrode and build a film growing in thickness with time, resulting in an increase of electron tunneling resistance hampering the further electrolyte reduction process. Thus, the SEI thickness is self-limited to a few nanometers, being the typical electron tunneling range.[79, 88, 92, 93, 95, 112, 115–120] The SEI-formation model based on electron tunneling was suggested by Peled[78] in his original SEI-paper and was also discussed by others.[79, 112, 117, 120–123] Besides the electron tunneling model a solvent diffusion model is suggested, where the diffusion rate of solvent molecules through the SEI towards the electrode surface determines the SEI growth rate.[124–126]

The tunneling resistance within the SEI gradually increases with increasing distance from the electrode, being associated with a potential drop and thus a decrease of reduction strength. Thus, in close vicinity to the electrode, the SEI components consist of stronger reduced species compared to components in contact with the electrolyte. Consequently, a larger content of organic compounds from the electrolyte decomposition is observed in larger distance from the electrode, whereas in close vicinity to the electrode a compact layer of fully reduced species as fluorides, oxides, and other elements has been found by a variety of studies.[79, 92, 116, 120, 127–130]

The electrode morphology is also found to influence the chemical composition and formation mechanism. Thinner SEI thicknesses for instance are reported on the graphite basal plane compared to the graphite cross-section, because of an increased reactivity of the cross-sectional surface compared to the basal plane towards the electrolyte reduction.[117, 131–134] The SEI at cross-sectional surfaces is also more inorganic compared to the basal plane, since the anion reduction proportion is increased.[131, 132]

In this thesis, the SEI-formation mechanism with respect to electrode potential and topographical appearance is illuminated and studied by EC-STM on an HOPG model electrode immersed in a 1 M $LiPF_6$ in EC/DMC electrolyte. Similar studies were already conducted earlier by Inaba *et al.*[135–140, 142] and others[91, 92, 143–145] by EC-STM and EC-AFM, however, these techniques can still give new insights, when modifying the experimental procedure. Inaba studied co-intercalation processes and the formation of ternary Li-GICs. His interest was dedicated to understand electrode degradation mechanisms induced by mechanical strain of the intercalated species and their electrochemical reduction inside the graphite lattice, leading to a subsurface gas evolution and graphene exfoliation. Besenhard *et al.*[146] first described the co-intercalation model. Compared to earlier studies, the experimental procedure is modified such that STM-imaging is not only conducted *in-situ*, *i.e.* at the same electrode position, but *in-operando*, *i.e.* with a real time observation of the electrode surface in parallel to the electrochemical processes.

The main focus of this thesis lies on gaining an understanding of fundamental electrode processes on a molecular level and to use this knowledge towards advancing new technologies such as Na-ion batteries. As will be shown later, also in NIBs an SEI-formation on the anode/cathode occurs, where in analogy to the mechanism just introduced and further studied in section 5.1 solvent molecules are reduced/oxidized. Thus, even though the SEI-formation introduced in LIBs in the previous paragraphs seems not to be related to NIBs, the SEI-formation is not fundamentally different, but follows the same principles.

In contrast to this, the intercalation of Na-ions into graphite is totally different to the Li-ion intercalation. A wide variety of materials for negative electrodes applicable in NIBs is already known, including Ti-based materials, metal oxides and sulfides, alloy based materials, organic composites as well as carbon-based materials.[22, 23, 29, 147–149] The Ti-based materials with anatase TiO_2 as the most prominent example, are potentially low cost, non-toxic and possess a high reversibility. However, the operation voltage and the achieved capacities are moderate. The advantages of metal oxides and sulfides with respect to their high capacities and energy densities are counteracted by large irreversible initial charge losses, large hysteresis and poor cycle stability. Alloy based materials, such as Sn or P, offer huge capacities and potentially low costs, however, they undergo a large volume expansion upon sodiation, limiting their lifetime. Organic compounds offer merits regarding the high abundance of the resources from biomass and an essentially unlimited variety of structural flexibility. A severe drawback of these compounds is their high solubility in organic media and the sluggish electrode kinetics.

From the perspective of the high elemental abundance of carbon in the earth´s crust, carbon-based electrodes are considered as an extremely low cost material with a good electronic conductivity and beneficial electrochemical properties. Hence, graphite is one of the most desired negative host materials for sodium ions, believed to be the missing step for NIB-commercialization.[24] Attempts to reversibly intercalate Na into graphite failed during the past twenty years.[25–27] The reason is found to be the electrolyte solvent, which in these studies were carbonates such as ethylene carbonate coordinating the Na-ions in solution. Once the Na-ions intercalate into the graphite lattice, they strip off their solvation shell, which results in the formation of energetically unstable binary Na-graphite intercalation compounds - opposite to stable binary Li graphite intercalation compounds - and hampered in-plane diffusion of the Na-ions in between the graphene sheets.[150–152] Carbon was first sodiated in 2000 by Stevens *et al.*,[153] where a hard carbon was used, *i.e.* carbon with a very low graphitization grade and large interlayer distances. Hard carbons, which can be synthesized from bio-waste materials,[154–156] however, suffer from poor high rate performances and serious safety hazards due to a facilitated Na-dendrite formation.[22] By the use of expanded graphite with an increased graphene layer spacing of 4.3 Å compared to the 3.35 Å of natural graphite, reasonable amounts of Na could be reversibly intercalated for numerous cycles and at higher rates.[157–159] Also graphene electrodes with their superior electronic conductivity were successfully used as anode material for NIBs, either as pure graphene[160–162] or as nitrogen doped,[163] boron doped[164] or reduced graphene oxide.[165, 166] Producing affordable amounts of graphene in an industrial scale, however, is still an issue.

The idea behind the use of hard carbons, expanded graphite and graphene materials is the increased interlayer distance between the graphene sheets, positively affecting the Na-graphene interaction and facilitating the sodiation. Another idea aims at modifying the Na-ion-graphite interaction by not purely inserting the Na-ions into the graphite, but by inserting them together with a solvation shell, which also beneficially effects the Na-graphite interaction force. In 2014 Jache *et al.*[18] discovered that Na-ions can reversibly intercalate (> 99.87 % coulombic efficiency) in reasonable amounts (100 mAh g^{-1}) into usual graphite, which is even cheaper than hard carbons, without showing a significant capacity loss for 1000 cycles, when coordinating them with diglyme-molecules (diethylene glycol dimethyl ether). It was found that Na can co-intercalate into graphite also when solvated in other linear glyme molecules and even when using other ether based electrolytes.[75, 167]

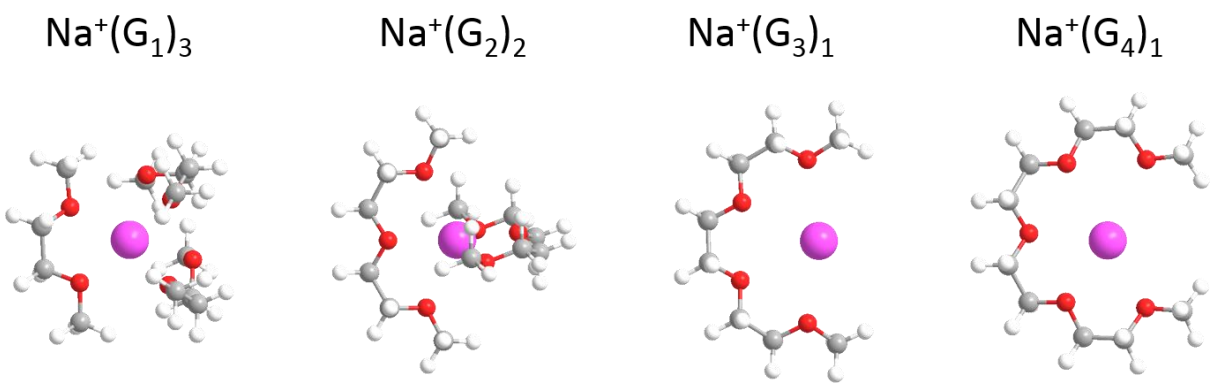

Figure 16: $Na^+(G_x)_y$ complexes for the different glyme solvents presented as ball-stick models resulting from an O-coordination number of 4 to 6.[167] *(pink: Na^+, red: O-atom, grey: C-atom, white: H-atom)*

For an ether based electrolyte (di-glyme, G_2) coordinating the Na-ions (Figure 16), the co-intercalation of Na-ions into the graphite with their glyme solvation shell was suggested by Jache to follow:[18]

$$C_n + e^- + Na^+ + yG_2 \rightleftharpoons Na^+(G_2)_y C_n^- \quad (43)$$

Follow up studies with other linear glymes showed an excellent cycling behavior over several thousand cycles without significant capacity losses and capacities above 100 mAh g^{-1}.[75, 167, 168] This led to the development of full cells operating with a graphite anode and a $Na_{1.5}VPO_{4.8}F_{0.7}$,[169] a $Na_3V_2(PO_4)_3$-C composite[168] or a P2-$Na_{0.7}CoO_2$[170] cathode in a glyme based electrolyte, respectively. Jache´s recent study focused on the differences of the four first glymes, showing a similar electrochemical behavior for mono-glyme (G_1), di-glyme and tetra-glyme (G_4). Tri-glyme (G_3) on the other hand behaved completely different, the cause of which is still an open question. Further studies on the intercalation of solvated Na-ions into graphite followed,[171–174] including an NMR-study,[175] which reveals the solvation structure of the intercalated $Na^+(G_2)_2$ complex, where each Na-ion is coordinated by two G_2-molecules. Another theoretical study examines the interplay among the graphite host and the solvated Na-ions and states that screening the Na-ions with a solvation shell prevents the direct interaction between graphene and Na.[176]

Besides the lack in understanding the intercalation electrochemistry in G_3 electrolytes, also the SEI formation in glyme based electrolytes as well as a mechanistic understanding of the phase transitions caused by the intercalation and the $Na^+(G_x)_y$ diffusion behavior inside the graphite host are not understood yet. These open questions have been tackled in this thesis by the combination of various powerful *in-operando* techniques, such as XRD, EC-STM and EQCM, which is operated as a novel *in-situ* hydrodynamic spectroscopy technique.[177] The section on the Na-intercalation into graphite is published in 'Energy & Environmental Science' to a great part and tries to illuminate the intercalation mechanism of Na-ions into graphite (section 5.2).[178]

Following the studies on the negative graphite electrodes in LIBs and NIBs, V_2O_5 is studied as a positive electrode material for application in a NIB in section 5.3. The major content of this passage is mainly based on results from two articles prepared for publication.

Recently, Na-containing layered transition metal oxides attracted great attention for use in NIBs, since their Li counterparts like Li_xCoO_2 and Li_xMnO_2 are successfully employed as high voltage, high capacity positive electrodes in LIBs. Moreover, they are relatively simple to synthesize. In NIBs, however, the capacities and voltages are less outstanding. Materials tested so far are $NaTiO_2$ (anode, 0.9 V, 152 mAh g^{-1}),[179, 180] $NaVO_2$ (1.6 V, 120 mAh g^{-1}),[181, 182] $NaCrO_2$ (2.9 V, 113 mAh g^{-1}),[183–185] $NaMnO_2$

(2.5 V, 146 mAh g^{-1}),[186–188] $NaFeO_2$ (3.3 V, 70 mAh g^{-1}),[189–191] $NaCoO_2$ (2.8 V, 118 mAh g^{-1})[189, 192] and $NaNiO_2$ (2.1 V, 115 mAh g^{-1}).[193, 194]

Another group of materials are polyanionic compounds such as phosphates ($NaFePO_4$ (2.7 V, 125 mAh g^{-1}),[195] $Na_3V_2(PO_4)_3$ (3.3 V, 119 mAh g^{-1})[196]), pyrophosphates ($Na_2MP_2O_7$ with M = Fe, Co, Mn (3.0 V – 3.6 V, 80 mAh g^{-1} – 90 mAh g^{-1})),[197–199] fluorophosphates ($NaVPO_4F$ (3.95 V, 121 mAh g^{-1}),[200] Na_2FePO_4F (3.0 V, 110 mAh g^{-1}),[201] Na_2CoPO_4F (4.3 V, 100 mAh g^{-1})[202]) as well as fluorosulfates ($KMSO_4F$ with M = Fe, Co, Ni (3.3 V, 120 mAh g^{-1}))[203] and sulfates ($Na_2Fe(SO_4)_2{\cdot}4H_2O$ and $Na_2Fe(SO_4)_2$ (3.3 V, < 100 mAh g^{-1})),[204] to name only the most important. High operating voltages are reported for these compounds, making them an attractive material for NIB application. However, the obtainable capacities are moderate and the electronic conductivity is poor, resulting in a low rate capability. A common strategy to overcome these issues is nano-structuring and carbonization of the electrodes, which also tend to increase the gravimetric capacity of the total electrode.[29, 30]

Prussian blue analogues or metal hexacyanometalates can be described with the general formula of $A_xP[R(CN)_6]_{1-y}{\cdot}\square_y{\cdot}nH_2O$, where A is an alkali metal ion, P is a N-coordinated transition metal ion, R is a C-coordinated transition metal ion and □ represents a $[R(CN)_6]$-vacancy in the cubic lattice structure. Due to their open cubic lattice framework with their large alkali ion diffusion channels, Prussian blue analogues recently arose the attention of the battery research community, since they can reversibly intercalate all alkali ions, such as Li^+, Na^+, K^+, Rb^+, Cs^+,[205–207] they can intercalate a variety of bivalent ions such as Mg^{2+}, Ca^{2+}, Sr^{2+}, Ba^{2+}, Co^{2+}, Ni^{2+}, Cu^{2+}, Zn^{2+} and Pb^{2+},[208–218] as well as several trivalent ions such as Al^{3+}, Y^{3+}, La^{3+}, Ce^{3+}, Nd^{3+}, Sm^{3+}.[215, 219] Prussian blue analogues are often synthesized via low-temperature water-based synthesis routes, which yields low-quality materials with interstitial water trapped in the $[R(CN)_6]$-vacancies of the crystal structure. In aqueous batteries, the operation of the Prussian blue electrodes is not disturbed by the trapped water, however, the cell voltage of the battery is limited by the small stability window of the aqueous electrolyte. Trying to increase the operation voltage by the use of organic electrolytes or ionic liquids, the trapped water becomes an issue, since it gets decomposed during operation, leading to low coulombic efficiencies and poor cycle lifes.[29, 30] Some of the metal hexacyanometalates used in NIBs for example are $Na_xFe[Fe(CN)_6]$ (3.3 V, 123 mAh g^{-1}),[220] $Na_xCo[Fe(CN)_6]$ (3.6 V, 130 mAh g^{-1}, aqueous)[221] or $Na_xNi[Fe(CN)_6]$ (3.3 V, 80 mAh g^{-1}, aqueous).[206]

Due to their potentially low costs, organic materials are also in the focus of research for high voltage electrodes. Two materials with promising operating voltage and capacities are an aniline-nitroaniline copolymer (3.2 V, 180 mAh g^{-1})[222] and a bipolar porous organic electrode consisting of a two-dimensional porous-honeycomb, polymeric framework of benzene rings and triazine rings (2.6 V, 240 mAh g^{-1}).[223] A general drawback of organic compounds is their sensitivity to the electrolyte solvent, resulting in rapid dissolution of the electrode and limiting the choice of electrolytes.

Even though huge progress on NIB-electrodes has been made recently, each category of materials still struggles from a weak point and the search for better materials must go on. A material well known for its diversity, for instance as intercalation host for monovalent ions like Li^+,[67,224–226] Na^+,[226–231] K^+,[226] Rb^+,[232] bivalent species such as Mg^{2+},[31, 233] Zn^{2+},[31] or even trivalent ions like Al^{3+},[31, 234, 235] is the orthorhombic V_2O_5. V_2O_5 was first applied as intercalation host for electrochemically inserted Na-ions by West *et al.*,[32] who showed a reversible Na^+ intercalation reaching high capacities of around 200 mAh g^{-1}, making V_2O_5 a potentially interesting material for Na^+ storage devices. A drawback of V_2O_5 is its poor cycle life upon continuous sodiation/de-sodiation and its low electronic conductivity. Researchers tried to improve the V_2O_5 electrodes by nano-structuring, for example by synthesizing single crystalline bilayered V_2O_5 nanobelts[228] or hierarchical orthorhombic V_2O_5 hollow nanospheres.[229] Uchaker *et al.*[230] tested amorphous and nano-crystalline V_2O_5 and found a strongly

increased lifetime for the amorphous sample. It is observed that nano-structuring increases the battery performance by enhancing the electrode lifetime and rate capability. To overcome the issue with the low electronic conductivity, nano-sized V_2O_5/C composite electrodes[236] and a restacked Na-V_2O_5-graphene nanocomposite[237] were prepared, where the carbon is used to increase the electronic contact to the V_2O_5 particles. Other attempts to improve the battery performance of V_2O_5 in NIBs is to hydrate the V_2O_5-crystal lattice, which yields larger interlayer spacings, being beneficial for higher capacities and facilitating Na-ion diffusion. Recently, a hydrated $V_2O_5{\cdot}nH_2O$ xerogel[238] as well as a hydrated bilayered nanostructured $V_2O_5{\cdot}nH_2O$[239] demonstrated a largely increased Na^+ storage capacity of initially more than 300 mAh g^{-1}, quickly fading though. Another property, which makes V_2O_5 an interesting material, is its large variety of microscopic topographies, ranging from micrometer size structures, such as hollow microspheres,[64–66, 240–247] solid microspheres,[248–251] yolk-shell particles,[68, 252–255] microflowers[256] and other porous microstructures[257, 258] to nanostructures, including nanoflakes,[259–262] nanofibers[67, 69, 263–279] and aerogels/xerogels.[280–283] In most cases, these materials were tested in LIBs, and few of them were already tested as positive electrode in NIBs, like nanostructured bilayered V_2O_5,[227, 228] amorphous V_2O_5[230] or hierarchical orthorhombic hollow V_2O_5 nanospheres.[229] V_2O_5 was also employed as negative electrode in NIBs, for example as a layered V_2O_5 aerogel.[231]

Sodiation of the orthorhombic α-phase V_2O_5, with a *Pmmn* lattice symmetry,[284] results in different phase transitions. For an *x*-value in the range of $0 < x < 0.02$, the $Na_xV_2O_5$ is in its α-phase,[285, 286] going over into the monoclinic β-phase when $0.2 < x < 0.4$ (*C2/m* space group).[285] The $Na_{0.64}V_2O_5$ composition is called τ-phase (*C2/m*)[285, 287] and when $0.7 < x < 1$, it is called α'-phase (*Pmmn*, orthorhombic).[287] Inserting more than one Na per V_2O_5 unit cell, one obtains the η-phase ($1.45 < x < 1.8$) and the κ-phase ($1.68 < x < 1.82$).[32, 288]

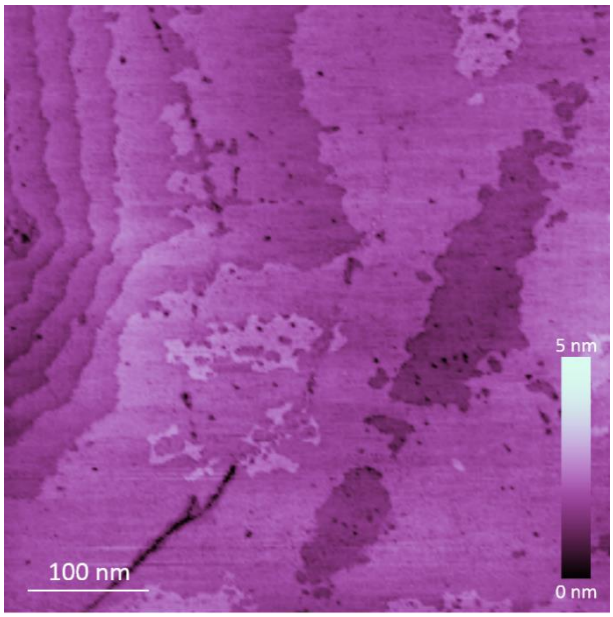

Figure 17: STM micrograph of the (001)-plane of an orthorhombic V_2O_5 single crystal with 4.5 Å step edges, corresponding to the 4.36 Å [001] lattice vector (scan size: 500 nm x 500 nm, tunneling current: 1 nA, bias: 2.1 V, tip velocity: 1µm s^{-1}).

Figure 17 shows an STM-micrograph of the (001)-plane of a V_2O_5 single crystal, showing the layered structure of the orthorhombic V_2O_5. The interlayer distance amounts to 4.5 Å, matching well with the [001] lattice vector length of 4.36 Å, found by XRD. The intercalation mechanism of low charge – low size cations (Li^+, Na^+, Mg^{2+} and Ca^{2+}) into orthorhombic V_2O_5 was studied in detail by Galy,[286] who

proposed a stage-2 type intercalation reaction (Figure 18 (a)). When the cations enter the V_2O_5 lattice, the interlayer distance of this layer is expanded, while the interplanar distance of the empty layers decreases. At the same time, the VO_5-pyramids, from which the V_2O_5 lattice is built up, reorient in the lattice (Figure 18 (b)).

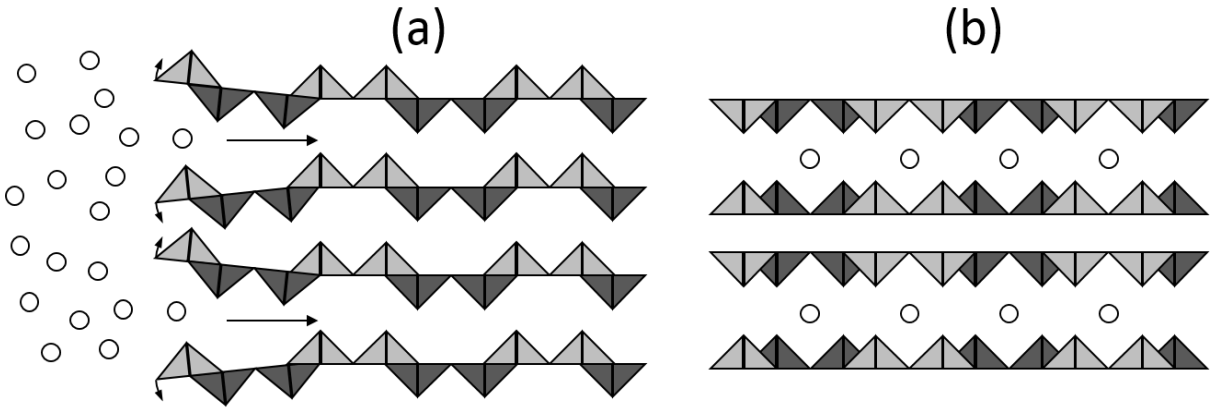

Figure 18: Scheme of (a) the cation intercalation into the orthorhombic V_2O_5 lattice and (b) the resulting lattice transition to a double layer V_2O_5 lattice, as proposed by Galy.[286]

In this thesis, a general understanding about the intercalation electrochemistry of Na-ions into V_2O_5 and the resulting phase transitions shall be gained, followed by a study on the influence of the electrode morphology on the Na^+-intercalation behavior and the electrode performance in a NIB. For this purpose, a family of different V_2O_5 structures were synthesized and operated as positive electrode in a Na|V_2O_5 half-cell.

Combining a negative intercalation electrode with a high voltage intercalation electrode, one gets rid of the potentially dangerous Na-metal negative electrode and obtains a fully operating, relatively safe NIB. So far, there are only a few reports, where a graphite negative electrode was combined with a high voltage positive electrode to a NIB full cell. In these studies a $Na_{1.5}VPO_{4.8}F_{0.7}$,[169] a $Na_3V_2(PO_4)_3$-C composite[168] or a P2-$Na_{0.7}CoO_2$[170] cathode were used as a positive electrode in combination with a graphite electrode. An energy density of 60 mWh g^{-1} based on the combined weight of the negative and positive electrode was reported for a graphite | P2-$Na_{0.7}CoO_2$ cell[170] and 120 mWh g^{-1} for a graphite | $Na_{1.5}VPO_{4.8}F_{0.7}$ cell.[169]

4 Advanced Methods for Battery Research

4.1 Scanning Probe Microscopy

4.1.1 Scanning Tunneling Microscopy

Electrochemical measurements alone in most cases are not sufficient to gain a complete understanding of the underlying processes. Combination with other methods is therefore required. One powerful method is Scanning Tunneling Microscopy (STM) that was invented in 1982 by Binnig and Rohrer, which were awarded the physics Nobel-prize in 1986.[289] The working principle of STM is sketched in Figure 19: a sharp metallic tip is close to an electronically conducting, flat sample, while a small bias voltage in the range of few millivolts to few volts is applied between them.

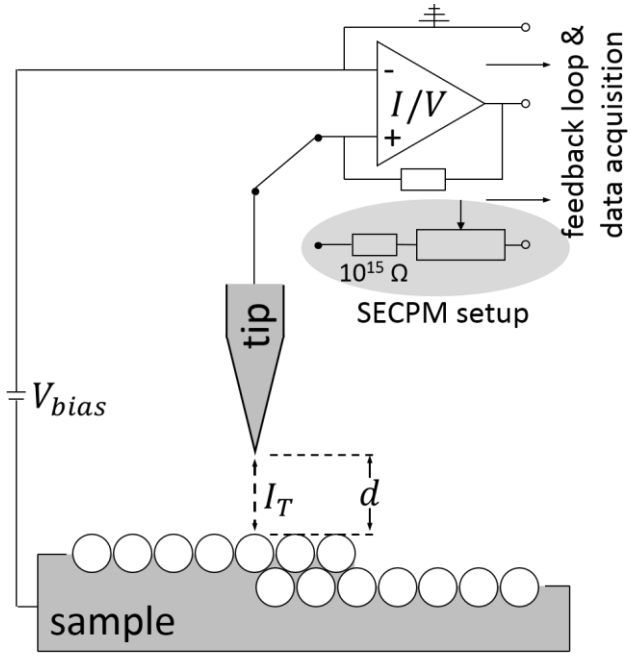

Figure 19: Scheme of a Scanning Tunneling Microscope and a Scanning Electrochemical Potential Microscope.

In close proximity of less than 1 nm, a quantum mechanical tunneling current I_T occurs as a result of electrons tunneling through the gap between tip and sample. Applying a small bias voltage V_{bias} initiates the electron tunneling and a corresponding current. Historically, the tunneling current was first empirically derived from a 1-dimensional quantum mechanical problem, where the Schrödinger equation for an electron approaching a potential step of certain height is solved.[290] Shortly afterwards, the quantum mechanical model was refined to an electron approaching an energy wall, corresponding to two metals with different Fermi-levels E_F being separated by a vacuum gap.[291] The latter situation is sketched in Figure 20, where a 1-dimensional energy wall of height $\phi(z)$ and width d hinders the direct flow of electrons from the tip to the sample and vice versa.

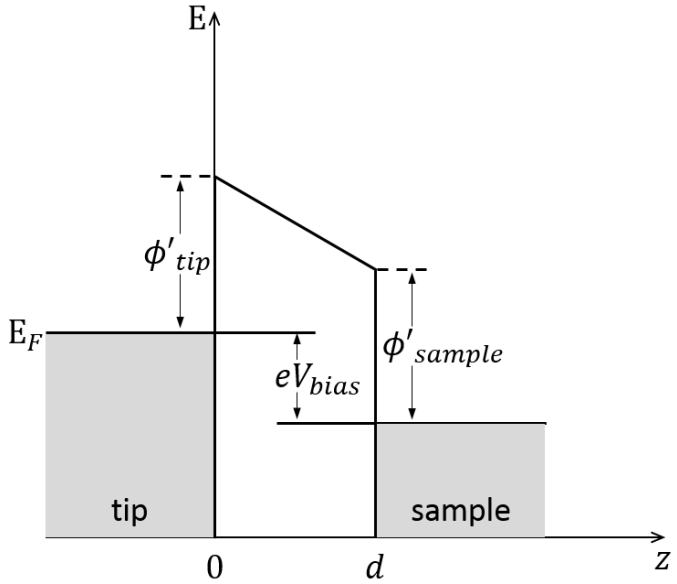

Figure 20: 1-dimensional potential wall used for the quantum mechanical derivation of the tunneling current caused by electrons tunneling through the potential barrier between tip and sample.

Assuming the 1-dimensional potential wall as illustrated in Figure 20, one can write the Schrödinger equation for an electron as follows:

$$-\frac{\hbar^2}{2m_e}\frac{\partial^2\psi_n(z)}{\partial z^2}+\phi(z)\psi_n(z)=\mathrm{E}\psi_n(z) \tag{44}$$

Solving this equation, one finds two solutions. Inside the tip or sample, where the electron energy E is larger than the potential barrier $\phi(z)$, *i.e.* $\mathrm{E} > \phi(z)$, the wave function of the electrons is:

$$\psi_n(z)=\psi_n(0)e^{\pm ikz} \tag{45}$$

with $k=\sqrt{2m_e(\mathrm{E}-\phi(z))}/\hbar$. Equation (45) is the wave function of a propagating wave in z-direction with wave vector k. Inside the barrier, *i.e.* when $\mathrm{E} < \phi(z)$, the solution equals to:

$$\psi_n(z)=\psi_n(0)e^{\pm\kappa z} \tag{46}$$

with $\kappa=\sqrt{2m_e(\phi'-\mathrm{E})}/\hbar$, the decay coefficient of the wave function inside the potential barrier. Inside the potential barrier, the electron wave function is exponentially decaying. ϕ' is the mean work function of sample and tip, which in the simplified case as shown in Figure 20 is $\phi'=\frac{1}{2}(\phi'_{tip}+\phi'_{sample})$. If the bias voltage V_{bias} is small compared to ϕ', *i.e.* $eV_{bias} \ll \phi'$, κ simplifies to $\kappa=\sqrt{2m_e\phi'}/\hbar$. The probability density P of a quantum mechanical particle is defined as the square of its wave function $\psi_n(z)$:

$$P \propto |\psi_n(0)|^2 e^{-2\kappa d} \tag{47}$$

Thus, the tunneling current through the barrier is the sum over the probability densities of all electrons:

$$I_T \propto \sum_{\mathrm{E}_F-eV}^{\mathrm{E}_F}|\psi_n(0)|^2e^{-2\kappa d} \tag{48}$$

Using the quantum mechanical expression of local density of states (LDOS), $\rho(z,\mathrm{E})$, which is defined as the sum of probability over energies in the range from E_F-eV_{bias} to E_F in small intervals ϵ

$$\rho(z,\mathrm{E}) \coloneqq \frac{1}{\epsilon}\sum_{\mathrm{E}-\epsilon}^{\mathrm{E}}|\psi_n(z)|^2, \tag{49}$$

one can rewrite equation (48) as

$$I_T \propto V\rho(0,\mathrm{E}_F)\,e^{-2\kappa d}, \tag{50}$$

which is the tunneling current building up between tip and sample when a small bias voltage is present. Bardeen[292] and later Tersoff and Hamann[293] used a pure theoretical approach based on first order perturbation theory to derive equation (50).

Equation (50) is the fundamental formula necessary to understand STM. One important feature of this equation is the exponential dependency of the tunneling current I_T on the tip-sample distance d. This dependence is used for surface imaging. When the tip is scanned in a defined line by line pattern across the sample surface, the distance between tip and sample alternates corresponding to the sample topography. When the tip is close to the surface, I_T will increase, when d increases, I_T decreases. This behavior can be fed into a feedback loop, by which the surface topography can be reconstructed.

Keeping the nominal distance between tip and substrate constant, and recording then I_T varying as a function of true d is also called 'constant height mode'. Alternatively, one can also apply a feedback loop in order to keep I_T constant and adjust d correspondingly. This operation mode is called 'constant current mode' and is usually used as operation mode in STM, as it directly provides information about height differences between different sample positions.

Another relationship in equation (50) is the link between I_T and the LDOS $\rho(z, \mathrm{E})$ plus the work function ϕ' in the exponent, two electronic properties of the tip and the sample. Thus, STM images shall never purely be interpreted as topographic images, but as a superposition of topography and electronic states of the tip and sample.

4.1.2 Electrochemical Scanning Tunneling Microscopy[294]

The section above treated the theory of quantum mechanical tunneling between two conductors separated by a vacuum gap. Operating the STM under ambient conditions, however, the theory must be adjusted, since electron tunneling is no longer a 2-state tunneling process, but occurs via n intermediate states. These intermediate states can result from adsorbates on the tip and sample, for instance adsorbed water from air humidity, or from an oxide layer, when tip or sample are exposed to air. Depending on the tip/substrate material, many other species can adsorb to the surface. In electrolytes with the presence of solvent molecules and ions, the tip-sample gap becomes a multistate tunneling gap.

Thus, equation (50) must be modified by the intermediated states and changes to:

$$I_T \propto V\rho(0, \mathrm{E}_F)\, e^{-2\kappa d/(n+1)} \tag{51}$$

Typically, $2 \leq n \leq 5$ and the tunneling barrier ϕ' reduces to an effective tunneling barrier ϕ_{eff}:

$$\phi_{eff} = \phi'/(n+1)^2 \tag{52}$$

Moreover, a mean distribution of density of states $\rho(0, \mathrm{E}_F)$ is assumed. From equation (51) one can see that intermediate tunneling states weaken the distance dependence of I_T, which at the same time leads to a decrease of signal to noise ratio.

In addition to the intermediate tunneling states in ambient conditions, the detected current signal at the operation amplifier in the STM scanner no longer purely detects the tunneling current I_T, but also currents originating from electrochemical processes. These can be non-faradaic processes like EDL charging of the tip, or faradaic processes caused by electrochemical reactions at the tip. In order to prevent disturbances from faradaic processes, one can use a tip material, which is as inert as possible, one can operate the tip at a potential in its EDL region, or one can try to minimize the exposed area of the tip in the electrolyte. This is usually done by coating the tip with an inert, insulating material, where special techniques allow to cover the tip completely with only the tip apex exposed to the electrolyte, which is required in order to collect the tunneling current. All these measures also help to minimize the effect of intermediate states and increase the signal to noise ratio.

Even though there are many disturbing factors negatively affecting the signal to noise ratio in ambient environments, EC-STM is one of the most powerful experimental techniques to study electrochemical surface processes – not only because of its high resolution, but also because of its advantage to image surface processes *in-situ*, *i.e.* at the same sample position, or even *in-operando*, which means under operating conditions at the same sample position. This is of major importance for systems like battery electrodes, when one wants to study processes like ion intercalation or the formation of the solid electrolyte interphase. As *in-situ* and *in-operando* EC-STM studies on battery electrodes are very rare

in literature, some of the benefits of EC-STM studies compared to other, less advanced battery characterization techniques shall be highlighted here.

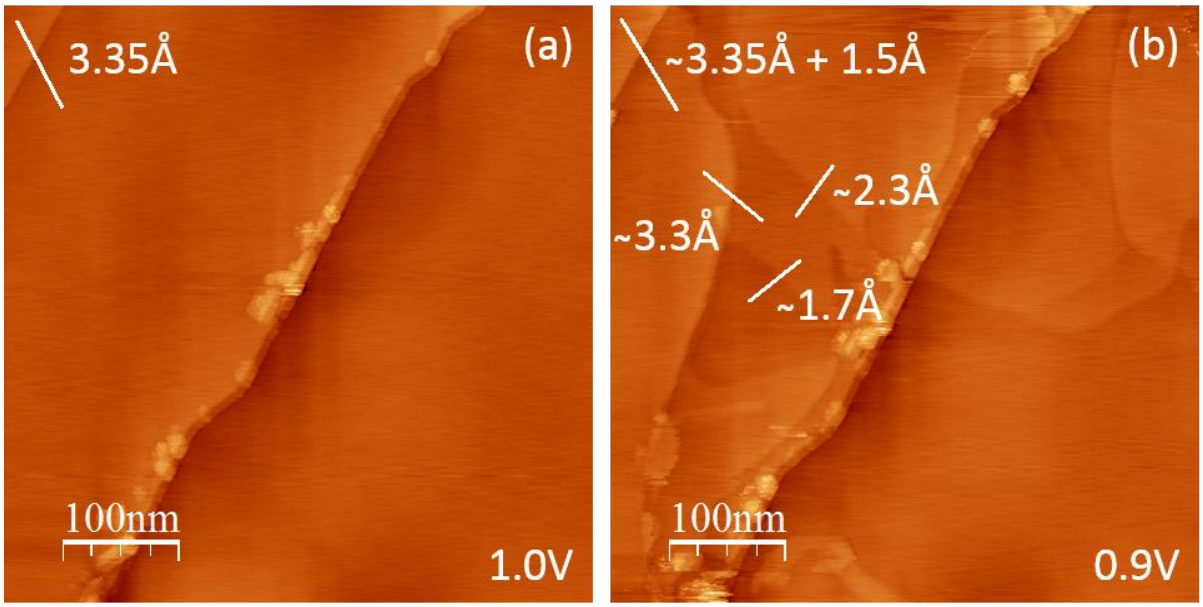

Figure 21: In-situ *EC-STM study of the co-intercalation of Li-ions and their solvation shell into graphite, where the electrode potential was set to 1.0 V (a) and to 0.9 V (b).*

Figure 21 for instance shows the co-intercalation of solvated Li-ions together with their EC/DMC solvation shell into a graphite electrode. The sample is a single crystalline HOPG electrode immersed in a 1 M $LiPF_6$ in EC/DMC electrolyte. Li-metal serves as counter and reference electrode and the entire microscope setup is placed in an Ar-filled glovebox (section 4.1.4.1). This specific system is optimized for microscopic *in-operando* studies on highly air- and humidity-sensitive electrochemical systems, as LIBs or NIBs. It permits to image an electrode surface while performing an electrochemical experiment. Figure 21 (a) shows the graphite (0001) surface after a CV to 1.0 V *vs.* Li/Li^+ was performed. The STM image was recorded at 2.0 V. To this point, no surface changes are visible by STM and the electrode surface shows the typical HOPG features, namely large extended, atomically smooth terraces, which are terminated by mostly monoatomic step edges with a height of 3.35 Å. This height corresponds to the distance between two graphene layers lying on top of each other.

In between two adjacent graphene sheets different species like Li-ions or solvated Li-ions can intercalate into the graphite crystal, for example as a result of applying a sufficiently negative potential. In a LIB, Li-ions co-intercalate into the graphite together with their carbonate solvation shell at voltages below 1.0 V prior to SEI-formation.[146] This can also be seen in the STM image in Figure 21 (b), where the previously flat terraces form some blisters and swell up in some regions. The lattice expansion caused by the intercalated species can then be independently analyzed for each expanded step edge and blister. This is a major advantage compared to integral techniques, such as dilatometry[146] or XRD,[295] where only average changes in the entire electrode can be analyzed, but no single defect or step edge.

Analyzing the lattice expansion from the topographic STM images and applying it to the co-intercalation model,[146] one can schematically explain the co-intercalation behavior as sketched in Figure 22. The pristine graphite lattice with its 3.35 Å layer separation is shown on the left. Upon intercalation of a Li-carbonate species, which is exemplarily shown for a Li-ion coordinated by four EC molecules, and which is a typical solvation shell in an EC-based electrolyte, the graphite layer

separation increases.[107, 296–298] How the solvation shell of the intercalated species with respect to number of EC and DMC molecules really is composed, is an open question. From the lattice expansions measured in Figure 21 (b), one finds that the previous 3.35 Å interlayer spacing expands by roughly 1.7 Å to about 5 Å.

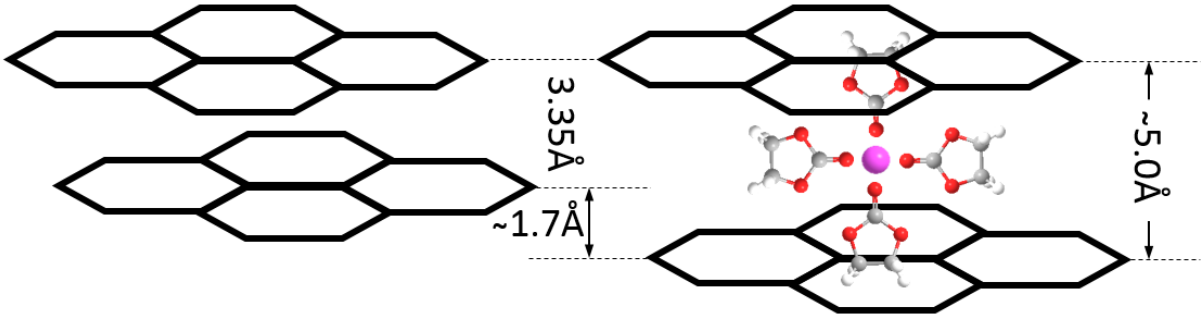

Figure 22: Schematic presentation of the empty layered honeycomb graphite lattice on the left and the graphite lattice after a solvated Li-ion intercalated on the right.

Thus, STM allows to study electrochemical processes on a molecular or atomic level, permitting insights into processes, which are not accessible by standard characterization techniques. In the course of this thesis, numerous further examples are studied, making use of this powerful and rare tool. Those include the Na-ion intercalation into graphite- and V_2O_5-single crystals allowing to image the intercalation processes, to quantify the lattice expansions they cause and the diffusion rate of the intercalated species. Another section is dedicated to the SEI-formation, where STM allows to systematically reveal its formation mechanism, simply by being able to image the surface on a molecular scale under operating conditions - a major advantage of EC-STM compared to other experimental techniques.

4.1.3 Scanning Electrochemical Potential Microscopy – Some Facts and Some Thoughts

One disadvantage of STM, however, is that it requires electronically conductive samples, which with respect to battery research is not always granted, as many electrode active materials are poorly conductive or even semiconductive. Attempts to perform *in-operando* EC-STM studies on V_2O_5 single crystals (section 5.3) for instance failed due to an enhanced tip failure rate coming along with a poor sample conductivity. An alternative microscopic technique, which is not restricted by these issues is the Scanning Electrochemical Potential Microscopy technique (SECPM). In contrast to STM, SECPM is not based on measuring the tunneling current between tip and sample, but on applying the tip as a potential sensor and therefore probing the potential gradient in the EDL (Figure 5). As semiconductors or substrates with a poor conductivity also possess an EDL,[47] SECPM might be used in cases, where STM struggles or fails. Because SECPM is a very novel technique, which is hardly understood and strongly debated, a short section of this thesis shall be dedicated to this interesting technique, sharing some experimental facts and some thoughts with the reader.

The method itself was first mentioned in 2004 by the microscope producer Veeco Instruments,[299] and patented in 2007.[300] Shortly afterwards, it was used by Woo *et al.*[301] to probe the potential dependent voltage gradient inside the EDL of a Au(111) in a 10 mM aqueous $NaBF_4$ solution. The first topographic SECPM image, a W-doped diamond-like carbon surface, is shown in a study by Corbella *et al.*[302]. A study of the potential gradient in the EDL on an insulating SiO_2 layer proved the superiority of SECPM compared to STM as a microscopic tool for samples with poor coductivity.[303] Imaging biologic species, such as cells, can also hardly be achieved by STM. In 2009, Baier *et al.*[304] could image single enzyme molecules and reveal their inner structure, which was not possible by STM. A direct comparison in an *in-situ* study showed that both methods, EC-STM and SECPM, deliver the same image quality for metal

surfaces.[305] All these studies indicated the technological and scientific potential of SECPM, albeit a clear explanation of its working principle was still lacking: Especially sigmoidally shaped potential-distance curves are measured in experiments, contradicting the Gouy-Chapman-Stern theory. Hamou *et al*.[306, 307] dedicated a series of theoretical studies to the shape and the protrusion of the tip apex into the EDL region, and it was claimed that the shape of the experimentally obtained potential-distance curves is a result of the EDL overlap of the sample and the tip. An experimental study of Yoon *et al*.[308] confirmed the sigmoidal potential gradient when approaching a tip to the electrode surface. In far distance to the electrode, the potential decay follows the theoretically predicted exponential behavior (equation (21)). The deviations from the exponential behavior towards the sigmoidal potential gradient at small distance, however, are not only attributed to the EDL overlap of tip and substrate, but also to electron tunneling. Traunsteiner *et al*.[309] picked up this idea and suggested that leakage currents in the device not only permit electron tunneling, but also other faradaic and non-faradaic currents, which makes SECPM a similar method as STM, since electron tunneling occurs for small tip-sample separations. Friedl *et al*.[49] denied this hypothesis regarding the leakage current, which according to the 10^{15} Ω input impedance of the potentiometer (Figure 19) should result in vanishing leakage currents. Instead, a new model was suggested, which claims that the tunneling current is balanced by faradaic processes at the tip surface in the bulk electrolyte. In summary, SECPM as a method currently is still not fully understood and there are various open questions. In the following, some experimental facts and some thoughts about SECPM shall be presented, contributing valuable knowledge about this technique.

Figure 23 illustrates an *in-situ* comparison of an EC-STM (a) and an SECPM (b) image measured on HOPG in 0.1 M H_2SO_4. A scheme of the microscope setup is shown in Figure 19. One can change from one imaging mode to the other by switching from the current amplifier used in STM to the potentiometer with its high input impedance, which minimizes the current flux necessary for the potential measurement. This switching can be done without retracting the tip from the sample surface, which results in very similar topographical images for both modes.

Analogous to STM, SECPM also allows to measure the atomic structure of the (0001) honeycomb graphite lattice (Figure 24), where the raw data is shown in (a). After a Fourier-transformation, a signal filtering and a Fourier-retransformation, the hexagonal lattice structure of the graphite crystal becomes clearly visible (b). The reciprocal lattice after the Fourier-transformation is shown in (c). The data shown in Figure 24 is the first demonstration of an atomic resolution achieved with SECPM. In the past Traunsteiner *et al*.[309] showed a molecular resolution of initial stages of the electrochemical Cu(111) oxidation and Baier *et al*.[304] showed a highly resolved enzyme on a graphite substrate. This remarkable spatial resolution, especially for less conductive samples, makes SECPM an interesting tool for a variety of scientific purposes and might open the door to a wide range of scientific fields, especially battery research.

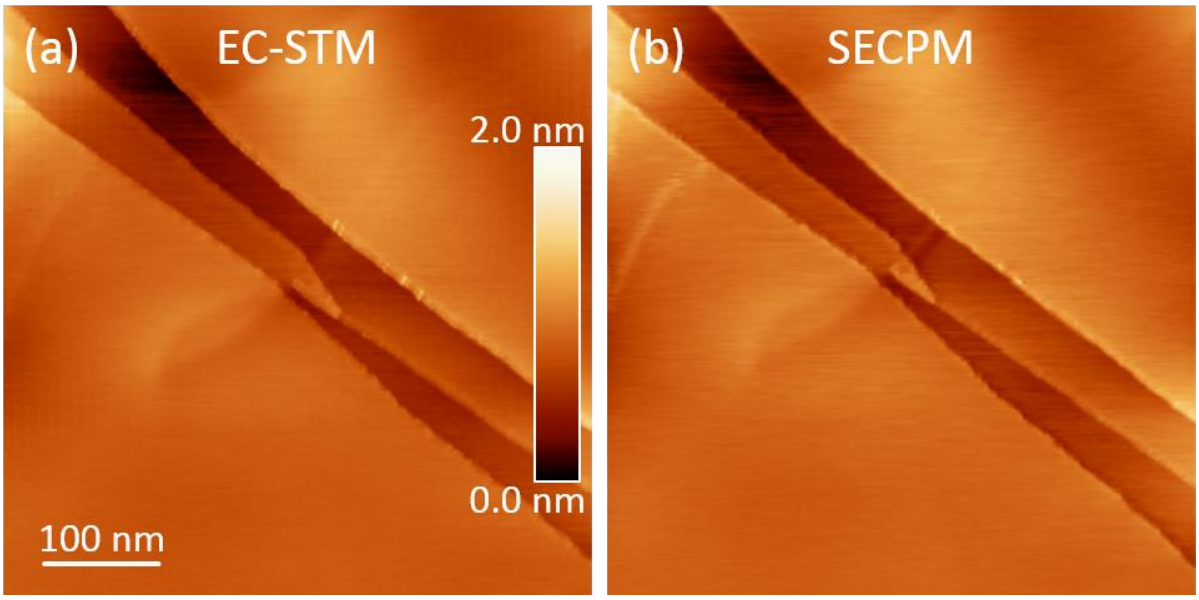

Figure 23: Comparison of EC-STM (a) and SECPM (b) on a graphite basal plane in 0.1 M H_2SO_4 (scan size: 500 nm x 500 nm, tunneling current in (a): 1 nA, potential setpoint in (b): 15 mV, tip potential in (a): 0.293 V vs. Pt, sample potential: 0.193 V vs. Pt in (a) and -0.707 V vs. Pt in (b), bias in (a): -0.1 V, tip velocity: 0.5 µm s^{-1}).

The atomic resolution on the other hand also creates some doubts about the originally suggested principle of SECPM, which stated to solely probe the potential decay within the EDL. Is the EDL-potential decay sensitive enough to permit atomic resolution? As the potential gradient within the EDL and thus the SECPM sensitivity are larger in close vicinity to the electrode (equation ((21)), the tip must be very close to the substrate. Additionally, the tip and the substrate are not at the same potential, but have a small voltage difference, the 'potential setpoint' necessary as feedback parameter for SECPM imaging. This voltage difference is in the range of few to several ten millivolts and acts in a similar way as the bias between tip and substrate in STM. Thus, the idea of Yoon *et al*.,[308] Traunsteiner *et al*.[309] and Friedl *et al*.[49] that electron tunneling occurs between tip and substrate in close distance seems plausible. This is also in agreement with unpublished observations[310] made in a systematic study about the potential setpoint, which showed a decreased image resolution with increased potential setpoint (alias bias in terms of STM). A larger potential setpoint increases the tip-sample separation, which is either a result of equation (21) or of equation (50). Hence, the fact that an atomic resolution can be achieved by SECPM and the fact that an increased potential setpoint acting as a bias between tip and substrate reduces the image quality both indicate that the electron tunneling model is reasonable.

Other interesting observations can be made when varying the electrolyte and hence the EDL structure. Figure 25 shows a study, where fundamentally different electrolytes with different ionic strengths are compared: (a) shows an SECPM image of HOPG in the ion-free ethylene glycol (EG) with an ionic strength of 0 mol l^{-1}, (b) was measured in pure H_2O with pH 7, corresponding to an ionic strength of 10^{-7} mol l^{-1}, (c) in 0.1 M H_2SO_4 (0.3 mol l^{-1}) and (d) in an electrolyte purely consisting of ions, the ionic liquid 1-Butyl-1-Methylpyrrolidinium Bis(trifluoromethylsulfonyl)imide (BMP-TFSI, 3.31 mol l^{-1}). In all solvents/electrolytes clear images of the HOPG surface are obtained. This is another indication for electron tunneling, since the imaging seems to be independent of the EDL structure. Moreover, the experiment in the ion-free EG shows that no ions are required for SECPM. As EG is a polar molecule possessing a dipole moment, the EG molecules can arrange at the charged electrode building up a double layer with a linear potential gradient within the sample and the EG layer. Thus, one can still

argue that SECPM might sense the potential gradient within this double layer without the necessity of electron tunneling. In order to fully rule out the potential sensing, one could measure SECPM in an ion-free, non-polar solvent, such as benzene or other molecules with a symmetric charge distribution. In such a solvent, it should neither build any double layer based on an ion arrangement at the electrode-electrolyte interphase, nor build any double layer composed of oriented dipoles at the electrode surface, provided that no dipole moment is induced into the molecule as a result of the charged electrode. If a SECPM image can be obtained in such a case, the electron tunneling model would be further evidenced.

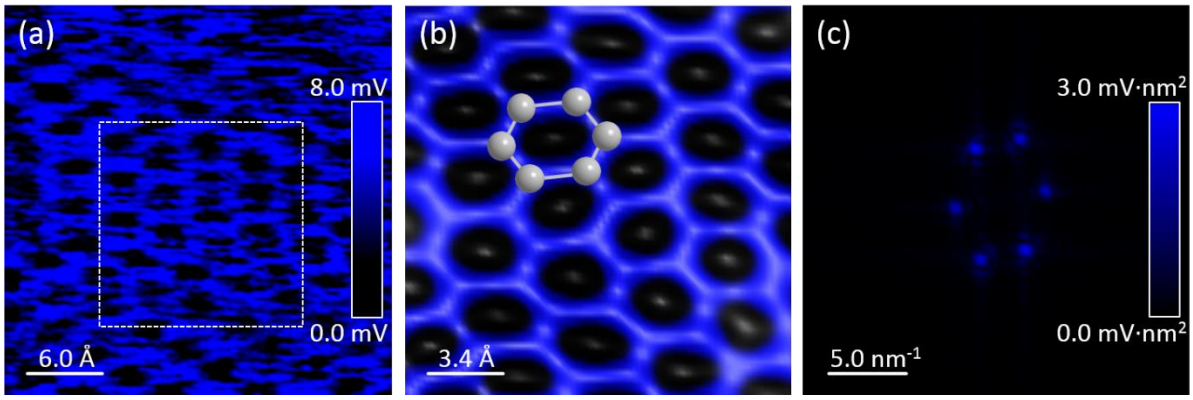

Figure 24: SECPM images of an atomically resolved graphite honeycomb (0001) basal plane in 0.1 M H_2SO_4 with the raw data in (a), a Fourier-filtered magnification (b) and the corresponding Fourier transform showing the hexagonal arrangement of the C-atoms in the reciprocal space (c) (scan size: 3 nm x 3 nm, potential setpoint (b): 15 mV, sample potential: -0.707 V vs. Pt, tip velocity: 0.24 µm s^{-1}).

The electron tunneling in SECPM was studied in more detail by Traunsteiner *et al*.[309] and Friedl *et al*.,[49] while there is a dispute regarding the origin of the current and the flux of the electrons. According to Traunsteiner, external currents, such as leakage currents, faradaic currents and non-faradaic currents are responsible for the transport of the tunneled electrons. The model suggested by Friedl does not require the leakage currents. In any case, higher leakage currents caused by the operational amplifier, leakages on the printed circuit board or an imperfect tip insulation would enhance electron tunneling and be beneficial for the image quality of SECPM. In EC-STM, leakage currents are parasitic and are tried to be suppressed by any means, like tip-coatings. SECPM also works with uncoated tips: Figure 25 (a) was measured with an uncoated Pt/Ir (8:2) tip and good SECPM images were even obtained in concentrated H_2SO_4 solutions.[310] This further supports the suggested electron tunneling model, which requires faradaic processes to transport away the electrons from the tip. The leakage current through the operation amplifier or the printed circuit board is no necessity to explain the electron tunneling in SECPM. Moreover, SECPM is in stark contrast to STM regarding leakage currents, which are parasitic in STM and helpful in SECPM, underlining a fundamental difference of the methods.

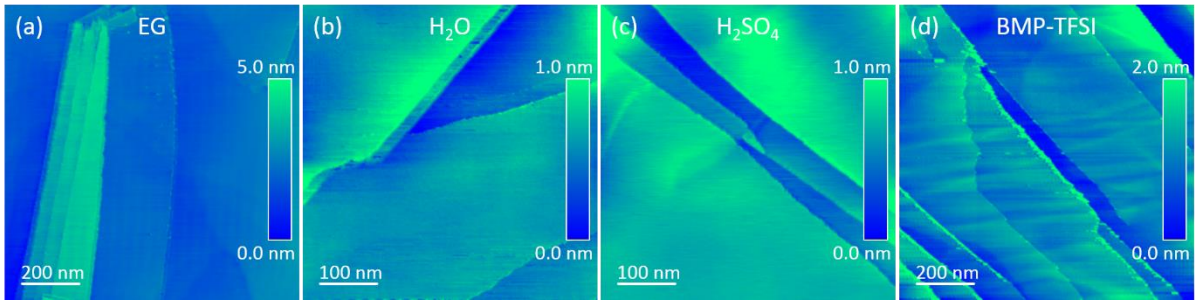

Figure 25: SECPM images of an HOPG surface measured in different electrolytes arranged according to their ionic strength I: (a) ethylene glycol (0 mol l^{-1}), (b) H_2O (10^{-7} mol l^{-1}), (c) 0.1 M H_2SO_4 (0.2 mol l^{-1}) and (d) BMP-TFSI (3.31 mol l^{-1}) (scan size: 500 nm x 500 nm (a, d) 1 µm x 1 µm (b, c), potential setpoint in (b): 100 mV (a), 20 mV (b), 15 mV (c), 50 mV (d), sample potential: 0.0 V vs. Pt (a, b), - 0.707 V vs. Pt (c), -1.2 V vs. Pt (d), tip velocity: 4 µm s^{-1} (a), 1 µm s^{-1} (b), 0.5 µm s^{-1} (c), 2 µm s^{-1} (d)).

4.1.4 Microscope Setups and Samples

4.1.4.1 Electrochemical STM in a glovebox

EC-STM was performed under an inert Ar-atmosphere in a specially adapted glovebox. That glovebox contains a heavy stone plate mount on mechanical damping elements, which decouple the microscope from environmental vibrations and mechanical disturbances. During imaging, the glovebox ventilation and vacuum pump were switched off to further reduce disturbances.

The microscope itself was a homemade system composed of a Pico STM S scanner, a PicoSPM STM base (Agilent Technologies®, formerly Molecular Imaging®) and a Nanoscope IIIA controller (Veeco Instruments Inc.®). An EC-Tec bipotentiostat/galvanostat BP600 and an EC-Tec biscangenerator SG600 were combined with the microscope. The STM software was the Nanoscope v5.31.r1 software and a labview® program BP600 was used to control and read out the potentiostats. The WSxM software[311] was used for STM data evaluation.

Mechanically cut Pt/Ir-tips (8:2, MaTecK) were used for imaging. Operating in carbonate based electrolytes, a standard coating of molten (180 °C) Apiezone® wax (Plano GmbH) was used. In ether based electrolytes, however, the Apiezone® wax and other standard coating materials like polyethylene are dissolved. Therefore, alternative options were explored. Eventually, a coating of the tips with molten (300 °C) polypropylene of a pipette tip (Eppendorf epT.I.P.S.® Standard, polypropylene) provided excellent stability in these solvents and permitted the STM operation.

The electrochemical cell of the STM setup was Teflon-made and contains an electrolyte volume of about 100 µl. Li- and Na-metal served as RE and CE, respectively.

4.1.4.2 SECPM Microscope

A Bruker Multimode 6 microscope with an open cell exposed to air atmosphere was used for SECPM experiments. A Pt-wire served as counter and as quasi reference electrode. The electrolytes used were H_2O (MilliQ, Millipore Integral 3, >18.2 MΩ, 3 ppb TOC), 0.1 M H_2SO_4 mixed from MilliQ water and H_2SO_4 (Merck, supra pure), ethylene glycol (Sigma Aldrich, 99.8 % anhydrous) and 1-Butyl-1-Methylpyrrolidinium Bis(trifluoromethylsulfonyl)imide (BMP-TFSI) (Iolitec, 99.5 %).

4.1.4.3 Graphite and V_2O_5 Single Crystal Model Electrodes

In order to perform STM experiments on an atomic scale, single crystalline model electrodes must be employed. Graphite single crystals are commercially available as highly oriented pyrolytic graphite (HOPG). HOPG (ZYB, 10 mm *x* 10 mm *x* 2 mm) samples were purchased from MikroMasch. Prior to

use, the HOPG surface was cleaved with an adhesive tape, removing the uppermost graphite layers and exposing fresh graphite layers to the electrode surface.

V_2O_5 single crystals were prepared following a slightly modified recipe from Kenny *et al*.[312] A commercial V_2O_5 powder (99.99 %, Alfa Aesar Puratronic®) was molten at 700 °C (V_2O_5 melting point: 690 °C) in an O_2-rich atmosphere (Carbolite HST Horizontal Split Tube Furnace 1200), before it was slowly quenched at 0.1 K min^{-1}. This resulted in the growth of single crystalline V_2O_5 needles with typical dimensions of up to 1 cm in length and 2 mm to 5 mm in breadth. The crystalline structure was examined by XRD, which yielded lattice vectors of $\vec{a} = 11.536$ Å ([100]), $\vec{b} = 4.360$ Å ([001]), $\vec{c} = 3.584$ Å ([010]), confirming the crystal parameters of orthorhombic V_2O_5. Figure 26 shows an example of a typical crystal obtained. STM can be performed on the single crystalline needles.

Figure 26: Photograph of a self-synthesized sample containing several large V_2O_5 single crystals.

4.2 Electrochemical Quartz Crystal Microbalance[313, 314]

The electrochemical quartz crystal microbalance technique (EQCM) stems from the application of resonating quartzes as mass sensitive devices. The working principle is based on the (converse) piezoelectric effect of quartzes. The actual EQCM device consists of a piezoelectric quartz with thickness t_q cut into a thin, circular disk coated with two metallic electrodes on each side of the quartz (compare to Figure 27). In most cases the electrodes have a keyhole shape and overlap in the center of the quartz. Applying a voltage between the two electrodes results in a mechanical deformation of the quartz lattice according to the converse piezoelectric effect.

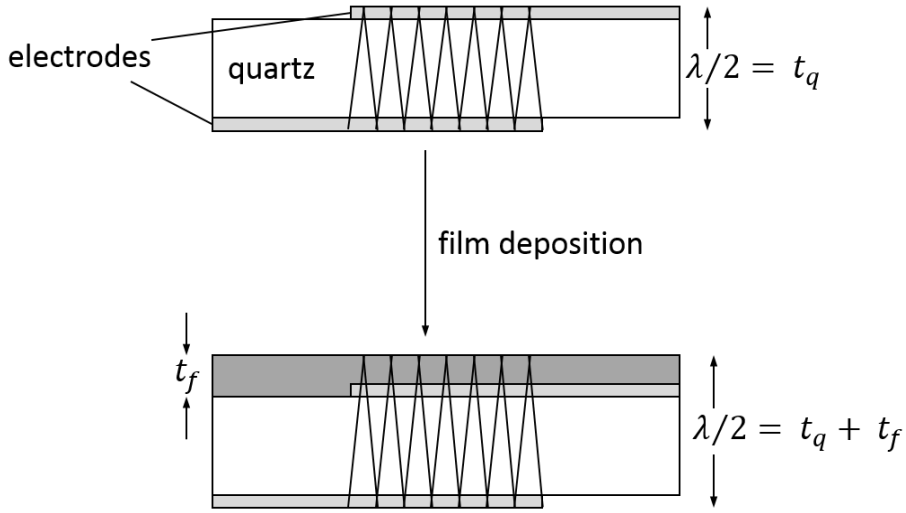

Figure 27: Scheme of the transverse shear wave in a quartz crystal resonator before and after depositing a thin film.[315]

If an alternating voltage is applied to the electrodes a mechanical oscillation is induced in the quartz crystal. At a certain frequency f_0, the system shows a resonant behavior, *i.e.* when the excitation frequency is in a range, where it can induce a transverse shear wave in the (AT cut) quartz crystal. The shear wave has a wavelength λ, which amounts to twice the thickness of the quartz, as illustrated in Figure 27. Thus, depending on the quartz thickness, the resonator has a characteristic resonance frequency. Changing the thickness by deposition of an (acoustically) thin film t_f, the wavelength of the shear wave and consequently the resonance frequency of the resonator changes.

Around its resonance frequency f_0, the quartz oscillation follows a Lorentzian shaped resonance curve in case of a small damping w (Figure 28). Energy losses in the resonating system cause the damping w, which is quantified and measured by the full width at half maximum. The broadening of the resonance curve is not solely an effect of damping, which is caused by a phase difference between the driving oscillation and the vibration of the quartz, but it can also be caused by a 'heterogeneous broadening', being caused by a number of slightly different resonance frequencies, for instance when the quartz-thickness is not homogeneous.

The resonance frequency, however, not only depends on the film thickness but on a variety of parameters. In operation, one usually analyzes the shift of resonance frequency Δf, which can be expressed as the sum of several terms[314]

$$\Delta f = \Delta f_m + \Delta f_\eta + \Delta f_P + \Delta f_R + \Delta f_{sl} + \Delta f_T, \tag{53}$$

where Δf_m represents the frequency change due to a mass loading as a result of a thin film deposition, as already illustrated in Figure 27. Also, the viscosity η and mass density ρ of the surrounding medium of the quartz have to be considered (Δf_η). Additionally, the hydrostatic pressure (Δf_P), the surface roughness (Δf_R), the slippage effect (Δf_{sl}) and the temperature (Δf_T) play a role.

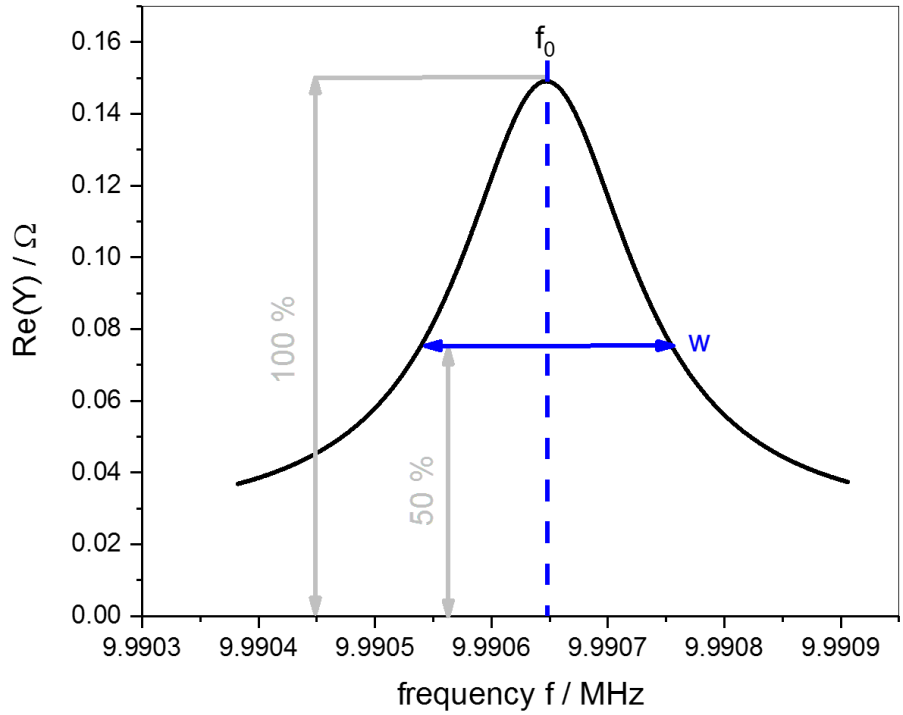

Figure 28: Lorentzian shaped resonance curve of a 10 MHz quartz in air atmosphere with a resonance frequency f_0 and damping w.

From equation (53) it is also obvious that the term 'microbalance' in the sense of mass (density) weighing is only correct under very strict conditions, *i.e.* when Δf_m is the only non-zero term. This is the case for acoustically thin ($kl = \omega\sqrt{\rho_q/\mu_q} \ll 1$), uniform films rigidly attached to the surface, with the wave vector of shear waves in the quartz k, the correlation length of surface roughness and non-homogeneous mass distribution l, the angular frequency of the oscillation ω, the density ρ_q and shear modulus μ_q of the quartz, respectively. Only under these strict conditions the quartz resonator can be used as a mass sensor, in which the frequency change can be correlated to a change in areal mass density Δm_f (in g cm^{-2}) applying the famous Sauerbrey equation:[313, 314, 316]

$$\Delta f = -\frac{2f_0^2 \Delta m_f}{(\mu_q \rho_q)^{1/2}} \tag{54}$$

When the condition of the rigidly bound film is no longer met, for example when the surface film cannot follow the oscillations of the quartz, due to the mass inertia, and as a consequence slips over the quartz surface, not only a frequency shift Δf is observed, but also a broadening of the resonance curve Δw:

$$\Delta f = -\frac{2f_0^2 \Delta m_a}{(\mu_q \rho_q)^{1/2}} \left[\frac{\chi^2}{\chi^2 + (2\pi f_0 \Delta m_a)^2}\right] \tag{55}$$

$$\Delta w = \frac{4f_0^2 \Delta m_a}{(\mu_q \rho_q)^{1/2}} \left[\frac{2\pi f_0 \Delta m_a \chi}{\chi^2 + (2\pi f_0 \Delta m_a)^2}\right] \tag{56}$$

A typical example is the weak adsorption of gases of mass Δm_a on the quartz, with the interfacial friction coefficient χ.

When immersed in a liquid, other frequency Δf_l and damping shifts Δw_l occur according to the Gordon-Kanazawa-Mason model:[313, 314, 317, 318]

$$\Delta f_l = -\frac{f_0^{3/2}(\rho\eta)^{1/2}}{(\pi\mu_q\rho_q)^{1/2}} \tag{57}$$

$$\Delta w_l = 2\frac{f_0^{3/2}(\rho\eta)^{1/2}}{(\pi\mu_q\rho_q)^{1/2}} \tag{58}$$

Again, the condition of a non-slipping must hold here, but in contrast to the pure mass loading under Sauerbrey conditions the effect of a liquid results not only in a negative frequency shift, but also in a broadening of the resonance. Considering slippage at the adsorbate/liquid interface, one obtains an expression containing both terms:[314]

$$\Delta f = -\frac{2f_0^2\Delta m_a}{(\mu_q\rho_q)^{1/2}} - \frac{f_0^{3/2}(\rho\eta)^{1/2}}{(\pi\mu_q\rho_q)^{1/2}}\left[\frac{1}{(1+\lambda/\delta)^2+\lambda/\delta^2}\right] \tag{59}$$

$$\Delta w = 2\frac{f_0^{3/2}(\rho\eta)^{1/2}}{(\pi\mu_q\rho_q)^{1/2}}\left[\frac{1+2\,\lambda/\delta}{(1+\lambda/\delta)^2+\lambda/\delta^2}\right] \tag{60}$$

Here, $\delta = \sqrt{2\eta/\omega_0\rho}$ is the velocity decay length of the shear wave, which for dilute aqueous electrolytes typically is in the range of 200 nm for a 10 MHz quartz.

So far, only smooth surfaces are considered. When introducing surface roughness, one has to take into consideration numerous additional effects like trapping of liquid in pores and cavities, generation of non-laminar motion or the conversion of in-plane surface motion to motion normal to the surface.[314] Moreover, one has to define some parameters to have a quantitative description of roughness. Since roughness can occur on any scale, Figure 29 compares two cases – slight and strong roughness.

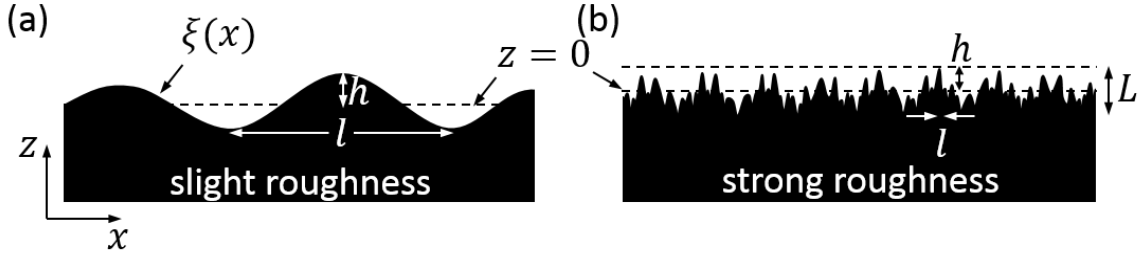

Figure 29: Comparison of (a) slight ($l > h$) and (b) strong ($l \approx h$) roughness, which can be described by a lateral l and a vertical h roughness parameter and which follows the roughness function $\xi(x)$. The reference line $z = 0$ is chosen such that the average of $\xi(x)$ is zero. L denotes the thickness of the porous layer (Figure adopted from Daikhin et al.[314, 319]*).*

Roughness can be described by a lateral l and a vertical h roughness parameter. While for slight roughness l is much larger than h, in case of strong roughness, both parameters become comparable. It already becomes obvious that no clear definition of roughness can be given, since it gradually changes. Thus, one should not describe the roughness by a single roughness function $\xi(x)$, but rather by a set of functions, each for a different specific scale i:

$$\xi(x) = \sum_i \xi_i\,(x) \tag{61}$$

Thus, the roughness is described by a set of characteristic parameters l_i and h_i. For small roughness, where $h/\delta \ll 1$, the frequency shift and peak broadening then can be described by:[314, 320, 321]

$$\Delta f = -\frac{f_0^2 \rho \delta}{\left(\mu_q \rho_q\right)^{1/2}} \left[1 + \frac{h^2}{l^2} F(l/\delta)\right] \tag{62}$$

$$\Delta w = \frac{2 f_0^2 \rho \delta}{\left(\mu_q \rho_q\right)^{1/2}} \left[1 + \frac{h^2}{l^2} \Phi(l/\delta)\right] \tag{63}$$

$F(l/\delta)$ and $\Phi(l/\delta)$ are scaling functions determined by the morphology of the surface:

$$F(l/\delta) = (l/\delta)\left[\sqrt{\pi} + 2\,\delta/l\right] \quad \text{at } l/\delta \ll 1 \tag{64}$$

$$F(l/\delta) = (l/\delta)\left[3\sqrt{\pi} - 2\,\delta/l\right] \quad \text{at } l/\delta \gg 1 \tag{65}$$

$$\Phi(l/\delta) = 2 \quad \text{at } l/\delta \ll 1 \tag{66}$$

$$\Phi(l/\delta) = 2(l/\delta)^2 \quad \text{at } l/\delta \gg 1 \tag{67}$$

Strong roughness can be modelled by equations based on Darcy´s[322] and Brinkman´s[323] formalism:[314, 324]

$$\Delta f_{film} = -\frac{2 f_0^2 \rho}{\left(\mu_q \rho_q\right)^{1/2}}\, Re\left\{\frac{1}{q_0} + \frac{L}{\xi_H^2 q_1^2} - \frac{1}{W}\frac{1}{\xi_H^2 q_1^2}\left[\frac{2q_0}{q_1}\left[\cosh(q_1 L) - 1\right] + \sinh(q_1 L)\right]\right\} \tag{68}$$

$$\Delta w_{film} = -\frac{4 f_0^2 \rho}{\left(\mu_q \rho_q\right)^{1/2}}\, Im\left\{\frac{1}{q_0} + \frac{L}{\xi_H^2 q_1^2} - \frac{1}{W}\frac{1}{\xi_H^2 q_1^2}\left[\frac{2q_0}{q_1}\left[\cosh(q_1 L) - 1\right] + \sinh(q_1 L)\right]\right\} \tag{69}$$

where $q_0 = (i2\pi f_0 \rho/\eta)^{1/2}$, $q_1^2 = q_0^2 + \xi_H^{-2}$ and $W = q_1 \cosh(q_1 L) + q_0 \sinh(q_1 L)$. ξ_H is a local permeability depending on the layer porosity. For $L = 0$ equations (68) and (69) reduce to the Gordon-Kanazawa-Mason equations (57) and (58) of the quartz response for the smooth quartz crystal/liquid interface. Equations (68) and (69) describe a thin, porous film rigidly attached to the quartz in a liquid environment.

Battery electrodes usually are rough particles attached to the electrode via a thin polymer binder film immersed in a liquid electrolyte. In order to account for the particles covered by the porous film, the model presented in equation (68) and (69) must be implemented into another model also describing the particles:[177, 325, 326]

$$\frac{\Delta f}{n} = \Delta f_{film}\,(1 - m\pi r^2)q - \frac{3}{2}\frac{f_0^2 \rho \delta}{\left(\rho_q \mu_q\right)^{1/2}}\, m r^2\, \frac{\pi^2}{2} - \frac{4}{3}\frac{f_0^2 \pi r^3}{\left(\rho_q \mu_q\right)^{1/2}}\, m(\rho_b + \rho) - (1 - q)\,\frac{2 f_0^2 \rho}{\left(\rho_q \mu_q\right)^{1/2}}\, Re\left(\frac{1}{q_0}\right) \tag{70}$$

$$\frac{\Delta w}{n} = \Delta w_{film}\,(1 - m\pi r^2)q + \frac{3 f_0^2 \rho \delta}{\left(\rho_q \mu_q\right)^{1/2}}\, m r^2 \frac{\pi^2}{2} - (1 - q)\frac{4 f_0^2 \rho}{\left(\rho_q \mu_q\right)^{1/2}}\, Im\left(\frac{1}{q_0}\right) \tag{71}$$

The overtone number n is an odd number and depends on which frequency mode the quartz resonator is operated. The particles must be hemi-spherical and have a radius r. The particle density on the quartz surface is described by m, while the quartz surface has a relative coverage q. The gravimetric density of the particles is described by ρ_b.

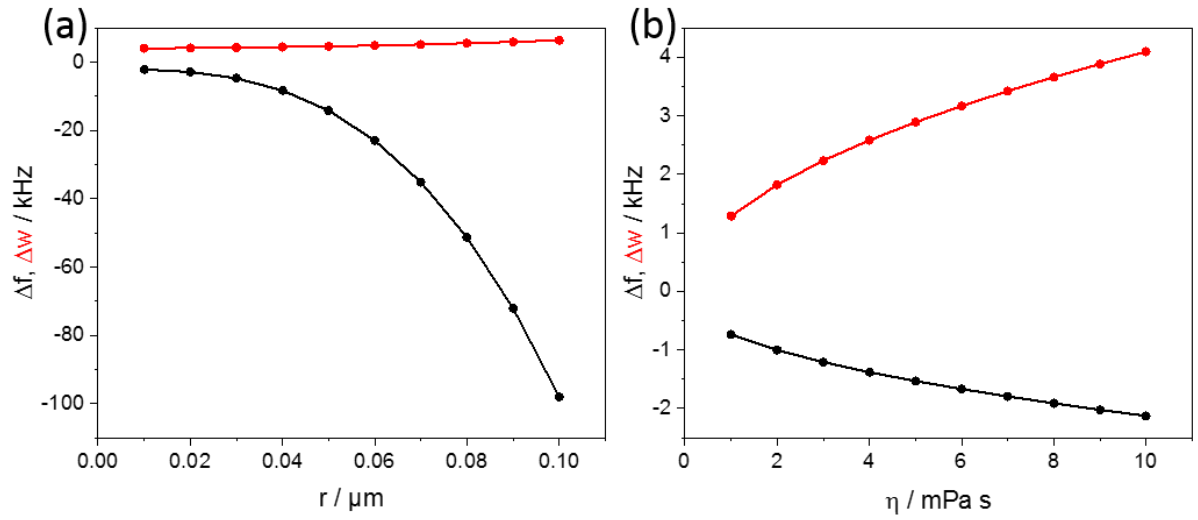

Figure 30: Graphical representation of Daikhin´s equations (70) and (71) as a function of the two main parameters affecting on Δf and Δw: (a) the particle radius r and (b) the electrolyte viscosity η. If not varied, the parameters for the simulation are n = 1, f_0 = 10 MHz, ρ = 1 g cm^{-3}, η = 10 mPa·s, μ_q = 2.947·10^{11} g·cm^{-1} s^{-2}, ρ_q = 2.648 g cm^{-3}, ρ_q = 1 g cm^{-3}, m = 100000 cm^{-2}, r = 0.01 µm, h = 100 nm, ξ_H = 100 nm.

Daikhin´s model in equations (70) and (71) is developed with the purpose to study surface parameters of the electrode particles during battery operation. Taking a close look at these equations, one finds that under otherwise identical conditions, the shift of the resonance frequency to lower values (corresponding to a more negative Δf) caused by a rough film containing hemi-spherical particles of radius r becomes the larger the larger the particle size r is, and the damping w increases as well, Δw being positive (Figure 30 (a)). Another parameter affecting Δf and Δw is the electrolyte viscosity η, where an increase in viscosity results in an increase of Δf to more negative values and an increase of Δw to more positive values (Figure 30 (b)). For this reason Daikhin *et al.*[177] have given this tool the name '*in-situ* hydrodynamic spectroscopy'.

As a summary of this section, Figure 31 gives an overview of the discussed models. Starting from the left, a quartz sensor in vacuum is shown. This can be either used as a mass sensitive device, when a thin and rigidly bond surface film is deposited on the quartz surface (Sauerbrey), or as a viscosity sensitive device, when immersed in a viscous medium (Gordon-Kanazawa-Mason). The model for surface roughness and porosity is based on formalisms of Darcy and Brinkman. Finally, Daikhin expanded the model in order to apply it to battery like coatings on the quartz. These models are

specific cases of relevance for the results presented in this thesis. For further details like the study of viscoelastic layers the reader is referred to the literature.

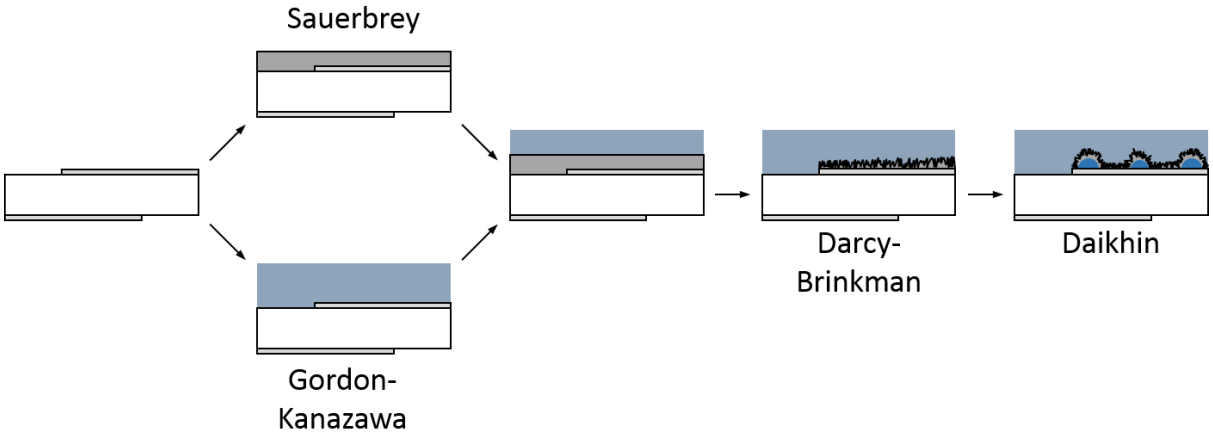

Figure 31: Schematic representation of the theoretical models discussed for the derivation of the above formalism. A quartz in vacuum is sketched on the left, which can be used as a mass sensor in case of a rigidly attached thin film (Sauerbrey) or as a viscosity sensitive device (Gordon-Kanazawa-Mason). Depositing a thin, rigid film on the quartz inside a viscous medium one obtains a mix of Sauerbrey and Gordon-Kanazawa-Mason. Considering surface roughness, another model must be applied (Darcy-Brinkman). For battery applications, where semi-spherical particles covered by a thin polymer film immersed into a liquid, Daikhin developed another model.

EQCM data were acquired by an Agilent E5100A network analyzer with a Delphi software to read out the admittance of the 10 MHz AT cut quartzes (KVG Quartz Crystal Technology) in parallel to electrochemical measurements. The accurate time at which the admittance spectrum was recorded was saved. The quartz resonators had a keyhole shaped Au-electrode on each side of the crystal with a Cr adhesive layer. One electrode was used as WE, which was coated with a thin film of graphite (C-NERGY SFG 6 L GRAPHITE, Imerys Graphite & Carbon Switzerland Ltd.). An airbrush gun (Sparmax AC-55) was used to spray coat a SFG6:PVDF (8:2) NMP-ink onto the Au-electrode. During spray coating, the quartz was heated to ca. 60 °C to 80 °C on a hotplate. In order to only cover the Au-electrode of the quartz by active material during coating, the quartz substrate was covered by nail polish, which after the coating procedure could be easily removed without any residues. The thickness of the coated graphite layer must be chosen thick enough that the electrochemical peaks in the CV are still recognizable and thin enough that the Q-factor (signal intensity to signal width ration) of the oscillator is still good enough for a reliable analysis. Typical loadings on the quartz were in a range of several 10 µg cm^{-2} (estimation from Sauerbrey´s[316] equation by comparing admittance spectra in air recorded before and after coating (Figure 32)).

The WE was connected to a potentiostat (Ivium Technologies CompactStat®) via an inductor and at the same time to the signal output connector of the network analyzer via a capacitor. The backside of the quartz was not in contact with the electrolyte and was directly connected via shielded BNC cables to the network analyzer signal input connector.

Before assembling the electrochemical cell with the coated quartz, a calibration with a short circuit ('Thru') was carried out in the relevant frequency range. Mounted into a suitable electrochemical Teflon cell, the quartz was sealed with Simriz™ O-rings and filled with 300 µl of electrolyte in an Ar-filled glovebox. CE and RE are Na-metal, which are inserted into the cell via two small holes in the lid of the cell, which closed the cell and avoided electrolyte evaporation.

A Levenberg-Marquard algorithm was used to fit the obtained admittance spectra to a Lorentz function, from which the shift in resonance frequency Δf and the peak broadening Δw can be obtained. Based on the measurement time Δf and Δw can be related to the electrochemical data points.

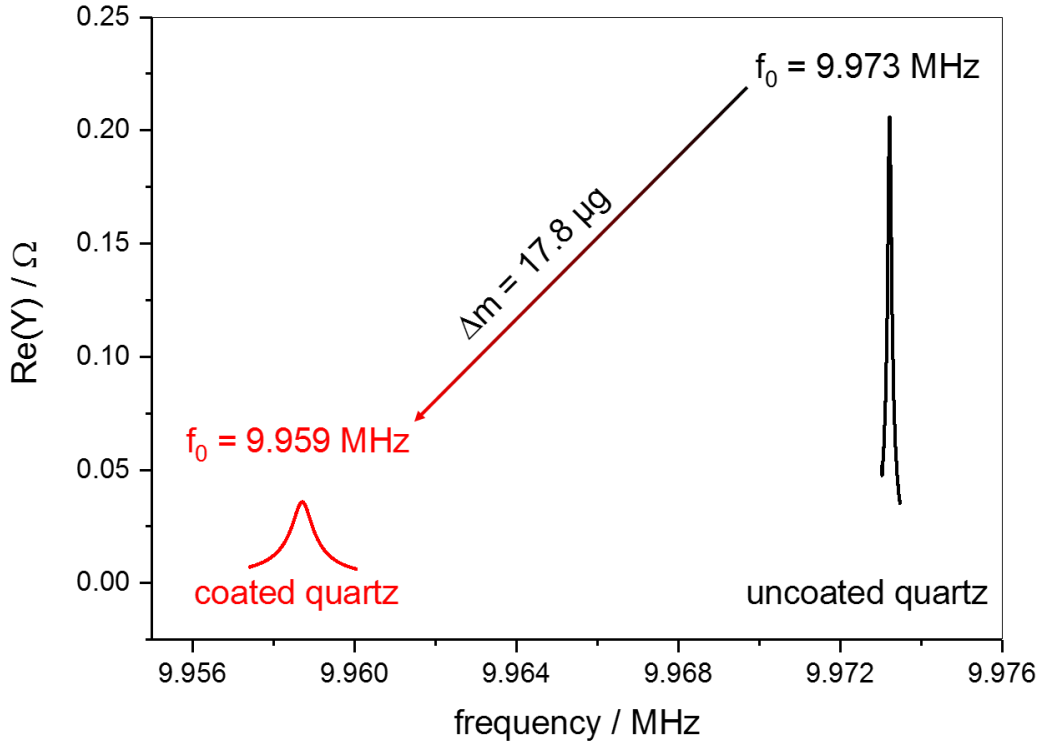

Figure 32: Effect of the electrode coating on the shape of the resonance signal. Besides the broadening of the peak, a 14 kHz frequency shift is observed for a typical graphite loaded quartz, corresponding to a Sauerbrey mass of 17.8 µg.

5 Battery Electrochemistry – from Fundamentals to Application

With the aid of the introduced and customized advanced characterization techniques, different battery electrochemistries with the goal of an application in a battery prototype are fundamentally studied in the following chapter. This chapter is divided into four parts: First the formation mechanism of the solid electrolyte interphase on graphite electrodes in LIBs is studied in detail, as this step is essential for the operation of graphite anodes (section 5.1). Thereafter the focus is laid onto Na-ion batteries. The intercalation of solvated Na-ions into graphite and the resulting formation of ternary Na-graphite intercalation compounds (GICs) is discussed in section 5.2, while in section 5.3 the V_2O_5-electrochemistry in NIBs as a positive electrode material is studied, with a focus on the influence of electrode morphology on performance. In the last section (section 5.4) finally the knowledge from the previous three parts is combined in order to demonstrate construction and characterization of a fully operating NIB with a graphite anode and a V_2O_5 cathode. Figure 33 shows an overview about the structure of a rocking chair battery and in which section each topic is treated. Thus, all fundamental aspects in batteries are covered in this chapter and based on this understanding, a full battery is built and operated.

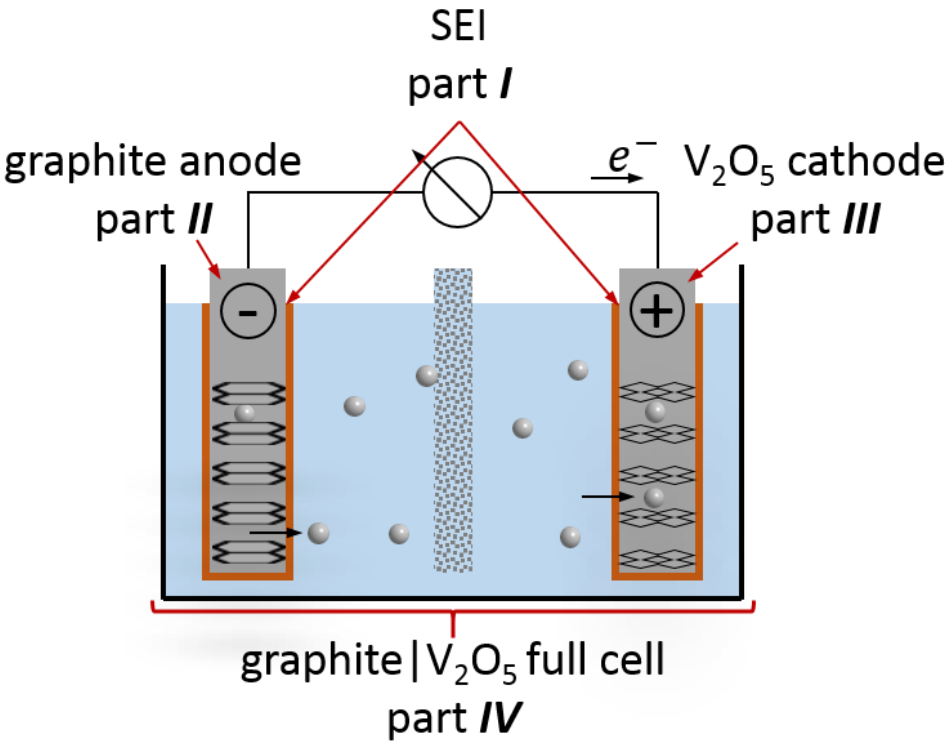

Figure 33: Structure of a rocking chair battery, indicating the section of this thesis in which each part is treated.

5.1 Formation Mechanism of the Solid Electrolyte Interphase on Graphite in LIBs

5.1.1 Electrochemistry of Graphite in LIBs

Before studying the SEI formation, it is worth to also understand Li-ion intercalation/de-intercalation into graphite. Figure 34 (a) shows charge/discharge profiles of a graphite electrode (MCMB) in a 1 M $LiPF_6$ in EC/DMC (1:1) electrolyte measured at a C-rate of C/10, *i.e.* at 37.2 mA g^{-1}. The voltage profiles show several plateaus and when fully discharged to 0.01 V, a total capacity of 354 mAh g^{-1} is obtained, which is close to the theoretical capacity of LiC_6 (372 mAh g^{-1}). The derivative of the capacity *vs*. the electrode potential gives the dQ/dV-plot (Figure 34 (b)), which illustrates the electrochemical processes as a function of electrode potential, similar to a CV. For an oxidation reaction electrons are removed from the electrode, which results in a positive differential charge. For a reduction reaction electrons are added to the electrode and the sign of dQ/dV is negative. As can be seen, three major electrochemical processes occur between 0.3 V and 0.01 V.

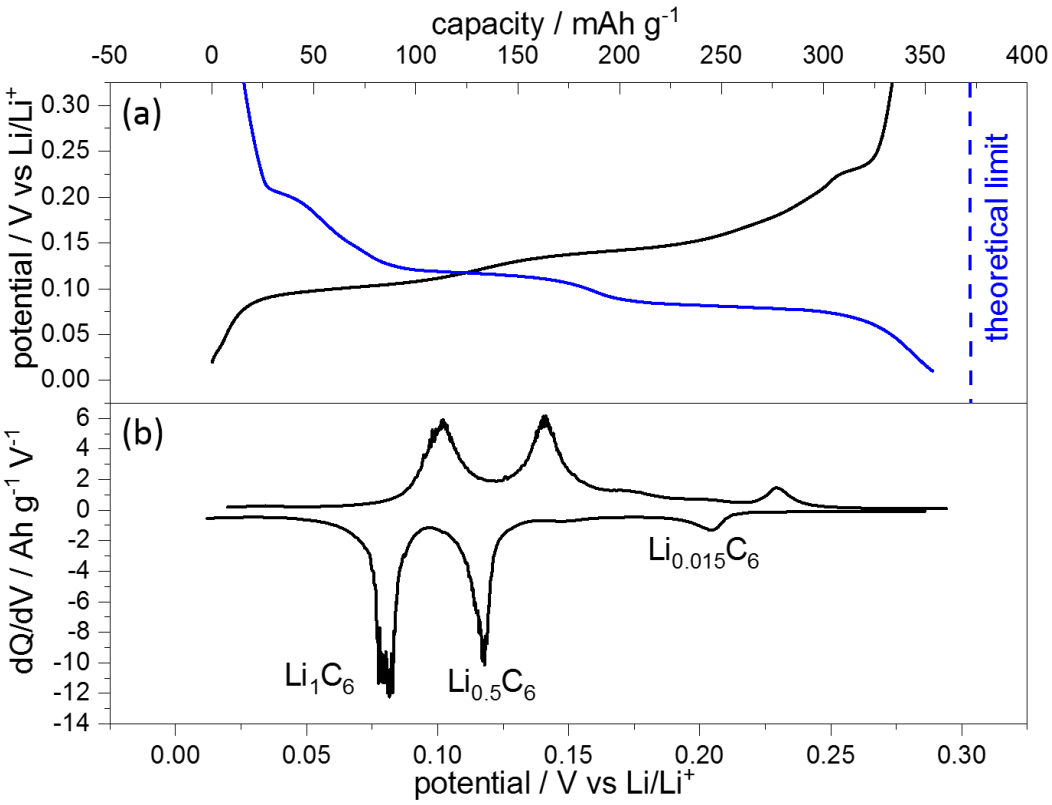

Figure 34: (a) charge (black) /discharge (blue) profile (C/10) of MCMB in 1 M $LiPF_6$ in EC/DMC and (b) the corresponding dQ/dV-plot.

These electrochemical processes can also be observed from other electrochemical experiments. Figure 35 (a) shows a plot of the differential capacity as a function of potential, which is obtained from a PITT measurement. For the PITT measurement the electrode potential was stepwise lowered by 3 mV starting from 0.3 V. Once 0.09 V was reached, the potential was again stepwise increased to 0.3 V. After each potential step, a 5 h current transient was measured. As above, three cathodic and anodic peaks are clearly visible. The differential capacity, which is calculated from the inserted charge during the 5 h current transients, is large, whenever a peak is observed in the dQ/dV-plot in Figure 34 (b). An exemplary current transient measured after a potential step from 0.213 V to 0.216 V is shown in Figure 35 (b), and in a different representation in Figure 35 (c). Here, it is plotted as $-\mathrm{It}^{-1/2}$ *vs.* $log(\mathrm{t})$. Between 1800 s and 3200 s a plateau can be observed in this plot.

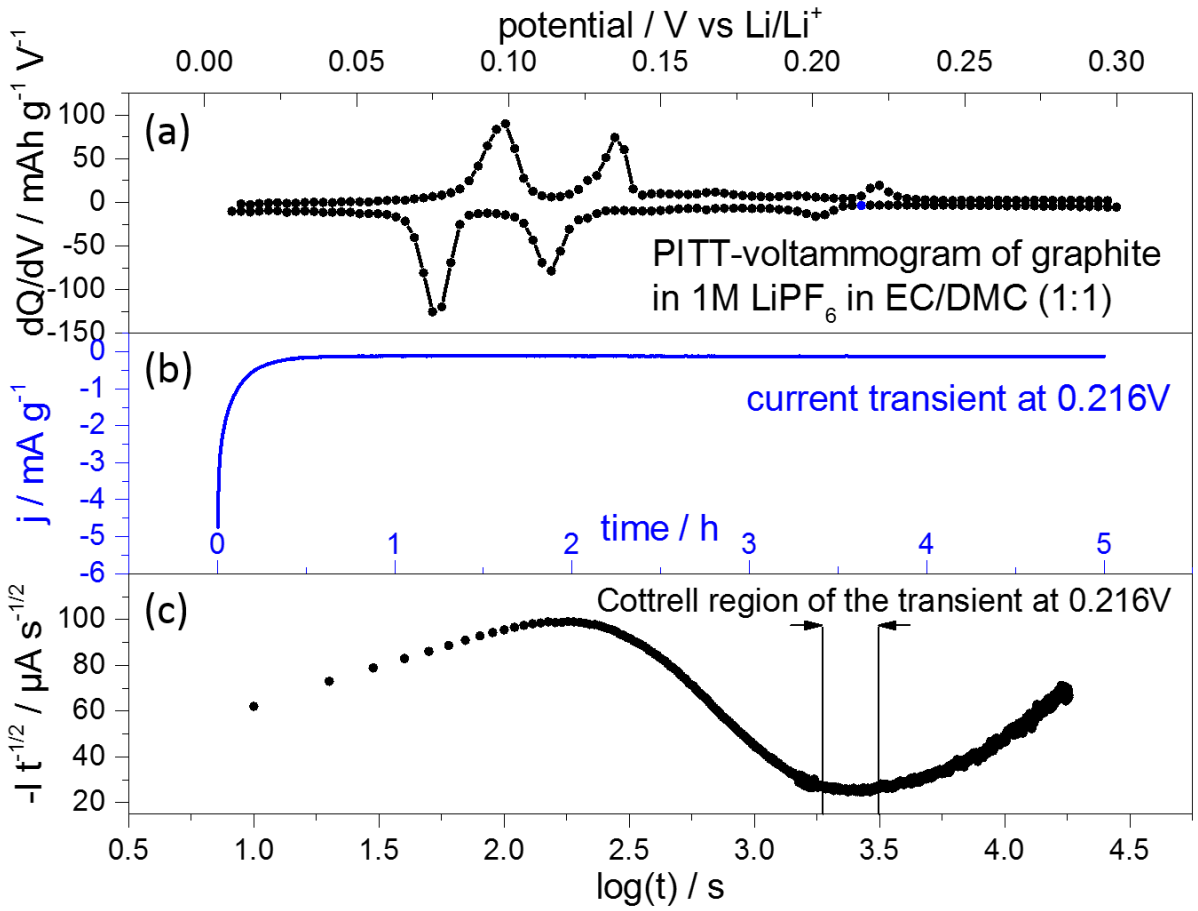

Figure 35: (a) differential capacity plot vs. electrode potential of a PITT measurement with a MCMB electrode in 1 M $LiPF_6$ in EC/DMC with 3 mV potential steps and a potential hold time of 5 h each. (b) shows an exemplary current transient measured at 0.216 V, which is again shown in (c) in the $-It^{-1/2}$ vs. $log(t)$ plot in order to determine the Cottrell region.

As will be discussed later, these electrochemical processes are caused by Li-ion intercalation (cathodic peaks) and by de-intercalation (anodic peaks). Intercalation processes, however, are not the main focus of this section, but rather the SEI-formation. The SEI-formation shows up in various electrochemical experiments such as CV (Figure 36 (a), (b)), PITT (Figure 36 (c), (d)) and charge/discharge measurements with their corresponding dQ/dV-plots (Figure 36 (e), (f)). Taking a close look at the first negative scan in the CV in Figure 36 (a), one can realize a slightly increased current compared to the negative scans of the consecutive cycles. A magnification of this region is shown in Figure 36 (b), where one can clearly see an increased cathodic current with shoulders at 1.4 V, 1.0 V and a peak at 0.75 V. At 0.4 V another peak is observed. These peaks are irreversible, since they are not accompanied by anodic peaks and they do not occur in the following cycles. Similar observations can be made in the magnifications of the PITT-voltammogram and dQ/dV-plot, though with slightly shifted potentials. Here, the current density of a current transient after a 10 mV step and 15 minutes potential hold is shown. All measurements show four distinguishable SEI-related features. Also in these measurements peaks at more negative potentials are visible. As above, they occur in the Li-intercalation/de-intercalation regime.

In order to study the SEI-formation by STM, which requires the use of a graphite single crystal, the electrochemistry of an HOPG model electrode must also be studied. Figure 37 shows an LSV with a

potential sweep towards more negative potentials of HOPG in 1 M $LiPF_6$ in EC/DMC, which in analogy to the powder electrodes studied in Figure 36 also shows four different SEI-features in the first scan.

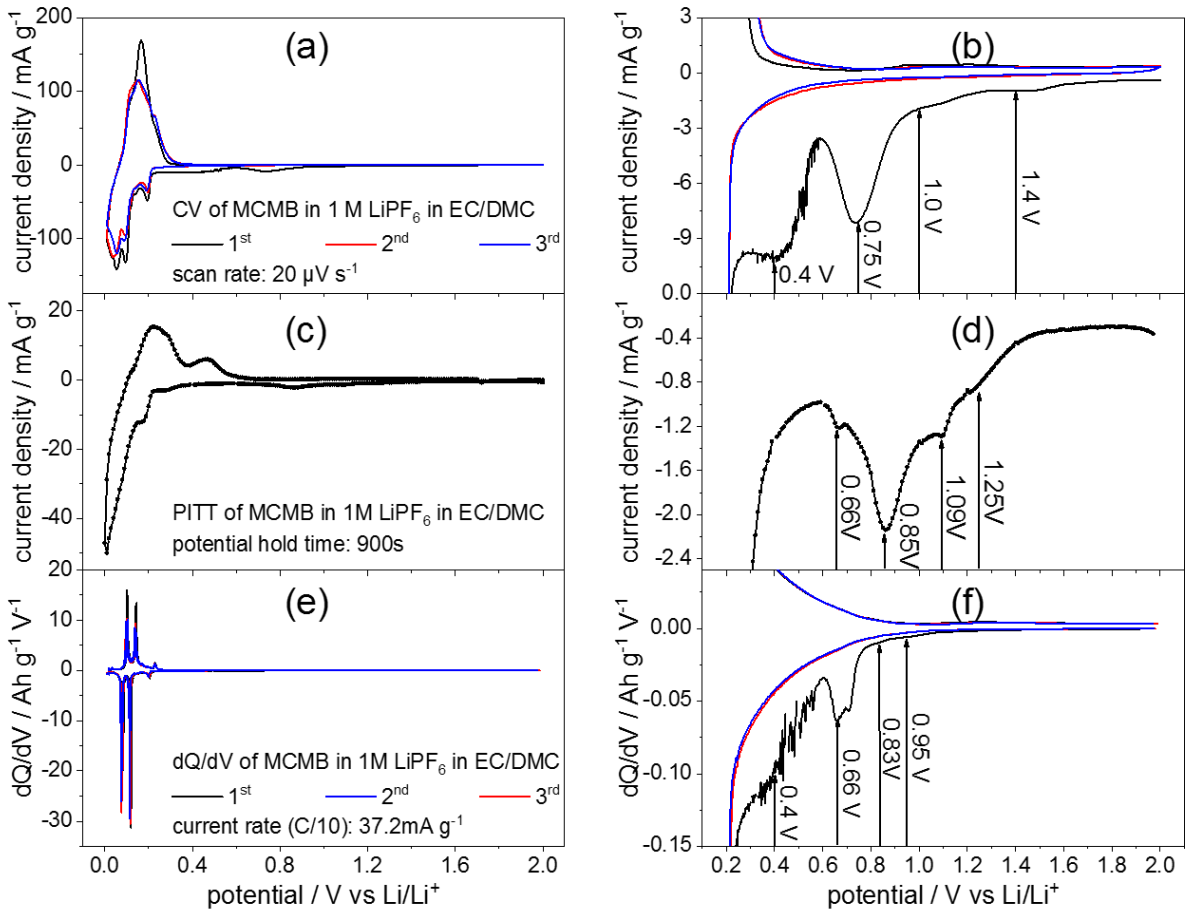

Figure 36: Different voltammograms / dQ/dV-plots of MCMB in 1 M $LiPF_6$ in EC/DMC measured by CV (a), (b), PITT (c), (d) and galvanostatic charge/discharge with its dQ/dV-plot (e), (f). The left column shows the full range data, while the right column shows a magnification of the SEI-relevant part. (CV: 20 µV s^{-1} potential sweep rate, PITT: 10 mV steps with 15 minutes potential hold and 15 minutes open circuit potential (OCP) hold, current value after 15 min plotted versus potential, charge/discharge: 0.372 mA g^{-1} (C/10) current density).

The main message from this section is that the SEI-formation of powder as well as single crystalline graphite is a multistep process occurring in four major steps. Additionally, the SEI-formation on real battery electrodes (MCMB) and model electrodes (HOPG) can be well compared and similar conclusions can be drawn for both systems.

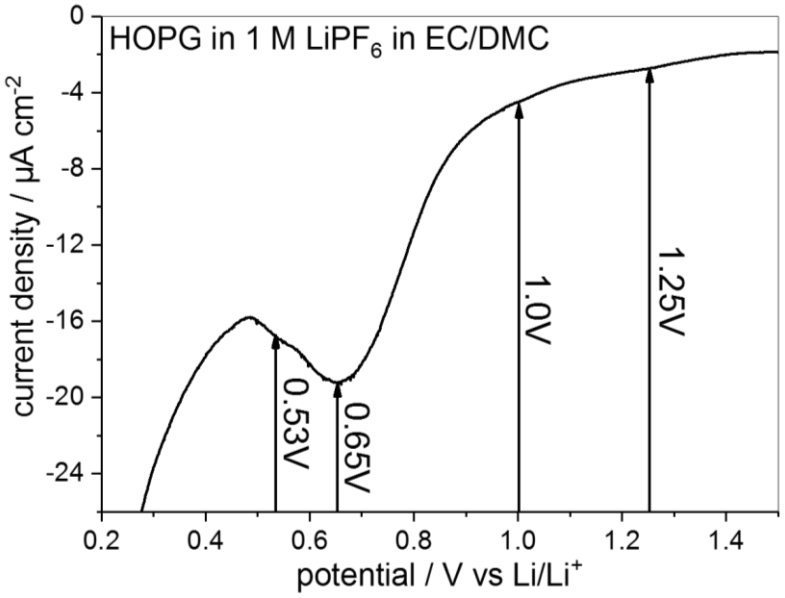

Figure 37: Cathodic potential sweep in the SEI-formation region on an HOPG sample in 1 M $LiPF_6$ in EC/DMC. (potential sweep rate: 20 µV s^{-1})

5.1.2 STM Studies on the SEI Formation

Gaining deeper understanding of the SEI-formation, complementary techniques like *in-situ* EC-STM are required. Figure 38 shows a series of STM images of an HOPG electrode in 1 M $LiPF_6$ in EC/DMC. The images are recorded at a constant potential of 2.0 V after they were set to the potential indicated in each image during cyclic voltammetry. The corresponding CVs are shown in Figure 39.

The pristine HOPG surface is shown in Figure 38 (a), and has the typical appearance of HOPG: large, atomically flat terraces are interrupted by monoatomic steps like in the upper left corner or by multilayer steps as in the center of the image. The interplanar spacing between two adjacent graphene sheets amounts to 3.35 Å[327], and thus the 2 nm step in the center of Figure 38 (a) consists of 6 layers. The bright spots along the step edge are exfoliated graphene flakes.

Stepwise reduction of the electrode potential does not show any persisting effect on the surface topography until a potential of 0.9 V is reached (Figure 38 (g)). Suddenly, the terraces are no longer flat, but develop some blisters. In some areas the graphite sheets swell up from the original 3.35 Å to ca. 8 Å. It is worth noting that the swollen regions overlap each other.

Further reduction of the lower CV potential enhances the graphite swelling until an exfoliation sets in at 0.6 V. Going even lower in potential, the exfoliation gets stronger leading to holes in the electrode surface and the delamination of larger graphene sheets, which eventually destroys the electrode. Additionally, one observes that the STM images become noisy below 0.5 V, which will be of importance in the later discussion.

The CVs (Figure 39) measured in between the STM measurements show some interesting features: in none of the CVs, except the CV measured to 0.0 V, anodic peaks can be observed, which is a clear indication for the irreversible charge loss caused by the SEI-formation. The 0.0 V CV is also the only CV showing a crossover of cathodic and anodic scan (trace crossing) at very low potential. Another observation is that the currents decrease scan by scan in the SEI potential-range. In this range, a barely visible cathodic shoulder at 1.0 V appears, followed by a cathodic peak at 0.48 V. This peak as well as the onset potential of the SEI-formation shift to less positive potentials from cycle to cycle, since the

SEI-growth rate and thus the charge consumption is slowed down with time due to the increased tunneling resistance of the electrons through the SEI-film.

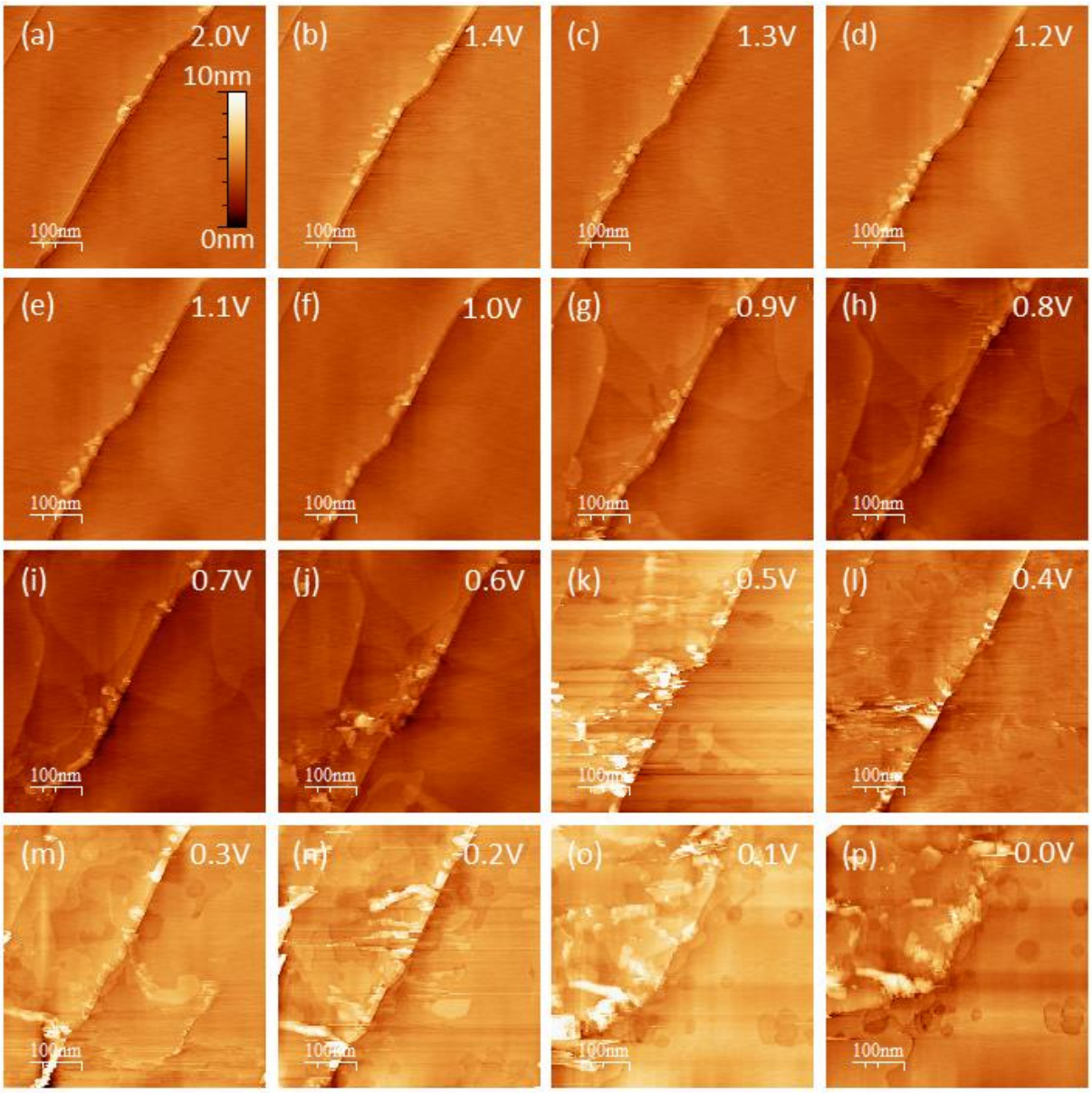

Figure 38: Series of in-situ *EC-STM images of HOPG in 1 M $LiPF_6$ in EC/DMC. Each image was measured at 2.0 V, after it was ramped to the potential indicated in each image at a potential sweep rate of 5 mV s^{-1}. (scan size: 500 nm x 500 nm, tunneling current: 500 pA, tip potential: 2.1 V, sample potential: 2.0 V, bias: 100 mV, tip velocity: 0.5 µm s^{-1})*

Similar studies as shown in Figure 38 have been presented in literature earlier, however, they suffer from two shortcomings. First, reversible processes only occurring at low electrode potential cannot be visualized, since imaging is always performed at high electrode potential. Secondly, no conclusions about time scales of surface processes can be drawn, since imaging is always performed at 'steady-state'. Operating STM *in-operando*, *i.e.* performing the potential scan of the electrode while imaging the surface by STM, can solve these problems.

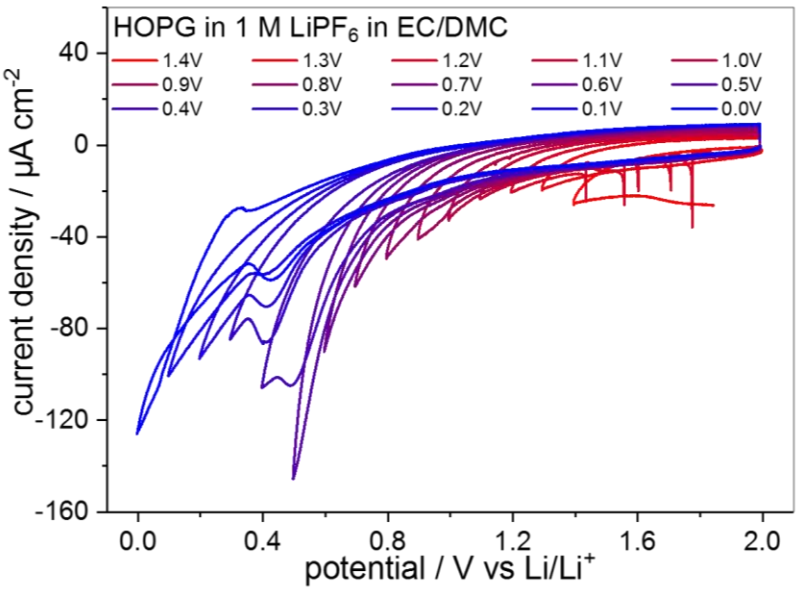

Figure 39: CV series of HOPG in 1 M $LiPF_6$ in EC/DMC measured in combination with the STM experiment in Figure 38 (potential sweep rate: 5 mV s^{-1}).

Thus, Figure 40 shows a series of 3D-STM images of an HOPG electrode, each time three subsequently recorded images in a row. STM images are recorded by a line-by-line scan of the electrode surface, where the scan rate can be set. Consequently, one can assign each line to the time, where the line was measured, converting thus the original *x-y* STM image into a *y-t* image. The time on the other hand can be matched with the measurement time of the potentiostat, as applied potential and current are also measured as a function of time. This way, one obtains an image as presented in Figure 40 (a) for instance. Here, the electrode surface is composed of atomically flat terraces interrupted by step edges. The blue line indicates, which potential was applied to the electrode during STM-scanning. Initially, the electrode is set to 2.0 V, from where it is lowered to 1.4 V and held there. As can be seen, the surface does not change: it remains atomically flat throughout the entire time of experiment.

The situation changes, when ramping the potential to 1.0 V (Figure 40 (b)). A surface film precipitation is visible, starting in a potential range between 1.2 V and 1.3 V. Keeping the electrode potential at 1.0 V, an initial increase of film thickness can be seen, which, however, stops after some time. An interesting observation is made, when increasing the potential to the original 2.0 V: the surface film is dissolving and disappears after short time, leaving behind an atomically smooth surface again.

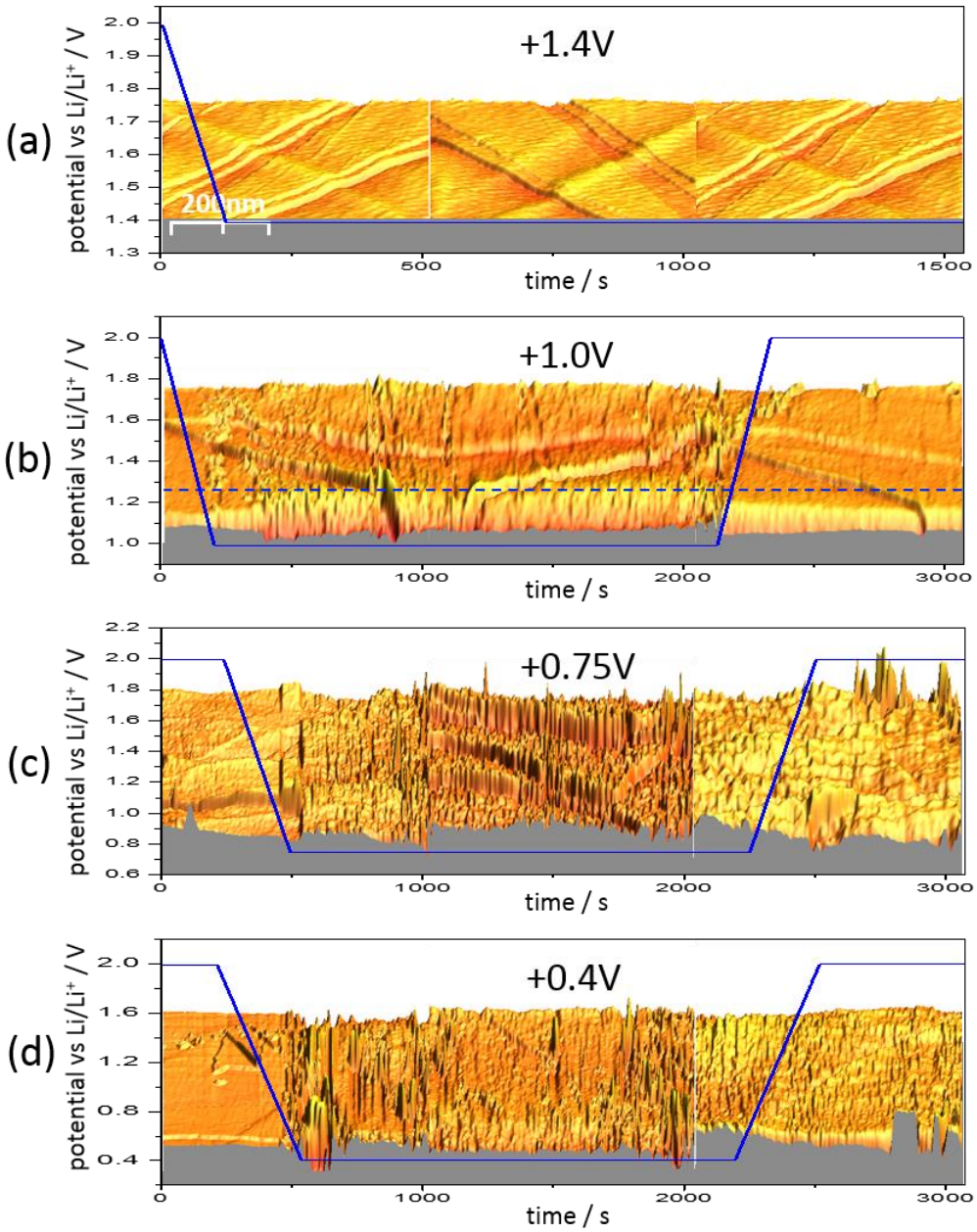

Figure 40: In-operando EC-STM of HOPG in 1 M $LiPF_6$ in EC/DMC. The x-axis is converted into a time axis (scan size: 500 nm x 500 nm, tunneling current: 500 pA, tip potential: 2.1 V, sample potential: variable, bias: variable, tip velocity: 1 µm s^{-1} for (a) and 0.5 µm s^{-1} for (b)-(d), potential sweep rate: 5 mV s^{-1}).

The SEI-growth rate can be illustrated by a height profile measured along the dashed blue line in Figure 40 (b). The height profile is shown in Figure 41, from which one can estimate a film thickness of roughly 2 nm and a growth time of around 200 s.

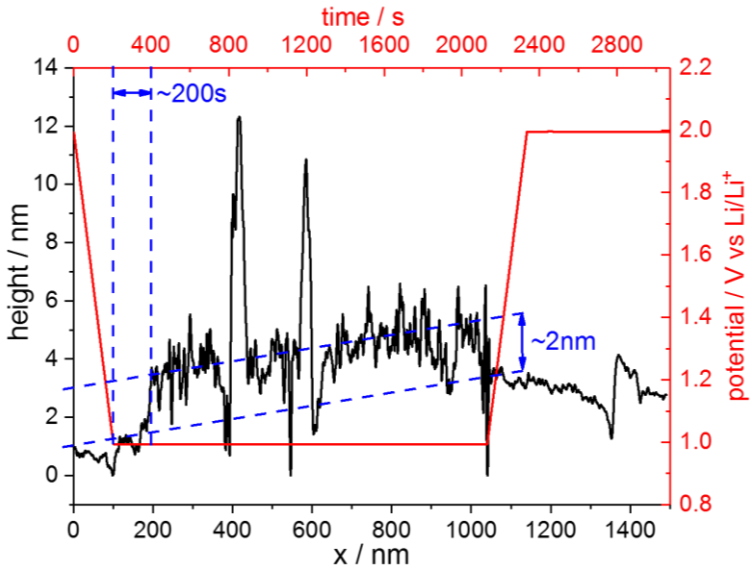

Figure 41: Height profile across the SEI-film measured at 1.0 V along the blue line in Figure 40 (b).

Lowering the electrode potential to 0.75 V (Figure 40 (c)), the situation initially is the same as when lowering the potential to 1.0 V (Figure 40 (b)). In the beginning, the electrode is atomically smooth, until the potential is low enough and a surface film can precipitate. The film growth happens within a specific time and is limited to a certain thickness. Ramping the electrode potential to larger values again does not result in a dissolution of the SEI-film, however. Thus, while the SEI-formation is reversible at 1.0 V, it becomes irreversible at 0.75 V. The same observation is made, when ramping the potential to 0.4 V (Figure 40 (d)). This experiment was only done for sake of completeness, since an additional SEI-formation step is expected from electrochemical measurements in this potential range (Figure 36 and Figure 37).

5.2 Intercalation mechanism of solvated Na-ions into graphite

The obtained knowledge of surface processes, such as the SEI formation or the Li-co-intercalation into graphite, helps to also study the graphite electrochemistry in NIBs. As mentioned in the Introduction, Na only intercalates into graphite to a minor extent in classical carbonate electrolytes, which is by far not sufficient for application in a battery. Figure 42 shows a study of graphite electrodes in two electrolytes typically used in NIBs, namely in a 1 M solution of $NaClO_4$ in EC/DMC (Figure 42 (a)) and in EC/PC (Figure 42 (b)). The first negative scan in the EC/DMC electrolyte shows a higher current compared to the consecutive cycles. In similarity to the SEI-observations made in section 5.1, this cathodic current is not matched by any corresponding anodic current. Moreover, the cathodic peaks occur at similar potentials as in Figure 36 (a) and (b) after correcting the potential scale of the Li/Li^+ to the Na/Na^+ system. The CVs also show a reversible peak pair in the low potential regime, which has an approximate capacity of below 10 mAh g^{-1}. In comparison to the Li-system in Figure 36 (a), the current densities are about one order of magnitude smaller here.

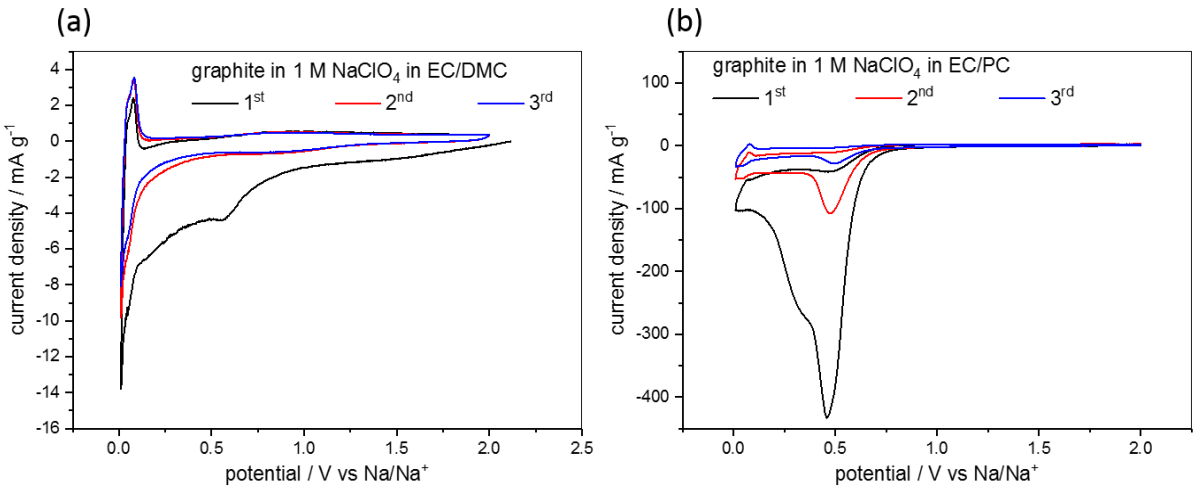

Figure 42: CVs of graphite in classical carbonate based electrolytes. (a) MCMB in 1 M $NaClO_4$ in EC/DMC and (b) MCMB in 1 M $NaClO_4$ in EC/PC. (potential sweep rate: 50 µV s^{-1})

Switching to the EC/PC electrolyte, the shape of the CV completely changes (Figure 42 (b)). The observed currents are strongly increased, the CV changes from cycle to cycle and new peaks appear. The cathodic peaks are not paired with any anodic peak, except a small reversible peak couple in the low voltage range.

In order to gain more insight into the electrochemistry of the latter system, an *in-situ* EC-STM study was conducted on an HOPG electrode in 1 M $NaClO_4$ in EC/PC (Figure 43). The experimental procedure was the same as described for the *in-situ* STM study in the Li-system in Figure 38. The CVs measured in between each STM image are shown in Figure 44.

Figure 43 (a) shows the pristine HOPG sample. The image quality is not the best, but one can recognize the terraces, which are decorated with graphene flakes. After ramping the sample to 1.4 V (Figure 43 (b)), the electrode surface does not change significantly. The image quality became better, since the STM tip probably lost some debris picked up earlier on. Moreover, the position on the sample shifted somewhat, due to the typical drift of STM. Also when cycling down to 1.2 V (Figure 43 (c)), the surface is not affected much. This changes, when reaching 1.0 V (Figure 43 (d)), where the graphite surface is now clearly decorated by numerous graphene flakes stemming from ruptured step edges. At 0.8 V (Figure 43 (e)), this issue becomes obvious and at 0.6 V most step edges are gone and the surface is covered by a surface film similar to that observed in the earlier SEI experiments in Figure 38 and Figure 40 (fuzziness). At lower potentials the electrode surface was completely destroyed, which made STM imaging impossible.

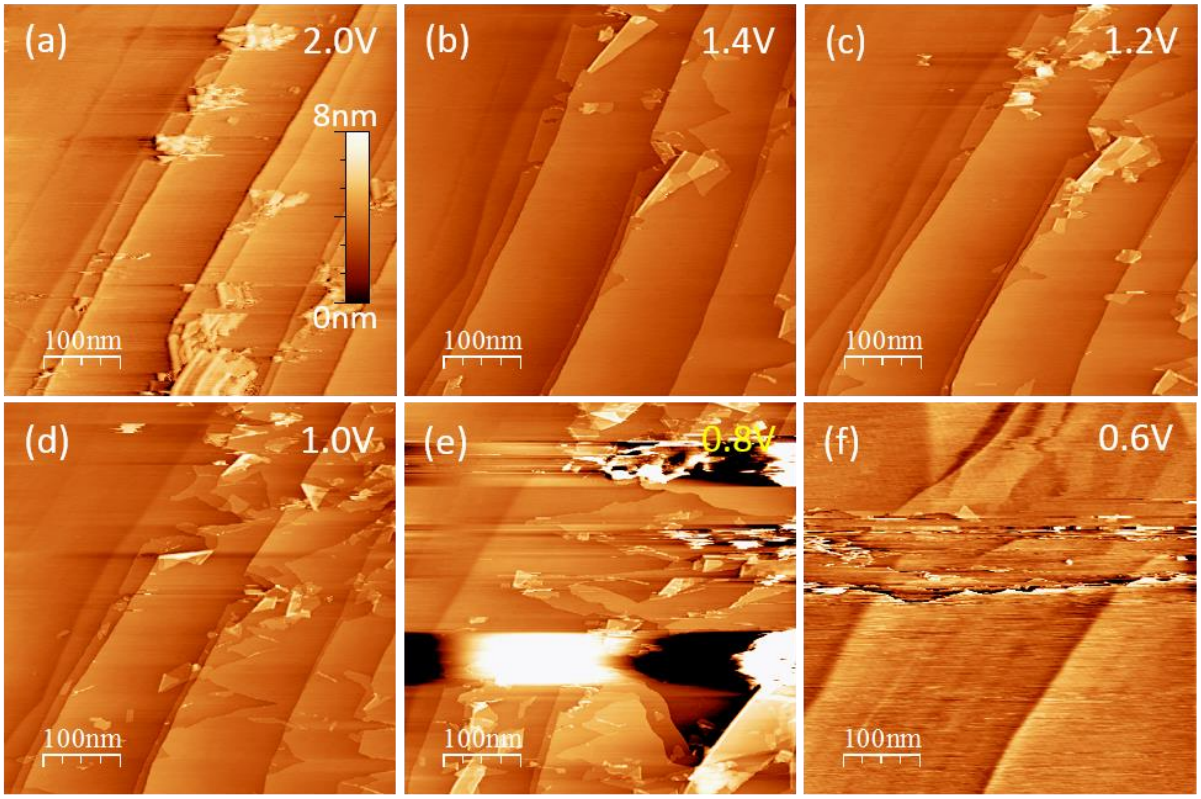

Figure 43: Series of in-situ *EC-STM images of HOPG in 1 M $NaClO_4$ in EC/PC. Each image was measured at 2.0 V, after it was ramped to the potential indicated in each image at a potential sweep rate of 5 mV s^{-1} (scan size: 500 nm x 500 nm, tunneling current: 100 pA, tip potential: 2.1 V, sample potential: 2.0 V, bias: 100 mV, tip velocity: 0.5 µm s^{-1}).*

The CVs measured during the STM experiment are shown in Figure 44 and show some similarities to the CVs measured on powder graphite in Figure 42. Below 0.7 V the cathodic current starts to increase. An anodic peak appears in the CVs measured to 0.4 V and below.

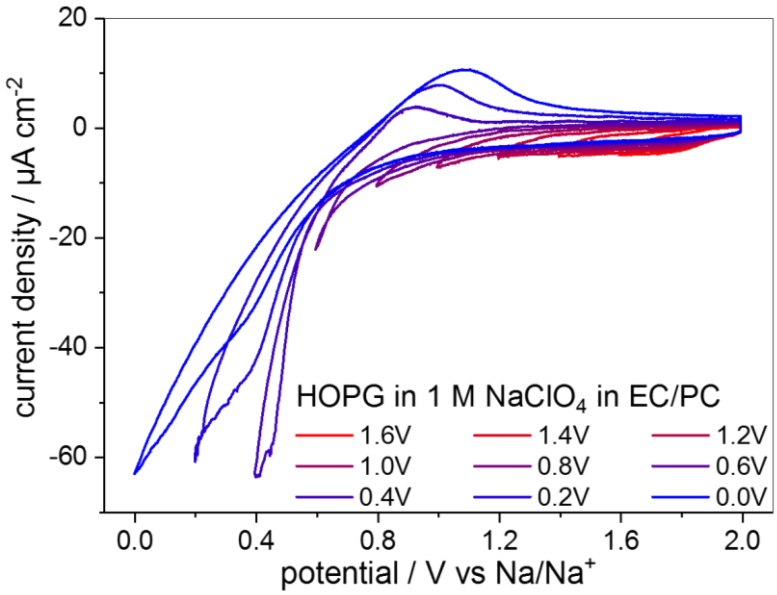

Figure 44: CV series of HOPG in 1 M $NaClO_4$ in EC/PC measured in combination with the STM experiment in Figure 43 (potential sweep rate: 5 mV s^{-1}).

Since Na cannot be intercalated into graphite from carbonate electrolytes, further studies are restricted to ether electrolytes, namely the four shortest linear glymes G_1, G_2, G_3 and G_4. A 1 M solution of $NaClO_4$ in each solvent was prepared for a comparative study of the influence of chain length on the electrochemical behavior at graphite electrodes.

Figure 45 shows CVs of a graphite electrode in solutions based on the four different glymes. At first glance, the CVs of G_1, G_2 and G_4 have some similarities, whereas the G_3-CV has unique features. For the first three electrolytes, the CV consists of four cathodic peaks shifting to more positive potential with increasing chain length. The cathodic peaks are accompanied by anodic peaks, which, however, are blurred and overlap over a wide potential range. Another peak pair appears in the low voltage range for the G_2 system, which also shifts to more positive potential for the G_4. The peak current densities increase with increasing length of the glyme molecule. In the G_3 electrolyte, a fundamentally different electrochemistry seems to take place. In the negative scan, no sharp peak appears, but it seems like two peaks are overlapped and smeared out over a wide potential window. In contrast to the other electrolytes, the anodic peaks are very pronounced.

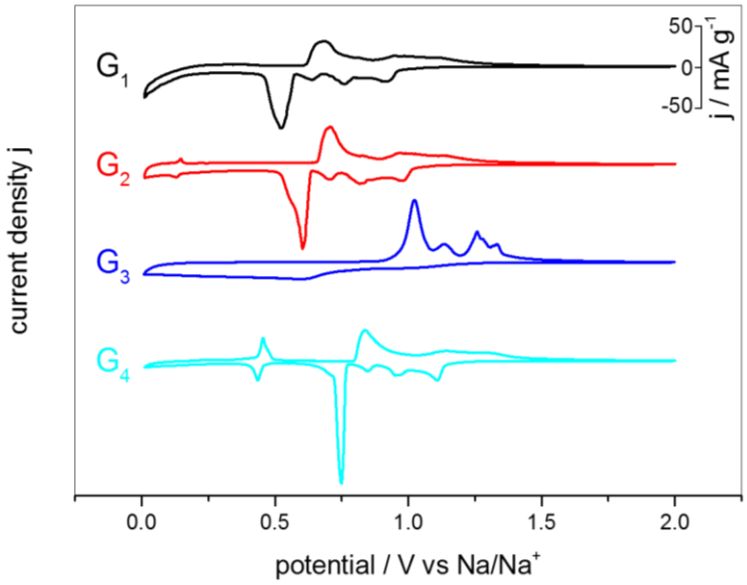

Figure 45: CVs of MCMB in 1 M $NaClO_4$ in G_1, G_2, G_3 and G_4 (potential sweep rate: 50 µV s^{-1}).

The CVs suggest that electric charge can be stored in the graphite electrodes when charging/discharging them. A charge/discharge test of a graphite electrode in the different glyme electrolytes is presented in Figure 46. The upper line shows the discharge (blue) and charge (black) profiles and the lower line the corresponding dQ/dV-plots. The indicated stoichiometries are calculated from the inserted electronic charge, once for the fully discharged and once for the 'half' discharged graphite, while 'half' refers to the main discharge plateau causing the sharp cathodic peak (except for G_3). The found capacities of the G_1, G_2 and G_4 electrolytes are around 100 mAh g^{-1}, while the G_3-batteries only have a capacity slightly larger than 70 mAh g^{-1}. The dQ/dV-plots reflect the behavior known from CV.

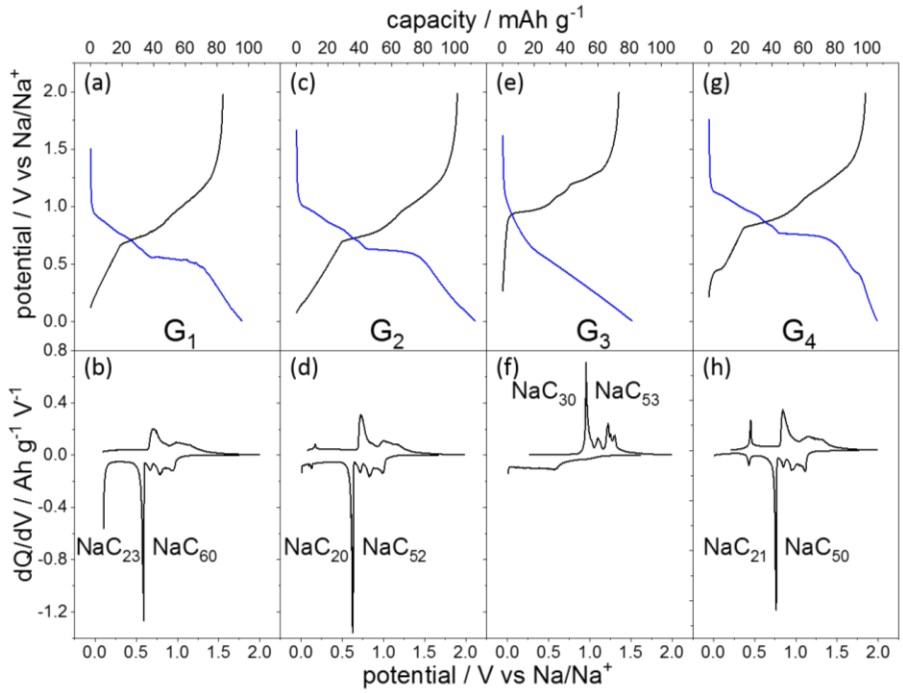

Figure 46: Charge (black) / discharge (blue) profiles and the corresponding dQ/dV-plot of the 2nd cycle for MCMB in 1 M $NaClO_4$ in (a, b) G_1, (c, d) G_2, (e, f) G_3 and (g, h) G_4. Indicated stoichiometries are calculated from the capacities above the main potential plateau and when fully sodiated (current density: 50 mA g^{-1}).

These electrochemical measurements give rise to couple of questions, which were already addressed in the introductory part of this section. This regards a lack of general understanding of the electrochemical processes as well as the different behavior of the G_3 electrolyte. XRD helps to understand such processes in more detail. For this purpose, an *in-operando* XRD study of graphite electrodes in the different electrolytes was made, meaning that the electrodes are analyzed by XRD while they are charged and discharged (Figure 47).

Figure 47 (a) shows a series of XRD patterns of a graphite electrode galvanostatically charged/discharged in the G_1 electrolyte. The first (t_0 = 0 h) diffractogram belongs to the pristine sample, while the later data are measured with a 10-minute time resolution. XRD shows the main (002)-graphite peak at 26.42 ° originating from the 3.35 Å interlayer spacing of the graphene layers. This peak splits into two peaks, when discharging the electrode. One peak shifts to lower angles, one to higher. After a certain time, these peaks' angles remain constant at 23.5 ° and 29.6 °, respectively, while simultaneously two new peaks appear (at 22.87 ° and 30.6 °). The appearance of the new peaks coincides with the 0.5 V plateau in the discharge curve in Figure 46 (a). Also lower/higher order peaks of this phase can be found at ca. 15.2 ° and 38.1 °. Charging the graphite reverses the observed processes, *i.e.* the latter phase gradually disappears as soon as the first anodic peak in the dQ/dV-plot is reached. At the same time the intermediate phase (23.5 ° and 29.6 °) is formed again, until they finally merge to the original peak at 26.42 ° of the empty graphite lattice upon full charge.

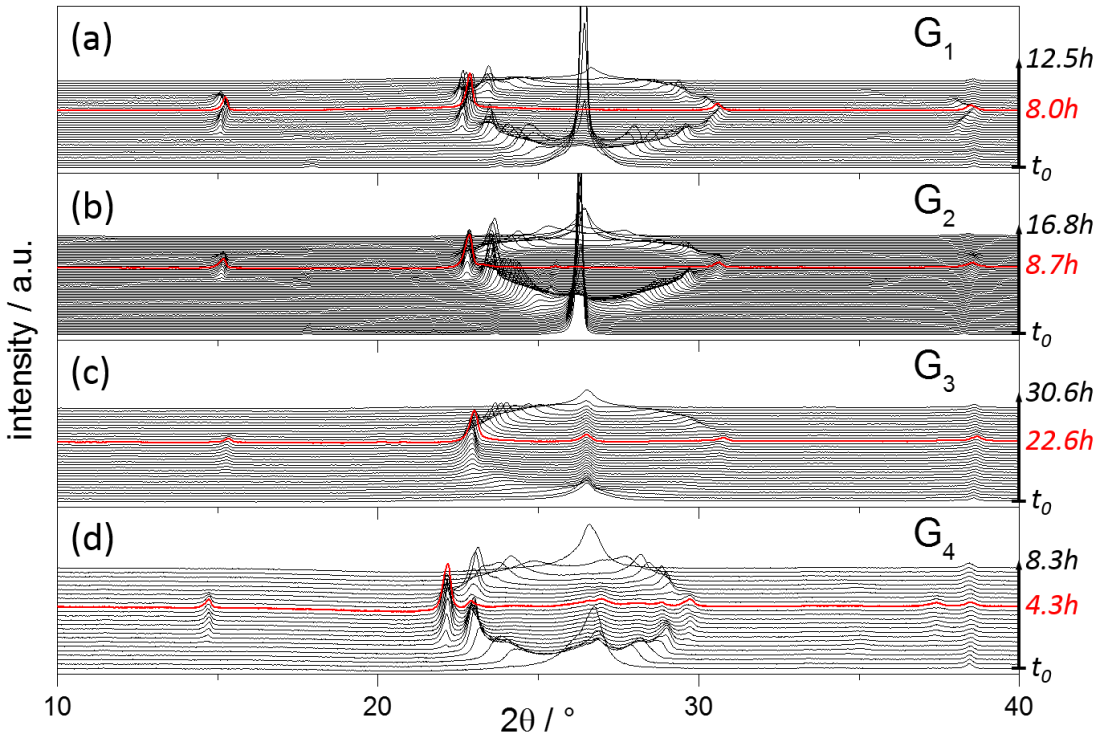

Figure 47: In-operando *XRD of MCMB in 1 M $NaClO_4$ in (a) G_1, (b) G_2, (c) G_3 and (d) G_4 during a discharge (front, t_0) and charge (in the rear) cycle. The red line shows the border between charge (de-intercalation) and discharge (intercalation). The time, after which each XRD diffractogram was measured is indicated on the right with the total time of discharge (in red) and discharge with charge (in black).*

Similar observations can be made for the other electrolytes. In all other electrolytes, *i.e.* G_2, G_3 and G_4, the original (002) peak splits up during discharge and merges upon charge. While the G_2 system shows only minor differences to the G_1 measurement, with slightly shifted peak positions, the G_3 and G_4 diffractograms at first sight seem apparently different. The main difference is the absence of the large main (002)-graphite peak in the beginning of the discharge/charge cycle. This can be easily explained, since in Figure 47 (a) and (b) the first discharge/charge cycle is shown, while in (c) and (d) it is a later one. The original intensity of this peak cannot be retained after a full cycle, as can also be seen in Figure 47 (a) and (b). Another difference concerns the G_3 system, where the ratio of peak intensities is different compared to the other electrolytes. Also part of the original (002)-graphite peak is visible throughout the entire measurement, being caused by loose graphite particles not having electric contact to the electrode and thus not participating in electrochemistry.

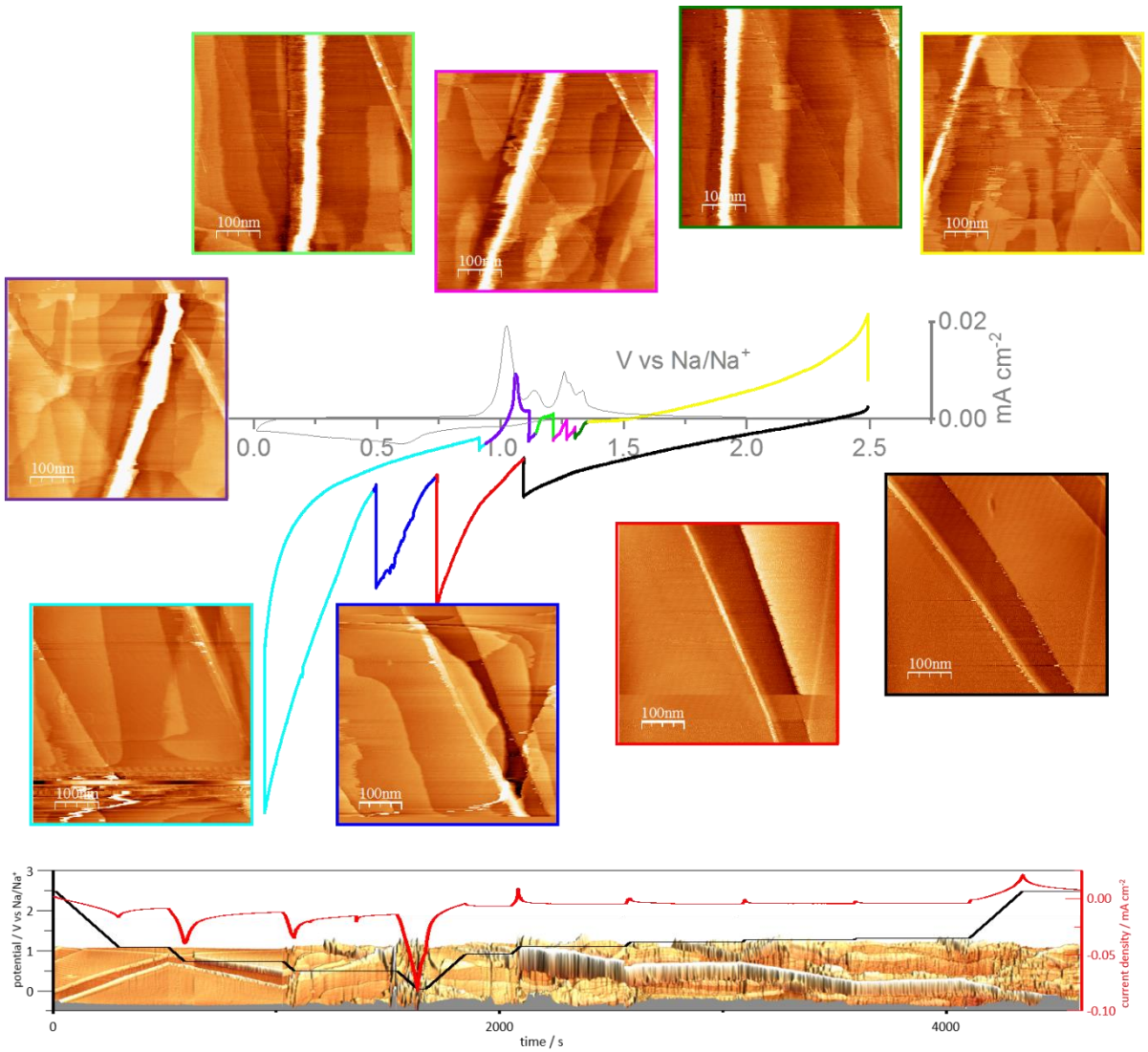

Figure 48: In-operando *EC-STM of HOPG in 1M $NaClO_4$ in G_3. The HOPG surface was scanned by EC-STM (scan size: 500 nm x 500 nm, tunneling current: 8 nA, tip potential: 2.6 V, sample potential: variable, bias: variable, tip velocity: 1 µm s^{-1}), while a CV with intermittent potential holds (sweep rate: 5 mV s^{-1}) as shown in the center was measured simultaneously. The colors of the frame around the STM-images indicate the potential range, which was covered during imaging, and corresponds to the colors used in the CV. The grey CV (sweep rate: 50 µV s^{-1}) corresponds to a MCMB electrode measured in a Swagelok® cell in the same electrolyte and serves as a reference. The figure on the bottom is the 3D representation of the* in-operando *EC-STM similar to the one presented in Figure 40 already.*

While the integral technique XRD can precisely probe the internal structure of a material, EC-STM as a local technique can shed light onto surface processes on a molecular/atomic scale. STM was conducted on HOPG electrodes in the G_3- and G_4-electrolyte to get further insight into the graphite electrochemistry in these systems. Since STM experiments usually last a couple of hours, one requirement to the electrolyte is a low volatility so that the electrolyte concentration remains unaltered. The volatile G_1 and G_2 solvents evaporate within several minutes in an open cell, like used in the STM setup. Thus, STM experiments were only possible in the G_3 and G_4 electrolyte, which both do not evaporate within several days so that a constant concentration can be guaranteed.

Figure 48 shows a series of *in-operando* EC-STM images recorded on HOPG in 1 M $NaClO_4$ in G_3, while measuring a CV. The center of this figure shows a grey CV, which is measured on a powder graphite

electrode and which has an arbitrary current unit here, since it only serves as a guide to the eye. The CV measured at the HOPG electrode was carried out stepwise with many potential holds in between. This CV is also shown in the center of this figure, and each separate stage of the CV is plotted in a different color. The STM images surrounding the CV were measured at the different stages of the CV. Each image is framed in a different color, which directly correlates it with the portion of the same color in the CV measured in parallel. Thus, the black framed image corresponds to the black section of the CV, etc. The figure on the bottom is the 3D presentation of the STM experiment.

The measurement started at 2.5 V, from where the potential was ramped to lower values at a sweep rate of 5 mV s^{-1}. While the first STM image (black) was recorded, the potential was lowered to 1.1 V. This image shows the pristine sample, with all the typical HOPG features as the flat terraces separated by a few step edges. No changes are visible at the surface. Further decreasing the potential to 0.75 V (red), the HOPG surface still does not show any changes. When the electrode potential, however, is lowered to 0.5 V (blue), the surface topography changes: the initially flat terraces swell up, similar as was already observed in case of the co-intercalation of the solvated Li-ions into the graphite in section 5.1 (Figure 38). Both images, *i.e.* pristine and sodiated HOPG, are magnified in Figure 49. The swollen regions spread through the graphite lattice and overlap each other. From height profiles, typical interlayer spacings of 10.9 Å are found. Attention should also be drawn to the appearance of the almost horizontal stripes in the upper part of image Figure 49 (b), which will be of importance later.

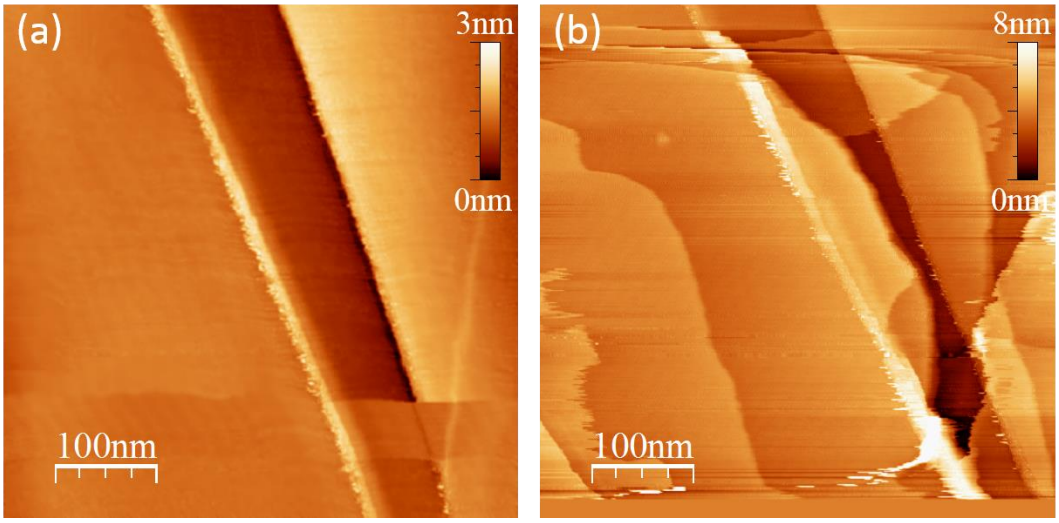

Figure 49: Magnification of two STM images from the STM series presented in Figure 48 of (a) the pristine and (b) the sodiated HOPG sample in 1 M $NaClO_4$ in G_3 (scan size: 500 nm x 500 nm, tunneling current: 8 nA, tip potential: 2.6 V, sample potential: variable, bias: variable, tip velocity: 1 µm s^{-1}) .

When the potential in Figure 48 is further lowered (lower part of the cyan image), many surface disturbances are observed in the STM image. This is not caused by a deficient tip, but by the dynamic electrode surface, as will be seen later. In the later course of this series, the images become less clear and a similar fuzziness, as already observed during the SEI-formation in LIBs (section 5.1) is visible. The 3D-plot of this experiment shows the surface film precipitation in more detail. It should also be mentioned that the anodic peaks as observed for the powder electrode are also clearly visible in the CV at HOPG. In general, both, graphite powder and HOPG, behave electrochemically very similar in these electrolytes.

In another STM experiment (Figure 50), where the HOPG surface is observed during a continuous potential scan from 2.5 V to 0.5 V, similar observations are made. When decreasing the potential to

0.5 V (Figure 50 (a)), vertical stripes appear at potentials well below 1.0 V. One should keep in mind that the STM images are turned by 90 ° as compared to those in Figure 49, in order to match them with the time axis of the electrochemical measurement. Thus, these vertical stripes are analogous to the horizontal lines observed in Figure 49 (b). Increasing the potential back up to 2.5 V, one can make out new vertical lines, when the electrode potential approaches 1.0 V. These vertical lines perfectly coincide with the anodic peaks measured in the CV, as can be seen from the turquoise line, representing the electrochemical current.

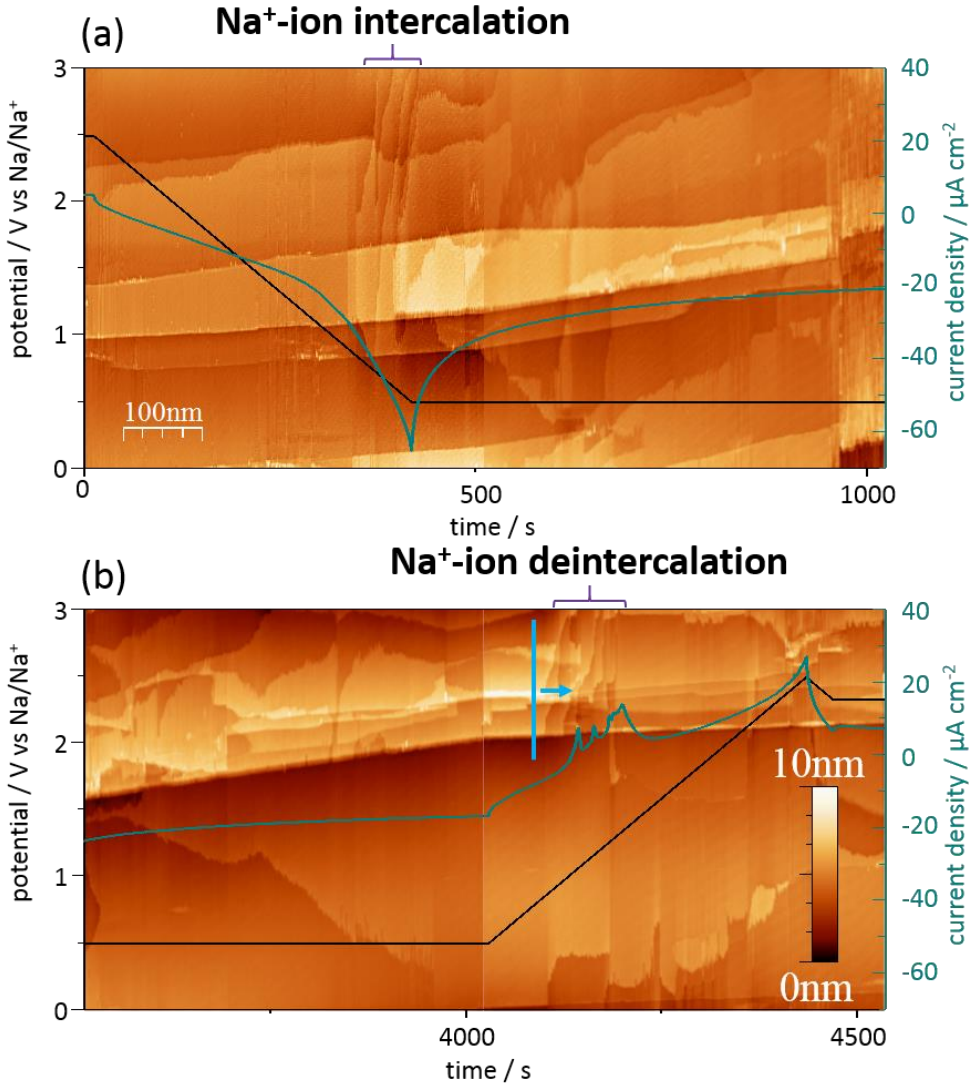

Figure 50: In-operando *EC-STM of HOPG in 1 M $NaClO_4$ in G_3 during (a) potentiostatic discharge and (b) charge (scan size: 500 nm x 500 nm, tunneling current: 8 nA, tip potential: 2.6 V, sample potential: variable, bias: variable, tip velocity: 1 µm s^{-1}, potential sweep rate: 5 mV s^{-1}).*

An *in-operando* STM-study was also measured for the G_4 electrolyte (Figure 51), which shall only be introduced briefly here. The first topography changes can be observed in the potential range after the onset of cathodic currents (red framed image), in the potential range where the MCMB powder shows many cathodic peaks. The image looks very disturbed, however, the tip quality is still good. As will be shown later, many phase transitions of the graphite lattice lead to a highly mobile surface, which results in the chaotic images. Here, one sees the graphite lattice expansion and the corresponding increase of interlayer spacing in real time, which according to a height profile analysis amounts to 10.7 Å. Also in the latter course of the experiment, the images seem to be disturbed, however, when

taking a look at the last image (purple), one can still make out a very clear step edge in the center of the image, showing that STM imaging is still having a good quality, but the mobile surface results in the disturbances. The 3D-plot of the experiment again shows a surface film precipitation at low potentials, which disappears towards the end of the experiment.

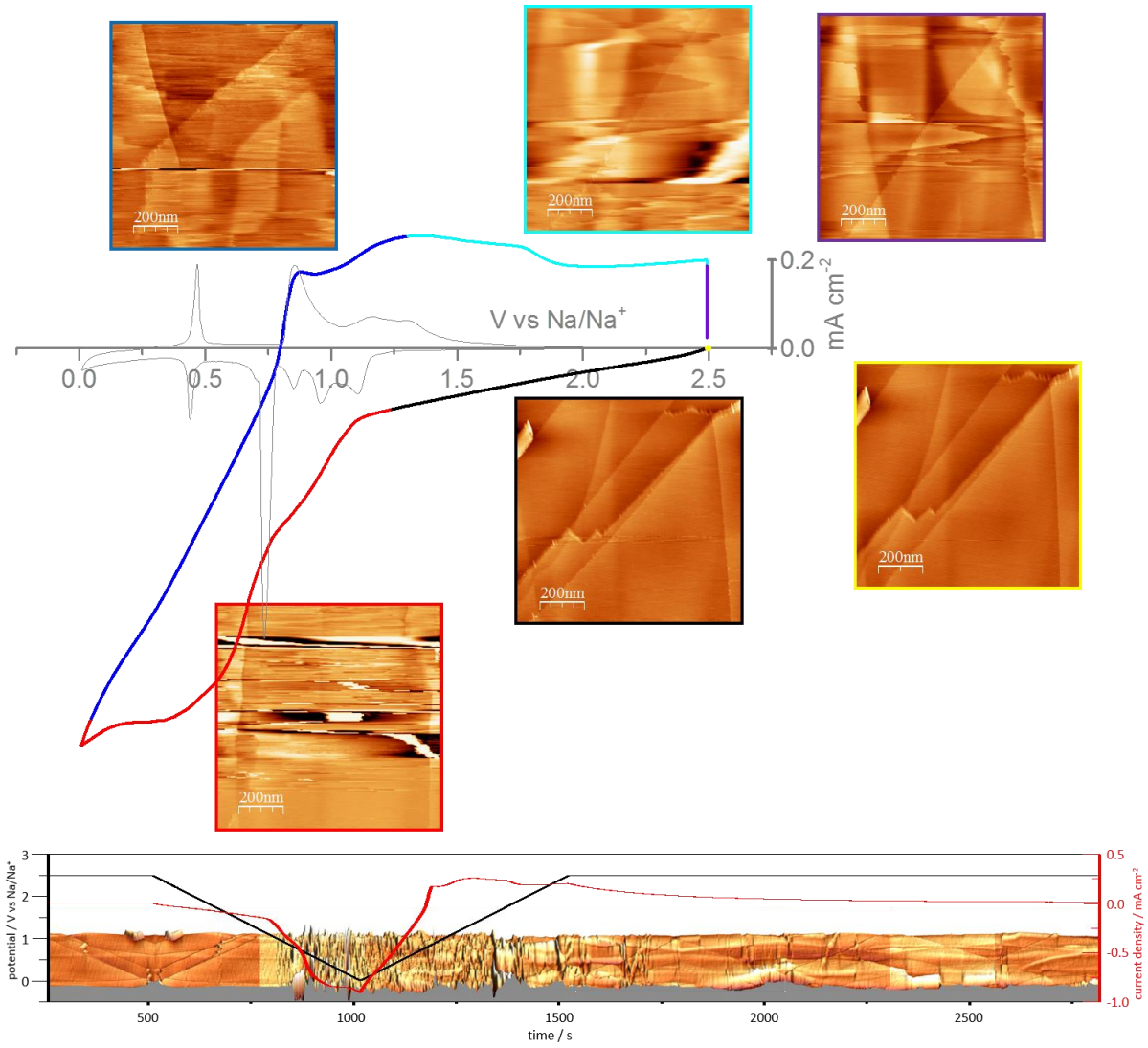

Figure 51: In-operando *EC-STM of HOPG in 1M $NaClO_4$ in G_4. The HOPG surface was scanned by EC-STM (scan size: 1 µm x 1 µm, tunneling current: 1 nA, tip potential: 2.6 V, sample potential: variable, bias: variable, tip velocity: 2 µm s^{-1}), while a CV (sweep rate: 5 mV s^{-1}) without potential hold was measured simultaneously. The colors of the frames around the STM-images indicate the potential ranges, which were applied during imaging, and correspond to the colors used in the CV. The grey CV (sweep rate: 50 µV s^{-1}) corresponds to a MCMB electrode measured in a Swagelok® cell and serves as a reference. The figure on the bottom is the 3D representation of the* in-operando *EC-STM.*

An experiment giving more insight into the electrochemistry of graphite in the G_4 electrolyte is presented in Figure 52. The left STM image in Figure 52 (a) shows the pristine HOPG sample at 2.5 V, where it remains unaltered for several hours. The image in the middle belongs to the sample, after it was ramped to 0.8 V (5 mV s^{-1}) and held there for 428 s before imaging, and where many surface disturbances are visible again. The right image shows the sample after its potential was increased and held for 428 s at 2.5 V. This image was measured from the bottom to top and one realizes that the disturbances become weaker with time. Height profiles, which are sketched in Figure 52 (b) are

measured along the lines drawn in the STM images. The height profiles reflect the stepped topography of the HOPG surface. Exposing the electrode to 0.8 V results in a lattice expansion of the graphite layers. Setting the electrode potential back to 2.5 V reverses the lattice expansion and the original state is regained.

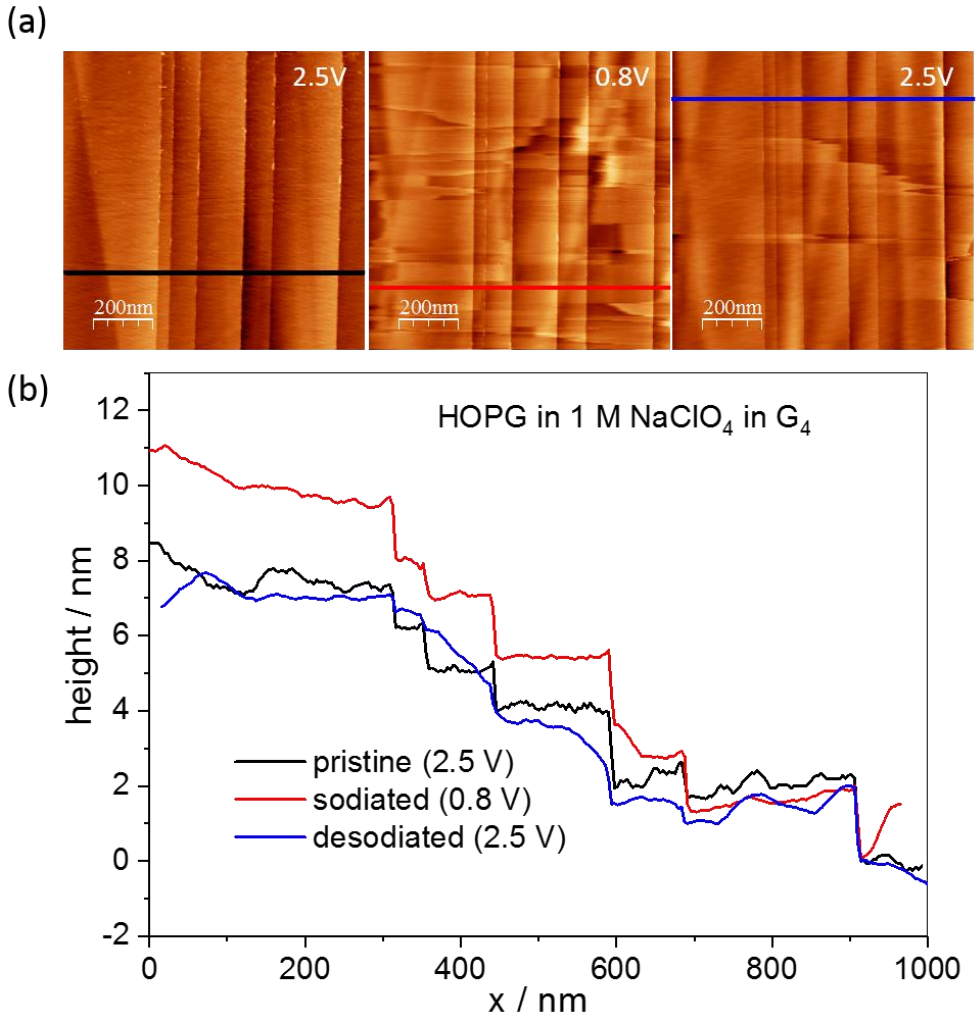

Figure 52: (a) In-operando *EC-STM of HOPG in 1 M $NaClO_4$ in G_4 showing the pristine sample at 2.5 V (left), the sample at 0.8 V (middle) and the sample after the potential is ramped back to 2.5 V again (right). (b) shows height profiles measured along the lines marked in the images in (a).*

The last experimental technique applied to this system is the EQCM technique. It again should be mentioned that the term microbalance is misleading, since in most cases the conversion of a frequency change into a mass change is inappropriate. Figure 53 (a) shows an *in-operando* EQCM measurement of an Au-quartz coated with graphite immersed into a 1 M $NaClO_4$ solution in G_3. The change of resonance frequency Δf (red line) as well as the change of signal width Δw (blue line) are recorded while measuring a CV (sweep rate: 2 mV s^{-1}, black line). The grey CV with an arbitrary current scale is the CV of a powder graphite electrode measured in a Swagelok® cell and serves as a guide to the eye.

When the electrode potential is lowered from OCP, which is at around 2.8 V, cathodic peaks appear close to 1.5 V. With the onset of these currents, a drop of Δf is triggered. At lower potential, another cathodic peak causes a further drop of Δf. Below 0.3 V, Δf reaches a plateau and stays constant until the first anodic peak at 1.0 V is reached. A magnification of the anodic peaks is shown in Figure 53 (b). As can be seen, Δf increases whenever a peak in the CV is reached. Moreover, the increase in

resonance frequency is almost proportional to the peak size. The damping Δw behaves opposite: in the potential range of the cathodic peaks, the damping increases until it reaches a constant value as soon as the positive sweep begins. It remains unaltered until the first anodic peak is reached, where it drops, whenever a new peak appears. For a fully reversible system, which a rechargeable battery is supposed to be, one would expect that Δf and Δw go back to their original value, which they, however, do not.

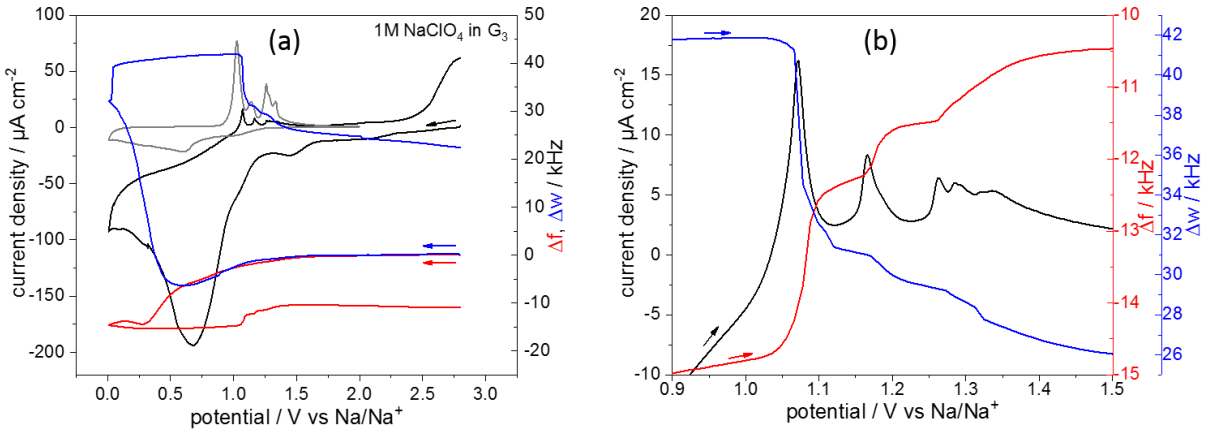

Figure 53: (a) In-operando *EQCM of a graphite (SFG6) coated Au-quartz in 1 M $NaClO_4$ in G_3 with (b) the magnification of the anodic peaks. The grey CV was measured with a MCMB electrode in a Swagelok® cell at slow scan rate (20 µV s^{-1}) and serves as guide to the eye with an arbitrary current scale (potential sweep rate: 2 mV s^{-1}).*

5.3 V_2O_5 electrochemistry in NIBs – a morphological study

5.3.1 Sample Characterization

Having studied graphite as the negative electrode in a NIB, the electrochemistry of V_2O_5 as positive electrode material can be explored. As already mentioned in section 2.3.1.2, different V_2O_5 powders were synthesized and tested with regard to the influence of the V_2O_5 morphology on the battery performance. A commercial V_2O_5 powder was used as benchmark system for comparison and served, due to its high purity and crystallinity, as a reference sample for powder characterizations. Figure 7 (a) and (b) show SEM micrographs of the commercial V_2O_5 powder, consisting of solid grains with typical dimensions of 0.5 µm x 0.5 µm x 1.0 µm, and thus, this powder in the following will be called *commercial V_2O_5 micro grains*. Figure 54 shows a series of baseline corrected XRD-patterns, where each diffractogram belongs to a different sample. The diffractograms are ordered according to their peak intensity, being linked to the order of crystallinity. The highly crystalline commercial V_2O_5 micro grains (purple) show all expected V_2O_5-reflexes, which are indexed with their Miller-indices. Figure 55 shows the XPS spectrum of this powder, proving its high purity and serving as reference to other samples. The O1s- as well as the V2p-peaks of this material are analyzed in more detail in Figure 56 (a) essentially showing the O1s(V^{5+}) peak at 529.3 eV, the $2p_{1/2}$(V^{5+}) peak at 523.7 eV and the $2p_{3/2}$(V^{5+}) peak at 516.4 eV.

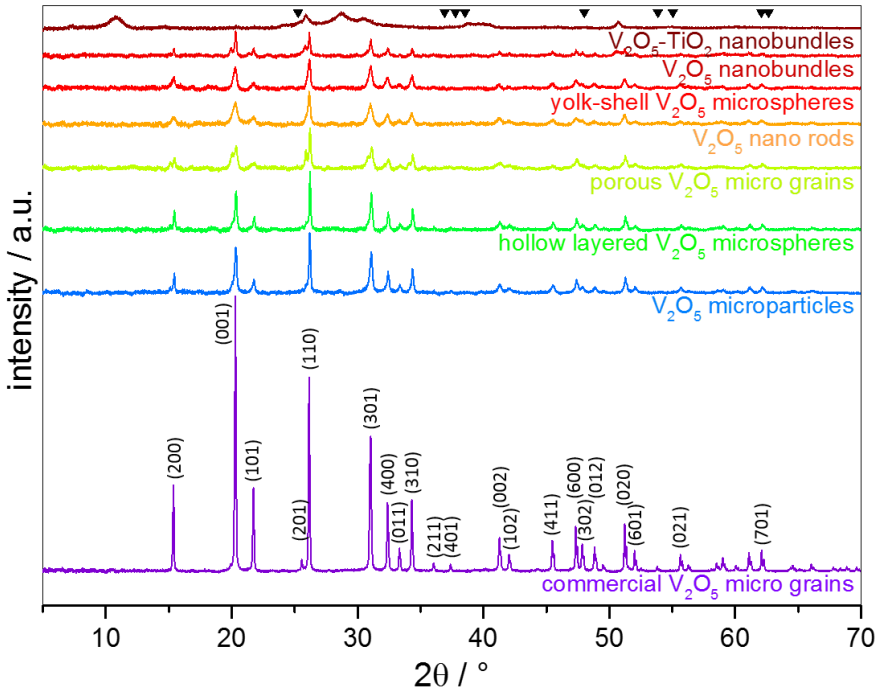

Figure 54: X-Ray Diffraction patterns of the synthesized V_2O_5 materials arranged according to their peak intensities: commercial V_2O_5 micro grains (Alfa Aesar Puratronic®, purple), V_2O_5 micro particles (slight blue), hollow layered V_2O_5 microspheres (light green), porous V_2O_5 micro grains (greenish yellow), V_2O_5 nano rods (orange), yolk-shell V_2O_5 microspheres (red) and V_2O_5 nanobundles (brownish red) and V_2O_5-TiO_2 nanobundles (brown) plus the expected reflexes for pure, anatase TiO_2 (black triangles).

The powder shown in Figure 7 (c) and (d) consists of agglomerated micro grains with dimensions of 0.1 µm x 0.1 µm x 0.1 µm. This electrode will be called *V_2O_5 micro particles*. The XRD peak intensities (light blue) and thus the crystallinity are significantly lower than the ones observed for the commercial V_2O_5 micro grains.

A material with similar XRD crystallinity (green) to the V_2O_5 micro particles is shown in Figure 7 (e) and (f). It consists of 3 µm to 5 µm spheres with a hollow core and a shell composed of smaller, solid particles with typical dimensions of 0.1 µm x 0.1 µm x 0.1 µm. Due to their structure, they are called *hollow layered V_2O_5 microspheres*. The XPS analysis (Figure 55) of this powder reveals a Na and an S contamination, both stemming from the synthesis. Moreover, the detailed analysis of the O1s- and the V2p-peak (Figure 56) shows the appearance of fully oxidized V, *i.e.* 'V^{5+}', as well as partially reduced V^{4+}. During synthesis, the V(V) might have been partially reduced by the ethylene glycol and an O-deficiency in the autoclave hindered the full oxidation at higher temperatures.

The next material synthesized is a sponge like, porous V_2O_5 micro powder, referred to as *porous V_2O_5 micro grains* (Figure 7 (g) and (h)). The particles are highly porous, with pore sizes below 100 nm. Its XRD pattern (Figure 54, greenish yellow) shows all typical V_2O_5 peaks.

V_2O_5 nano rods (Figure 7 (i) and (j)) are agglomerated particles with a length of 0.5 µm and thicknesses of well below 50 nm. The XRD-intensities (Figure 50, orange) are further lowered compared to the previous powders.

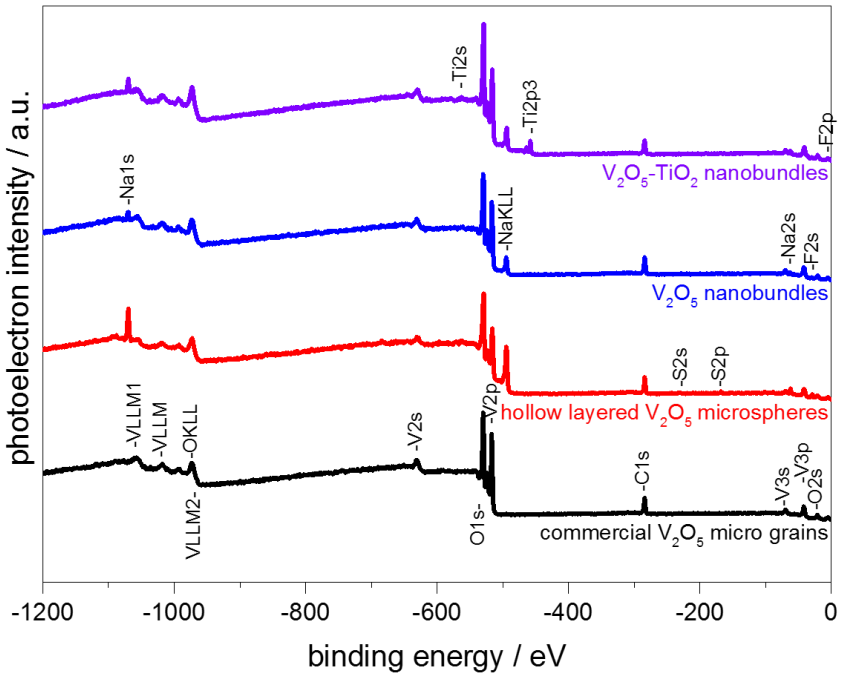

Figure 55: X-Ray Photoelectron Spectra of selected V_2O_5 powders: commercial V_2O_5 micro grains (Alfa Aesar Puratronic®, black), hollow layered V_2O_5 microspheres (red), V_2O_5 nanobundles (blue) and V_2O_5-TiO_2 nanobundles (purple).

An even less crystalline material (red XRD data in Figure 50) is composed of V_2O_5 spheres with dimensions around 500 nm (Figure 7 (k) and (l)). These spherical particles have a solid core and a thin V_2O_5-shell, reminding of the structure of an egg. Thus, these particles are called *yolk-shell V_2O_5 microspheres*.

A pure nanomaterial consisting of V_2O_5 nanobundles with thicknesses below 20 nm and lengths of around 500 nm is shown in Figure 7 (m) and (n). XRD-peaks (Figure 50, brownish red) are further diminished and the XPS-spectrum in Figure 55 (blue) shows a Na and F contamination stemming from the synthesis. The O1s, $V2p_{1/2}$ and $V2p_{3/2}$ peaks in Figure 56 (c) only show V^{5+} peaks, being expected for fully oxidized V_2O_5. This sample is called *V_2O_5 nanobundles*.

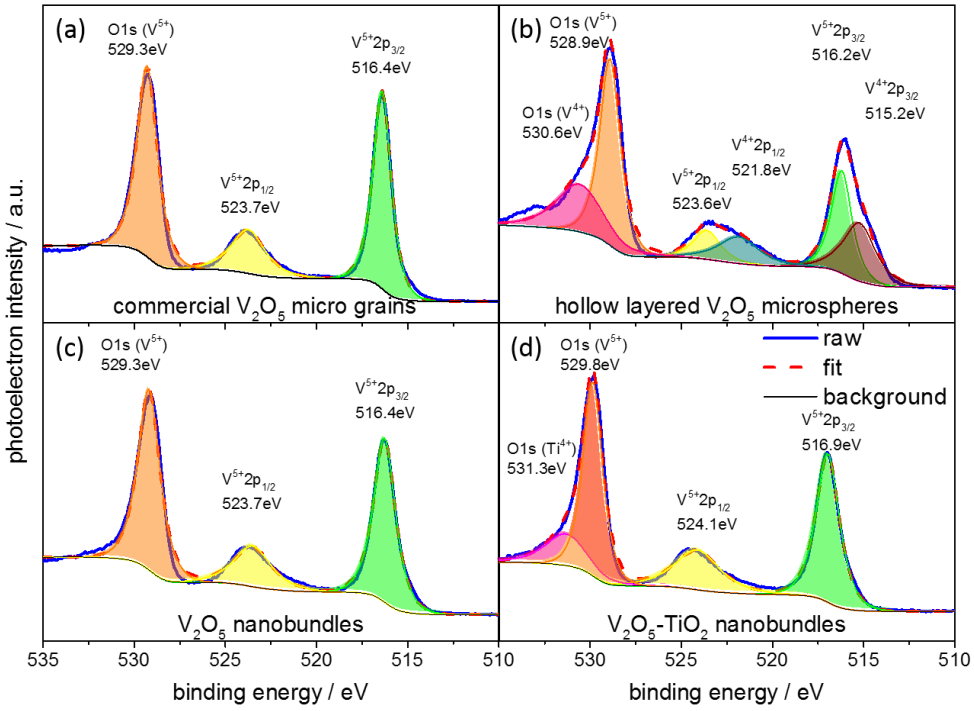

Figure 56: X-Ray Photoelectron Spectra of the O1s- and V2p-peaks of (a) the commercial V_2O_5 micro grains (Alfa Aesar Puratronic®), (b) the hollow layered V_2O_5 microspheres, (c) the V_2O_5 nanobundles and (d) the V_2O_5-TiO_2 nanobundles.

A similar powder applying the same synthetic route is TiO_2-blended V_2O_5 (Figure 7 (o) and (p)), consisting of 1 µm long and less than 50 nm thin needles, named as *V_2O_5-TiO_2 nanobundles*. This powder has the lowest crystallinity of all powders and no clear TiO_2 peaks can be found in the XRD data (Figure 50, brown), where the black triangles mark the expected peak positions for anatase TiO_2. Besides Na and F traces from the synthesis, XPS (Figure 55, purple) also shows a Ti signal and both, the O1s(V^{5+})- and O1s(Ti^{4+})-peaks (Figure 56 (d)), stemming from the vanadium, respectively titanium coordinated oxygen. The EDS analysis (Figure 57) of this sample shows an even distribution of the V, the O and the Ti throughout the analyzed needle. The F contamination also occurs homogenously in the needle.

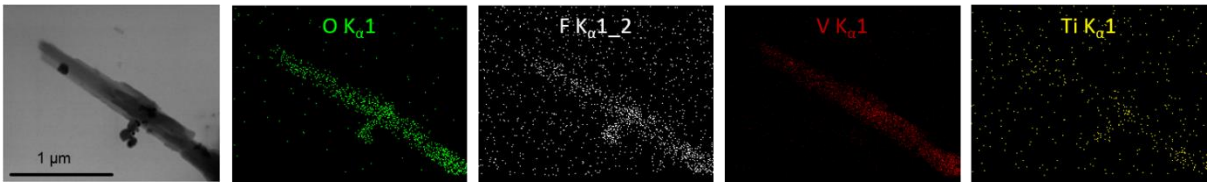

Figure 57: Energy Dispersive X-Ray Spectroscopy of the V_2O_5-TiO_2 nanobundles.

5.3.2 Electrochemical $Na_xV_2O_5$ Phase Transitions

Before comparing the battery performances of the above introduced V_2O_5-powders in NIBs, the general electrochemistry and the related $Na_xV_2O_5$ phase transitions upon sodiation must be clarified. The depth of discharge or grade of sodiation of V_2O_5 is linked to different phase transitions, strongly affecting the cycling behavior. The cycling behavior of a V_2O_5 electrode in a NIB can be studied by CV (Figure 58), which was conducted for a V_2O_5 electrode cycled in 1 M $NaClO_4$ in EC/PC at 50 µV s^{-1}. Here, the potential sweep started at OCP (3.2 V to 3.4 V) and the lower cutoff voltage was limited to 1.5 V in Figure 58 (a), to 1.0 V in (b) and to 0.01 V in (c), resulting in different phase transitions.

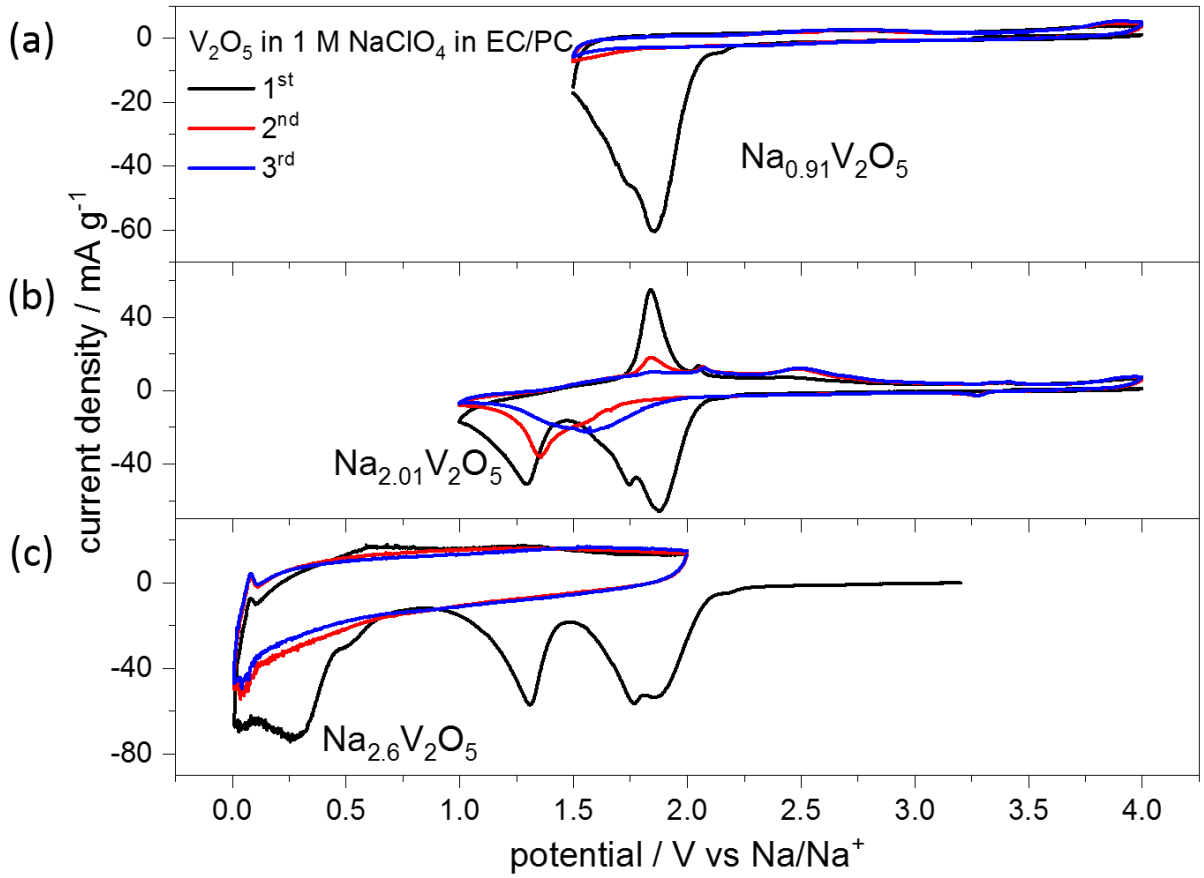

Figure 58: Cyclic Voltammograms of the commercial V_2O_5 micro grains (Alfa Aesar Puratronic®) in 1 M $NaClO_4$ in EC/PC (1:1) showing the potential dependency of the $Na_xV_2O_5$ phase transitions: potential sweep at 50 µV s^{-1} (a) from OCP to 4.0 V to 1.5 V, (b) from OCP to 4.0 V to 1.0 V and (c) from OCP to 0.01 V to 2.0 V.

The first positive scan to 4.0 V in Figure 58 (a) starting at OCP is featureless and also the negative scan does not show any peaks above 2.25 V. Below, a broad cathodic twin peak arises, ranging down to 1.5 V. With the assumption of Na^+-intercalation, a stoichiometry of $Na_{0.91}V_2O_5$ can be calculated for this peak from the discharge capacities. As no corresponding anodic peak occurs to this phase transition upon charging, the inserted Na irreversibly remains in the $Na_xV_2O_5$ lattice after the first discharge. In all consecutive cycles, the CV does not show any further peaks.

Lowering the lower cutoff voltage to 1.0 V (Figure 58 (b)), a second phase transition corresponding to a $Na_{2.01}V_2O_5$ stoichiometry appears between 1.5 V and 1.0 V. In contrast to the previous phase transition, this one is (chemically) reversible, as indicated by the anodic peaks appearing in the positive potential sweep. They occur at much more positive potential, however, indicating poor kinetics. Upon further cycling, the peak potentials shift and the shape of the initially sharp peaks changes to blurred and broadened peaks.

A deep discharge to 0.01 V (Figure 58 (c)) results in another irreversible phase transition ($Na_{2.6}V_2O_5$) at potentials below 0.75 V. Once this phase is formed, no further peaks appear in the consecutive cycles.

Additional information about the $Na_xV_2O_5$ phase transitions upon sodiation/de-sodiation can be gained from STM, which was conducted as an *ex-situ* study for the present case, *i.e.* on a V_2O_5 single crystal cycled in a 1 M $NaClO_4$ in EC/PC (1:1) solution (Figure 59). Since V_2O_5 has a relatively low

electronic conductivity, long time *in-situ*, respectively *in-operando* STM measurements are difficult, since the tip-failure rate is quite high. For simplicity, an *ex-situ* study was performed such that the pristine V_2O_5 single crystal is first imaged by STM (Figure 59 (a)). Afterwards, the sample was mounted into an electrochemical cell and ramped from 4.0 V to 1.0 V and held there for 30 minutes to give the system more time to equilibrate. Then, the sample was dismounted and transferred to the STM cell in the same glovebox, where it was imaged another time (Figure 59 (b)). Then, the procedure was repeated after ramping the potential back to 4.0 V again (not shown), and later to 0.05 V (Figure 59 (c)) and back to 4.0 V (not shown). The black and blue CVs in Figure 59 were measured in another set of experiments with a V_2O_5 single crystal in the same electrolyte, illustrating the electrochemical behavior of this system. Thus, the image in Figure 59 (b) was recorded after a potential ramp beyond the first cathodic peak, which - in contrast to the measurements at a powder electrode (light grey CV) also appears in the second cycle of the CV (blue) again. Upon prolonged cycling, however, this peak gradually disappears, indicating that the 30 minutes potential hold at 1.0 V is not long enough to complete the phase transition, also in view of the faster potential sweep rate of 5 mV s^{-1} compared to the 50 µV s^{-1} for the powder electrode. The light grey CV has an arbitrary current scale and was measured with a V_2O_5 powder electrode and only serves as a guide to the eye and to compare the two systems. The peaks of the single crystal electrode are shifted to lower potentials compared to the powder electrodes, due to the higher scan rates and the large ohmic resistance of the single crystalline material.

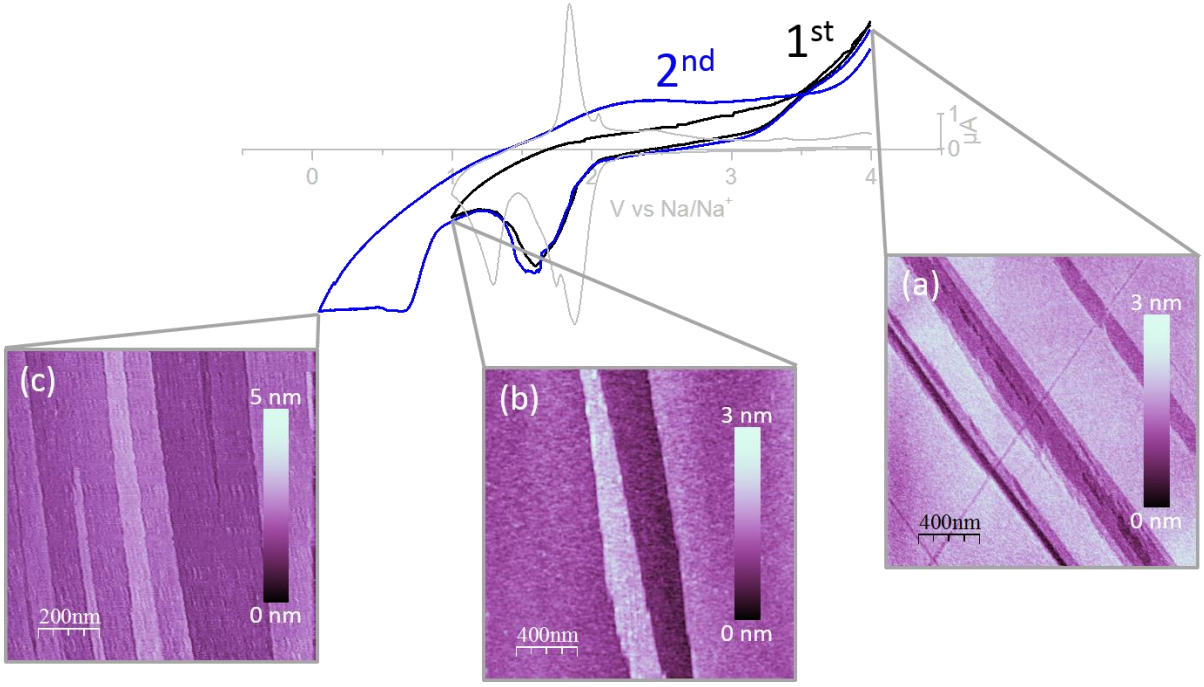

Figure 59: Ex-situ *STM experiment measured at a V_2O_5 single crystal after setting it to different potentials in a 1 M $NaClO_4$ in EC/PC (1:1) electrolyte (scan size: 2 µm x 2 µm ((a), (b)), 1 µm x 1 µm (c), tunneling current: 500 pA (b), 1 nA ((a), (c)) bias: 2 V, tip velocity: 4 µm s^{-1}((a), (b)), 0.5 µm s^{-1} (c)). The experiment was conducted as follows: first, the pristine sample was imaged, then the crystal was mounted into the electrochemical cell with a Na-CE and -RE, and a potential ramp to 1.0 V at 5 mV s^{-1} was performed with a potential hold at 1.0 V for 30 min. Afterwards, the sample was removed from the electrochemical cell and imaged by STM. This procedure was repeated after a potential ramp to 4.0 V, 0.05 V and 4.0 V again. The shown CVs (black and blue) are from a separate experiment with a V_2O_5 single crystal and shall illustrate the electrochemistry (potential sweep rate: 5 mV s^{-1}). The slight*

grey CV serves as a guide to the eye and is a reference CV measured with a V_2O_5 powder (potential sweep rate: 50 µV s^{-1}).

In order to better understand the $Na_xV_2O_5$ phase transitions, a statistical evaluation of step edges was conducted, where the step edge height from numerous measurements was analyzed. The outcome of this analysis is shown in Figure 60, where (a) shows the statistical distribution of step edge heights measured for the pristine orthorhombic V_2O_5 with an [001] lattice parameter of 4.36 Å. The STM data scatter around this value, and the scattering is quite severe. The reason is simply the poor electronic conductivity of the single crystal and the resulting poor image quality and low signal to noise ratio. In Figure 60 (b), in addition the height distribution after holding the sample at 1.0 V is shown, resulting in a shift to slightly larger values. At 1.0 V, the V_2O_5 single crystal passed the first phase transition, which for a powder electrode is already formed at 1.5 V.

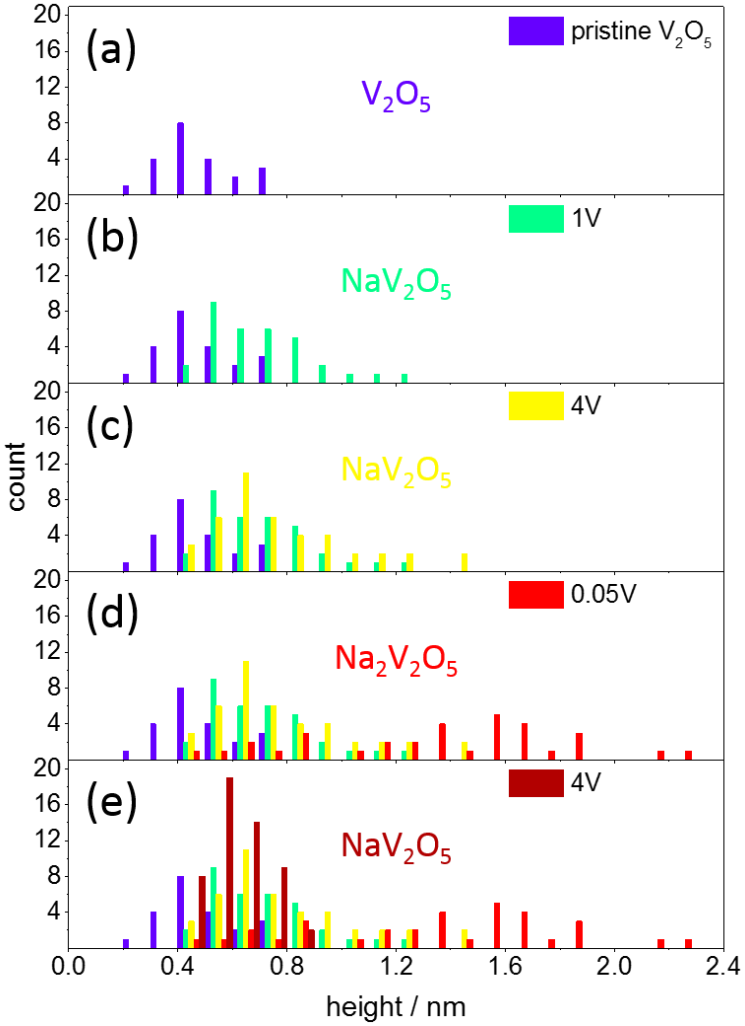

Figure 60: Histograms of the (001)-step height of the V_2O_5 single crystal analyzed at the different steps of the experiment presented in Figure 59 with (a) the pristine orthorhombic V_2O_5, (b) the sodiated NaV_2O_5 after setting the potential to 1 V, (c) the irreversibly sodiated NaV_2O_5 at 4 V, (d) the $Na_2V_2O_5$ after a potential exposure to 0.05 v and (e) the de-sodiated NaV_2O_5 after de-intercalating the second Na-ion.

Ramping the potential back up to 4.0 V (Figure 60 (c)) does not result in any shift of the step edge height distribution, which is in agreement with the observations already made for a powder electrode having formed the irreversible $Na_1V_2O_5$ phase (Figure 58 (a)). Setting the potential to 0.05 V (Figure 60

(d)), *i.e.* running through the $Na_2V_2O_5$ phase transition (Figure 58 (a)), the lattice parameter strongly increases. Going back to 4.0 V again (Figure 60 (e)) leads to a shrinkage of the lattice parameter to the previously observed value in Figure 60 (c).

5.3.2.1 Influence of the electrode morphology on the battery performance

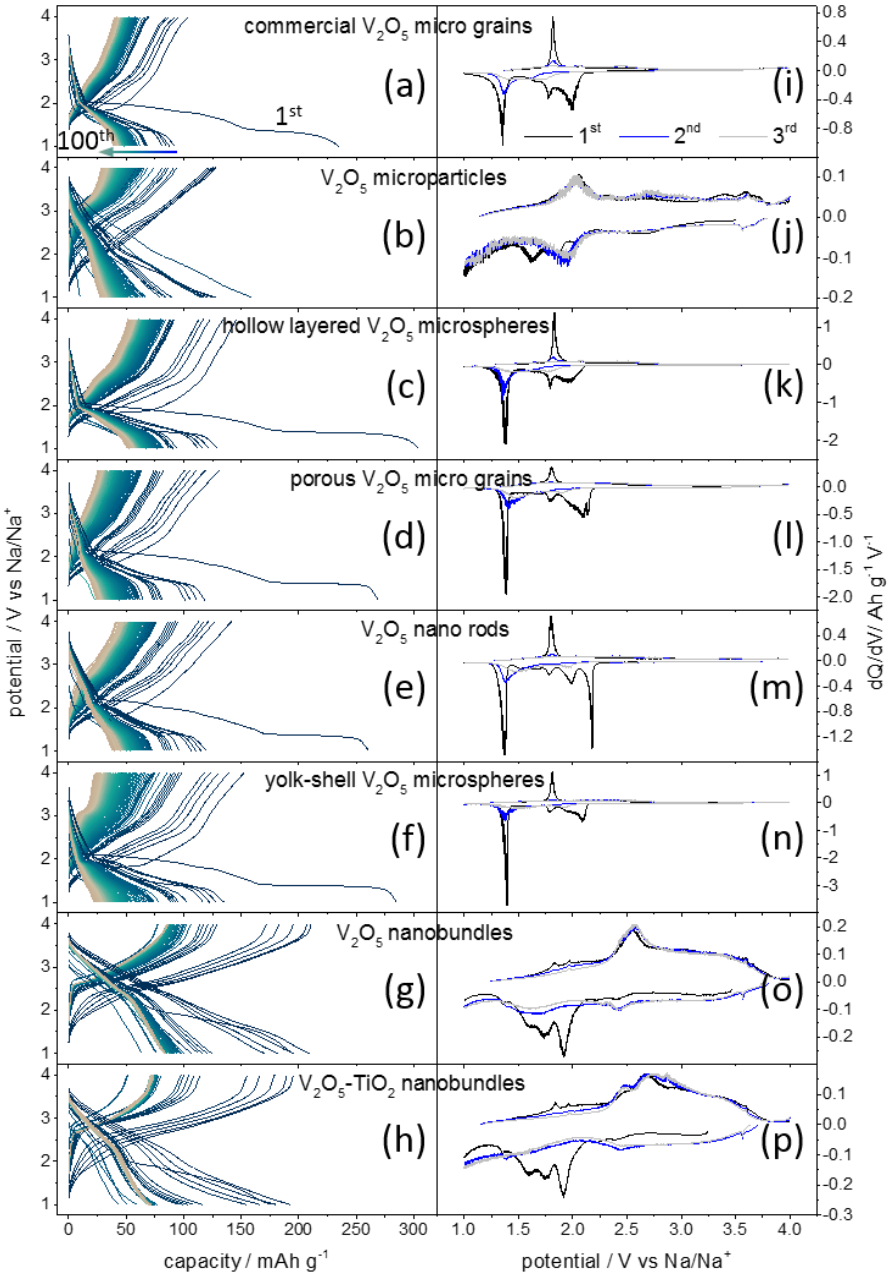

Figure 61: Charge-/discharge-profiles of (a) the commercial V_2O_5 micro grains (Alfa Aesar Puratronic®), (b) the V_2O_5 microparticles, (c) the hollow layered V_2O_5 microspheres, (d) the porous V_2O_5 micro grains, (e) the V_2O_5 nano rods, (f) the yolk-shell V_2O_5 microspheres, (g) the V_2O_5 nanobundles and (h) the V_2O_5-TiO_2 nanobundles. The corresponding dQ/dV-plots of the first three cycles obtained by the derivative of the capacity Q with respect to the voltage V are shown on the right in (i) to (p). (Electrolyte: 1 M $NaClO_4$ in EC/PC (1:1), cycle 1 to 5: 20 mA g^{-1}, cycle 6 to 10: 50 mA g^{-1}, cycle 11 to 15: 100 mA g^{-1}, cycle 16 to 20: 200 mA g^{-1}, cycle 21 to 100: 50 mA g^{-1}).

The above CV-studies on the $Na_xV_2O_5$ phase transitions (Figure 58) suggest to cycle the $Na_xV_2O_5$ electrodes in a potential window ranging from 4.0 V to 1.0 V, in order to compare the battery

performance of the different V_2O_5-morphologies. Figure 61 (a) to (h) shows the charge-/discharge-profiles of all tested V_2O_5 powders cycled in a 1 M $NaClO_4$ in EC/PC (1:1) electrolyte. The dQ/dV-plots of the first three cycles of each electrode are shown in Figure 61 (i) to (p).

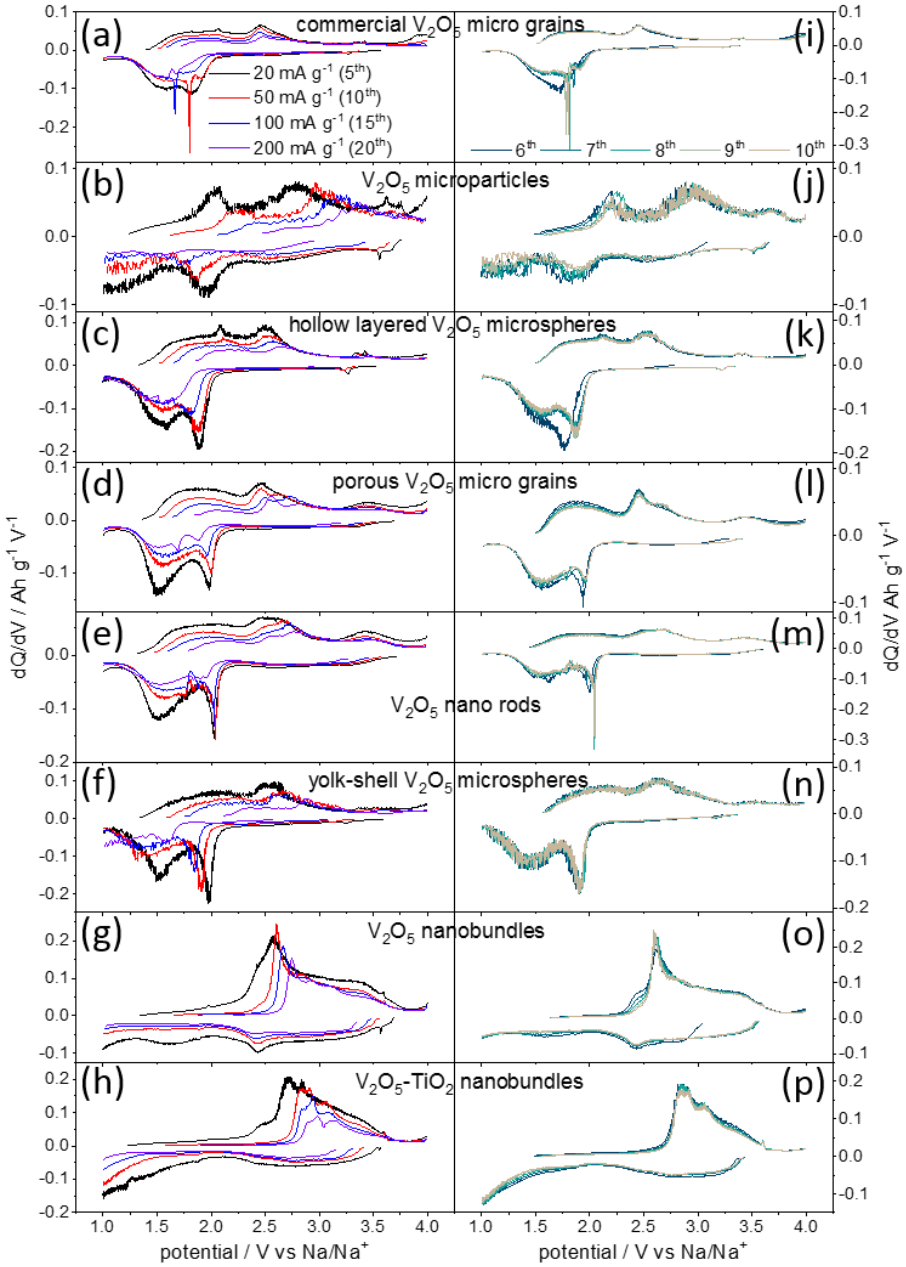

Figure 62: (a) to (h) show the dQ/dV-plots at different rates (as indicated) determined from the experiment shown in Figure 61, showing the effect of larger currents on the potentials of the phase transitions. (i) to (p) show five consecutive cycles measured at 50 mA g^{-1} and illustrate that the observed shift of the phase transitions in potential is an effect of rate and not of cycle number. ((a) and (i) commercial V_2O_5 micro grains (Alfa Aesar Puratronic®), (b) and (j) V_2O_5 microparticles, (c) and (k) hollow layered V_2O_5 microspheres, (d) and (l) porous V_2O_5 micro grains, (e) and (m) V_2O_5 nano rods, (f) and (n) yolk-shell V_2O_5 microspheres, (g) and (o) V_2O_5 nanobundles, (h) and (p) V_2O_5-TiO_2 nanobundles).

With the exception of the V_2O_5 microparticles (Figure 61 (b)), and the two nanomaterials, V_2O_5 nanobundles (Figure 61 (g)) and V_2O_5-TiO_2 nanobundles (Figure 61 (h)), all V_2O_5 materials show a high discharge capacity of more than 200 mAh g^{-1} during the first discharge with a pronounced voltage

plateau at 1.4 V. A big part of this capacity is irreversibly lost and cannot be regained after the first charge. Only for the exceptions of the V_2O_5 microparticles, the V_2O_5 nanobundles and the V_2O_5-TiO_2 nanobundles, the discharge capacity of the second cycle is increased compared to the first discharge capacity.

The first cycle discharge capacity of the commercial V_2O_5 (Figure 61 (a)) amounts to 234.6 mAh g^{-1} and drops to 92.0 mAh g^{-1} in the second cycle. Continuing to cycle, the capacity steadily fades and the initially clearly pronounced potential plateaus lose shape. This can also be seen from the dQ/dV-plots of the first three cycles in Figure 61 (i), which show the same behavior as the CVs of this powder (Figure 58 (b)). The cathodic peak above 1.5 V corresponds to the voltage plateau during first discharge. As observed above in the CV-studies (Figure 58), these peaks belong to an irreversible process. The low voltage plateau above 1.0 V corresponds to the second cathodic peak, which is accompanied by an anodic peak. All observed peaks lose intensity and shift to higher potentials with prolonged cycling.

Similar observations can be made for the other materials, where the V_2O_5 microparticles, the V_2O_5 nanobundles and the V_2O_5-TiO_2 nanobundles are exceptional. For all other materials, however, the discharge capacity of the first discharge is larger than in the consecutive cycles, the peaks in the dQ/dV-plots, which are differently pronounced from sample to sample, partially disappear or shift in potential upon cycling and the electrode capacities fade with time. The three exceptional materials, *i.e.* the V_2O_5 microparticles, the V_2O_5 nanobundles and the V_2O_5-TiO_2 nanobundles, have a first cycle discharge capacity slightly lower than the capacity of the second cycle. Moreover, the peaks in the dQ/dV-plot are not as pronounced as for the other materials and the potential difference between positive and negative sweep is increased. Additionally, one can see that especially the two nanomaterials, the V_2O_5 nanobundles and the V_2O_5-TiO_2 nanobundles, show phase transitions at more positive voltages than the other materials.

Figure 62 (a) to (h) illustrates the effect of higher charging/discharging rates on the potentials of the phase transitions. These plots show the dQ/dV-plot measured at a rate of 20 mA g^{-1}, 50 mA g^{-1}, 100 mA g^{-1} and 200 mA g^{-1}, respectively. As in Figure 61, the dQ/dV plots reveal the potentials of the phase transitions. Here, the increased operating voltage of the nanomaterials is even more obvious than before. Increasing the charging/discharging current, one essentially makes the observation that the peak intensities decrease and the anodic peaks shift to more positive potential, while the cathodic potentials shift to more negative values. Thus, the voltage difference between charging and discharging increases, and therefore the energy efficiency decreases. The dQ/dV-plots in Figure 62 (i) to (p) show five consecutive cycles measured at 50 mA g^{-1} and prove that the observed shifts of the peaks are not an effect of increased cycle number, because such a peak shift for the five consecutive cycles is not observed.

Plotting the electrode capacities of the charge/discharge experiment presented in Figure 61 as a function of cycle number, one obtains the graph shown in Figure 63 (a) with the solid symbols being the charge capacity and the open symbols being the coulombic efficiency. During the first 20 cycles, the electrodes were charged/discharged at a current density of 20 mA g^{-1}, 50 mA g^{-1}, 100 mA g^{-1} and 200 mA g^{-1} for five cycles each, respectively, where an increased rate in general results in a drop of capacity and where the nanomaterials, especially the V_2O_5 nanobundles, retain the largest capacity. One can also see that during the first few cycles all self-synthesized materials have a larger capacity than the commercial V_2O_5 benchmark material. Moreover, the color code is the same as already used in the XRD sample characterization in Figure 54, *i.e.* the commercial V_2O_5 micro grains (purple) have the largest crystallinity, while the V_2O_5-TiO_2 nanobundles (brown) have the smallest crystallinity. Taking a close look onto the order of electrode capacities in the beginning of the experiment, one

realizes that there might be a certain order in electrode capacities linked to their crystallinity, namely an increase in capacity with decreasing crystallinity.

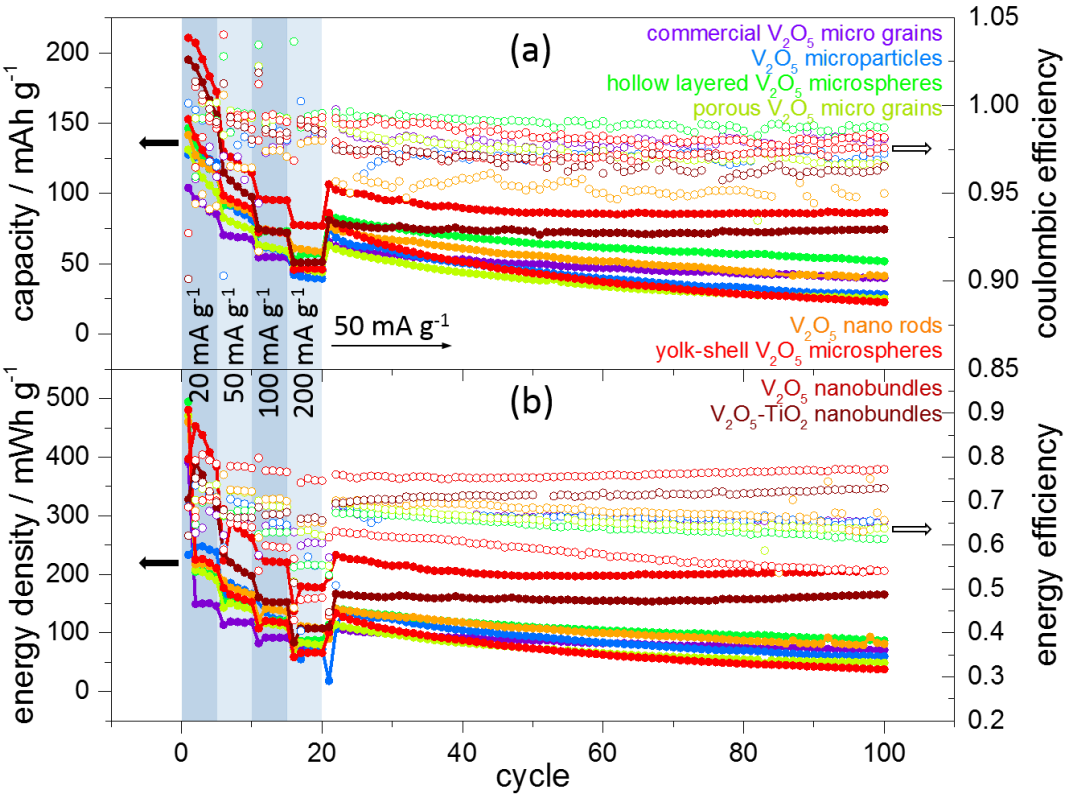

Figure 63: Comparison of battery performance of the different V_2O_5 electrodes as a function of cycle number with (a) the electrode charge capacities (solid symbols) and the coulombic efficiencies (open symbols) as well as (b) the discharge energy densities (solid symbols) with the energy efficiencies (open symbols).

Long term cycling at 50 mA g^{-1} shows the capacity fading of each material. Every material shows a drop of capacity upon cycling, which is differently severe for each sample. The two materials also performing best here are the V_2O_5 nanobundles as well as the V_2O_5-TiO_2 nanobundles, which after an initial capacity drop cycle fairly stable and retain a capacity of 86 mAh g^{-1} and 74 mAh g^{-1} after 100 cycles, respectively.

The coulombic efficiencies, *i.e.* the charge storage efficiency, of all materials is larger than 95 % after 100 cycles, while the V_2O_5 nanobundles even reach more than 98 %. The coulombic efficiency of the V_2O_5-TiO_2 nanobundles with 96 % in comparison is rather poor. The hollow layered V_2O_5 microspheres with close to 99 % are the best material.

The electrode capacity itself is not the only parameter to rate the quality and performance of an electrode material. The crucial parameter is the energy density, which besides the amount of stored electric charge also depends on the electrode potential. The energy density can be obtained from integrating the voltage profiles in Figure 61 and is plotted against cycle number in Figure 63 (b) (solid symbols). In comparison to the other materials, the V_2O_5 nanobundles again perform best with an initial energy density of close to 500 mWh g^{-1}, of which more than 200 mWh g^{-1} remain after 100 cycles.

The open symbols in Figure 63 (b) show the energy efficiency, *i.e.* a measure for how efficient energy can be stored by the electrode, also including energy losses. Again, the V_2O_5 nanobundles with an

energy efficiency of close to 80 % after 100 cycles is the by far best material, while most of the other materials remain below 70 % energy efficiency. At higher rates the advantage of the nanomaterials also becomes obvious: almost no loss in energy efficiency is observed for them, whereas huge drops, *i.e.* energy losses are observed for the other materials.

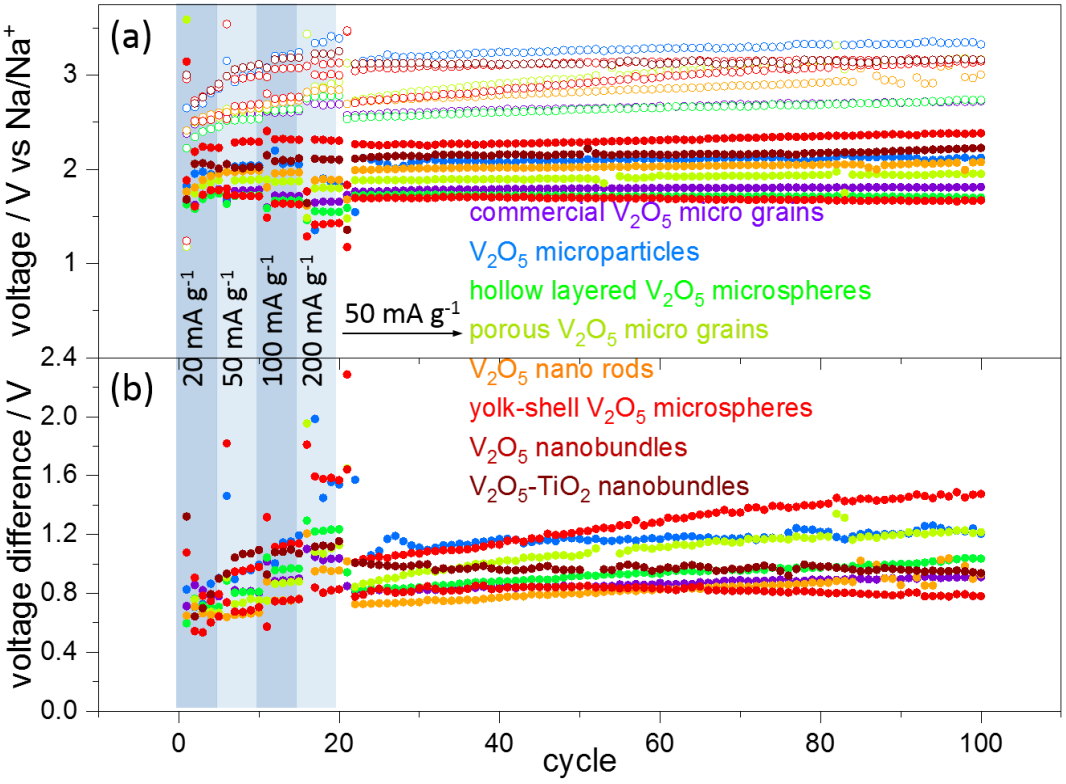

Figure 64: (a) Operating voltage of the V_2O_5 electrodes upon discharge (solid symbols) and upon charge (open symbols) as well as (b) the voltage difference between charge and discharge as a function of cycle number. The operating voltage can be calculated from the quotient of the energy density and the specific capacity.

Electric energy is defined as the product of electric charge and voltage. Thus, building the quotient of energy density and the specific electrode capacity, one can determine the (average) operating voltage of the electrode (in this case measured versus the Na reference electrode), shown in Figure 64 (a), with the charge voltage (open symbols) and the discharge voltage (solid symbols). In general, the three materials, which already showed an exceptional behavior in the dQ/dV-plots, *i.e.* the V_2O_5 microparticles, the V_2O_5 nanobundles and the V_2O_5-TiO_2 nanobundles have an increased operating voltage, for both charge and discharge. With almost 2.4 V, the discharge voltage of the V_2O_5 nanobundles is highest of all materials and more than 0.7 V larger than the worst material in this category, the yolk-shell V_2O_5 microspheres. This is beneficial in order to reach high power and energy densities. The charge voltage of the V_2O_5 nanobundles with more than 3.3 V is not necessarily beneficial for a battery, since the voltage difference between charge and discharge is also reflected in the energy efficiency.

A good measure to rate the operating voltages is the voltage difference between charge and discharge (the total voltage difference at a given rate), which is shown in Figure 64 (b). As in almost all categories before, the V_2O_5 nanobundles perform best, since they show the smallest voltage differences, not only at long term cycling, but also at high charging/discharging rates, where the operating voltage almost remains unaffected by higher rates.

The core findings of the electrode performance parameters of the charge-/discharge-tests of the tested materials are summarized in Table 1. The second column from left shows the electrode capacity of the first discharge, which for most materials contains an irreversible capacity loss after the first cycle (third column). Here, one again should mention the exceptional behavior of the V_2O_5 microparticles, the V_2O_5 nanobundles and the V_2O_5-TiO_2 nanobundles, which do not have this loss or even show a slight capacity increase. The coulombic efficiency in the fourth column is a measure of how efficient electric charge can be stored in the electrode. In the beginning of the battery life, this parameter can be affected by several processes, which is why the parameters of the 100th cycle are shown here. The capacity loss per cycle (between cycle 20 and 100) serves as measure for the electrode lifetime and is shown in the fifth column. This value is by far best for the V_2O_5-TiO_2 nanobundles. Besides this, column six and seven show the energy density and efficiency of the 100th cycle, respectively. Finally, the eighth column compares the discharge voltages of each material after 100 cycles. The best parameters of each category are highlighted in green and the worst in red.

Table 1: Comparison and summary of the battery performance parameters of the tested V_2O_5 electrode materials including the first discharge capacity, the irreversible capacity loss after the first discharge, the coulombic efficiency after 100 cycles, the capacity loss per cycle, the energy density and energy efficiency after 100 cycles as well as the discharge voltage at the 100th cycle.

V_2O_5 sample	Capacity 1st discharge / mAh g^{-1}	Irreversible capacity 1st cycle / mAh g^{-1}	Coulombic efficiency 100th / %	Capacity loss per cycle / mAh g^{-1}	Energy density 100th / mWh g^{-1}	Energy efficiency 100th / %	Discharge voltage *vs* Na/Na^+ 100th / V
commercial micro grains	234.6	142.7	98.1	0.320	70.8	65.3	1.81
microparticles	127.8	2.1	97.2	0.574	59.8	65.6	2.12
hollow layered microspheres	303.6	174.2	98.7	0.408	86.9	61.4	1.70
porous micro grains	268.9	150.9	96.6	0.473	49.0	63.8	1.95
nano rods	260.9	140.9	95.0	0.439	81.1	65.6	2.08
yolk-shell microspheres	284.7	149.7	98.2	0.793	37.7	54.1	1.67
nanobundles	195.3	-13.9	97.6	0.251	205.8	77.2	2.38
V_2O_5-TiO_2 nanobundles	175.7	-16.6	96.5	0.081	165.6	72.9	2.23

5.4 Graphite | V_2O_5 full cell

5.4.1 Finding a suitable electrolyte

Knowing about the electrochemical behavior of graphite and V_2O_5 in NIBs, both systems can be united and studied in a full graphite | V_2O_5 cell. The studies presented in section 5.2 suggested that Na-ions can intercalate into graphite from the four shortest glymes used as a solvent in the electrolyte. In the G_3-electrolyte, the obtained capacities with 70 mAh g^{-1} were diminished compared to the other

systems with 112 mAh g^{-1}, *i.e.* G_1, G_2 and G_4. Another important parameter to evaluate the suitability of an electrolyte is the cycling stability, which is best for the G_4-electrolyte. These data can be found elsewhere.[178] The excellent cycling stability of a graphite electrode in the G_4-electrolyte is shown in Figure 65, where a graphite electrode was cycled in a 2016 coin cell with a 1 M $NaClO_4$ in G_4 electrolyte.

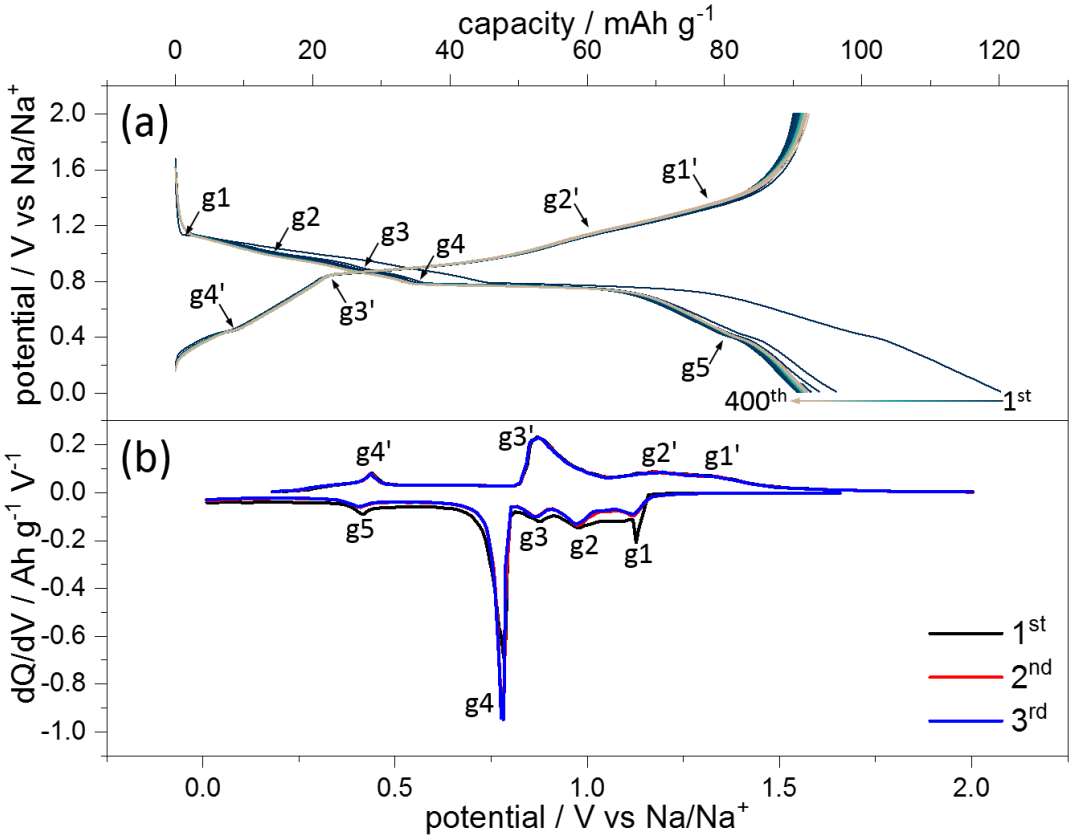

Figure 65: (a) voltage profiles of 400 charge/discharge cycles of a graphite electrode (MCMB) in 1 M $NaClO_4$ in G_4 (current density: 55.5 mA g^{-1}) and (b) the dQ/dV-plots of the first three cycles. The labels in the graphs help to correlate voltage plateaus in (a) to peaks in (b), which will be of importance later.

Figure 65 (a) shows 400 charge/discharge profiles. The discharge capacity of the first cycle (120 mAh g^{-1}) is increased compared to the consecutive cycles (90 mAh g^{-1}), which repeat and match pretty well. The voltage profiles show several plateaus, which cause the corresponding peaks in the dQ/dV-plots shown in Figure 65 (b). Here, one can also see that the differential capacity of the first negative going sweep is larger than for the consecutive cycles below 1.2 V, resulting in the increased capacity. The peak labels indicate the connection between a plateau in the voltage profile (Figure 65 (a)) and the dQ/dV-plot (Figure 65 (b)). This nomenclature will be of importance later.

The measured capacities and coulombic efficiencies as a function of cycle are shown in Figure 66 (a). More than 90 mAh g^{-1} are obtained and no significant capacity loss is observed, even after 400 cycles. The coulombic efficiency stays well above 99.8 % after a few cycles. From the integral of the voltage profiles, the energy density can be determined, which is sketched as a function of cycle number in Figure 66 (b). The energy density is considerably smaller than for V_2O_5 for instance (Figure 63), as the operating voltage of the graphite is lower. As graphite is the negative electrode in the full cell, the absolute energy density (with respect to a Na negative electrode) is not important. More relevant is the difference of 20 mWh g^{-1} observed between charging the graphite electrode (82 mWh g^{-1}) and discharging it (62 mWh g^{-1}), resulting in an energy efficiency of around 75 % and being caused by the

voltage difference between charge and discharge (Figure 66 (c)). The voltage necessary to charge the graphite electrode is about 0.2 V larger than the voltage one obtains when discharging it.

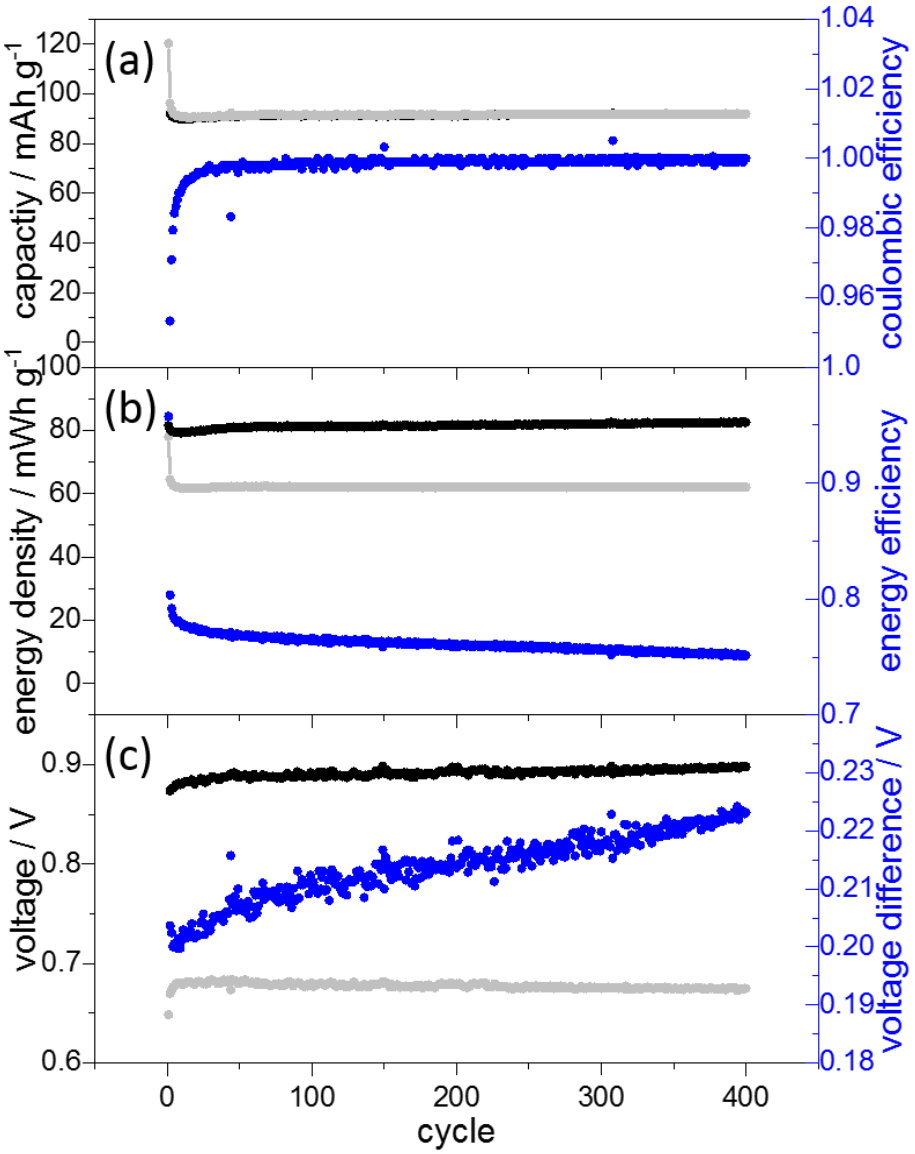

Figure 66: cycle performance of graphite (MCMB) in 1 M $NaClO_4$ in G_4 with (a) the specific capacity (discharge: grey, charge: black) and the coulombic efficiency (blue), (b) the energy density (discharge: black, charge: grey) and the energy efficiency (blue) and (c) the average voltage (discharge: black, charge: grey) and the voltage difference between charge and discharge (blue).

In section 5.2 co-intercalation phenomena were observed, where the Na-ions drag their solvation shell into the graphite lattice upon intercalation. In order to clarify the intercalation mechanism of the Na-ions into the V_2O_5 lattice, and whether co-intercalation also occurs in the V_2O_5 electrodes when using glyme-electrolytes, the experiment in Figure 67 was conducted. Here, CVs of the commercial V_2O_5 micro grains were measured using different electrolyte solvents, *i.e.* EC/PC in (a), EC/DMC in (b), G_1 in (c), G_2 in (d), G_3 in (e) and G_4 in (f).

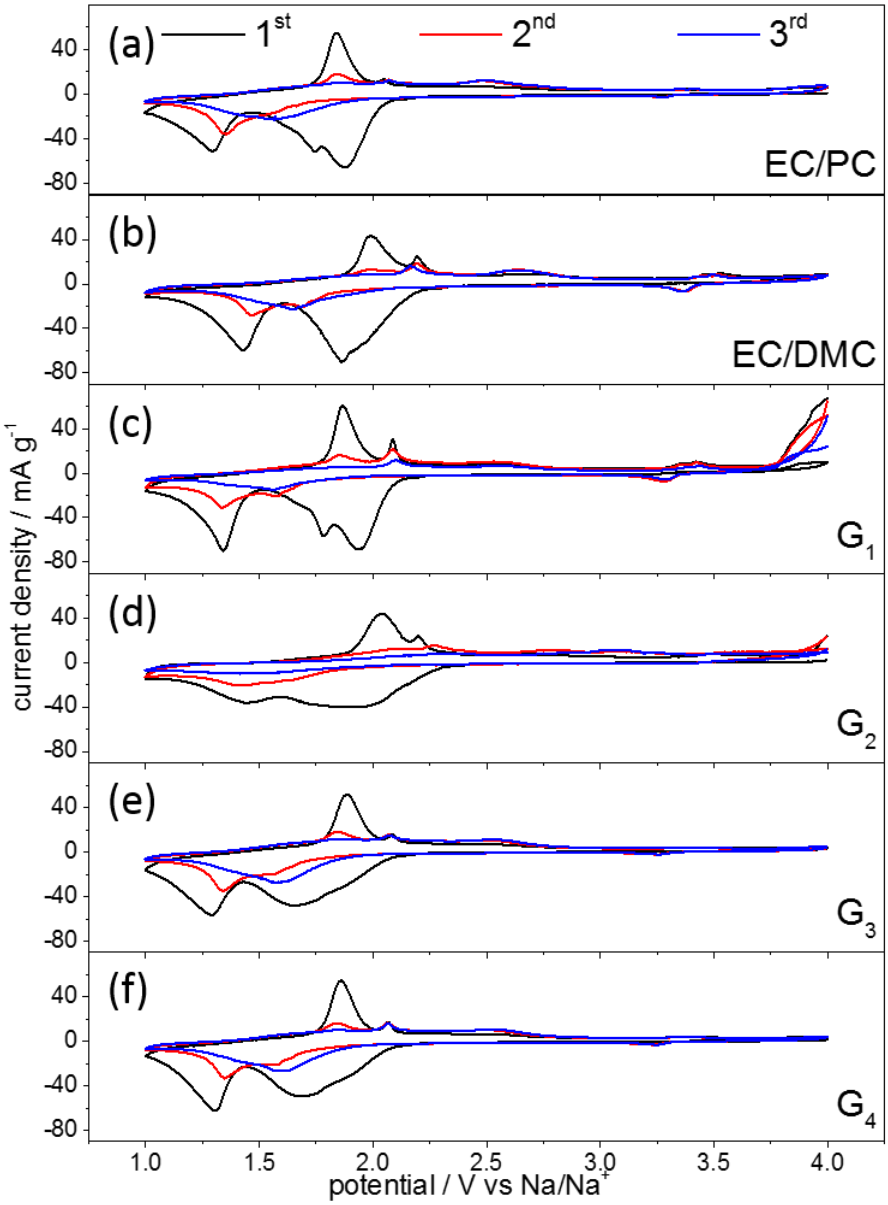

Figure 67: CVs of the commercial V_2O_5 micro grains in different electrolytes composed of 1 M $NaClO_4$ in (a) EC/PC, (b) EC/DMC, (c) G_1, (d) G_2, (e) G_3 and (f) G_4 (potential sweep rate: 50 µV s^{-1}).

The general appearance of the CVs is similar and shows the same features as already observed above in Figure 58 (b). Only minor differences between the solvents are observable. This for example concerns the shape of the irreversible cathodic twin peak of the first cycle and the appearance of an oxidative current at a voltage above 3.8 V for the G_1 and G_2 electrolyte. Electrolyte oxidation is a harmful, undesired process in a battery, limiting its lifetime.

5.4.2 Battery test of the graphite | V_2O_5 full cell

The outcome of the previous section suggests to use the G_4-electrolyte in a graphite | V_2O_5 full cell, as the graphite electrode shows a remarkable cycling stability therein and no big influence of the electrolyte solvent on the intercalation behavior of Na-ions into V_2O_5 is observed. Consequently, a full cell was assembled and tested employing a MCMB graphite electrode, a V_2O_5 nanobundles electrode, which showed the best battery performance in section 5.3, and a 1 M $NaClO_4$ in G_4 electrolyte. When building a full cell, care has to be taken to match the capacities of both electrodes. This is not

straightforward, especially when the electrode capacity does not remain constant while cycling. Since the specific capacity of the graphite remains constant at around 90 mAh g^{-1} (Figure 66) and the capacity of the V_2O_5 nanobundles reaches a similar value after prolonged cycling (Figure 63), electrodes were chosen such that the mass of active material was equal for both, the graphite and the V_2O_5 electrode. In the above half-cell studies and the coin cell study, the Na-CE served as Na-ion source, which is missing in a full cell. In order to introduce a Na-ion source, the V_2O_5 nanobundles electrode was first discharged, *i.e.* sodiated, to 1 V *vs.* Na/Na^+ with a Na-CE at a slow rate of 5 mA g^{-1} prior to assembling the full cell with the graphite negative electrode.

Figure 68 (a) shows the voltage profiles of the charge/discharge experiment of the graphite | 1 M $NaClO_4$ in G_4 | V_2O_5 full cell, which was operated at a current density of 50 mA g^{-1} between 4 V and 0 V. As the full cell is operated in a two electrode setup and no Na/Na^+ RE is employed, the voltages used in the following denote the voltage difference between the graphite and the V_2O_5 electrode. The charge capacity of the first cycle with 174 mAh g^{-1} is much larger than in the second cycle (95 mAh g^{-1}), indicating an irreversible process. The specific capacity denotes the capacity of the V_2O_5 electrode in the following (*i.e.* battery capacity in mAh normalized to the active V_2O_5 mass). In the course of cycling, a gradual drop in capacity is observed. The dQ/dV-plot in Figure 68 (b) illustrates the potential position of the voltage plateaus. In short, one can say that with the exception of the first positive scan (charge), all cycles match each other. The first cycle shows an increase of differential capacity at 0.75 V (called as g1 + SEI) and a broad peak centered around 2.2 V (g4 + vo2'). Also some minor positive peaks appear at 1.8 V (g2 + g3) and 2.7 V (g5). In the following cycles, negative peaks appear at 2.8 V (g4') and 1.8 V (g3') coupled to positive peaks at 1.8 V and 2.5 V. The peak nomenclature introduced here will help to understand the origin of the peaks later.

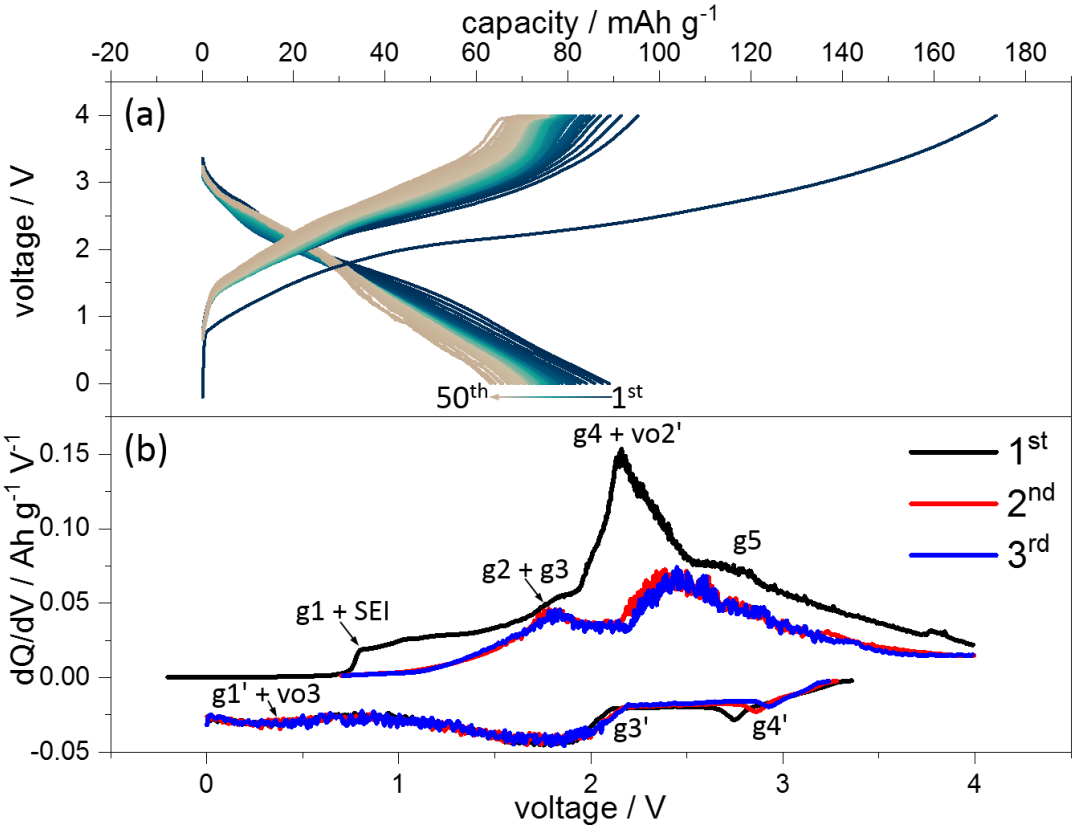

Figure 68: (a) voltage profiles of the graphite | 1 M $NaClO_4$ in G_4 | V_2O_5 full cell (current density: 50 mA g^{-1}) with (b) the dQ/dV-plots of the first three cycles.

The cycling performance of the full cell with its capacity is plotted in Figure 69 (a) with the charge (black) and discharge (grey) capacity and the corresponding coulombic efficiency (blue). After an irreversible capacity loss in the first cycle, the battery has a specific capacity of initially 89 mAh g^{-1} dropping to 64 mAh g^{-1} after 50 cycles, being equivalent to a capacity loss of 0.50 mAh g^{-1} per cycle. The coulombic efficiency is above 90 %. The energy density of the battery is plotted in Figure 69 (b), where a huge gap between the charge and the discharge curve is observed. This is also reflected in the energy efficiency, which after 50 cycles amounts to 51.8 %. After 50 cycles, the energy necessary to charge the battery amounts to 190 mAh g^{-1}, while only 98 mAh g^{-1} are available for discharge. This mainly originates from a voltage difference between charge and discharge (Figure 69 (c)). After 50 cycles the battery has an average discharge voltage of 1.4 V, whereas almost 3.0 V are necessary to recharge the battery. The essential parameters of the charge/discharge test of the graphite | V_2O_5 full cell are summarized in Table 2.

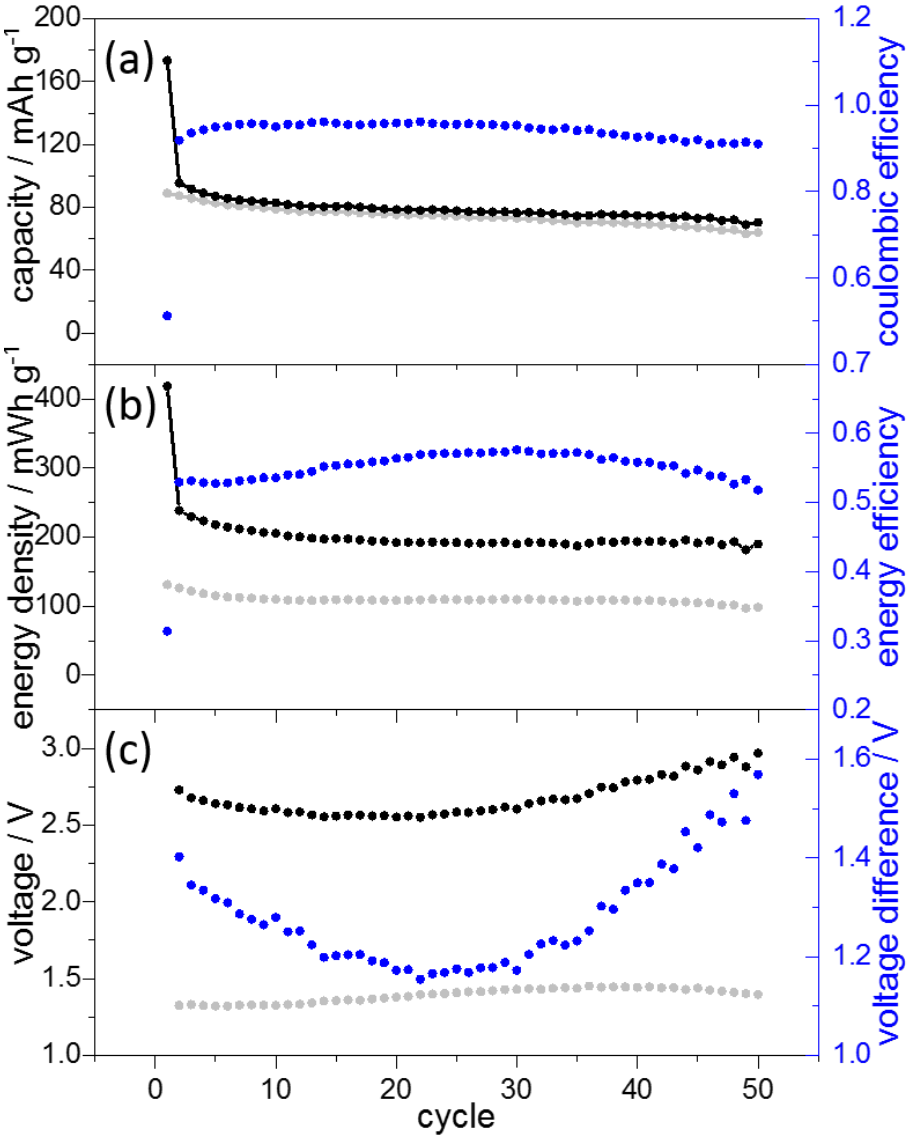

Figure 69: Battery performance of the graphite | 1 M $NaClO_4$ in G_4 | V_2O_5 full cell with (a) the capacity (charge: black, discharge: grey) and the coulombic efficiency (blue), (b) the energy density (charge: black, discharge: grey) and the energy efficiency (blue) and (c) the operating voltage (charge: black, discharge: grey) with the voltage difference between charge and discharge (blue) as a function of cycle.

Table 2: Summary of the battery performance parameters of the graphite | V_2O_5 full cell.

Capacity 1st charge / mAh g^{-1}	Irreversible capacity 1st / mAh g^{-1}	Capacity 50th discharge/ mAh g^{-1}	Coulombic efficiency 50th / %	Capacity loss per cycle / mAh g^{-1}	Energy density 50th / mWh g^{-1}	Energy efficiency 50th / %	Discharge voltage 50th / V
173.5	78.2	64.0	91.0	0.50	98.3	51.8	1.40

6 Discussion

Experimental results on important aspects of metal ion batteries have been presented in chapter 5. These were the SEI-formation on a graphite electrode operated in a LIB (section 5.1), the intercalation mechanism of $Na^+(G_x)_y$-complexes into graphite (section 5.2), the V_2O_5 electrochemistry in a NIB (section 5.3) and an experimental demonstration of a graphite | V_2O_5 full cell NIB prototype (section 5.4). In the following, these results shall be discussed in detail. Afterwards, a general discussion putting each section into relation to another concludes this chapter.

6.1 SEI Formation Mechanism on Graphite in LIBs

Prior to the discussion about the SEI-formation, the Li^+ intercalation shall be shortly discussed here. Both charge/discharge (Figure 34) as well as PITT (Figure 35) experiments showed three reversible peak pairs in the dQ/dV- respectively differential capacity-plot. It is well known from literature that Li^+ intercalation into the graphite causes the cathodic peaks, while the anodic peaks are caused by de-intercalation.[121] The small peak pair above 0.2 V corresponds to the phase transition caused by the insertion of 0.015 Li-ion for each C_6-cell, which is close to the stage 4 LiC_{72} stoichiometry. The concept of staging is often used in the graphite electrochemistry. It describes to which extent graphite layers are filled by species such as Li. In a stage 1 GIC, every graphite interlayer is filled, in a stage 2 GIC, two graphene layers separate one Li-layer and so on. The second peak pair above 0.1 V originates from the $Li_{0.5}C_6$ formation, respectively the stage 2 LiC_{12} phase. Below 0.1 V, one can finally find the full lithiation of the graphite according to LiC_6, which is a stage 1 GIC.

PITT gives further insight into the Li-graphite electrochemistry. Analyzing the current transients by plotting them as a $-\mathrm{It}^{-1/2}$ *vs.* $\log(\mathrm{t})$ plot (Figure 35(c)), one can read out the Cottrell diffusion controlled regime, where the Cottrell equation (equation (34)) can be applied and the diffusion coefficient D_0 of the Li-ions in the graphite host can be determined.[63] Figure 70 shows the diffusion coefficient as a function of electrode potential. When lithiating the graphite, the diffusion coefficient is in the range of 10^{-11} cm^2 s^{-1}, which is a typical value for Li-diffusion in graphite. Unfortunately, the current transients did not reach equilibrium in the intercalation regimes, which is why the diffusion coefficient could not be determined for the two major cathodic peaks. In the range of the intercalation peak above 0.2 V, however, one can also see a slightly increased diffusion coefficient. When the graphite is fully loaded with Li, it is facile to release the Li, which can also be seen from the diffusion coefficient being several orders of magnitude larger than in the same potential range upon lithiation. The driving force is the repulsive interaction between the Li^+ in the graphite lattice. The graph in Figure 70 also shows a slightly elevated diffusion rate for the de-intercalation peak above 0.1 V. All in all, one can say that lithium intercalates into graphite well below 0.3 V and does not interfere with the SEI-formation at more positive potentials.

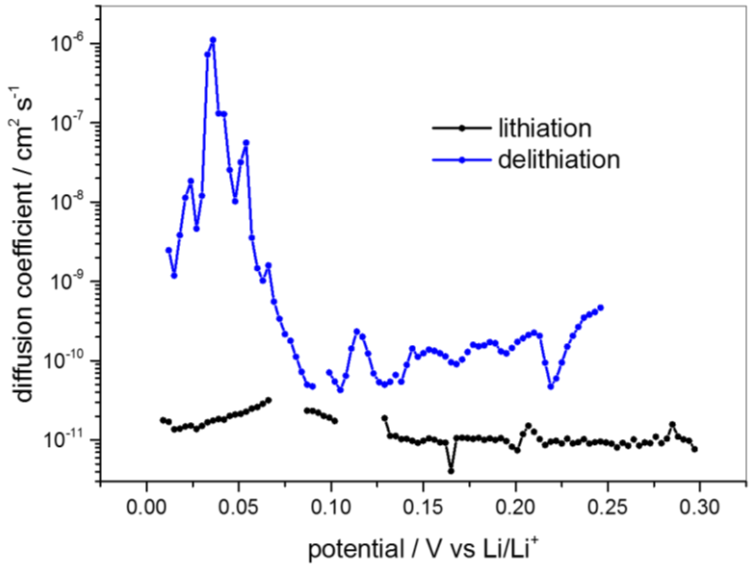

Figure 70: Li^+ diffusion coefficient in graphite as a function of electrode potential.

With respect to the SEI-formation electrochemical measurements of MCMB and HOPG (Figure 36 and Figure 37) indicate a multistep process. As proposed in literature, the SEI-formation is initiated by the solvent reduction, namely both, the linear DMC as well as the cyclic EC. Depending on the electrode potential, the cyclic carbonates can either undergo a 1-electron-reduction or a 2-electron-reduction, including a ring opening step.[101–104, 106] Before the actual SEI-formation, a re-coordination of the solvation shell around the Li-ions in the outer Helmholtz plane occurs. This process is also called double layer establishment and happens at potentials above 1.4 V.[328] Consequently, the first cathodic shoulder in Figure 36 and Figure 37 can probably be assigned to the double layer establishment. Below 1.0 V the electrode potential is low enough to break the EC-ring and the solvent molecules can either be reduced via the 2-electron-reduction pathway[79, 106, 111, 329–332], which changes over to the 1-electron-reduction at 0.8 V.[102, 106] At very low potentials of close to 0.4 V and below, the electrode reduction strength is strong enough to also reduce Li_xPF_y species.

The multistep nature of SEI-formation can also be revealed by *in-situ* STM as presented in Figure 38. Similar studies have already been conducted in literature,[91, 135–140, 137–145] which showed co-intercalation of Li^+ together with their solvation shell, exfoliation processes as well as the SEI precipitation on the graphite basal plane. The increased reactivity of graphite step edges is often discussed to be the initiator of SEI-precipitation,[117, 133, 134] which also might explain the observed step edge roughness. The step edge roughness seen in Figure 38, however, is already present on the pristine sample and does not change with decreasing potential. As mentioned earlier, one probably sees exfoliated graphene flakes decorating the step edges. There is no hint from the presented STM data towards an increased SEI-formation reactivity at the step edges in comparison to the basal plane. Additionally, STM cannot be conducted on a cross-sectional graphite, preventing a direct comparison between basal- and cross-sectional SEI-formation.

The origin of the swellings found in the STM images in Figure 38 (g) after ramping the sample to 0.9 V is the simultaneous intercalation of the Li-ions together with their solvation shell. The solvated Li-ions intercalate in different graphite layers, as the swollen regions overlap each other, which cannot be explained otherwise. Unsolvated Li-ions can only be intercalated at more negative potentials. This observation is in agreement to Inaba´s STM work, where co-intercalation of solvated Li-ions was also observed in similar electrolytes at potentials close to 1.0 V.[133–135, 139]

The graphene exfoliation setting in below 0.6 V (Figure 38 (j)) can have two reasons: the first one is mechanical stress induced by the co-intercalated species[80, 82, 172–175, 178–180, 183] while the second one is a subsurface gas evolution taking place inside the graphite lattice from the electrochemical reduction of co-intercalated solvent species.[80, 82, 91, 136–138, 142, 333–337] As was shown in section 5.2, the first reason can probably be discarded, since the co-intercalation of solvated Na-ions into graphite results in a strongly increased lattice expansion, which, however, does not result in exfoliation.

Below 0.5 V (Figure 38 (k)) the STM images become slightly fuzzy. At these low potentials the SEI-film on the graphite basal plane changes from an organic (oligomers, polymers) to a more inorganic nature (oxides, fluorides, phosphates).[79, 116, 127–130] The comparatively soft organic species can in part be penetrated by the STM tip pushing through to the HOPG basal plane. Thus, as long as the SEI is still more organic at high potentials, STM imaging is not affected that much by the SEI. However, when the organic species are further reduced to more rigid inorganic species at lower potentials, electron tunneling between tip and sample is strongly disturbed resulting in noisy images, causing the fuzziness. Wang *et al.* also noticed a similar fuzziness.[143] This strong reduction of the SEI components leading to the formation of inorganic species represents the last SEI-formation step and probably causes the low voltage SEI-peak observed in electrochemical experiments (Figure 36 and Figure 37).

The CVs (Figure 39) measured at HOPG in between the *in-situ* STM scans show the continuous irreversible charge consumption at the graphite electrode during the negative sweep to lower potentials. Since the major part of the HOPG surface consists of a basal plane with a low quantity of step edges, which are the intercalation sites for the Li-ions, it is believed that the intercalation/de-intercalation is suppressed and does not show up in these CVs. Additionally, the potential sweep rate of 5 mV s^{-1} is probably too fast to resolve the intercalation/de-intercalation peaks separately. The crossover observed below 0.1 V in the CV is accompanied by an anodic peak at 0.3 V and indicates reversible Li-plating/-stripping.

The *in-operando* STM study presented in Figure 40 reveals additional information about the SEI-formation mechanism. When the sample potential is set to 1.4 V (Figure 40 (a)), which corresponds to the first cathodic shoulder in the electrochemical experiments (Figure 36 and Figure 37), the SEI-formation is associated with the double layer establishment.[102, 106] This is a process, which cannot be observed by STM, as it neither alters surface morphology nor changes the tunneling barrier significantly.

In contrast to the double layer establishment, a reversible surface film precipitation occurring between 1.3 V and 1.0 V (Figure 40 (b)) is detectable by STM. This SEI-formation step must be related to a reversible surface reaction. Taking a look at the EC reduction scheme in Figure 14, one understands that step (1) can occur reversibly, while the ring opening in step (2) must be irreversible. Thus, the Li^+ uptake in step (1) is believed to cause the second cathodic shoulder in the electrochemical experiments (Figure 36 and Figure 37). The same argumentation also holds true for the first DMC reduction step (Figure 15 step (1)).

When the molecular structure of the solvent molecules is destroyed (ring opening of the EC molecule (Figure 14 step (2)) and fracture of the DMC molecule (Figure 15 step (2))), the SEI-formation must also become irreversible. This can be seen in Figure 40 (c), where the electrode was set to 0.75 V, and the formed surface film does not dissolve anymore. Thus, the main SEI peak observed in electrochemistry (Figure 36 and Figure 37) contains the 2-electron- and 1-electron-reduction of EC as well as the DMC reduction to lithium methyl carbonate.

Since STM is insensitive towards the discrimination of chemical species, not many conclusions can be drawn from Figure 40 (d). At such low potentials (0.4 V) it is known from literature that also the PF_6^- anion can be reduced to a variety of fluorides, oxides, phosphates and other inorganic species.[79, 92, 101, 103, 107–110]

STM does not solely detect the surface topography, but rather measures a convolution of topography and electronic states (equation (50)). Thus, the 'height' information gained from the height profile in Figure 41 is a convolution of both and must be taken with care. Additionally, only a fraction of the SEI can be visualized by STM, because the outer SEI components farther away from the electrode surface are composed of soft, nonconductive oligomers/polymers, which cannot be detected by the STM tip easily. Hence, only a small portion of the real SEI can be detected by STM and the height profile in Figure 41 does not show the full SEI thickness. Instead it rather represents the lower limit of SEI thickness.

In summary, the application of *in-situ* and especially *in-operando* STM revealed a new understanding of the SEI-formation mechanism. In particular, it is possible to put the different formation steps into relation with electrode potential. Figure 71 summarizes the core findings of the above studies. At high voltage, the double layer establishment initializes the SEI-formation.[102, 106] Between 1.3 V and 1.0 V the solvent molecules take up a Li-ion and an electron, which is the first reduction step and which is still a reversible process.

Afterwards, solvated Li-ions co-intercalate at around 0.9 V (Figure 38 (g)). It is, however, unclear, to which extend the Li-ions are still solvated when intercalating, *i.e.* how many solvent molecules coordinate the Li-ion. In bulk electrolyte, the coordination number y of the $Li^+(EC)_y$ complex is usually ranging from one to five.[107, 296–298]

Further reduction results in the irreversible destruction of the molecular structure, for instance by the EC ring opening or the DMC fracture. A 2-electron-reduction at more positive potentials[79, 101–111, 329–332] and a 1-electron-reduction at less positive potential[101–106] lead to the precipitation of an irreversible deposit on the surface (Figure 40 (c)).

Below 0.6 V the electrode reduction strength finally is strong enough to form a complex multicomponent mosaic structure of inorganic compounds such as oxides, fluorides, phosphates and carbonates,[79, 116, 127–130] disturbing STM imaging slightly. The reduction strength decays with increasing distance from the surface resulting in an inorganic layer in close vicinity to the electrode, gradually becoming more organic towards the bulk electrolyte.

Finally, one more comment should be made regarding the SEI-formation on battery cathodes (*i.e.* the positive electrode). In analogy to the reductive SEI-formation on a battery anode, an oxidative SEI-formation can take place at the cathode. In carbonate based electrolytes a variety of SEI compounds can be found, including alkoxy species (RO), ethers (ROR), esters (ROOR), alkyl fluoroformates (ROCOF), carboxylic acids (RCOOR), lithium carbonates (Li_2CO_3), lithium alkyl carbonates ($ROCO_2Li$), fluorophosphates (PF_x), carboxylates (-COO-) and CO_2.[338–340]

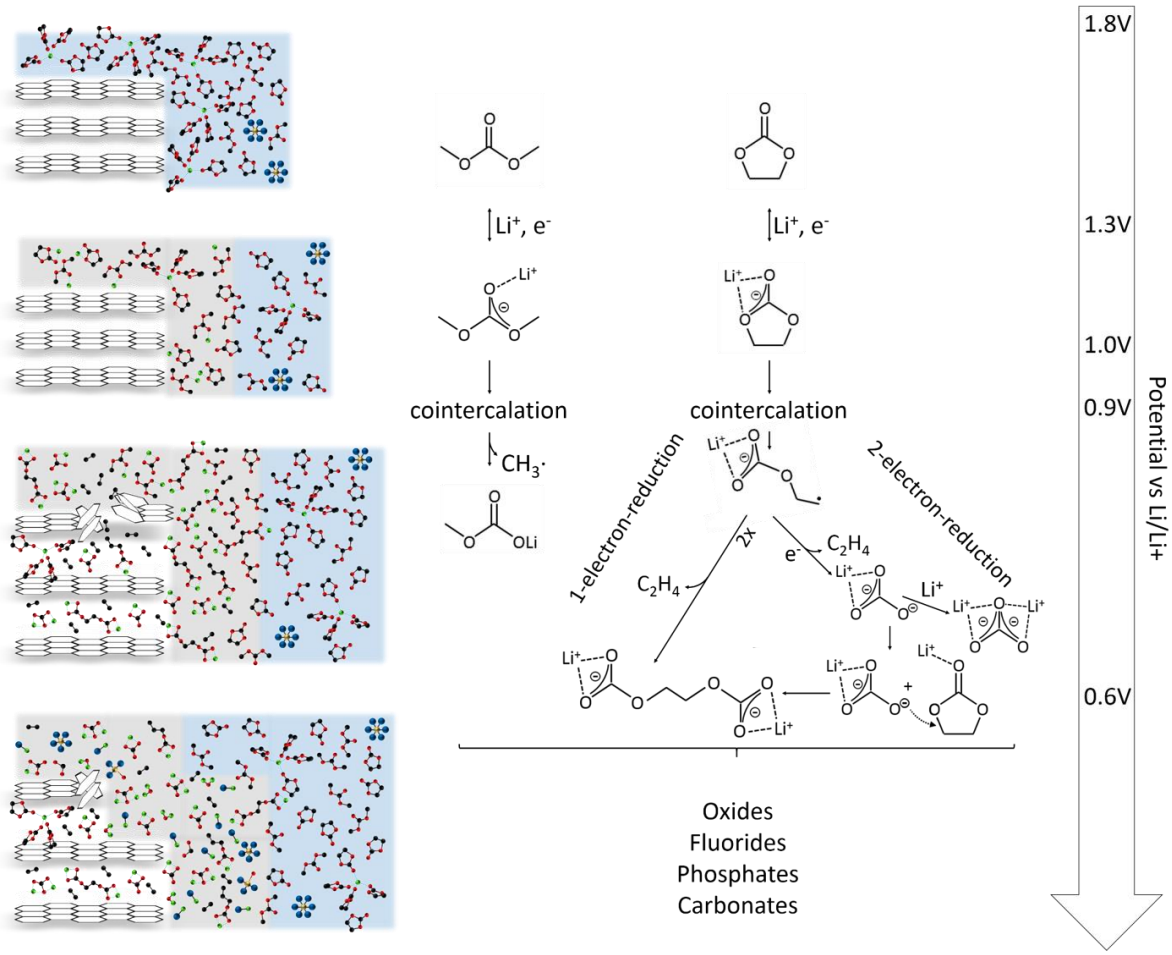

Figure 71: Scheme of the SEI-formation on graphite anodes in carbonate based electrolytes summarizing the core findings of section 5.1.

6.2 Formation mechanism of ternary Na-GICs

Comparing the electrochemistry of classical carbonate electrolytes (Figure 42) to the electrochemistry of glyme electrolytes (Figure 45 and Figure 46), it is obvious that the intercalation mechanism must be fundamentally different. Carbonate based Na-ion electrolytes bring about two major problems: the inability regarding Na-intercalation and the electrode destruction (exfoliation), which is specially enhanced in PC-electrolytes.

As was already observed in the discussion about the SEI-formation in section 5.1 (Figure 38), an exfoliation is also observed in EC-containing electrolyte, however, compared to the PC-containing electrolyte (Figure 43), the detachment of graphene flakes in a PC-free electrolyte is much weaker. The driving force of exfoliation is discussed to be caused by either a mechanical stress on the graphite lattice induced by co-intercalated species[80, 82, 172–175, 177–180, 183] or by a subsurface gas evolution triggered by the electrochemical reduction and an accompanied gas release inside the graphite lattice.[80, 82, 91, 136–138, 142, 333–337] The first mechanism seems unacceptable, since the lattice expansions observed for the intercalation of the solvated $Na^+(G_x)_y$-complexes (> 11 Å) is larger than the lattice expansion of co-intercalated Li-ions (ca. 5 Å). The subsurface gas evolution mechanism on the other hand is enhanced for the propylene release (PC-reduction) compared to ethylene release (EC-reduction).[136, 139, 142, 341] Thus, the strong exfoliation observed in Figure 43 from 1.0 V and below results from propylene gas evolving in the inner graphite lattice, leading to delamination.

This also explains the shape of the graphite CV in the PC-electrolyte (Figure 42 (b)): The irreversible SEI-formation consumes charge for the electrolyte reduction. As was shown in section 5.1, the SEI-formation is a self-limited growth process, since the SEI-film increases the tunneling barrier for electrons from the electrode to the electrolyte, slowing down the SEI-growth with increasing thickness. In case of the PC-electrolyte, graphene sheets exfoliate from the surface, exposing a fresh graphite surface, where the SEI formation can proceed. Thus, the SEI-formation in a PC-electrolyte is not only strongly enhanced compared to an EC-electrolyte, but also is not limited to the first cycle, since exfoliation can also take place later. The increased exfoliation in PC-electrolytes will be of importance in section 5.4, where a full Na-ion cell with a graphite anode and a V_2O_5 cathode is presented, which to date are mostly cycled in PC-containing electrolytes.

So far, the limited capacity obtainable from carbonate based electrolytes in NIBs prevented the application of graphite electrodes. Operating graphite in glyme electrolytes (Figure 45 and Figure 46), in turn, provides reasonable capacities of around 100 mAh g^{-1}. One fundamental difference between the intercalation mechanism in carbonate electrolytes to the glyme electrolytes is that the Na-ions co-intercalate with their glyme solvation shell as $Na^+(G_x)_y$-complex forming ternary Na-GICs, while in carbonate electrolytes the Na-intercalation, apart from an initial co-intercalation during SEI-formation, would result in the formation of binary Na-GICs. Binary Na-GICs are energetically unstable and the in-plane Na diffusion is hampered.[150–152] One strategy to overcome these issues is to modify the interaction energy between Na-ion and graphite lattice by a solvation shell.[342]

Very recent literature[18, 75, 167, 168, 170–176] investigated the intercalation behavior of solvated Na-ions into graphite electrodes, but the intercalation mechanisms are still not understood to a great part. This for example includes the phase transitions and the unique behavior of the G_3-system observed in the electrochemical experiments (Figure 45 and Figure 46). From the inserted electric charge during galvanostatic cycling (Figure 46), a stoichiometry of close to NaC_{18} (theoretical capacity: 112 mAh g^{-1}) can be calculated for the fully sodiated graphite in the G_1, G_2 and G_4 electrolytes. In the G_3 cell, a stoichiometry of NaC_{30} (70 mAh g^{-1}) is found. Discharging the graphite to the main plateaus, respectively the sharp cathodic peak ('half' sodiated), an intermediate NaC_{48} compound is found in all electrolytes.

These phase transitions were illuminated further by XRD and STM. Both techniques give insight into the graphite lattice expansions upon sodiation. As mentioned above, height profiles across the expanded graphite lattice in STM-images reveal an interlayer spacing of 10.9 Å (G_3) and 10.7 Å (G_4). This finding is confirmed by the XRD analysis according to Bragg´s law (equation (38)), which is the more accurate method, since it is an integral technique (Table 3):

Table 3: Interlayer spacings for graphene planes with intercalation layer and staging numbers of the ternary Na-GICs found by XRD. The difference between interlayer spacing and lattice constant of the stage 2 Na-GICs equals the plane to plane distance of two adjacent graphene layers.

Electrolyte	Interlayer spacing / lattice constant c (intermediate stage 2 Na-GIC) / Å	Interlayer spacing (fully discharged stage 1 Na-GIC) / Å	Miller indices l	Staging x
1 M $NaClO_4$ G_1	11.77 / 15.12	11.65	$5 \rightarrow 4 \rightarrow 3$	$3 \rightarrow 2 \rightarrow 1$
1 M $NaClO_4$ G_2	11.70 / 15.05	11.85	$5 \rightarrow 4 \rightarrow 3$	$3 \rightarrow 2 \rightarrow 1$
1 M $NaClO_4$ G_3	11.60 / 14.95	11.59	$4 \rightarrow 3$	$2 \rightarrow 1$
1 M $NaClO_4$ G_4	12.12 / 15.47	12.01	$5 \rightarrow 4 \rightarrow 3$	$3 \rightarrow 2 \rightarrow 1$

Sodiating the graphite to the intermediate state ('half' discharged), interlayer spacings of more than 11 Å are found, which is much larger than the ionic radius of Na-ions (1.02 Å).[13] Hence, it does not seem very plausible that the Na-ions purely intercalate into the graphite, but together with a solvation shell (lateral dimensions of a $Na^+(G_2)_1$-complex with 7.27 Å) leading to the formation of a ternary Na-GIC.[18, 75, 167, 168, 190–193, 195, 196, 343]

Applying equation (40) to the XRD peaks, the Miller indices l of the GIC can be determined. Figure 72 shows the development of l as a function of the state of charge. Taking a look at the G_1 system for instance (Figure 72 (a)), l continuously drops until it reaches a value of 4 when the main discharge plateau at 0.5 V is reached. At the same time, the development of a new phase (l = 3) is observed, while the first phase (l = 4) disappears upon further discharge. Upon charging, this behavior is reversed and when the first charge plateau is reached, the intermediate phase (l = 4) returns, while the phase with l = 3 disappears. Later, a phase with l = 5 is formed, from which l continuously increases again, before the original state of the graphite is reached when fully charged at 2.0 V.

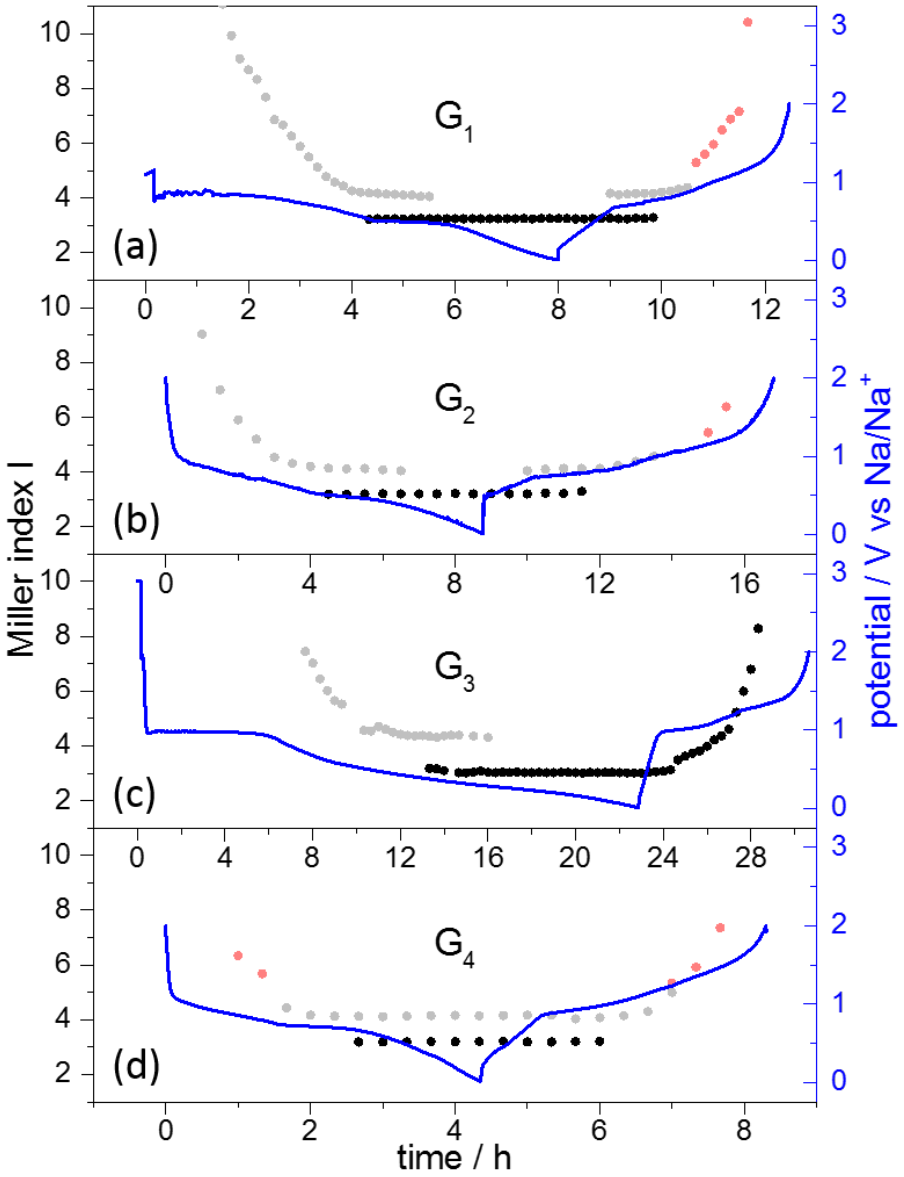

Figure 72: Miller index l in the course of a discharge/charge cycle determined from the XRD peak positions of the in-operando *XRD measurement in Figure 47.*

With this knowledge one can convert the d-spacings determined from the XRD peaks by the Bragg equation to the lattice constants *c* of the different GICs. For the G_1-system, those amount to *e.g.* 15.12 Å for the 23.5 ° peak (004) and to 11.65 Å for the intermediate phase causing the 22.87 ° peak. These findings are in full agreement with results of Kim *et al.*[75].

Similar observations are made for the other systems, which all reach an intermediate l = 4 phase when they are in the 'half' sodiated state. Further discharge leads to a sharp transition to a new l = 3 GIC. The continuous decrease of l during the first three reduction peaks might be caused by the continuous change of lattice constant. Due to the limited time resolution of XRD measurements, an association of those peaks with higher 'stable' Miller indices cannot be excluded.

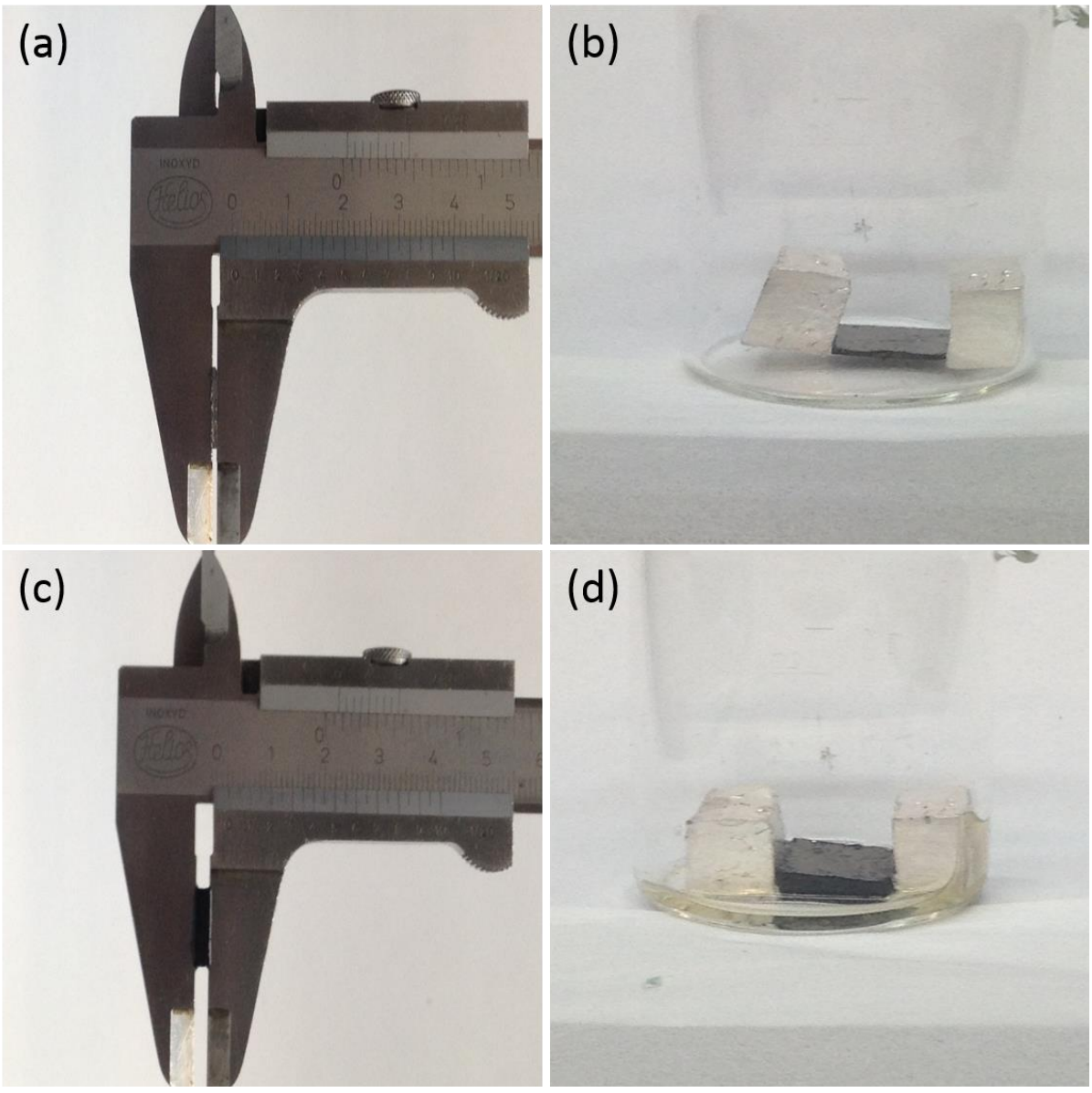

Figure 73: Determination of the staging number from sodiating an HOPG chip in 1 M $NaClO_4$ in G_3. (a) Original thickness of the pristine HOPG sample (0.8 mm) and the experimental setup in (b) with the HOPG chip sandwiched between two Na-blocks touching the open facets without an electrolyte. As soon as the electrolyte is added, a volume expansion (2.4 mm) of the HOPG sample is observed (c), which can also be seen in direct comparison by eye in the beaker cell (d).

Kim *et al.*[75] conducted an experiment, where they fully sodiated an HOPG chip in a 1 M $NaPF_6$ in G_2 electrolyte, which led to a volume expansion, allowing to determine the staging number x of the Na-GICs from the Miller indices l. They found that upon full sodiation, the Miller index l = 3 corresponds to a staging number x = 1 for the G_1, G_2 and G_4 electrolyte. Moreover, they concluded that a Miller index of l = 4 must correspond to a stage 2 Na-GIC. A similar experiment was conducted in this thesis for the G_3 electrolyte, shown in Figure 73, where the open facets of the HOPG sample (initial thickness: 0.8 mm) were brought into contact with metallic Na. After addition of the 1 M $NaClO_4$ in G_3 electrolyte, the HOPG starts to swell up until it reaches a thickness of 2.4 mm after around 20 minutes, which is considerably longer than in the case of Kim, where the HOPG sodiation was completed after around 3 minutes, being a hint for a slower Na^+-diffusion rate in the graphite lattice in G_3.

Fully sodiated with $Na^+(G_3)$-complexes, the interlayer spacing of the graphene layers in the graphite amounts to 11.59 Å, while the empty graphite has an interlayer spacing of 3.35 Å. Following Kim´s argumentation, one would expect a volume expansion by a factor of 11.59 Å / 3.35 Å = 3.46 for a stage 1 Na-GIC. For a stage 2 Na-GIC, the lattice constant, which is then the sum of the interlayer spacing for one intercalated and one un-intercalated layer, is expected to expand by 11.59 Å / (3.35 + 3.35) Å = 1.73, if it is assumed that the empty graphite layers maintain their original thickness. The experimentally observed volume expansion of the HOPG chip from 0.8 mm to 2.4 mm correlates to a factor of 3, being pretty close to the theoretical value expected for a stage 1 Na-GIC. Thus, it can be concluded that also in the G_3-electrolyte, graphite forms a stage 1 Na-GIC upon full sodiation (l = 3) and an intermediate stage 2 Na-GIC with l = 4.

Another interesting question, which can be answered with this experiment is the number of G_3-molecules coordinating the Na^+ upon intercalation. The original HOPG sample had a weight of 0.1865 g, which after sodiation amounts to 0.2912 g. Thus, the weight increased by a factor of 1.56. The molar weight of the fully sodiated stage 1 $Na(G_3)_1C_{30}$-compound amounts to 561.55 g mol^{-1}, whereas the empty C_{30}-compound has a molar weight of 360.11 g mol^{-1}, being equivalent to a weight increase by a factor of 1.56. Consequently, one can conclude that the Na-ions are coordinated by one G_3-molecule when intercalating into the graphite.

Thus, the intermediate phase is a ternary stage 2 Na-GIC with a layer of doubly stacked $Na^+(G_x)_y$-complexes sandwiched between two graphene sheets, *i.e.* two Na-layers in between two graphene layers, going over into a stage 1 Na-GIC upon full sodiation.[75] Additionally, a phase transition from a stage 3 via a stage 2 Na-GIC is observed. In a classical staging model (Figure 74 (a)) every second graphite interlayer is occupied by an intercalated species in a stage 2 GIC, while in a stage 3 GIC every third graphene layer is occupied. Such a model fails to describe the transition from stage 3 to stage 2, since this would require a perpendicular diffusion through the graphene layers of the $Na^+(G_x)_y$-complexes, which, considering the small diameter of the carbon-honeycomb (2.84 Å),[344] does not seem realistic. The Daumas-Herold[345] staging mechanism, as presented in Figure 74 (b), instead, can explain a transition from a stage 3 to a stage 2 GIC, by a continuous filling of the graphene layers with intercalated species.

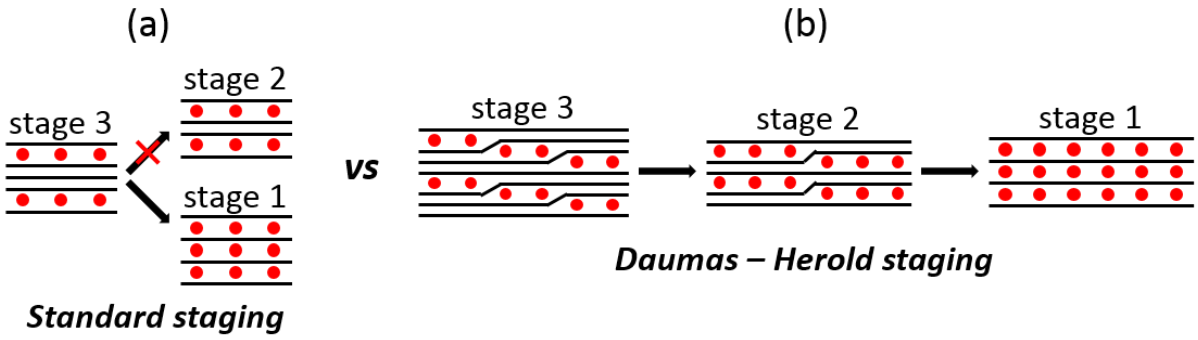

Figure 74: Comparison of the classical staging model (a) and the Daumas-Herold[345] staging (b).

Also with respect to the beginning of intercalation into the still empty graphite, where the ions arbitrarily intercalate into a random layer, since all graphene layers should be equally prone to host ions, this mechanism appears more plausible. It is believed that intercalation starts at a random site. Mechanical swelling and electrostatic interactions, however, result in an energetically favorable filling of the lattice and the formation of stage 2 domains according to the Daumas-Herold model. In the Daumas-Herold model, Na-ions intercalate into an arbitrary graphite layer and migrate into the bulk of the electrode. Additionally inserted ions push further the previously intercalated ions from another layer until domains of a certain staging are formed. A NaC_{48} stoichiometry can be approximated from electrochemical data. For a stage 2 Na-GIC, this corresponds to one Na-ion for 24 C-atoms in the adjacent graphene layer or rather the Na_2C_{48} for a double stacked Na-GIC. Considering the size of the solvated Na-ions and the graphite honeycomb units, further Na insertion into a single graphene layer is not possible. Therefore, further intercalation is connected to a major phase transition, resulting in the large reduction peak in the voltammograms and the dQ/dV-plots. Here, the stage 1 Na-GIC is formed at the expense of the intermediate stage 2 phase, both being present in parallel, until the phase transformation is complete.

STM can directly visualize the phase transitions of the graphite lattice. Above (section 5.2), the appearance of horizontal (Figure 49 (b)), respectively vertical lines (Figure 50) was mentioned. As was shown, these lines occur in a potential range, where phase transitions are observed, *i.e.* the graphite lattice expands as a result of the inserted $Na^+(G_x)_y$-complexes. These complexes diffuse into the bulk of the electrode when sodiating the electrode. Since in STM the tip scans over the surface in a line by line raster, STM images are not snapshots of the surface, but rather a steady capture of the dynamic electrode. Thus, the horizontal lines observed in Figure 49 (b), for instance, are the direct visualization of the graphite lattice expansion as a result of the insertion of the $Na^+(G_3)_1$-complex. This lattice expansion is propagating with time, while the rate of propagation is directly linked to the diffusion rate of these complexes inside the graphite layers.

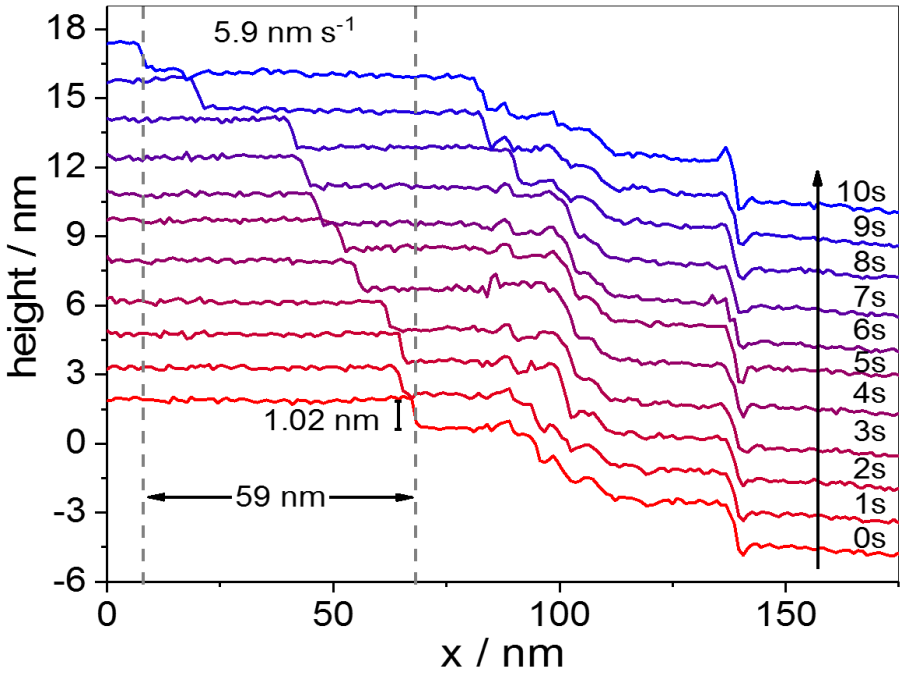

Figure 75: Temporal propagation of the graphite lattice expansion measured along the height profile highlighted by the blue line in Figure 50 (b).

This can nicely be demonstrated with the aid of Figure 50 (b), where a height profile was measured along the blue line in the range of phase transitions. This height profile is then shifted pixel by pixel, which corresponds to a time difference of 1 s. Plotting a series of such height profiles along such a phase transition, one obtains a graph as shown in Figure 75. Here, the disappearance of a 1.02 nm expansion, caused from a de-intercalation phase transition, can be followed with time. It propagates 59 nm in 10 s, which is equivalent to a diffusion rate of 5.9 nm s^{-1}. Such an analysis was done for numerous phase transitions, also for data not shown here, which gives an average diffusion rate of (5.9 ± 1.2) nm s^{-1}. A similar analysis can also be made with the G_4 experiments (Figure 51 and Figure 52), where the phase transitions, however, are not as clearly separated as in the G_3-system. Doing so, one obtains a $Na^+(G_4)_1$-diffusion rate of (22.1 ± 5.5) nm s^{-1}. The decreased diffusion rate of the $Na^+(G_3)_1$-complexes in the graphite lattice can also explain the prolonged time necessary to sodiate the HOPG in the G_3-electrolyte in comparison to the observations made by Kim *et al.* in the G_2-electrolyte.[75]

The question arises, why the diffusion rate of the $Na^+(G_4)_1$-complex is so much higher than that of the $Na^+(G_3)_1$-complex. According to literature, the solvation shell of the Na-ions is determined by the favorable oxygen coordination by the glyme molecules, which is in the range from 4 to 7 for an alkali ion in glyme solution.[346–350] The resulting complexes are a $Na^+(G_1)_3$-, a $Na^+(G_2)_2$- and a $Na^+(G_4)_1$-complex. The $Na^+(G_3)_1$-complex has a coordination number of 4 and is slightly under-coordinated, whereas the $Na^+(G_3)_2$-complex with a coordination number of 8 is over-coordinated. A simple evaporation experiment of each electrolyte, which removed the unbound glyme molecules by vacuum, and the experiment with the sodiated HOPG clearly suggest a $Na^+(G_3)_1$-complex. In principle, one can also think of a $Na^+(G_3)_2$-complex, which however is not consistent with the presented experimental evidence. Such a $Na^+(G_3)_2$-complex would be very bulky and could reach its favored coordination number by only coordinating to six oxygen atoms. This would result in a dangling tail of the glyme molecule, in turn increasing the van-der-Waals interaction between the $Na^+(G_3)_2$-complex and the graphite lattice. Such a steric hindrance, as suggested by Jache *et al.*,[167] can, however, be ruled

out, since the more probable geometry is the $Na^+(G_3)_1$-complex. A better explanation for the sluggish diffusion of the $Na^+(G_3)_1$-complex is its under-coordination, affecting the interaction between $Na^+(G_3)_1$--complex and graphite lattice. For a proper solid state diffusion, the balance between covalent and ionic bonding between the graphite lattice and the $Na^+(G_3)_1$-complex must be correct.[342]

Having understood the origin of the horizontal/vertical line features appearing in the STM images, one can also interpret them easier. The lines occurring in the G_3-systems are much clearer and well separated compared to the G_4-system, where many phase transitions occur in parallel, overlapping each other. Taking a close look at each phase transition, especially when measuring height profiles, one discovers some systematics in Figure 51. At potentials above the intercalation regime, the surface shows all typical HOPG features. Entering the intercalation potential range, phase transitions occur, which all are accompanied by a lattice expansion. This observation can be made for all phase transitions occurring until de-intercalation starts in the bluely framed image. The transition between intercalation and de-intercalation occurs close to the time (potential), where the bright horizontal line in the lower third of that image appears. All phase transitions happening before this point are caused by intercalation, *i.e.* they are lattice expansions, whereas afterwards they are lattice contractions. Thus, even though the images at first sight look disturbed, they contain a lot of valuable information, for instance about diffusion rates or the graphite lattice expansion of monoatomic steps.

The 3D-images in Figure 48 and Figure 51 also show an SEI-formation caused by the reduction of the glyme solvents, leading to the observed film precipitation at low electrode potentials. The SEI-film in Figure 48 remains on the surface when the potential cycle is done, speaking for the irreversible character of the SEI-formation. In Figure 51 this is not the case. Here, the surface film disappears with time. Contrary to the case in Figure 48, there is almost no drift of the tip over the surface in that measurement. Thus, the tip always scans the exact same area of the surface, and with time sweeps away the SEI, which probably is the reason for the SEI-disappearance in this case. A similar SEI-film on graphite electrodes in a G_4-electrolyte was recently studied with a synchrotron XPS by Maibach *et al.*,[174] who found a 3 nm to 8 nm thick SEI-film mainly composed of hydrocarbons and Na-salt decomposition products.

Hints for an SEI-formation can also be found in the EQCM data in Figure 53. The fact that the resonance frequency as well as the damping of the EQCM signal does not return to their original value indicate an irreversible change of the electrode-electrolyte interface. This can be viscosity changes of the electrolyte, roughness changes of the sample surface or the precipitation of a surface film, such as the SEI.

The more interesting part of the EQCM data is the frequency Δf and damping changes Δw coinciding with the intercalation/de-intercalation peaks (Figure 53 (b)). As mentioned above, the term EQCM should be handled with care, since this technique is far from being a mass sensor, especially when the electrode surface is not an acoustically thin, homogenous and rigid film.[313, 315, 319] The more accurate terminology is, as was proposed by Daikhin *et al.*,[177] *in-situ* hydrodynamic spectroscopy. According to equations (70) and (71), a simultaneous analysis of the resonance frequency f and the damping w of the quartz oscillator provides a tool to study structural changes of a porous electrode in a similar manner as other techniques, like XRD for instance.

In the present case, where the electrode is coated with an inhomogeneous layer of porous, thick particles, immersed into an electrolyte, the system is far from the ideal Sauerbrey conditions. If one treated the first de-intercalation peak in Figure 53 (b) with the purely gravimetric Sauerbrey model, one would obtain a frequency change of 500 Hz from the expected mass decrease estimated by the electric charge of the CV-peak. In fact, a 2 kHz frequency shift is detected.

Thus, more advanced models, such as the Daikhin model[177, 319] must be applied. This model takes viscoelastic effects and morphological parameters of the particles on the quartz, like particle size, roughness and porosity, into account. On the other hand, this model requires semi-spherical, homogenously distributed particles with a sharp size distribution. These requirements can hardly be met, which is why Daikhin´s model is only applied qualitatively here. A close look to equations (70) and (71) reveals that under otherwise identical conditions, an increase of particle size r results in a lowering of Δf and an increase of Δw (Figure 30).

Hence, the decrease of frequency during the negative scan in Figure 53 (a) can be explained by the growth of graphite particles, when inserting the $Na^+(G_3)_1$-complexes, which also leads to the expected increase of the damping Δw. Below 0.3 V Δf remains constant, since here, the electrode is probably fully sodiated and the particle size no longer changes. Until the de-sodiation peaks are reached, Δf and Δw remain constant, and with the onset of de-intercalation the previous processes are reversed.

Daikhin´s model can be nicely discussed for the example of the de-sodiation peaks in Figure 53 (b). As is known from XRD, graphite undergoes a phase transition from a stage 1 to a stage 2 GIC, being associated with a considerable particle shrinkage. The larger step of Δf towards less negative values and of Δw (less positive) in fact is fully consistent with the predictions from this model. Other than by XRD, however, the subsequent smaller de-intercalation peaks can be resolved by EQCM, while the change in Δf roughly scales with the amount of electric charge involved. In the purely gravimetric Sauerbrey-model, the change in Δf would also be expected, since it is directly connected to a mass change of the electrode layer. Even though no quantitative analysis can be done here, the stepwise change of the EQCM-signals might be explained by the stepwise change in particle size when they undergo transitions from the stage 2 to higher stage compounds in the regime of the later de-intercalation peaks. A quantitative analysis requires further experimental studies with optimized coatings and model refinements. Nevertheless, it is remarkable, how well the EQCM responds to structural changes in the graphite particles in this system. *In-operando* XRD cannot resolve the phase transitions of the higher staging GICs.

It is worth mentioning that researchers have been seeking for possibilities to apply EQCM to battery research by decorating the quartz with electrode particles. In literature, a few examples can be found, where the SEI formation in LIBs,[145] the Li^+-intercalation into V_2O_5[351, 352] or the charging behavior of carbon cathodes in Li-S-batteries are studied.[353] The only reasonable frequency changes, which are in the same order of magnitude as in the present study, were observed in the study by Novák et al.,[145] while in all other studies frequency changes of only a few Hz upon charging/discharging are observed, which is more than doubtful to relate them to intercalation phenomena. Moreover, the herein presented experiment with the sodiation/de-sodiation of graphite in the G_3-electrolyte with its excellent correlation between EQCM signal and electrochemical phase transitions can be an ideal reference system to prove predictions of theoretical models and to close the gap between theory and experiment. This on the other hand requires to make use of particles, which are at least approximately semi-spherical, equally distributed on the quartz and homogenous in size distribution.

In summary of this section, the reversible intercalation/de-intercalation behavior of solvated Na-ions into graphite and the concomitant formation of ternary Na-GICs was studied by a variety of *in-operando* techniques. XRD, STM and EQCM complement each other and help to gain deeper understanding of the classical electrochemical measurements. Upon discharge in the glyme electrolytes, the graphite electrodes intercalate $Na^+(G_x)_y$-complexes, which results in a stage 2 Na-GIC (NaC_{48}) in all electrolytes. A full discharge forms a stage 1 Na-GIC with a stoichiometry of NaC_{18} for the G_1, G_2 and G_4 system, while a NaC_{30}-stoichiometry is reached for the G_3-electrolyte. The direct visualization of ion-intercalation phase transitions of a battery electrode is visualized by STM on an

atomic scale for the first time here. This technique provides a, so far unique, direct measure of local diffusion rates of intercalated species in an electrode host. When applied as *in-situ* hydrodynamic spectroscopy technique, EQCM can give additional information about the intercalation mechanism, which cannot be resolved so well by other techniques, such as XRD. In total, one can say that a valuable understanding of the, until recently still as impossible believed Na-intercalation into graphite is gained, which is the basis for the further development of the NIB technology.

6.3 Morphological effect of V_2O_5 cathodes in NIBs

The electrochemical phase transitions of a V_2O_5 positive electrode operated in a NIB are systematically studied in Figure 58. Discharging the electrode to 1.5 V results in a sodiation of the pristine layered orthorhombic α-V_2O_5 (*Pmmn* space group)[287] with an interlayer spacing of 4.4 Å[229, 354] to the α'-NaV_2O_5 phase (*Pmmn* space group).[287] From the electric charge inserted during this phase transition and its irreversible character, the following irreversible reaction is suggested:

$$V_2O_5 + Na^+ + e^- \rightarrow NaV_2O_5 \quad (72)$$

The α'-NaV_2O_5 has a slightly increased interlayer distance with 4.8 Å.[229, 354] The *ex-situ* STM experiment in Figure 59 also shows a slight increase of the interlayer spacing (Figure 60 (b)) after having passed the first cathodic reduction peak in the CV. An exact quantification of the lattice expansion, however, is difficult, since, due to the large level of noise, there is a relatively large uncertainty connected to the STM data. The irreversible character of this phase transition is also confirmed by STM, because no change of the interlayer spacing is observed, when the potential of the V_2O_5 single crystal is increased to 4 V again (Figure 60 (c)).

Exposing the NaV_2O_5 to an even lower potential, *i.e.* to 1.0 V for the powder electrode (Figure 58 (b)) and to 0.05 V for the single crystal (Figure 59), a second Na-ion is inserted into the electrode:

$$NaV_2O_5 + Na^+ + e^- \rightleftharpoons Na_2V_2O_5 \quad (73)$$

This phase transition now is reversible, as the cathodic reduction peaks in the CV are accompanied by anodic peaks. The theoretical capacity of $Na_2V_2O_5$ is 235.2 mAh g^{-1}, which is almost reached during the first discharge of the commercial V_2O_5 micro grains (Table 1). According to literature, the $Na_2V_2O_5$ crystal has a bilayered structure with a lattice parameter of 16.1 Å.[227] This is in agreement with the observations made by STM (Figure 60 (d)), where an increase of the step heights is observed, underlying a strong scattering though. The reversible character of this phase transition also shows up in STM, where the de-sodiation of the $Na_2V_2O_5$ to the NaV_2O_5 results in a shrinkage of the lattice back to the previously observed value for the NaV_2O_5 (Figure 60 (e)).

A deep discharge to 0.01 V for the powder electrode (Figure 58 (c)) is believed to be connected to the insertion of a third Na-ion:

$$Na_2V_2O_5 + Na^+ + e^- \rightleftharpoons Na_3V_2O_5 \quad (74)$$

The experimentally observed difference of the $Na_{2.6}V_2O_5$ stoichiometry to the suggested $Na_3V_2O_5$ structure can be explained by the fact that the inserted charge in this case was obtained from the CV peak and not as in the other cases from the voltage profiles of the first discharge curve, which usually is the more accurate method. The $Na_3V_2O_5$ stoichiometry was also found by others, for instance Moretti *et al.*[231], who used a V_2O_5-aerogel negative electrode. The cathodic reduction peak connected to this phase transition only occurs in the first cycle (Figure 58 (c)) and thereafter the CV becomes smooth and featureless with an increased current difference between positive and negative scan. According to Moretti´s study,[231, 32] the insertion of a third Na-ion into the electrode results in an irreversible crystal structure formation with a destroyed long-range order.

With the knowledge about the electrochemical phase transitions caused by the insertion of Na-ions into the V_2O_5 lattice, one can discuss the effect of electrode morphology on the battery performance. The two best performing materials are the nano-structured V_2O_5 nanobundles and the V_2O_5-TiO_2 nanobundles, where especially the V_2O_5 nanobundles showed an outstanding performance. This concerns the much higher energy densities, energy efficiencies and operating voltages of those materials compared to the other V_2O_5 electrodes, coupled to a much depressed capacity fading and prolonged lifetime plus a better response to high current rates.

Discharging the V_2O_5 nanobundles and the V_2O_5-TiO_2 nanobundles for the first time, does not, in contrast to most other materials, result in an irreversible capacity loss, meaning that the intercalation mechanism discussed in equations (72) to (74) as observed for the highly crystalline commercial V_2O_5 micro grains must be different. From the electric charge inserted into the V_2O_5 nanobundles more than one Na-ion is reversibly intercalated/de-intercalated, namely $Na_{1.42}V_2O_5$. This might result from an increased defect density of the nano-sized needles and an increased degree of amorphization. Another factor contributing might be the fluoride traces from the synthesis procedure.

The different shape of the dQ/dV-plots (Figure 61 and Figure 62) of both materials reminds of a capacitive double layer charging, which from an estimation of pure non-faradaic currents can be ruled out, since this would yield much smaller capacities than those observed here. Hence, the charge/discharge capacities of the V_2O_5 nanobundles and the V_2O_5-TiO_2 nanobundles result from faradaic processes and are not simply a consequence of a capacitive charging due to the increased surface area.

The increased operating voltage of the nanomaterials is remarkable. Moreover, when taking a look at the dQ/dV-plots of the first three cycles of the 'highly' crystalline materials (Figure 61), one sees a peak shift of the reversible peaks to more positive potentials each cycle. Intercalating ions such as Na^+ or K^+ leads to an amorphization of the vanadium-oxide lattice, decreasing the electrode lifetime.[355] A greenish discoloration of the glass fiber separators found after cell disassembly (*post mortem*) is another indication of an amorphization and loss of structural integrity of the V_2O_5 particles upon continuous sodiation/de-sodiation. Thus, the increased voltage of the amorphous nanomaterials and the voltage increase concomitant to the particle amorphization during cycling indicate a relation between operating voltage and grade of amorphization, where Na-ions can intercalate/de-intercalate at more positive potential for more amorphous materials. A reason for this might be the increased number of surface defects, offering more and energetically different intercalation sites. Additionally, the intercalation sites of the nanostructured materials are all 'near surface' and the increased number of defects might lead to energetic deviations from the ideal crystalline structure, which both can thermodynamically facilitate the Na-ion insertion/de-insertion and increase the operating voltage.

The observed capacity drop and the increased voltage difference between oxidation and reduction at higher current rates are influenced by the electronic resistance of the electrode layer, the charge transfer resistance and the Na-ion diffusion within the electrode material. In order to reach their intercalation sites, Na-ions have to diffuse through the electrode material, which can limit the applicable charge/discharge rates. In nanomaterials, the surface to bulk ratio is increased, decreasing the diffusion length and minimizing the diffusion limitation. Moreover, the contact of the V_2O_5 nanomaterials to the conductive carbon is increased compared to micro materials, reducing the electronic resistance, also favoring the rate capability and lowering the voltage differences between oxidation and reduction. Also for other electrode materials with poor electronic conductivity, for instance the polyanionic compound $Na_3V_2(PO_4)_3$, nano-structuring helps to increase the electronic contact to the conductive carbon.[29, 356]

The prolonged lifetime of the nanomaterials is strongly increased compared to more crystalline materials, where the capacity fading might be related to an amorphization of the V_2O_5 particles and loss of electric contact of the active material. Also in LIBs, V_2O_5 electrodes suffer from similar problems. Here, a common strategy to increase the stability and battery lifetime is to blend the V_2O_5 with small amounts of TiO_2.[357–362] Different stabilizing effects are debated in literature, where Davies *et al.*[357] suggested a mechanism based on the preferential reduction of Ti^{4+} compared to V^{5+}, preventing a reorganization of the V_2O_5 microstructure. Another mechanism proposed is a change of the lattice structure and interaction force between two adjacent vanadium-oxide layers by adding TiO_2.[358] A third possibility discussed is the prevention of V_2O_5 particle detachment into the electrolyte by embedding them into a TiO_2 matrix.[360, 361] In the present study, the stabilizing principle of the V_2O_5 electrodes with TiO_2 against degradation was transferred to a NIB. XRD data of the V_2O_5-TiO_2 nanobundles only shows very weak peaks, probably due to the high grade of amorphization. The 531.3 eV binding energy of the O1s XPS-peak is also close to the typical value (529.4 eV to 531.2 eV) known for TiO_2.[363] Thus, XRD and XPS data suggest a homogeneous mixture of V_2O_5 and TiO_2 rather than an integration of the latter into the V_2O_5 lattice, ruling out the stabilization mechanism with an increased interaction force between two adjacent V_2O_5 layers.

The V_2O_5-TiO_2 nanobundles show the weakest performance loss of all materials (Figure 63 and Table 1), closely followed by the pure V_2O_5 nanobundles. In fact, the energy density as well as the capacity of the V_2O_5-TiO_2 nanobundles are significantly smaller than for the pure V_2O_5 nanobundles. This on the other hand means that the V_2O_5 amorphization indeed is a plausible degradation mechanism, since compared to highly crystalline materials, the 'amorphous' nanomaterials degrade much less, because they are already amorphous from the beginning. Similar observations were also made by Uchaker *et al.*[230] Thus, due to a reduced loss of electric contact of the V_2O_5 with the conductive carbon and current collector, an amorphous morphology of the V_2O_5 electrode is beneficial compared to highly crystalline V_2O_5 materials with regard to the cycling stability.

The lower capacity and energy density of the V_2O_5-TiO_2 nanobundles compared to the pure V_2O_5 nanobundles amounts to 12 %, respectively 16 %, while the weight contribution of TiO_2 to the active material with 10 % is similarly high. Thus, it seems that all the TiO_2 is electrochemically inactive and only lowers the specific capacity and energy density accordingly.

In conclusion, one can say that the V_2O_5 nanobundles outperform all other materials in battery performance. As such, they possess a practical capacity (100^{th} cycle) of 85 mAh g^{-1} with a 83 % capacity retention after 100 cycles, an energy density of 266.5 mWh g^{-1}, a 2.4 V discharge voltage with 98 % coulombic and 77.2 % energy efficiency. Moreover, it was found that the grade of amorphization is the key parameter determining the battery performance: amorphous V_2O_5 degrades much less compared to highly crystalline materials, has a better contact to the conductive carbon lowering voltage losses and has decreased diffusion paths being beneficial at high current rates.

6.4 Graphite | V_2O_5 full cell

The superior performance of the graphite electrode in the G_4-electrolyte motivated the choice of this electrolyte for the full cell studies. Moreover, the influence of the electrolyte solvent on the Na-intercalation electrochemistry with V_2O_5 was minor (Figure 67). Thinking about the graphite electrochemistry, huge differences were observed between carbonate and glyme electrolytes. In carbonate electrolytes, the Na-ions would need to strip off their solvation shell before intercalating into the graphite, contrary to the glyme electrolytes, where the Na-ions co-intercalate together with their solvation shell. Since no big difference of the intercalation behavior of Na-ions into V_2O_5 between the classical carbonate based electrolytes to the glyme solvents is observed, a solvent independent

intercalation mechanism can be assumed and thus, it can be concluded that also in glyme electrolytes, the Na-ions lose their solvation shell before intercalating into the V_2O_5 lattice. The minor differences observed between the different solvents mainly concern the high voltage regime of the G_1- and G_2-CVs (Figure 67 (c) and (d)). In both cases an oxidative current is found above 3.8 V, which probably can be linked to an SEI-formation since the G_1 and G_2 are oxidized.

The irreversible capacity observed during the first discharge (sodiation) of a graphite electrode in Figure 65 is caused by an SEI-formation, also showing up in the increased differential capacity in the dQ/dV-plot of the first cycle.[174] This SEI-formation is also responsible for the irreversible capacity loss of the graphite | V_2O_5 full cell when charging it the first time (Figure 68 (a)), since then the negative graphite electrode is sodiated, going along with an electrolyte reduction.

The dQ/dV-plot (Figure 68 (b)) is not straightforward to interpret, since its negative sweep is a superposition of the negative sweep of the V_2O_5 electrode and the positive sweep of the graphite electrode. The positive sweep of the dQ/dV-plot on the other hand is a superposition of the positive V_2O_5 electrode sweep and the negative graphite sweep. Moreover, the voltage cannot be related to a reference potential, since the full cell was operated in a two-electrode configuration and no Na-RE was used. The increased differential capacity of the first charge, however, can be ascribed to the SEI-formation on the graphite electrode.

For further information, one can try to reconstruct the charge/discharge behavior of the full cell (Figure 68) from two separate half-cell studies, a Na-graphite (MCMB) and a Na-V_2O_5 (nanobundles) half-cell. Figure 76 (a) for example shows the discharge curve of the V_2O_5 electrode (sodiation) and the charge curve of the graphite electrode (de-sodiation), as it happens during discharge in a graphite | V_2O_5 full cell. At the intersection of both curves, the expected cell voltage of the full battery is zero. Reversing both processes would correspond to the full cell charging (Figure 76 (b)). Both electrodes had an approximate reversible capacity of 90 mAh g^{-1} and were cycled at 50 mA g^{-1}. From the voltage differences of both charge/discharge profiles in Figure 76 (a) and (b) the voltage profile in (c) can be calculated, which is the theoretically expected charge/discharge behavior of a full cell computed from two half-cell experiments. This curve qualitatively resembles the voltage profile of the real full cell in Figure 68 (a). Figure 76 (d) shows the corresponding dQ/dV-plot.

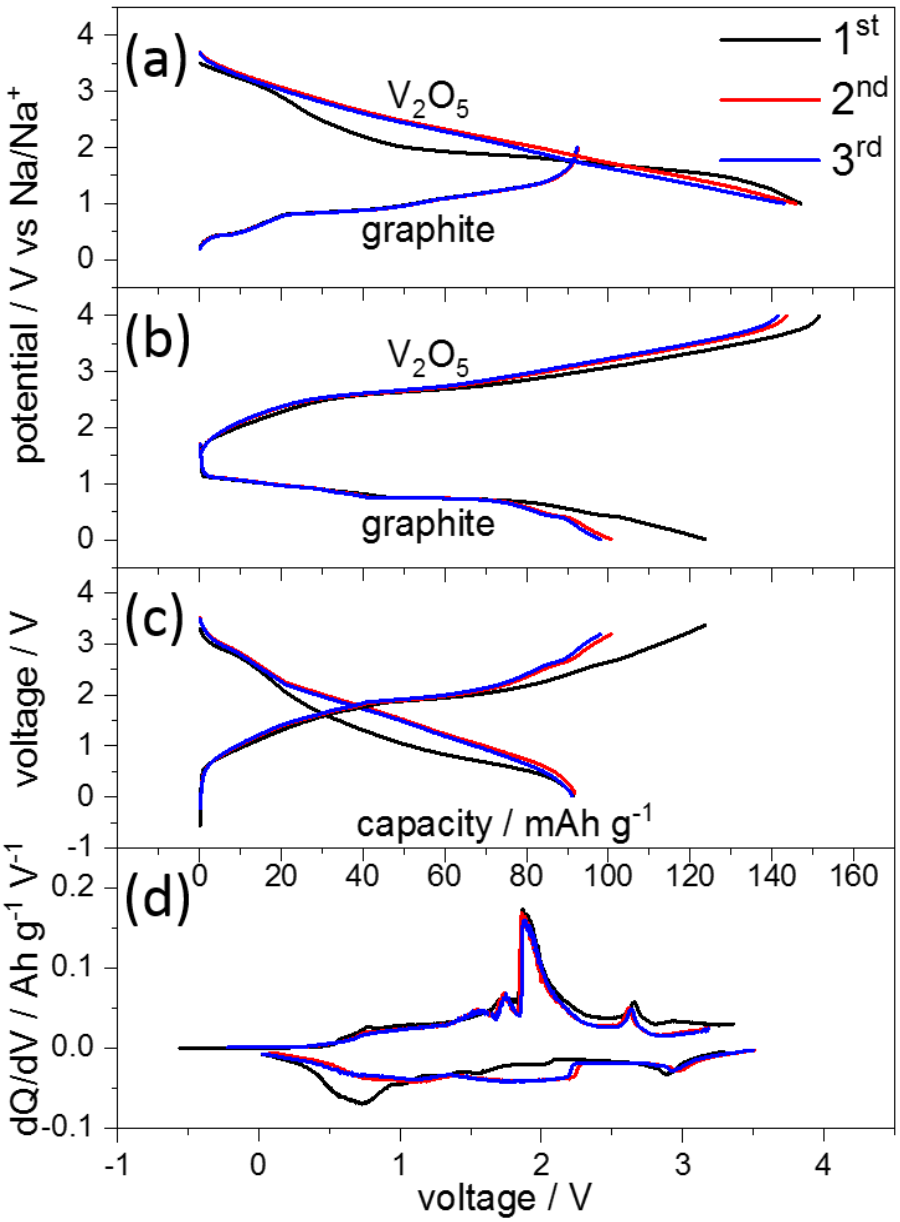

Figure 76: In order to understand the phase transitions observed in the charge/discharge experiment with the graphite | V_2O_5 full cell presented in Figure 68 (a), one has to consider each half-cell reaction separately. Upon discharge of the full cell the V_2O_5 positive electrode (nanobundles) is sodiated (discharged) and the graphite negative electrode (MCMB) is de-sodiated (charged) (a). Both processes are reversed when charging the full cell (b). From the voltage difference between both curves in (a) and (b), one obtains the charge/discharge profiles 'predicted' for the graphite | V_2O_5 full cell from pure half-cell studies (c). These voltage profiles finally result in the dQ/dV-plots shown in (d), which can be compared to the experimentally measured dQ/dV-plot of the real full cell in Figure 68 (b). Both half-cell studies shown here were measured with a graphite and a V_2O_5 electrode (both with ca. 90 mAh g^{-1} reversible capacity) at 50 mA g^{-1} in 1 M $NaClO_4$ in G_4 with a Na counter electrode.

Now, the above introduced peak nomenclature comes into play: each peak in Figure 77 (a) and (b) is uniquely labelled and numbered for the graphite, respectively V_2O_5 electrode. From the peak potentials of the two half-cells (Figure 77 (a) and (b)), each peak of the pure materials can be ascribed to a peak in the dQ/dV-plot of the computed full cell (black curve in Figure 77 (c)). Overlaying the computed dQ/dV-plot with the experimentally measured curve of the full cell (grey), certain

similarities become obvious. Both curves for instance show a large positive peak surrounded by different smaller peaks and several similar looking negative peaks. The computed curve on the other hand shows sharper and more separated peaks than the dQ/dV-plot of the real full cell. Moreover, the negative peaks of the real cell are shifted to more negative voltages and the positive peaks to more positive values compared to the predicted values. This might have different reasons, for instance the initially unbalanced electrodes in the full cell. The electrodes were chosen such that the capacities of the graphite and the V_2O_5 electrode match after prolonged cycling. Hence, the observed voltage shift can be explained by the fact that the V_2O_5 electrode is only partially sodiated/de-sodiated during the first cycles, as it has a much larger capacity than the graphite electrode. From the peak-assignment in Figure 77 (c), one also sees that most of the peaks observed in the dQ/dV-plot of the full cell mainly originate from phase transitions of the graphite electrode, while the vanadium oxide rather contributes to the constant background in differential capacity.

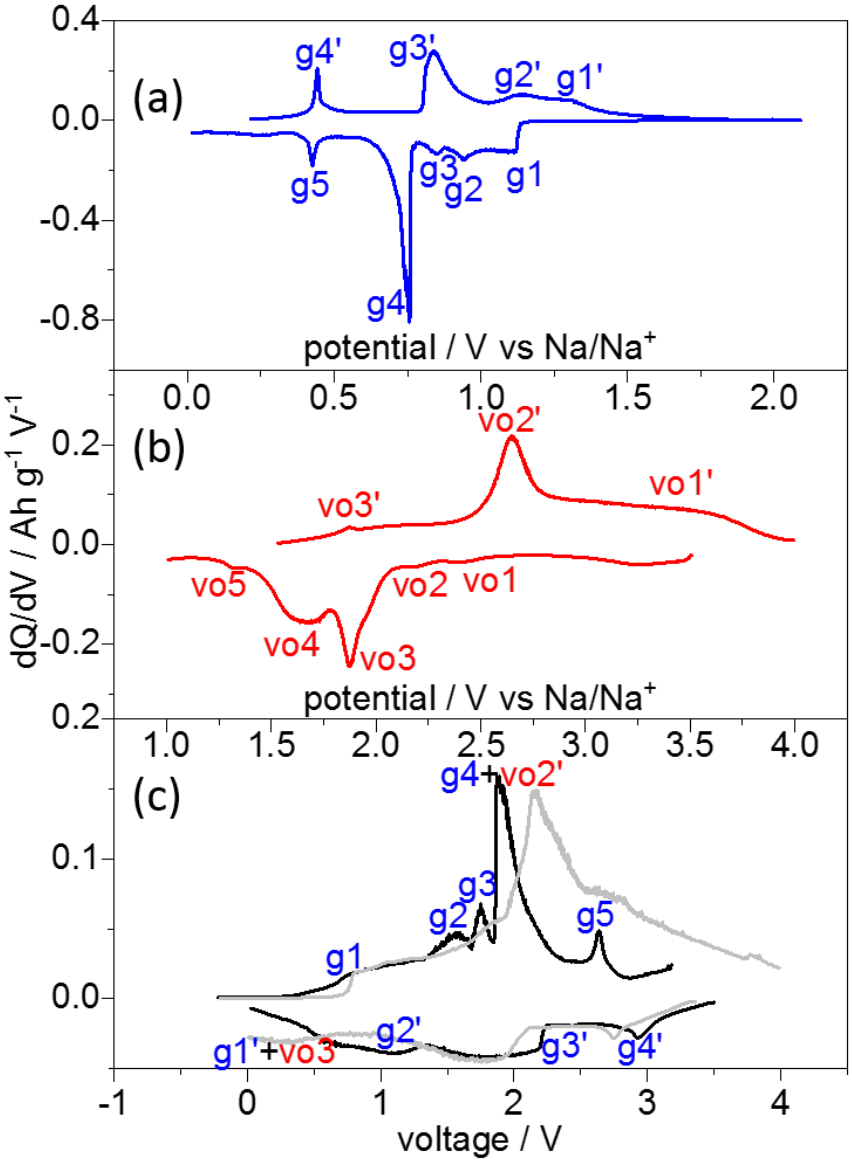

Figure 77: dQ/dV-plots of a graphite (MCMB) (a) and a V_2O_5 (nanobundles) electrode (b) of a half-cell as well as a comparison of the theoretically expected full cell dQ/dV-plot (black) determined in Figure 76 (d) to the measured curve (grey) from Figure 68 (b). All experiments were measured at a rate of 50 mA g^{-1} in 1 M $NaClO_4$ in G_4.

Analyzing the battery capacity (Figure 69 (a)), one sees that the initial capacity is close to 90 mAh g^{-1}, which is a typical value for the graphite electrode. When assembling the battery, the graphite and V_2O_5 electrodes were chosen such that both electrodes have the same capacity after having surpassed the initial capacity drop of the V_2O_5 electrode. Thus, in the beginning of cycling the full cell, the cell capacity is limited by the capacity of the graphite electrode. At the same time, one observes a decrease in capacity, which, however, is much weaker than when cycling V_2O_5 in a full cell. The reason for this might be that the V_2O_5 electrode in the full cell is only partially charged/discharged, which limits the V_2O_5 degradation. In addition, the irreversible first cycle V_2O_5 capacity loss has already been dealt with when sodiating the V_2O_5 electrode before putting it into the full cell.

For energy storage, the energy density and the energy efficiency are of interest (Figure 69 (b)). Here, one has to pay a huge energy penalty between charging and discharging this battery, which is reflected by the energy efficiency. In the present case, the energy efficiency is slightly larger than 50 %, which is lower than for other (commercial) electrochemical energy storage devices like LIBs (ca. 90%),[5, 6] lead-acid batteries (70 % - 90 %),[5, 6, 364] Ni-Cd batteries (60 % - 70 %),[5] Na-S batteries (75 % - 85 %),[6, 364] vanadium redox flow batteries (60 % - 90 %)[5, 6] or supercapacitors (90 % - 95 %).[5, 6] Fuel cells have a relatively low round trip efficiency of 20 % to 50 %,[5, 6] since the hydrogen production through electrolysis with < 60 % is relatively inefficient.[5, 6] Other technologies with high energy efficiency are mechanical flywheels (> 90 %)[5, 6] and superconducting magnetic energy storage devices (> 90 %).[5, 6] Pumped hydro power (60% - 90 %)[5, 6, 364] and compressed air (50 % - 90 %)[5, 6, 364] have intermediate energy efficiencies, whereas considerable energy losses occur for thermal energy storage devices (30 % - 60 %).[5, 6] Considering the total weight of active material, the obtained energy density of the graphite | V_2O_5 cell amounts to 49.2 mWh g^{-1}. An energy density of 60 mWh g^{-1} was reported for a graphite | P2-$Na_{0.7}CoO_2$ cell[170] and 120 mWh g^{-1} for a graphite | $Na_{1.5}VPO_{4.8}F_{0.7}$ cell.[169] The low energy efficiency and density of the graphite | V_2O_5 NIB originates from voltage losses mainly stemming from the V_2O_5 electrode (0.8 V, Figure 64 (b)) and less from the graphite (0.2 V, Figure 66 (c)), as already discussed in section 5.3.

6.5 General Discussion

Having discussed the SEI-formation, the $Na^+(G_x)_y$ co-intercalation, the $Na_xV_2O_5$ electrochemistry and the graphite | V_2O_5 full cell separately in the previous sections, correlations between the different aspects shall be discussed in the following. Moreover, the specialties of the advanced experimental techniques shall be compared here.

A process observed in all electrochemical systems studied in this thesis is the SEI-formation. The SEI can either be a consequence of an electrolyte reduction at the negative electrode or of an electrolyte oxidation at the positive electrode. SEI components at the positive electrode found in carbonate based electrolytes contain alkoxy species (RO), ethers (ROR), esters (ROOR), alkyl fluoroformates (ROCOF), carboxylic acids (RCOOR), lithium carbonates (Li_2CO_3), lithium alkyl carbonates ($ROCO_2Li$), fluorophosphates (PF_x), carboxylates (-COO-) and CO_2,[338–340] whereas the negative electrode SEI is a complicated multicomponent structure composed of inorganic compounds such as oxides, fluorides, phosphates and carbonates in vicinity to the electrode, and of more organic species like oligomers and polymers in farther distance to the electrode.[79, 116, 127–130]

Depending on the electrolyte solvent used, huge differences in the SEI-formation and the battery lifetime can be observed: while EC seems to be a good SEI-former, PC is fairly harmful for graphite electrodes, as a strongly enhanced propylene gas formation upon PC reduction delaminates graphene flakes, destroying the electrode. Often, electrolyte additives are used to improve the SEI properties, for example ethers such as linear glymes, which are beneficial because they inhibit detrimental side

reactions by chelating harmful species like LiF in LIBs.[365–367] That pure glyme electrolytes work well for LIBs and NIBs was demonstrated by Jache *et al*.[18] in 2014. The experiments conducted in this thesis also showed an SEI-formation on the graphite electrodes in all tested electrolytes: in LIBs with an EC/DMC electrolyte and in NIBs with an EC/DMC, EC/PC and G_x electrolyte. In all cases, the SEI-formation was a result of the electrolyte reduction resulting in a precipitation of a thin SEI layer on the graphite surface.

In direct comparison between the SEI-formation in a LIB and a NIB with an EC/DMC electrolyte, the SEI-formation follows similar mechanisms, as can be seen from the CVs in Figure 36 (b) and Figure 42 (a) after correcting the potential scales of the Li/Li^+ respectively Na/Na^+ reference electrodes. The SEI-formation in glyme based electrolytes is still subject of various research topics, such as for graphite electrodes in NIBs,[368] or the dendrite free reversible plating of different alkali metals for applications in metal-ion,[369] metal-air[370] or metal-sulfur batteries.[371] The SEI-formation on a graphite electrode with a glyme-based electrolyte in a NIB results in a very thin surface film of thicknesses in the range of 10 nm,[368] which is in the same range as observed in the STM studies (Figure 48 and Figure 51) and SEI-films in classical carbonate electrolytes (Figure 40). In all cases, *i.e.* for EC/DMC and G_x electrolytes, the SEI properties are beneficial for a proper operation as a reversible battery electrode.

Another commonality observed in the LIB and NIB electrochemistry of graphite electrodes is the co-intercalation of solvated Li- and Na-ions. When solvated $Li^+(EC)_y$ complexes intercalate into graphite, an interlayer spacing of roughly 5.0 Å versus a twice as thick interlayer spacing for the $Na^+(G_x)_y$ intercalation was found. Another difference between the co-intercalation of Li- and Na-ions is the fact that the Li-co-intercalation is irreversible in carbonate electrolytes, whereas for Na-ions in glyme electrolytes it is reversible. Both can be explained by the difference of the solvent, since the co-intercalation of $Li^+(G_x)_y$ and $Na^+(G_x)_y$ complexes is very similar and reversible in both cases.[18] One interesting observation of Jache´s *et al*.[18] results is that the electrode capacity of graphite upon lithiation reduces to ca. 100 mAh g^{-1} when switching the electrolyte solvent from EC/DMC (ca. 370 mAh g^{-1}) to a glyme-electrolyte, where the electrode capacity is the same for a LIB and a NIB. Thus, once one co-intercalated $Li^+(G_x)_y$ respectively $Na^+(G_x)_y$ complexes into the graphite, further intercalation of uncoordinated ions is prevented, even though only a third of the theoretical capacity of a graphite electrode in a LIB is reached. The lower capacities in G_x electrolytes might be explained by the bulky $Li^+(G_x)_y$ respectively $Na^+(G_x)_y$ complexes, which of course have a much larger volume compared to the naked ions.

Another question about the differences of the reversible co-intercalation in G_x electrolytes and the irreversible co-intercalation in EC/DMC electrolytes is, whether the capacity of the irreversible $Li^+(EC)_y$ complexes and of the reversible $Li^+(G_x)_y$ complexes is the same. And why is the co-intercalation of the $Li^+(EC)_y$ complexes irreversible and the co-intercalation of $Li^+(G_x)_y$ complexes reversible? In a LIB with a graphite electrode, the irreversible capacity loss during first discharge in an EC/DMC electrolyte is pretty close to the reversible co-intercalation capacity with a glyme electrolyte.[372] The answer to the question, why the $Li^+(EC)_y$ complexes are irreversibly trapped in the graphite after co-intercalation and the $Li^+(G_x)_y$ complexes are still accessible, might help to make the irreversible capacity loss of LIBs during the first lithiation of the graphite utilizable and to significantly increase the reversible electrode capacity.

The direct comparison of the SEI-formation and the co-intercalation in the EC/DMC and G_x electrolytes leads to couple of questions: Does the EC/DMC-SEI seal the graphite step edges for solvated ions and remain permeable for unsolvated ions, while the G_x-SEI permits a transport of solvated ions? Does this in turn mean that if one first formed an EC/DMC-SEI and then exchanged the electrolyte for a G_x-electrolyte, one would prevent any intercalation? Or in other words: Would an electrode with a G_x-SEI

operated in an EC/DMC electrolyte permit a reversible Li-ion intercalation without the irreversible capacity loss caused by the trapped ions in the electrode? The fact that coulombic efficiencies in G_x electrolytes are far above 99.9 % (Figure 66 (a)) after finalizing the SEI-formation indicates that once the G_x-SEI is formed, no further solvent is reduced. This is a clear indication that the G_x molecules are more stable against an electrochemical reduction on a graphite electrode compared to the carbonates.

It is also of interest to compare the Li- and the Na-ion diffusion behavior in graphite. From the PITT measurement in Figure 35 conducted on the Li intercalation/de-intercalation in a graphite electrode, potential dependent diffusion coefficients can be determined (Figure 70). At the same time, the STM experiments conducted on the $Na^+(G_x)_y$ co-intercalation into graphite (Figure 50) allowed to determine a mean diffusion rate of the $Na^+(G_x)_y$ complexes inside the graphite lattice, which within a 10 s time interval amounted to 5.9 nm s^{-1} for the $Na^+(G_3)_1$ complex and to 22.1 nm s^{-1} for the $Na^+(G_4)_1$ complex (Figure 75). Considering the ion diffusion inside the graphite as a random walk problem, the mean displacement in *x*-direction $\overline{x^2}$ of an ion after a certain time t is linked to its diffusion coefficient D according to:[47]

$$\overline{x^2} = 2Dt \tag{75}$$

From this equation a time dependent diffusion velocity or rate $v_D := \bar{x}/t$ can be determined, which is:

$$v_D = \sqrt{\frac{2D}{t}} \tag{76}$$

Thus, the diffusion rate of the $Na^+(G_x)_y$ complexes in the graphite can be - considering a constant diffusion rate within the 10 s time period - translated into a diffusion coefficient. For the $Na^+(G_3)_1$ complex one calculates a diffusion coefficient of 8.7 10^{-12} cm^2 s^{-1} and for the $Na^+(G_4)_1$ complex one obtains 1.2 10^{-10} cm^2 s^{-1} as a diffusion coefficient. This is in good agreement with the diffusion coefficients found for the Li-ions, which most of the time is in the range from 10^{-10} to 10^{-11} cm^2 s^{-1}. This comparison further underlines the scientific potential of *in-operando* STM, as it was used in the present studies.

Picking up on the different *in-operando* techniques used, one can say that each method brings about some advantages. XRD is an integral technique and allows to very precisely determine crystal structures and to follow their changes as one conducts electrochemical experiments. The XRD cell used in this study was a custom made cell specifically designed for battery applications, where the cell is sealed via a very thin (6 µm) Al-foil, which is transparent for the X-rays and allows to analyze the electrode under operating conditions without exposure to air, which is a major drawback of *ex-situ* XRD-studies mostly conducted in literature. The time resolution, however, is limited to several minutes. EQCM with the graphite coated quartzes is another integral technique to detect particle growth/shrinkage upon intercalation/de-intercalation and has a time resolution of a few seconds. The EQCM data presented in Figure 53 are the first ever published data showing a direct relation between EQCM signal and ion intercalation into a battery electrode material. At the same time, the resolution of this technique surpasses the XRD resolution, as it can clearly resolve each phase transition of the graphite lattice upon sodiation. This novel technique must still be further optimized and theoretical models must be refined in order to explore the full capabilities of this method. Compared to XRD and EQCM, STM is no integral technique. That is a major advantage in terms of quantifying topographical surface changes on an atomic level. Moreover, STM is an imaging method, permitting direct visualizations of surface changes, giving valuable local information about various surface processes.

Besides the quantification of lattice expansions, STM also allows to localize the intercalation sites, to visualize SEI-formation and to measure ion diffusion all at the same time within the same cell and under identical experimental conditions. A shortcoming of STM regarding the necessity of a conductive sample, thinking about the semi-conductive V_2O_5 electrodes, might be circumvented by using SECPM as a similar SPM technique. Here, only preliminary SECPM results were shown, which demonstrated an equal spatial resolution as in STM without being limited by the sample conductivity. Also here, further fundamental work is required to fully understand the method and to optimize it for applications, such as imaging battery processes on poorly conductive substrates.

7 Summary and Conclusions

To summarize, the development of a fully operating NIB is shown, ranging from fundamental studies via optimization studies of the electrolyte and electrode morphology to studies of a full cell, combining the knowledge gained before. The fundamental studies gave an atomistic understanding of the relevant processes, such as the formation of a solid electrolyte interphase and intercalation mechanisms of Li- and Na-ions into graphite as well as V_2O_5. Based on these studies, different battery components like the electrolyte and the electrode morphology were optimized and finally unified in a rechargeable graphite | V_2O_5 NIB.

Besides the battery studies, a multitude of advanced characterization techniques was applied and further developed. Here, two techniques shall be highlighted: STM, operated as *in-operando* technique and EQCM with graphite coated quartzes, also known as *in-situ* hydrodynamic spectroscopy. For the latter, an experimental proof of principle for application to battery materials and the corresponding theoretical model to understand the observed changes in damping and resonance frequency was given for the first time. The *in-operando* mode of STM allowed to conduct mechanistic studies on the atomic level (SEI-formation and intercalation processes) and to get insight into timescales of these processes and study kinetic parameters such as the ion diffusion inside the electrode lattice.

First, the formation mechanism of the SEI on a graphite electrode in a LIB was studied in section 5.1. The use of STM and its application as *in-operando* technique revealed different stages of SEI-formation, which could be related to different reduction steps of the solvent molecules, *i.e.* EC and DMC, which in an initial step of SEI-formation co-intercalate into the graphite electrode when being coordinated around the Li-ions. The linkage of Li-ions with the solvent molecules is related to the first reduction step, which initially is still reversible. The reversibility of this process was proven for the first time. Later, an irreversible destruction of the solvent molecules and the release of ethylene gas explain the irreversible charge consumed during the SEI-formation and the partial exfoliation of graphene sheets from the graphite electrode. Real time STM imaging also allows to gain insight into timescales of the SEI growth. It was found that the SEI growth is a self-limited process lasting around 200 s under the experimental conditions applied herein.

Following the principle of *in-operando* STM and using other *in-operando* techniques like XRD and EQCM, the SEI-formation was also partially studied on graphite electrodes in glyme-based electrolytes for NIBs. The main focus of section 5.2, however, was to understand the intercalation mechanism of solvated Na-ions into graphite. Until 2014, the intercalation of Na-ions into graphite was still believed to be impossible, as the formation of binary Na-GICs is energetically instable and the Na-ion diffusion in the graphite lattice is hampered, because the interaction force between a Na-ion and graphite lattice is too large. It was shown that this issue can be circumvented by reducing the Na^+-graphite interaction force when co-intercalating the Na-ions together with their solvation shell and forming ternary Na-GICs. Concretely, the intercalation mechanism of $Na^+(G_x)_y$-complexes was studied with

linear ethylene glycol dimethyl ether homologues G_x, with x+1 O-atoms and where $1 < x < 4$. STM allowed to image the phase transitions, which concurs with the electrochemistry and which allows to measure diffusion rates of the $Na^+(G_x)_y$-complexes inside the graphite lattice. For the $Na^+(G_3)_1$- and the $Na^+(G_4)_1$-complex a diffusion rate of 5.9 nm s^{-1} and 22.1 nm s^{-1} was found, respectively. With the other methods of EQCM and XRD, the understanding of the electrochemical phase transitions could be deepened: Na-insertion into graphite results in a multitude of phase transitions, which is similar in the G_1-, G_2- and G_4-electrolytes. Here, the ternary Na-GIC first forms higher order staging Na-GICs, continuously changing following a Daumas-Herold staging mechanism by reaching a stage 3 and an intermediate stage 2 Na-GIC. Finally, a stage 1 Na-GIC is formed when fully sodiating the graphite. The G_3-electrolyte showed a unique electrochemistry, strongly differing from the other electrolytes. The under-coordination of the Na-ion with O-atoms of only one G_3-molecule in the solvation shell has a strong effect on the intercalation mechanism, since the interaction force between the Na-ion and the graphite lattice is increased, not only hampering the in-plane diffusion of the ions in the graphite lattice, but also leading to a decreased specific capacity.

In the next section (section 5.3) the focus changed from graphite to V_2O_5 as electrode material for the positive electrode. Also here, fundamental studies on the Na-intercalation electrochemistry were conducted. First, a combination of cyclic voltammetry with an *ex-situ* STM study clarified the phase transitions the $Na_xV_2O_5$ undergoes upon charging and discharging. The same phase transitions were found in the glyme electrolytes, where the Na-ions, in contrast to the graphite electrode, strip off their solvation shell before intercalating into the V_2O_5. Sodiating the pristine V_2O_5, which has an orthorhombic lattice with an interlayer distance of 4.4 Å, a first Na-ion is irreversibly inserted into the electrode forming an as well orthorhombic $Na_1V_2O_5$ with a slightly increased interlayer spacing of 4.8 Å. For the reversible charge storage, a second Na-ion is inserted, resulting in a major phase transition to a bilayered $Na_2V_2O_5$ with a 16.1 Å lattice parameter. In contrast to the graphite electrode, the Na-ions lose their solvation shell prior to intercalation.

The knowledge about the $Na_xV_2O_5$ phase transitions helped to optimize the powder morphology of the V_2O_5 electrodes for battery operation. A widespread of V_2O_5 morphologies was synthesized, ranging from micrometer-sized powders with hollow or yolk-shell microspheres down to nanostructures such as V_2O_5 nanobundles. Tested in a NIB, a strong effect of the electrode topography on the battery performance is observed. This can also be seen in the Ragone plot in Figure 78, where the different V_2O_5 electrodes (purple symbols) are compared to each other and to electrode materials of different material classes presented in literature. Those include layered transition metal oxides (red), polyanionic compounds (yellow), hexacyanometalates (green) and organic materials (blue). In comparison to the other material classes, the V_2O_5 has slightly lowered operating voltages and relatively large capacities, counterbalancing each other. Consequently, with respect to energy density, V_2O_5 electrodes show a comparable performance, which of course is not the only criterion to judge electrode materials. One also has to consider material and fabrication costs, toxicity and other hazards as well as the lifetime. In order to illustrate the effect of lifetime, the measured battery parameters of the V_2O_5 powders are sketched in the Ragone plot twice, once at the beginning of cycle life (solid symbols) and once at the end of life (open symbols). Even though the layered transition metal oxides (red) seem to have a lowered energy density, they are a very promising material for NIB cathodes, since they possess a high cycling stability.

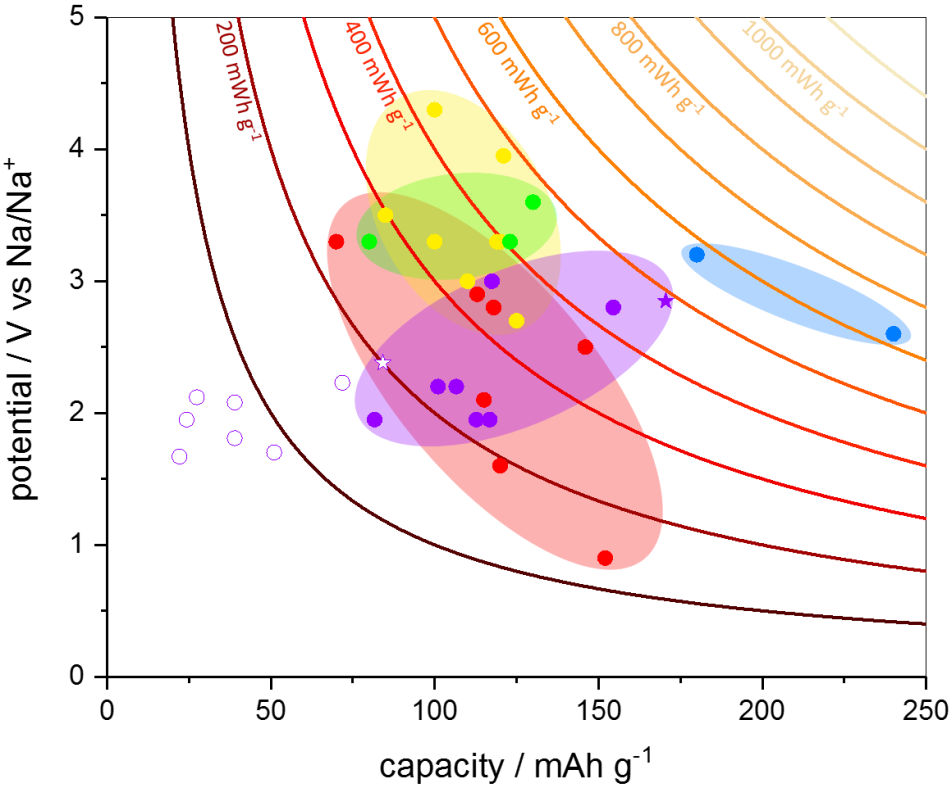

Figure 78: Ragone plot comparing the most prominent NIB positive electrode materials of different material classes, such as layered transition metal oxides (red), polyanionic compounds (yellow), hexacyanometalates (green), organic materials (blue) and the V_2O_5 electrodes presented in this study with their performance in the beginning of life (solid purple symbols) and end of life (open purple symbols). The star symbol marks the V_2O_5 nanobundles.[50–75, 77, 91–94]

The Ragone plot also shows, how the electrode morphology affects the battery performance of the V_2O_5 electrodes. The measured capacities and operating voltages scatter over a wide range resulting in very different energy densities. It was found that nano-sized V_2O_5 nanobundles (star symbol) show the best battery performance in a NIB amongst all other synthesized V_2O_5 morphologies with an energy density almost reaching 500 mWh g^{-1} in the beginning of cycle life and maintaining a practical energy density of 200 mWh g^{-1} after 100 cycles. Moreover, the energy efficiency and the response characteristics to fast charging/discharging was much improved. The reason for the superiority of this material is the nano-size of the V_2O_5 bundles, which (i) reduces the diffusion length of Na-ions being beneficial for high rates, (ii) increases the surface to bulk ratio and thus increases the contact to the conductive carbon facilitating the electronic transport, (iii) offers more 'near-surface' intercalation sites resulting in larger voltages and (iv) suppresses electrode degradation being beneficial for a prolonged cycle life.

Finally, a full Na-ion battery with a graphite and a V_2O_5 electrode was assembled and tested. The rechargeable battery cycled well, showing high energy losses in the round trip efficiency, however. Compared to commercialized and well established battery technologies like the lead-acid (70 % - 90 %)[5, 6, 364] or Ni-Cd batteries (60 % - 70 %),[5] the achieved energy efficiency of more than 50 % of the graphite | V_2O_5 NIB prototype seems quite reasonable. The gap to the mature LIB technology (ca. 90 %)[5, 6] can be closed by further understanding, tuning and optimizing the battery components. The reason for the high energy losses was mainly found to be the V_2O_5 electrode, where the interplay with the graphite electrode and the electrolyte in the full cell is still unclear.

In view of the NIB technology in general, V_2O_5 might not take the step beyond the prototype level, mainly due to its limited lifetime. The application of graphite electrodes on the other hand seems to fulfill all necessary electrode requirements better than other materials, such as reasonable energy and power densities, lifetime, benign hazards and low costs, bringing the NIB technology one step closer to commercialization.

8 References

1 R. K. Pachauri, M. R. Allen, V. R. Barros, J. Broome, W. Cramer, R. Christ, J. a. Church, L. Clarke, Q. Dahe, P. Dasgupta, N. K. Dubash, O. Edenhofer, I. Elgizouli, C. B. Field, P. Forster, P. Friedlingstein, J. Fuglestvedt, L. Gomez-Echeverri, S. Hallegatte, G. Hegerl, M. Howden, K. Jiang, B. Jimenez Cisneros, V. Kattsov, H. Lee, K. J. Mach, J. Marotzke, M. D. Mastrandrea, L. Meyer, J. Minx, Y. Mulugetta, K. O'Brien, M. Oppenheimer, J. J. Pereira, R. Pichs-Madruga, G. K. Plattner, H.-O. Pörtner, S. B. Power, B. Preston, N. H. Ravindranath, A. Reisinger, K. Riahi, M. Rusticucci, R. Scholes, K. Seyboth, Y. Sokona, R. Stavins, T. F. Stocker, P. Tschakert, D. van Vuuren and J.-P. van Ypersele, *IPCC, 2014: CLIMATE CHANGE 2014 - Synthesis Report*, 2014.

2 Kristin Seyboth, F. Sverrisson, F. Appavou, A. Brown, B. Epp, A. Leidreiter, C. Lins, E. Musolino, H. E. Murdock, K. Petrichenko, T. C. Farrell, T. T. Krader, A. Tsakiris, J. L. Sawin, J. Skeen and B. Sovacool, *Renewables 2016 Global Status Report*, Paris, 2016.

3 Bundesministerium für Wirtschaft und Energie, *Erneuerbare Energien in Zahlen - Nationale und internationale Entwicklung im Jahr 2015*, 2015.

4 V. A. Boicea, *Proc. IEEE*, 2014, **102**, 1777–1794.

5 H. Chen, T. N. Cong, W. Yang, C. Tan, Y. Li and Y. Ding, *Prog. Nat. Sci.*, 2009, **19**, 291–312.

6 T. Kousksou, P. Bruel, A. Jamil, T. El Rhafiki and Y. Zeraouli, *Sol. Energy Mater. Sol. Cells*, 2014, **120**, 59–80.

7 P. Denholm and G. L. Kulcinski, *Energy Convers. Manag.*, 2004, **45**, 2153–2172.

8 G. L. Soloveichik, *Annu. Rev. Chem. Biomol. Eng.*, 2011, **2**, 503–527.

9 B. Dunn, H. Kamath and J.-M. Tarascon, *Science*, 2011, **334**, 928–35.

10 S. Chu and A. Majumdar, *Nature*, 2012, **488**, 294–303.

11 H. Pan, Y.-S. Hu and L. Chen, *Energy Environ. Sci.*, 2013, **6**, 2338.

12 J. B. Dunn, L. Gaines, M. Barnes, J. Sullivan and M. Wang, *Material and Energy Flows in the Materials Production, Assembly, and End-of-Life Stages of the Automotive Lithium-Ion Battery Life Cycle*, 2012.

13 N. Yabuuchi, K. Kubota, M. Dahbi and S. Komaba, *Chem. Rev.*, 2014, **114**, 11636–11682.

14 M. D. Slater, D. Kim, E. Lee and C. S. Johnson, *Adv. Funct. Mater.*, 2013, **23**, 947–958.

15 D. Kundu, E. Talaie, V. Duffort and L. F. Nazar, *Angew Chem Int Ed Engl*, 2015, **54**, 3431–3448.

16 M. Lee, S. Lee, P. Oh, Y. Kim and J. Cho, *Nano Lett.*, 2014, **14**, 993–999.

17 E. M. Erickson, C. Ghanty and D. Aurbach, *J. Phys. Chem. Lett.*, 2014, **5**, 3313–3324.

18 B. Jache and P. Adelhelm, *Angew. Chem. Int. Ed. Engl.*, 2014, **53**, 10169–73.

19 *www.alibaba.com*.

20 *www.metalary.com*.

21 V. Alekseenko and A. Alekseenko, *J. Geochemical Explor.*, 2014, **147**, 245–249.

22 H. Kang, Y. Liu, K. Cao, Y. Zhao, L. Jiao, Y. Wang and H. Yuan, *J. Mater. Chem. A*, 2015, **3**, 17899–17913.

23 Y. Kim, K. H. Ha, S. M. Oh and K. T. Lee, *Chem. - A Eur. J.*, 2014, **20**, 11980–11992.

24 R. Yazami and P. Touzain, *J. Power Sources*, 1983, **9**, 365–371.

25 M. M. Doeff, Y. Ma, S. J. Visco and L. C. De Jonghe, *J. Electrochem. Soc.*, 1993, **140**, L169–L170.

26 P. Thomas, J. Ghanbaja and D. Billaud, *Electrochim. Acta*, 1999, **45**, 423–430.

27 P. Thomas and D. Billaud, *Electrochim. Acta*, 2002, **47**, 3303–3307.

28 J. Xu, D. H. Lee and Y. S. Meng, *Funct. Mater. Lett.*, 2013, **6**, 1330001.

29 X. Xiang, K. Zhang and J. Chen, *Adv. Mater.*, 2015, **27**, 5343–5364.

30 H. Kim, H. Kim, Z. Ding, M. H. Lee, K. Lim, G. Yoon and K. Kang, *Adv. Energy Mater.*, 2016, 1600943.

31 D. B. Le, S. Passerini, F. Coustier, J. Guo, T. Soderstrom, B. B. Owens and W. H. Smyrl, *Chem. Mater.*, 1998, **4756**, 682–684.

32 K. West, B. Zachau-Christiansen, T. Jacobsen and S. Skaarup, *Solid State Ionics*, 1988, **28**–**30**, 1128–1131.

33 D. Linden and T. B. Reddy, *Handbook of Batteries - 3rd edition*, McGraw-Hill, New York, 3., 2002.

34 S. Patoux, L. Sannier, H. Lignier, Y. Reynier, C. Bourbon, S. Jouanneau, F. Le Cras and S. Martinet, *Electrochim. Acta*, 2008, **53**, 4137–4145.

35 J. B. Goodenough and Y. Kim, *Chem. Mater.*, 2010, **22**, 587–603.

36 H. Li, Z. Wang, L. Chen and X. Huang, *Adv. Mater.*, 2009, **21**, 4593–4607.

37 N. Nitta, F. Wu, J. T. Lee and G. Yushin, *Mater. Today*, 2015, **18**, 252–264.

38 D. Andre, H. Hain, P. Lamp, F. Maglia and B. Stiaszny, *J. Mater. Chem. A Mater. energy Sustain.*, 2017, **5**, 17174–17198.

39 J. Cabana, L. Monconduit, D. Larcher and M. R. Palacín, *Adv. Mater.*, 2010, **22**, E170–E192.

40 Y. X. Yin, S. Xin, Y. G. Guo and L. J. Wan, *Angew. Chemie - Int. Ed.*, 2013, **52**, 13186–13200.

41 A. Manthiram, Y. Fu, S. Chung, C. Zu and Y. Su, *Chem. Rev.*, 2014, **114**, 11751–11787.

42 B. L. Ellis and L. F. Nazar, *Curr. Opin. Solid State Mater. Sci.*, 2012, **16**, 168–177.

43 G. Girishkumar, B. McCloskey, A. C. Luntz, S. Swanson and W. Wilcke, *J. Phys. Chem. Lett.*, 2010, **1**, 2193–2203.

44 J. Christensen, P. Albertus, R. S. Sanchez-Carrera, T. Lohmann, B. Kozinsky, R. Liedtke, J. Ahmed and A. Kojic, *J. Electrochem. Soc.*, 2012, **159**, R1.

45 T. Placke, O. Fromm, S. F. Lux, P. Bieker, S. Rothermel, H.-W. Meyer, S. Passerini and M. Winter, *J. Electrochem. Soc.*, 2012, **159**, A1755–A1765.

46 Y.-G. Guo, H.-R. Yao, Y. You, Y.-X. Yin and L. Wan, *Phys. Chem. Chem. Phys.*, 2016, **18**, 9326–9333.

47 A. J. Bard and L. R. Faulkner, *Electrochemical Methods - Fundamentals and Applications*, John Wiley & Sons, INC., Weinheim, 2., 2001.

48 D. C. Grahame, *Chem. Rev.*, 1947, **41**, 441–501.

49 J. Friedl, J. Gu, U. Stimming and B. R. Horrocks, *ChemElectroChem*, 2017, **4**, 1–5.

50 H. Helmholtz, *Ann. der Phys. und Chemie*, 1853, **165**, 211–233.

51 M. Gouy, *J. Phys. Theor. Appl.*, 1910, **9**, 457–468.

52 D. L. Chapman, *Philos. Mag. Ser. 6*, 1913, **25**, 475–481.

53 O. Stern, *Zeitschrift fur Elektrochemie*, 1924, **30**, 508–516.

54 J. O. Bockris, M. A. V. Devanathan and K. Müller, *Proc. R. Soc. A Math. Phys. Eng. Sci.*, 1963, **274**, 55–79.

55 S. Trasatti, *J. Electroanal. Chem.*, 1981, **123**, 121–139.

56 B. E. Conway and E. Gileadi, *Trans. Faraday Soc.*, 1962, **58**, 2493–2509.

57 R. A. Marcus, *J. Chem. Phys.*, 1956, **24**, 966–978.

58 R. A. Marcus, *J. Chem. Phys.*, 1956, **24**, 979–989.

59 W. Schmickler and D. Henderson, *J. Chem. Phys.*, 1984, **80**, 3381.

60 W. Schmickler and D. Henderson, *Prog. Surf. Sci.*, 1986, **22**, 323–419.

61 R. Atkin, S. A. El Zein, R. Hayes, L. H. S. Gasparotto, N. Borisenko and F. Endres, *J. Phys. Chem. C*, 2009, **113**, 13266–13272.

62 P. Debye and E. Hückel, *Phys. Zeitschrift*, 1923, **24**, 185–206.

63 M. D. Levi, E. A. Levi and D. Aurbach, *J. Electroanal. Chem.*, 1997, **421**, 89–97.

64 A.-M. Cao, J.-S. Hu, H.-P. L. Liang and L.-J. Wan, *Angew. Chemie - Int. Ed.*, 2005, **44**, 4391–4395.

65 E. Uchaker, N. Zhou, Y. Li and G. Cao, *J. Phys. Chem. C*, 2013, 1621–1626.

66 A. Pan, T. Zhu, H. Bin Wu and X. W. D. Lou, *Chemistry*, 2013, **19**, 494–500.

67 G. Li, S. Pang, L. Jiang, Z. Guo and Z. Zhang, *J. Phys. Chem. B*, 2006, **110**, 9383–9386.

68 J. Liu, Y. Zhou, J. Wang, Y. Pan and D. Xue, *Chem. Commun. (Camb).*, 2011, **47**, 10380–10382.

69 C.-J. Mao, H.-C. Pan, X.-C. Wu, J.-J. Zhu and H.-Y. Chen, *J. Phys. Chem. B*, 2006, **110**, 14709–14713.

70 J. Goldstein, D. Newbury, D. Joy, C. Lyman, P. Echlin, E. Lifshin, L. Sawyer and J. Michael, *Scanning electron microscopy and X-ray microanalysis*, Springer, New York, 3., 2003, vol. 3.

71 L. De Broglie, 1924.

72 P. van der Heide, *X-Ray Photoelectron Spectroscopy; An Introduction to Principles and Practices*, John Wiley & Sons, Inc., Hoboken, 2012.

73 Y. Waseda, E. Matsubara and K. Shinoda, *X-Ray Diffraction Crystallography*, Springer-Verlag, Berlin, Heidelberg, 2011.

74 W. H. Bragg and W. L. Bragg, *Proc. R. Soc. London*, 1913, **88**, 428–438.

75 H. Kim, J. Hong, G. Yoon, H. Kim, K.-Y. Park, M.-S. Park, W.-S. Yoon and K. Kang, *Energy Environ. Sci.*, 2015, **8**, 2963–2969.

76 S. Hartung, N. Bucher, R. Bucher and M. Srinivasan, *Rev. Sci. Instrum.*, 2015, **86**, 86102-1-86102–3.

77 L. Seidl, S. Martens, J. Ma, U. Stimming and O. Schneider, *Nanoscale*, 2016, **8**, 14004–14014.

78 E. Peled, *J. Electrochem. Soc.*, 1979, **126**, 2047–2051.

79 P. B. Balbuena and Y. Wang, *Lithium-Ion Batteries Solid-Electrolyte Interphase*, Imperial College Press, London, 2004.

80 W. Märkle, C.-Y. Lu and P. Novák, *J. Electrochem. Soc.*, 2011, **158**, A1478–A1482.

81 M. Winter, J. O. Besenhard, M. E. Spahr and P. Novák, *Adv. Mater.*, 1998, **10**, 725–763.

82 H. Buqa, A. Würsig, J. Vetter, M. E. Spahr, F. Krumeich and P. Novák, *J. Power Sources*, 2006, **153**, 385–390.

83 H. Tavassol, J. W. Buthker, G. A. Ferguson, L. A. Curtiss and A. A. Gewirth, *J. Electrochem. Soc.*, 2012, **159**, A730–A738.

84 I. V. Veryovkin, C. E. Tripa, A. V. Zinovev, S. V. Baryshev, Y. Li and D. P. Abraham, *Nucl. Instruments Methods Phys. Res. Sect. B Beam Interact. with Mater. Atoms*, 2014, **332**, 368–372.

85 H. Bülter, F. Peters, J. Schwenzel and G. Wittstock, *Angew. Chem. Int. Ed. Engl.*, 2014, **53**, 10531–5.

86 H. Bülter, F. Peters, J. Schwenzel and G. Wittstock, *J. Electrochem. Soc.*, 2015, **162**, A7024–A7036.

87 H. Bülter, F. Peters, J. Schwenzel and G. Wittstock, *J. Electrochem. Soc.*, 2016, **163**, A27–A34.

88 M. Nie, D. Chalasani, D. P. Abraham, Y. Chen, A. Bose and B. L. Lucht, *J. Phys. Chem. C*, 2013, **117**, 1257–1267.

89 J. T. Lee, N. Nitta, J. Benson, A. Magasinski, T. F. Fuller and G. Yushin, *Carbon N. Y.*, 2013, **52**, 388–397.

90 M. Ayache, D. Jang, J. Syzdek and R. Kostecki, *J. Electrochem. Soc.*, 2015, **162**, A7078–A7082.

91 L. Wang, D. Deng, L. C. Lev and S. Ng, *J. Power Sources*, 2014, **265**, 140–148.

92 A. v. Cresce, S. M. Russell, D. R. Baker, K. J. Gaskell and K. Xu, *Nano Lett.*, 2014, **14**, 1405–1412.

93 G. Zampardi, S. Klink, V. Kuznetsov, T. Erichsen, A. Maljusch, F. La Mantia, W. Schuhmann and E. Ventosa, *ChemElectroChem*, 2015, **2**, 1607–1611.

94 P. Ganesh, P. R. C. Kent and D. Jiang, *J. Phys. Chem. C*, 2012, **116**, 24476–24481.

95 N. Takenaka, Y. Suzuki, H. Sakai and M. Nagaoka, *J. Phys. Chem. C*, 2014, **118**, 10874–10882.

96 S.-D. Xu, Q.-C. Zhuang, J. Wang, Y.-Q. Xu and Y.-B. Zhu, *Int. J. Electrochem. Sci.*, 2013, **8**, 8058–8076.

97 S.-H. Lee, I.-S. Jo and J. Kim, *Surf. Interface Anal.*, 2014, **46**, 570–576.

98 Y. Zhu, M. D. Casselman, Y. Li, A. Wei and D. P. Abraham, *J. Power Sources*, 2014, **246**, 184–191.

99 P. Verma and P. Novák, *Carbon N. Y.*, 2012, **50**, 2599–2614.

100 P. Verma, T. Sasaki and P. Novák, *Electrochim. Acta*, 2012, **82**, 233–242.

101 A. M. Haregewoin, E. G. Leggesse, J.-C. Jiang, F.-M. Wang, B.-J. Hwang and S. D. Lin, *Electrochim. Acta*, 2014, **136**, 274–285.

102 G. Gourdin, J. Collins, D. Zheng, M. Foster and D. Qu, *J. Phys. Chem. C*, 2014, **118**, 17383–17394.

103 K. Xu, Y. Lam, S. S. Zhang, T. R. Jow and T. B. Curtis, *J. Phys. Chem. C*, 2007, **111**, 7411–7421.

104 J.-S. Bridel, S. Grugeon, S. Laruelle, J. Hassoun, P. Reale, B. Scrosati and J.-M. Tarascon, *J. Power Sources*, 2010, **195**, 2036–2043.

105 J. M. Vollmer, L. A. Curtiss, D. R. Vissers and K. Amine, *J. Electrochem. Soc.*, 2004, **151**, A178–A183.

106 G. Gourdin, D. Zheng, P. H. Smith and D. Qu, *Electrochim. Acta*, 2013, **112**, 735–746.

107 Y. Wang, S. Nakamura, M. Ue and P. B. Balbuena, *J. Am. Chem. Soc.*, 2001, **123**, 11708–11718.

108 S. Leroy, H. Martinez, R. Dedryvère, D. Lemordant and D. Gonbeau, *Appl. Surf. Sci.*, 2007, **253**, 4895–4905.

109 I. A. Shkrob, Y. Zhu, T. W. Marin and D. P. Abraham, *J. Phys. Chem. C*, 2013, **117**, 19255–19269.

110 Y. Wu, N. Hu, L. Wei and Y. Dai, *ECS Electrochem. Lett.*, 2014, **3**, A50–A53.

111 D. Aurbach, A. Zaban, Y. Ein-Eli, I. Weissman, O. Chusid, B. Markovsky, M. D. Levi, E. Levi, A. Schechter and E. Granot, *J. Power Sources*, 1997, **68**, 91–98.

112 D. Aurbach, M. Moshkovich, Y. Cohen and A. Schechter, *Langmuir*, 1999, **15**, 2947–2960.

113 G. G. Eshetu, S. Grugeon, G. Gachot, D. Mathiron, M. Armand and S. Laruelle, *Electrochim. Acta*, 2013, **102**, 133–141.

114 V. A. Agubra and J. W. Fergus, *J. Power Sources*, 2014, **268**, 153–162.

115 X. Zhang, R. Kostecki, T. J. Richardson, J. K. Pugh and P. N. Ross, *J. Electrochem. Soc.*, 2001, **148**, A1341–A1345.

116 S. P. Kim, A. C. T. Van Duin and V. B. Shenoy, *J. Power Sources*, 2011, **196**, 8590–8597.

117 M. Tang and J. Newman, *J. Electrochem. Soc.*, 2012, **159**, A1922–A1927.

118 P. Murmann, P. Niehoff, R. Schmitz, S. Nowak, H. Gores, N. Ignatiev, P. Sartori, M. Winter and R. Schmitz, *Electrochim. Acta*, 2013, **114**, 658–666.

119 X. Deng, X. Liu, H. Yan, D. Wang and L. Wan, *Sci. China Chem.*, 2014, **57**, 178–183.

120 D. Li, D. Danilov, Z. Zhang, H. Chen, Y. Yang and P. H. L. Notten, *J. Electrochem. Soc.*, 2015, **162**, A858–A869.

121 D. Aurbach, B. Markovsky, I. Weissman, E. Levi and Y. Ein-Eli, *Electrochim. Acta*, 1999, **45**, 67–86.

122 L. M. Moshurchak, C. Buhrmester, R. L. Wang and J. R. Dahn, *Electrochim. Acta*, 2007, **52**, 3779–3784.

123 K. Leung, *Chem. Phys. Lett.*, 2013, **568**–**569**, 1–8.

124 H. J. Ploehn, P. Ramadass and R. E. White, *J. Electrochem. Soc.*, 2004, **151**, A456A462.

125 M. Safari, M. Morcrette, A. Teyssot and C. Delacourt, *J. Electrochem. Soc.*, 2009, **156**, A145–A153.

126 S. Sankarasubramanian and B. Krishnamurthy, *Electrochim. Acta*, 2012, **70**, 248–254.

127 E. Peled, D. Golodnitsky and G. Ardel, *J. Electrochem. Soc.*, 1997, **144**, 208–210.

128 D. Bar-Tow, E. Peled and L. Burstein, *J. Electrochem. Soc.*, 1999, **146**, 824–832.

129 V. Eshkenazi, E. Peled, L. Burstein and D. Golodnitsky, *Solid State Ionics*, 2004, **170**, 83–91.

130 Z. Ogumi, A. Sano, M. Inaba and T. Abe, *J. Power Sources*, 2001, **97**–**98**, 156–158.

131 E. Peled, D. Bar Tow, A. Merson, A. Gladkich, L. Burstein and D. Golodnitsky, *J. Power Sources*, 2001, **97**–**98**, 52–57.

132 J. Yan, J. Zhang, Y. C. Su, X. G. Zhang and B. J. Xia, *Electrochim. Acta*, 2010, **55**, 1785–1794.

133 M. Tang, K. Miyazaki, T. Abe and J. Newman, *J. Electrochem. Soc.*, 2012, **159**, A634–A641.

134 A. C. Chu, J. Y. Josefowicz and G. C. Farrington, *J. Electrochem. Soc.*, 1997, **144**, 4161.

135 M. Inaba, Z. Siroma, A. Funabiki, Z. Ogumi, T. Abe, Y. Mizutani and M. Asano, *Langmuir*, 1996, **12**, 1535–1540.

136 M. Inaba, Z. Siroma, Y. Kawatate, A. Funabiki and Z. Ogumi, *J. Power Sources*, 1997, **68**, 221–226.

137 M. Inaba, Y. Kawatate, A. Funabiki, S.-K. Jeong, T. Abe and Z. Ogumi, *Electrochim. Acta*, 1999, **45**, 99–105.

138 Z. Ogumi, S.-K. Jeong, M. Inaba and T. Abe, *Macromol. Symp.*, 2000, **156**, 195–202.

139 S.-K. Jeong, M. Inaba, R. Mogi, Y. Iriyama, T. Abe and Z. Ogumi, *Langmuir*, 2001, **17**, 8281–8286.

140 S.-K. Jeong, M. Inaba, T. Abe and Z. Ogumi, *J. Electrochem. Soc.*, 2001, **148**, A989–A993.

141 M. Inaba, Z. Siroma, Y. Kawatate, A. Funabiki and Z. Ogumi, *J. Power Sources*, 1997, **68**, 221–226.

142 S.-K. Jeong, M. Inaba, Y. Iriyama, T. Abe and Z. Ogumi, *J. Power Sources*, 2003, **119**–**121**, 555–560.

143 L. Wang, X. Deng, P.-X. Dai, Y.-G. Guo, D. Wang and L.-J. Wan, *Phys. Chem. Chem. Phys.*, 2012, **14**, 7330–7336.

144 D. Alliata, R. Kötz, P. Novák and H. Siegenthaler, *Electrochem. commun.*, 2000, **2**, 436–440.

145 P. Novák, F. Joho, M. Lanz, B. Rykart, J.-C. Panitz, D. Alliata, R. Kötz and O. Haas, *J. Power Sources*, 2001, **97**–**98**, 39–46.

146 J. O. Besenhard, M. Winter, J. Yang and W. Biberacher, *J. Power Sources*, 1995, **54**, 228–231.

147 M. H. Han, E. Gonzalo, G. Singh and T. Rojo, *Energy Environ. Sci.*, 2015, **8**, 81–102.

148 V. Palomares, P. Serras, I. Villaluenga, K. B. Hueso, J. Carretero-González and T. Rojo, *Energy Environ. Sci.*, 2012, **5**, 5884.

149 K. Kubota, N. Yabuuchi, H. Yoshida, M. Dahbi and S. Komaba, *MRS Bull.*, 2014, **39**, 416–422.

150 W. Wan and H. Wang, *Int. J. Electrochem. Sci.*, 2015, **10**, 3177–3184.

151 K. Nobuhara, H. Nakayama, M. Nose, S. Nakanishi and H. Iba, *J. Power Sources*, 2013, **243**, 585–587.

152 Y. Okamoto, *J. Phys. Chem. C*, 2013, **118**, 16–19.

153 D. Stevens and J. R. Dahn, *J. Electrochem. Soc.*, 2000, **147**, 1271–1273.

154 W. Lv, F. Wen, J. Xiang, J. Zhao, L. Li, L. Wang, Z. Liu and Y. Tian, *Electrochim. Acta*, 2015, **176**, 533–541.

155 L. Wu, D. Buchholz, C. Vaalma, G. A. Giffin and S. Passerini, *ChemElectroChem*, 2016, **3**, 292–298.

156 P. Liu, Y. Li, Y. Hu, H. Li, L. Chen, X. Huang, J. A. Mater Chem, B. Pin Liu, Y. Li, Y.-S. Hu, H. Li, L. Chen, X. P. Huang Liu, Y. M. Li, Y. Hu, L. Q. Chen and X. J. Huang, *J. Mater. Chem. A Mater. energy Sustain.*, 2016, **4**, 13046–13052.

157 Y. Wen, K. He, Y. Zhu, F. Han, Y. Xu, I. Matsuda, Y. Ishii, J. Cumings and C. Wang, *Nat. Commun.*, 2014, **5**, 4033.

158 Z. L. Yu, S. Xin, Y. You, L. Yu, Y. Lin, D. W. Xu, C. Qiao, Z. H. Huang, N. Yang, S. H. Yu and J. B. Goodenough, *J. Am. Chem. Soc.*, 2016, **138**, 14915–14922.

159 A. Ramos, I. Cameán, N. Cuesta, C. Antuña and A. B. García, *Electrochim. Acta*, 2016, **187**, 496–507.

160 A. Ramos, I. Cameán, N. Cuesta and A. B. García, *Electrochim. Acta*, 2015, **178**, 392–397.

161 Y. S. Yun, Y. U. Park, S. J. Chang, B. H. Kim, J. Choi, J. Wang, D. Zhang, P. V. Braun, H. J. Jin and K. Kang, *Carbon N. Y.*, 2016, **99**, 658–664.

162 Y. Liu, L.-Z. Fan and L. Jiao, *J. Mater. Chem. A*, 2017, **5**, 1698–1705.

163 H. G. Wang, Z. Wu, F. L. Meng, D. L. Ma, X. L. Huang, L. M. Wang and X. B. Zhang, *ChemSusChem*, 2013, **6**, 56–60.

164 C. Ling and F. Mizuno, *Phys. Chem. Chem. Phys.*, 2014, **16**, 10419–10424.

165 Y. X. Wang, S. L. Chou, H. K. Liu and S. X. Dou, *Carbon N. Y.*, 2013, **57**, 202–208.

166 L. David and G. Singh, *J. Phys. Chem. C*, 2014, **118**, 28401–28408.

167 B. A. Jache, J. O. Binder, T. Abe and P. Adelhelm, *Phys. Chem. Chem. Phys.*, 2016, **18**, 14299–14316.

168 Z. Zhu, F. Cheng, Z. Hu, Z. Niu and J. Chen, *J. Power Sources*, 2015, **293**, 626–634.

169 H. Kim, J. Hong, Y.-U. Park, J. Kim, I. Hwang and K. Kang, *Adv. Func. Mater.*, 2014, 534–541.

170 I. Hasa, X. Dou, D. Buchholz, Y. Shao-Horn, J. Hassoun, S. Passerini and B. Scrosati, *J. Power Sources*, 2016, **310**, 26–31.

171 G. C. Ri, C. J. Yu, J. S. Kim, S. N. Hong, U. G. Jong and M. H. Ri, *J. Power Sources*, 2016, **324**, 758–765.

172 H. Kim, G. Yoon, K. Lim and K. Kang, *Chem. Commun.*, 2016, **52**, 12618–12621.

173 Z. Guan, X. Shen, R. Yu, Z. Wang and L. Chen, *Electrochim. Acta*, 2016, **222**, 1365–1370.

174 J. Maibach, F. Jeschull, D. Brandell, K. Edstrom and M. Valvo, *ACS Appl. Mater. Interfaces*, 2017, **9**, 12373–12381.

175 K. Gotoh, H. Maruyama, T. Miyatou, M. Mizuno, K. Urita and H. Ishida, *J. Phys. Chem. C*, 2016, **120**, 28152–28256.

176 G. Yoon, H. Kim, I. Park and K. Kang, *Adv. Energy Mater.*, 2016, 1601519.

177 N. Shpigel, M. D. Levi, S. Sigalov, O. Girshevitz, D. Aurbach, L. Daikhin, P. Pikma, M. Marandi, A. Jänes, E. Lust, N. Jäckel and V. Presser, *Nat. Mater.*, 2016, **15**, 570–577.

178 L. Seidl, N. Bucher, E. Chu, S. Hartung, S. Martens, O. Schneider and U. Stimming, *Energy Environ. Sci.*, 2017, **10**, 1631–1642.

179 D. Wu, X. Li, B. Xu, N. Twu, L. Liu and G. Ceder, *Energy Environ. Sci.*, 2015, **8**, 195–202.

180 A. Vasileiadis and M. Wagemaker, *Chem. Mater.*, 2017, **2**, acs.chemmater.6b03928.

181 C. Didier, M. Guignard, C. Denage, O. Szajwaj, S. Ito, I. Saadoune, J. Darriet and C. Delmas, *Electrochem. Solid-State Lett.*, 2011, **14**, A75.

182 D. Hamani, M. Ati, J. M. Tarascon and P. Rozier, *Electrochem. commun.*, 2011, **13**, 938–941.

183 C. Y. Chen, K. Matsumoto, T. Nohira, R. Hagiwara, A. Fukunaga, S. Sakai, K. Nitta and S. Inazawa, *J. Power Sources*, 2013, **237**, 52–57.

184 K. Kubota, I. Ikeuchi, T. Nakayama, C. Takei, N. Yabuuchi, H. Shiiba, M. Nakayama and S. Komaba, *J. Phys. Chem. C*, 2015, **119**, 166–175.

185 S. H. Bo, X. Li, A. J. Toumar and G. Ceder, *Chem. Mater.*, 2016, **28**, 1419–1429.

186 X. Ma, H. Chen and G. Ceder, *J. Electrochem. Soc.*, 2011, **158**, A1307.

187 I. H. Jo, H. S. Ryu, D. G. Gu, J. S. Park, I. S. Ahn, H. J. Ahn, T. H. Nam and K. W. Kim, *Mater. Res. Bull.*, 2014, **58**, 74–77.

188 J. Billaud, R. J. Clément, A. R. Armstrong, J. Canales-Vázquez, P. Rozier, C. P. Grey and P. G. Bruce, *J. Am. Chem. Soc.*, 2014, **136**, 17243–17248.

189 K. Kubota, T. Asari, H. Yoshida, N. Yaabuuchi, H. Shiiba, M. Nakayama and S. Komaba, *Adv. Funct. Mater.*, 2016, **26**, 6047–6059.

190 X. Wang, G. Liu, T. Iwao, M. Okubo and A. Yamada, *J. Phys. Chem. C*, 2014, **118**, 2–8.

191 R. Kataoka, K. Kuratani, M. Kitta, N. Takeichi, T. Kiyobayashi and M. Tabuchi, *Electrochim. Acta*, 2015, **182**, 871–877.

192 T. Shibata, Y. Fukuzumi, W. Kobayashi and Y. Moritomo, *Sci. Rep.*, 2015, **5**, 9006.

193 M. H. Han, E. Gonzalo, M. Casas-Cabanas and T. Rojo, *J. Power Sources*, 2014, **258**, 266–271.

194 K. Park, B. C. Yu and J. B. Goodenough, *Chem. Mater.*, 2015, **27**, 6682–6688.

195 S. M. Oh, S. T. Myung, J. Hassoun, B. Scrosati and Y. K. Sun, *Electrochem. commun.*, 2012, **22**, 149–152.

196 W. Shen, C. Wang, H. Liu and W. Yang, *Chem. - A Eur. J.*, 2013, **19**, 14712–14718.

197 H. Kim, R. A. Shakoor, C. Park, S. Y. Lim, J. S. Kim, Y. N. Jo, W. Cho, K. Miyasaka, R. Kahraman, Y. Jung and J. W. Choi, *Adv. Funct. Mater.*, 2013, **23**, 1147–1155.

198 P. Barpanda, T. Ye, S. I. Nishimura, S. C. Chung, Y. Yamada, M. Okubo, H. Zhou and A. Yamada, *Electrochem. commun.*, 2012, **24**, 116–119.

199 P. Barpanda, T. Ye, Y. Yamada, S. C. Chung, S. Nishimura, M. Okubo, H. Zhou and A. Yamada, *ECS Trans.*, 2013, **50**, 71–77.

200 Y. L. Ruan, K. Wang, S. D. Song, X. Han and B. W. Cheng, *Electrochim. Acta*, 2015, **160**, 330–336.

201 Y. Kawabe, N. Yabuuchi, M. Kajiyama, N. Fukuhara, T. Inamasu, R. Okuyama, I. Nakai and S. Komaba, *Electrochem. commun.*, 2011, **13**, 1225–1228.

202 K. Kubota, K. Yokoh, N. Yabuuchi and S. Komaba, *Electrochemistry*, 2014, **82**, 909–911.

203 N. Recham, G. Rousse, M. T. Sougrati, J. N. Chotard, C. Frayret, S. Mariyappan, B. C. Melot, J. C. Jumas and J. M. Tarascon, *Chem. Mater.*, 2012, **24**, 4363–4370.

204 M. Reynaud, G. Rousse, A. M. Abakumov, M. T. Sougrati, G. Van Tendeloo, J.-N. Chotard and J.-M. Tarascon, *J. Mater. Chem. A*, 2014, **2**, 2671.

205 X. Wu, M. Shao, C. Wu, J. Qian, Y. Cao, X. Ai and H. Yang, *ACS Appl. Mater. Interfaces*, 2016, **8**, 23706–23712.

206 J. Yun, J. Pfisterer and A. S. Bandarenka, *Energy Environ. Sci.*, 2016, **9**, 955–961.

207 R. A. Huggins, *J. Electrochem. Soc.*, 2013, **160**, A3020–A3025.

208 Y. Mizuno, M. Okubo, E. Hosono, T. Kudo, H. Zhou and K. Oh-Ishi, *J. Phys. Chem. C*, 2013, **117**, 10877–10882.

209 D. M. Kim, Y. Kim, D. Arumugam, S. W. Woo, Y. N. Jo, M. S. Park, Y. J. Kim, N. S. Choi and K. T. Lee, *ACS Appl. Mater. Interfaces*, 2016, **8**, 8554–8560.

210 Z. Liu, G. Pulletikurthi and F. Endres, *ACS Appl. Mater. Interfaces*, 2016, **8**, 12158–12164.

211 T. Shiga, H. Kondo, Y. Kato and M. Inoue, *J. Phys. Chem. C*, 2015, **119**, 27946–27953.

212 R. Y. Wang, C. D. Wessells, R. A. Huggins and Y. Cui, *Nano Lett.*, 2013, **13**, 5748–5752.

213 S. Yagi, M. Fukuda, T. Ichitsubo, K. Nitta, M. Mizumaki and E. Matsubara, *J. Electrochem. Soc.*, 2015, **162**, A2356–A2361.

214 X. Sun, V. Duffort and L. F. Nazar, *Adv. Sci.*, 2016, **3**, 1–7.

215 R. Y. Wang, B. Shyam, K. H. Stone, J. N. Weker, M. Pasta, H. W. Lee, M. F. Toney and Y. Cui, *Adv. Energy Mater.*, 2015, **5**, 1–10.

216 L. Zhang, L. Chen, X. Zhou and Z. Liu, *Sci. Rep.*, 2015, 1–11.

217 T. Gupta, A. Kim, S. Phadke, S. Biswas, T. Luong, B. J. Hertzberg, M. Chamoun, K. Evans-Lutterodt and D. A. Steingart, *J. Power Sources*, 2016, **305**, 22–29.

218 M. S. Chae, J. W. Heo, H. H. Kwak, H. Lee and S.-T. Hong, *J. Power Sources*, 2017, **337**, 204–211.

219 S. Liu, G. L. Pan, G. R. Li and X. P. Gao, *J. Mater. Chem. A*, 2014, **3**, 959–962.

220 Y. Yang, E. Liu, X. Yan, C. Ma, W. Wen, X.-Z. Liao and Z.-F. Ma, *J. Electrochem. Soc.*, 2016, **163**, A2117–A2123.

221 X. Wu, M. Sun, S. Guo, J. Qian, Y. Liu, Y. Cao, X. Ai and H. Yang, *ChemNanoMat*, 2015, **1**, 188–

193.

222 R. Zhao, L. Zhu, Y. Cao, X. Ai and H. X. Yang, *Electrochem. commun.*, 2012, **21**, 36–38.

223 K. Sakaushi, E. Hosono, G. Nickerl, T. Gemming, H. Zhou, S. Kaskel and J. Eckert, *Nat. Commun.*, 2013, **4**, 1485.

224 K. West, B. Zachau-Christiansen, T. Jacobsen and S. Skaarup, *Mater. Res. Soc. Symp. Proc.*, 1991, **210**, 449–460.

225 C. K. Chan, H. Peng, R. D. Twesten, K. Jarausch, X. F. Zhang and Y. Cui, *Nano Lett.*, 2007, **7**, 490–495.

226 G. T. Chandrappa, G. Vijayakumar and J. Livage, *J. Sol-Gel Sci. Technol.*, 2014, **73**, 215–219.

227 S. Tepavcevic, H. Xiong, V. R. Stamenkovic, X. Zuo, M. Balasubramanian, V. B. Prakapenka, C. S. Johnson and T. Rajh, *ACS Nano*, 2012, **6**, 530–538.

228 D. Su and G. Wang, *ACS Nano*, 2013, **7**, 11218–11226.

229 D. W. Su, S. X. Dou and G. X. Wang, *J. Mater. Chem. A*, 2014, **2**, 11185–11194.

230 E. Uchaker, Y. Z. Zheng, S. Li, S. L. Candelaria, S. Hu and G. Z. Cao, *J. Mater. Chem. A*, 2014, **2**, 18208–18214.

231 A. Moretti, M. Secchiaroli, D. Buchholz, G. Giuli, R. Marassi and S. Passerini, *J. Electrochem. Soc.*, 2015, **162**, A2723–A2728.

232 Y. Oka, T. Yao, N. Yamamotot and N. Yamamotoc, *J. Mater. Chem.*, 1995, **5**, 1423–1426.

233 A. Mukherjee, N. Sa, P. J. Phillips, A. Burrell, J. Vaughey and R. F. Klie, *Chem. Mater.*, 2017, acs.chemmater.6b05089.

234 J. R. González, F. Nacimiento, M. Cabello, R. Alcántara, P. Lavela and J. L. Tirado, *RSC Adv.*, 2016, **6**, 62157–62164.

235 L. D. Reed and E. Menke, *J. Electrochem. Soc.*, 2013, **160**, 915–917.

236 G. Ali, J. H. Lee, S. H. Oh, B. W. Cho, K. W. Nam and K. Y. Chung, *ACS Appl. Mater. Interfaces*, 2016, **8**, 6032–6039.

237 B. Park, S. M. Oh, Y. K. Jo and S. J. Hwang, *Mater. Lett.*, 2016, **178**, 79–82.

238 Q. Wei, J. Liu, W. Feng, J. Sheng, X. Tian, L. He, Q. An and L. Mai, *J. Mater. Chem. A Mater. energy Sustain.*, 2015, **3**, 8070–8075.

239 A. Moretti and S. Passerini, *Adv. Energy Mater.*, 2016, 1600868.

240 H.-L. Fei, H.-J. Zhou, J.-G. Wang, P.-C. Sun, D.-T. Ding and T.-H. Chen, *Solid State Sci.*, 2008, **10**, 1276–1284.

241 E. Armstrong, M. Osiak, H. Geaney, C. Glynn and C. O'Dwyer, *CrystEngComm*, 2014, **16**, 10804–10815.

242 Q. Yue, H. Jiang, Y. Hu, G. Jia and C. Li, *Chem. Commun.*, 2014, **50**, 13362–13365.

243 H. Fu, X. Jiang, X. Yang, A. Yu, D. Su and G. Wang, *J. Nanoparticle Res.*, 2012, **14**, 871.

244 C. F. Zhang, Z. X. Chen, Z. P. Guo and X. W. Lou, *Energy Environ. Sci.*, 2013, **6**, 974–978.

245 A. Dhayal Raj, P. Suresh Kumar, Q. Yang, D. Mangalaraj, N. Ponpandian and A. Albert

Irudayaraj, *J. Phys. Chem. Solids*, 2013, **74**, 897–901.

246 H. Bai, Z. Liu, D. D. Sun and S. H. Chan, *Energy*, 2014, **76**, 607–613.

247 Y. Dong, H. Wei, W. Liu, Q. Liu, W. Zhang and Y. Yang, *J. Power Sources*, 2015, **285**, 538–542.

248 S. Wang, Z. Lu, D. Wang, C. Li, C. Chen and Y. Yin, *J. Mater. Chem.*, 2011, **21**, 6365.

249 J. Shao, X. Li, Z. Wan, L. Zhang, Y. Ding, L. Zhang, Q. Qu and H. Zheng, *ACS Appl. Mater. Interfaces*, 2013, **5**, 7671–7675.

250 D. Su, S. Dou and G. Wang, *ChemSusChem*, 2015, **8**, 2877–2882.

251 H.-E. Wang, D.-S. Chen, Y. Cai, R.-L. Zhang, J.-M. Xu, Z. Deng, X.-F. Zheng, Y. Li, I. Bello and B.-L. Su, *J. Colloid Interface Sci.*, 2014, **418**, 74–80.

252 H.-B. Wu, A. Pan, H. H. Hng and X. W. Lou, *Adv. Funct. Mater.*, 2013, **23**, 5669–5674.

253 H. Pang, P. Cheng, H. Yang, J. Lu, C. X. Guo, G. Ning and C. M. Li, *Chem. Commun. (Camb).*, 2013, **49**, 1536–8.

254 Y. N. Ko, Y. Chan Kang and S. Bin Park, *Nanoscale*, 2013, **5**, 8899.

255 A. Pan, H. Bin Wu, L. Yu and X. W. D. Lou, *Angew. Chemie*, 2013, **125**, 2282–2286.

256 A. Pan, H. Bin Wu, L. Yu, T. Zhu and X. W. Lou, *ACS Appl. Mater. Interfaces*, 2012, **4**, 3874–3879.

257 K. Zhu, C. Zhang, S. Guo, H. Yu, K. Liao, G. Chen, Y. Wei and H. Zhou, *ChemElectroChem*, 2015, **2**, 1660–1664.

258 Y. Li, M. Hibino, Y. Tanaka, Y. Wada, Y. Noguchi, S. Takano and T. Kudo, *Mater. Charact.*, 2001, **288**, 67–72.

259 L. Mai, Q. An, Q. Wei, J. Fei, P. Zhang and X. Xu, *small*, 2014, **10**, 1–6.

260 X. Yu, Z. Lu, G. Zhang, X. Lei, J. Liu, L. Wang and X. Sun, *Rsc Adv.*, 2013, **3**, 19937–19941.

261 Y. Liu, W. Zhong, Y. Du, Q. X. Yuan, X. Wang and R. Jia, *J. Alloys Compd.*, 2015, **633**, 353–358.

262 X. Rui, Z. Lu, H. Yu, D. Yang, H. H. Hng, T. M. Lim and Q. Yan, *Nanoscale*, 2013, **5**, 556–560.

263 R. Yu, C. Zhang, Q. Meng, Z. Chen, H. Liu and Z. Guo, *ACS Appl. Mater. Interfaces*, 2013, **5**, 12394–12399.

264 L. Mai, F. Dong, X. Xu, Y. Luo, Q. An, Y. Zhao, J. Pan and J. Yang, *Nano Lett.*, 2013, **13**, 740–745.

265 A. M. Glushenkov, M. F. Hassan, V. I. Stukachev, Z. Guo, H. K. Liu, G. G. Kuvshinov and Y. Chen, *J. Solid State Electrochem.*, 2010, **14**, 1841–1846.

266 J.-M. Li, K.-H. Chang and C.-C. Hu, *Electrochim. Acta*, 2010, **55**, 8600–8605.

267 H. Yu, J. Yu, B. Cheng and S. Liu, *Nanotechnology*, 2007, **18**, 65604.

268 Y. Liu, E. Uchaker, N. Zhou, J. Li, Q. Zhang and G. Cao, *J. Mater. Chem.*, 2012, **22**, 24439–24445.

269 C. V. S. Reddy, S. a. Wicker, E. H. Walker, Q. L. Williams and R. R. Kalluru, *J. Electrochem. Soc.*, 2008, **155**, A599.

270 H. Wang, D. Ma, Y. Huang and X. Zhang, *Chem. - A Eur. J.*, 2012, **18**, 8987–8993.

271 G. Nagaraju, P. Chithaiahb, S. Ashokac and N. Mahadevaiah, *Cryst. Res. Technol.*, 2012, **875**, 868–875.

272 Y. Wang, H. J. Zhang, K. W. Siah, C. C. Wong, J. Y. Lin and A. Borgna, *J. Mater. Chem.*, 2011, **21**, 10336–10341.

273 X. Rui, J. Zhu, W. Liu, H. Tan, D. Sim, C. Xu, H. Zhang, J. Ma, H. H. Hng, T. M. Lim and Q. Yan, *RSC Adv.*, 2011, **1**, 117.

274 M. L. Qin, Q. Liang, A. Q. Pan, S. Q. Liang, Q. Zhang, Y. Tang and X. P. Tan, *J. Power Sources*, 2014, **268**, 700–705.

275 C. Niu, J. Li, H. Jin, H. Shi, Y. Zhu, W. Wang and M. Cao, *Electrochim. Acta*, 2015, **182**, 621–628.

276 D. L. da Silva, R. G. Delatorre, G. Pattanaik, G. Zangari, W. Figueiredo, R.-P. Blum, H. Niehus and A. a. Pasa, *J. Electrochem. Soc.*, 2008, **155**, E14–E17.

277 H. Yin, K. Yu, H. Peng, Z. Zhang, R. Huang, J. Travas-Sejdic and Z. Zhu, *J. Mater. Chem.*, 2012, **22**, 5013–5019.

278 H. Yin, C. Song, Y. Wang, S. Li, M. Zeng, Z. Zhang, Z. Zhu and K. Yu, *Electrochim. Acta*, 2013, **111**, 762–770.

279 C.-C. Hu, K.-H. Chang, C.-M. Huang and J.-M. Li, *J. Electrochem. Soc.*, 2009, **156**, D485.

280 E. Shouji and D. A. Buttry, *Electrochim. Acta*, 2000, **45**, 3757–3764.

281 F. Huguenin and R. M. Torresi, *J. Braz. Chem. Soc.*, 2003, **14**, 536–543.

282 A. Moretti, F. Maroni, I. Osada, F. Nobili and S. Passerini, *ChemElectroChem*, 2015, **2**, 529–537.

283 S. Passerini, J. J. Ressler, D. B. Le, B. B. Owens and W. H. Smyrl, *Electrochim. Acta*, 1999, **44**, 2209–2217.

284 A. Byström, K.-A. Wilhelmi and O. Brotzen, *Acta Chem. Scand.*, 1950, 4, 1119–1130.

285 J.-M. Savariault, J.-L. Parize, D. Ballivet-Tkatchenko and J. Galy, *J. Solid State Chem.*, 1996, **6**, 1–6.

286 J. Galy, *J. Solid State Chem.*, 1992, **100**, 229–245.

287 R. Haberkorn, J. Bauer and G. Kickelbick, *Zeitschrift für Anorg. und Allg. Chemie*, 2014, **640**, 3197–3202.

288 M. Pouchard, A. Casalot, J. Galy and P. Hagenmuller, *Bull. Soc. Chim. Fr.*, 1967, **11**, 4343–4348.

289 G. Binnig, H. Rohrer, C. Gerber and E. Weibel, *Phys. Rev. Lett.*, 1982, **49**, 57–61.

290 R. H. Fowler and L. Nordheim, *Proc. R. Soc. London*, 1928, **119**, 173–181.

291 J. Frenkel, *Phys. Rev.*, 1930, **36**, 1604–1618.

292 J. Bardeen, *Phys. Rev. Lett.*, 1961, **6**, 57–59.

293 J. Tersoff and D. R. Hamann, *Phys. Rev. B*, 1985, **31**, 805–813.

294 J. Halbritter, G. Repphun, S. Vinzelberg, G. Staikov and W. J. Lorenz, *Electrochim. Acta*, 1995, **40**, 1385–1394.

295 H. Moon, R. Tatara, T. Mandai, K. Ueno, K. Yoshida, N. Tachikawa, T. Yasuda, K. Dokko and M. Watanabe, *J. Phys. Chem. C*, 2014, **118**, 20246–20256.

296 D. M. Seo, T. Afroz, J. L. Allen, P. D. Boyle, P. C. Trulove, H. C. De Long and W. A. Henderson, *J. Phys. Chem. C*, 2014, **118**, 25884–25889.

297 X. Bogle, R. Vazquez, S. Greenbaum, A. V. W. Cresce and K. Xu, *J. Phys. Chem. Lett.*, 2013, **4**, 1664–1668.

298 M. T. Ong, O. Verners, E. W. Draeger, A. C. T. van Duin, V. Lordi and J. E. Pask, *J. Phys. Chem. B*, 2015, **119**, 1535–1545.

299 S. Badger, *Phys. Low-Dimensional Struct.*, 2004, 19–24.

300 US 7,156,965 B1, *United States Pat.*, 2007, 1–8.

301 D.-H. Woo, J.-S. Yoo, S.-M. Park, I. C. Jeon and H. Kang, *Bull. Korean Chem. Soc.*, 2004, **25**, 577–580.

302 C. Corbella, E. Pascual, G. Oncins, C. Canal, J. L. Andújar and E. Bertran, *Thin Solid Films*, 2005, **482**, 293–298.

303 C. Hurth, C. Li and A. J. Bard, *J. Phys. Chem. C*, 2007, **111**, 4620–4627.

304 C. Baier and U. Stimming, *Angew. Chem. Int. Ed. Engl.*, 2009, **48**, 5542–4.

305 H. H. Wolfschmidt, C. Baier, S. Gsell, M. Fischer, M. Schreck and U. Stimming, *Materials (Basel).*, 2010, **3**, 4196–4213.

306 R. F. Hamou, P. U. Biedermann, A. Erbe and M. Rohwerder, *Electrochem. commun.*, 2010, **12**, 1391–1394.

307 R. F. Hamou, P. U. Biedermann, A. Erbe and M. Rohwerder, *Electrochim. Acta*, 2010, **55**, 5210–5222.

308 Y.-H. Yoon, D.-H. Woo, T. Shin, T. D. Chung and H. Kang, *J. Phys. Chem. C*, 2011, **115**, 17384–17391.

309 C. Traunsteiner, K. Tu and J. Kunze-liebhäuser, *ChemElectroChem*, 2015, **1**, 77–84.

310 M. Herpich, L. Seidl, J. Gu, Y. Liang, O. Schneider and U. Stimming, *Unpubl. results*.

311 I. Horcas, R. Fernández, J. M. Gómez-Rodríguez, J. Colchero, J. Gómez-Herrero and A. M. Baro, *Rev. Sci. Instrum.*, 2007, **78**, 13705.

312 N. Kenny, C. R. Kannewurf and D. H. Whitmore, *J. Phys. Chem. Solids*, 1966, **27**, 1237–1246.

313 D. Johannsmann, *The Quartz Crystal Microbalance in Soft Matter Research - Fundamentals and Modeling*, Springer, Cham, Heidelberg, NewYork, Dordrecht, London, 2015.

314 V. Tsionsky, L. Daikhin, M. Urbakh and E. Gileadi, *Looking at the metal/solution interface with the electrochemical quartz crystal microbalance: theory and experiment*, 2004.

315 D. A. Buttry and M. D. Ward, *Chem. Rev.*, 1992, **92**, 1355–1379.

316 G. Sauerbrey, *Zeitschrift für Phys.*, 1959, **155**, 206–222.

317 K. K. Kanazawa and J. G. Gordon, *Anal. Chem.*, 1985, **57**, 1770–1771.

318 S. Bruckenstein and M. Shay, *Electrochim. Acta*, 1985, **30**, 1295–1300.

319 L. Daikhin, E. Gileadi, G. Katz, V. Tsionsky, M. Urbakh and D. Zagidulin, *Anal. Chem.*, 2002, **74**, 554–561.

320 M. Urbakh and L. Daikhin, *Langmuir*, 1994, **10**, 2836–2841.

321 M. Urbakh and L. Daikhin, *Phys. Rev. B*, 1994, **49**, 4866–4870.

322 H. P. G. Darcy, *Les fontaines publiques de la ville de Dijon: exposition et application des principes à suivre et des formules à employer dans les questions de distribution d'eau*, Grenoble, 1856.

323 H. C. Brinkmann, *Appl. Sci. Res.*, 1947, **A1**, 27–34.

324 L. Daikhin and M. Urbakh, *Langmuir*, 1996, **12**, 6354–6360.

325 M. D. Levi, S. Sigalov, G. Salitra, P. Nayak, D. Aurbach, L. Daikhin, E. Perre and V. Presser, *J. Phys. Chem. C*, 2013, **117**, 15505–15514.

326 L. Daikhin, S. Sigalov, M. D. Levi, G. Salitra and D. Aurbach, *Anal. Chem.*, 2011, **83**, 9614–9621.

327 S. R. Sharma, G. Parthasarathy and B. Kumar, *J. Geol. Soc. India*, 1998, **51**, 517–522.

328 J. Vatamanu, O. Borodin and G. D. Smith, *J. Phys. Chem. C*, 2012, **116**, 1114–1121.

329 D. Aurbach, A. Zaban, A. Schechter, Y. Ein-Eli, E. Zinigrad and B. Markovsky, *J. Electrochem. Soc.*, 1995, **142**, 2873–2882.

330 A. Naji, J. Ghanbaja, I. S. Humbert, P. Willmann and D. Billaud, *J. Power Sources*, 1996, **63**, 33–39.

331 R. Imhof and P. Novák, *J. Electrochem. Soc.*, 1998, **145**, 1081–1087.

332 A. Schechter, D. Aurbach and H. Cohen, *Langmuir*, 1999, **15**, 3334–3342.

333 D. Aurbach, *J. Power Sources*, 2003, **119–121**, 497–503.

334 J. Wang, K. K. Manga, Q. Bao and K. P. Loh, *J. Am. Chem. Soc.*, 2011, **133**, 8888–8891.

335 J. Vetter, P. Novák, M. R. Wagner, C. Veit, K.-C. Möller, J. O. Besenhard, M. Winter, M. Wohlfahrt-Mehrens, C. Vogler and A. Hammouche, *J. Power Sources*, 2005, **147**, 269–281.

336 J. S. Gnanaraj, R. W. Thompson, J. F. DiCarlo and K. M. Abraham, *J. Electrochem. Soc.*, 2007, **154**, A185–A191.

337 G. V. Zhuang, H. Yang, B. Blizanac and P. N. Ross, *Electrochem. Solid-State Lett.*, 2005, **8**, A441–A445.

338 N. Membreño, K. Park, J. B. Goodenough and K. J. Stevenson, *Chem. Mater.*, 2015, **27**, 3332–3340.

339 Y.-M. Liu, B. G. Nicolau, J. L. Esbenshade and A. A. Gewirth, *Anal. Chem.*, 2016, **88**, 7171–7177.

340 M. A. Teshager, S. D. Lin, B. J. Hwang, F. M. Wang, S. Hy and A. M. Haregewoin, *ChemElectroChem*, 2016, **3**, 337–345.

341 M. R. Wagner, P. R. Raimann, A. Trifonova, K. C. Möller, J. O. Besenhard and M. Winter, *Anal. Bioanal. Chem.*, 2004, **379**, 272–276.

342 H. Moriwake, A. Kuwabara, C. A. J. Fisher, M. Nose, H. Nakayama, S. Nakanishi, H. Iba and Y. Ikuhara, *Meet. Abstr. - ECS PRiME 2016*, 2016.

343 B. A. Jache, J. O. Binder, T. Abe and P. Adelhelm, *Phys. Chem. Chem. Phys.*, 2016, **18**, 14299–14316.

344 P. Trucano and R. Chen, *Nature*, 1975, **258**, 136–137.

345 N. Daumas and A. Hérold, *C. R. Seances. Acad. Sci.*, 1969, **Ser. C 268**, 373.

346 C. J. Pedersen and H. K. Frensdorff, *Angew. Chemie Int. Ed. English*, 1972, **11**, 16–25.

347 C. J. Pedersen, *Angew. Chemie*, 1988, **100**, 1053–1059.

348 T. Matsui and K. Takeyama, *Electrochim. Acta*, 1998, **43**, 1355–1360.

349 C. P. Rhodes, M. Khan and R. Frech, *J. Phys. Chem. B*, 2002, **106**, 10330–10337.

350 W. A. Henderson, *J. Phys. Chem. B*, 2006, **110**, 13177–13183.

351 H.-K. Park, K. Podolske, Z. Munshi, W. H. Smyrl and B. B. Owens, *J. Electrochem. Soc.*, 1991, **138**, 627–628.

352 E. Shouji and D. A. Buttry, *Electrochim. Acta*, 2000, **45**, 3757–3764.

353 H. L. Wu, L. A. Huff, J. L. Esbenshade and A. A. Gewirth, *ACS Appl. Mater. Interfaces*, 2015, **7**, 20820–20828.

354 D. Wang, H. Liu, J. D. Elliott, L.-M. Liu and W.-M. Lau, *J. Mater. Chem. A*, 2016, **4**, 12516–12525.

355 S. Hartung, N. Bucher, J. B. Franklin, A. M. Wise, L. Y. Lim, H. Y. Chen, J. N. Weker, M. E. Michel-Beyerle, M. F. Toney and M. Srinivasan, *Adv. Energy Mater.*, 2016, **6**, 1502336.

356 Q. Wang, B. Zaho, S. Zhang, X. Gao and C. Deng, *J. Mater. Chem. A*, 2015, **3**, 7732–7740.

357 A. Davies, R. J. Hobson, M. J. Hudson, W. J. Macklin and R. J. Neat, *J. Mater. Chem.*, 1996, **6**, 49–56.

358 Y. Wang, K. Takahashi, K. H. Lee and G. Z. Cao, *Adv. Funct. Mater.*, 2006, **16**, 1133–1144.

359 M. J. Armstrong, D. M. Burke, T. Gabriel, C. O'Regan, C. O'Dwyer, N. Petkov and J. D. Holmes, *J. Mater. Chem. A*, 2013, **1**, 12568.

360 S. Tian, A. Xing, H. Tang, Z. Bao and G. Wu, *J. Mater. Chem. A*, 2014, **2**, 2896.

361 X. Zhou, T. He, X. Chen, L. Sun and Z. Liu, *RSC Adv.*, 2016, **6**, 53925–53932.

362 M. Xie, X. Sun, H. Sun, T. Porcelli, S. M. George, Y. Zhou and J. Lian, *J. Mater. Chem. A*, 2016, **4**, 537–544.

363 A. V. Naumkin, A. Kraut-Vass, S. W. Gaarenstroom and C. J. Powell, *NIST X-ray Photoelectron Spectrosc. Database*, 2017, March 2017, http://srdata.nist.gov/xps/.

364 J. K. Kaldellis and D. Zafirakis, *Energy*, 2007, **32**, 2295–2305.

365 F. Chrétien, J. Jones, C. Damas, D. Lemordant, P. Willmann and M. Anouti, *J. Power Sources*, 2014, **248**, 969–977.

366 S. Xiong, Y. Diao, X. Hong, Y. Chen and K. Xie, *J. Electroanal. Chem.*, 2014, **719**, 122–126.

367 T. Husch and M. Korth, *Phys. Chem. Chem. Phys.*, 2015, **17**, 22799–22808.

368 J. Maibach, F. Jeschull, D. Brandell, K. Edström and M. Valvo, *ACS Appl. Mater. Interfaces*, 2017, **9**, 12373–12381.

369 N. Xiao, W. D. Mcculloch and Y. Wu, *J. Am. Chem. Soc.*, 2017, **139**, 9475–9478.

370 L. Lutz, D. Alves, D. Corte, M. Tang, E. Salager, M. Deschamps, A. Grimaud, L. Johnson and P. G. Bruce, *Chem. Mater.*, 2017, **29**, 6066–6075.

371 M. I. Nandasiri, L. E. Camacho-forero, A. M. Schwarz, V. Shutthanandan, S. Thevuthasan, P. B. Balbuena, K. T. Mueller and V. Murugesan, *Chem. Mater.*, 2017, **29**, 4728–4737.

372 C. Yuqin, L. Hong, W. Lie and L. Tianhong, *J. Power Sources*, 1997, **68**, 187–190.

9 Appendix

9.1 Abbreviations

abbreviation	***full name***
AFM	Atomic Force Microscopy
BET	Brunauer-Emmett-Teller Theory / Technique
BMP-TFSI	1-Butyl-1-Methylpyrrolidinium Bis(trifluoromethylsulfonyl)imide
CE	Counter Electrode
CV	Cyclic Voltammetry / Voltammogram
DMC	Dimethyl Carbonate
DMF	N,N-Dimethylformamide
EC	Ethylene Carbonate
EC-STM	Electrochemical Scanning Tunneling Microscopy / Microscope
EDL	Electrochemical Double Layer
EIS	Electrochemical Impedance Spectroscopy
EQCM	Electrochemical Quartz Crystal Microbalance
EDS	Energy Dispersive X-Ray Spectroscopy
EG	Ethylene Glycol
FTIR	Fourier Transformed Infrared Spectroscopy
G_1	Monoglyme / Ethylene Glycol Dimethyl Ether
G_2	Diglyme / Diethylene Glycol Dimethyl Ether
G_3	Triglyme / Triethylene Glycol Dimethyl Ether
G_4	Tetraglyme / Tetraethylene Glycol Dimethyl Ether
GIC	Graphite Intercalation Compound
GITT	Galvanostatic Intermittent Titration Technique

HOPG	Highly Oriented Pyrolytic Graphite
LDOS	Local Density of States
LIB	Li-Ion Battery
LSV	Linear Sweep Voltammetry
MCMB	Mesocarbon Microbeads
NIB	Na-Ion Battery
NMP	N-Methyl-2-pyrrolidone
NMR	Nuclear Magnetic Resonance Spectroscopy
NSOM	Near-field Scanning Optical Microscopy
OCP	Open Circuit Potential
PC	Propylene Carbonate
PITT	Potentiostatic Intermittent Titration Technique
ppm	parts per million
PVDF	Polyvinylidene Fluoride
PVP	polyvinylpyrrolidone
PZC	Potential of Zero Charge
RE	Reference Electrode
SECM	Scanning Electrochemical Microscopy
SEI	Solid Electrolyte Interphase
SEM	Scanning Electron Microscopy / Microscope
STM	Scanning Tunneling Microscopy / Microscope
TAB	Teflonized Acetylene Black
TEM	Transmission Electron Microscopy
TOF SIMS	Time of Flight Secondary Ion Mass Spectrometry
WE	Working Electrode
XPS	X-Ray Photoelectron Spectroscopy
XRD	X-Ray Diffraction

9.3 Symbols

symbol	*name*	*typical value / unit*
a	collision frequency of species Ox and Red	s^{-1}
A	electrode surface	cm^{-2}
a_i	activity of species i	
a_{ox}	activity of oxidized species	
a_{red}	activity of reduced species	
α	electron transfer coefficient	
c	c-vector length perpendicular to the (00l)-plane	Å
C	reactant concentration	$mol \cdot l^{-1}$
C_o	bulk electrolyte concentration	$mol \cdot l^{-1}$
C_{EDL}	electrochemical double layer capacity	μF
$C_{ox}(x,t)$	concentration of oxidized species at position x and time t	$mol \cdot l^{-1}$
C_{ox}^*	bulk concentration of oxidized species	$mol \cdot l^{-1}$
$C_{red}(x,t)$	concentration of reduced species at position x and time t	$mol \cdot l^{-1}$
C_{red}^*	bulk concentration of reduced species	$mol \cdot l^{-1}$
d	tip-sample distance	nm
d_{EDL}	EDL interpolate spacing	Å
d_{hkl}	lattice constant of the (hkl)-plane	Å
D_0	diffusion coefficient	$cm^2 \cdot s^{-1}$
δ	velocity decay length in a liquid $\sqrt{\eta/\pi\rho f_0}$	nm
e	elementary charge	$1.602 \cdot 10^{-19}\ C$
ε	Dielectric constant	$F \cdot m^{-1}$
ε_0	vacuum permittivity	$8.854 \cdot 10^{-12}\ F \cdot m^{-1}$
ϵ	infinitesimal energy interval	eV
E	electron energy	eV
$E_{binding}$	electron binding energy	eV
E_F	Fermi energy	eV
$E_{kinetic}$	kinetic electron energy	eV

F	Faraday constant	$96485 \cdot C \cdot mol^{-1}$
$F(l/\delta)$	scaling factor of surface roughness	
f_0	quartz resonant frequency	MHz
Δf	resonant frequency shift	Hz
Δf_{film}	surface film induced frequency shift	Hz
Δf_l	liquid-induced frequency shift	Hz
Δf_m	mass-induced frequency shift	Hz
Δf_η	viscosity-induced frequency shift	Hz
Δf_P	pressure-induced frequency shift	Hz
Δf_R	roughness-induced frequency shift	Hz
Δf_{sl}	slippage-induced frequency shift	Hz
Δf_T	temperature-induced frequency shift	Hz
ΔG	Gibbs free energy	J
$\Delta G_{ox}^{\ddagger}$	reduction energy barrier for oxidized species	J
$\Delta G_{0,ox}^{\ddagger}$	reduction energy barrier of oxidized species at equilibrium	J
$\Delta G_{red}^{\ddagger}$	oxidation energy barrier for reduced species	J
$\Delta G_{0,red}^{\ddagger}$	oxidation energy barrier for reduced species at equilibrium	J
γ_i	Activity coefficient of species i	
h	root mean square of a roughness	nm
$h\nu$	photon energy	eV
$\hbar$	Planck constant	$1.055 \cdot 10^{-34}\, J \cdot s$
i	Integer	$1, 2, 3, \ldots$
I	ionic strength	$mol \cdot l^{-1}$
I	current	A
I_p	peak current	A
I_T	tunneling current	nA
j	current density	$A \cdot cm^{-2}$ / $A \cdot g^{-1}$
j_0	exchange current density	$A \cdot cm^{-2}$ / $A \cdot g^{-1}$

j_a	anodic current density	$A \cdot cm^{-2}$ / $A \cdot g^{-1}$
j_c	cathodic current density	$A \cdot cm^{-2}$ / $A \cdot g^{-1}$
k	wave vector	nm^{-1}
k_0	standard rate constant	s^{-1}
k_B	Boltzmann constant	$1.381 \cdot 10^{-23}\ J \cdot K^{-1}$
k_{ox}	standard rate constant of oxidation	s^{-1}
k_{red}	standard rate constant of reduction	s^{-1}
κ	decay coefficient of a wave function	nm^{-1}
l	Miller index	
	correlation length of surface roughness	nm
	characteristic diffusion length	nm
L	thickness of interfacial layer	nm
λ	wave length	nm
$\lambda_{De\ Broglie}$	De Broglie wave length	nm
m	particle density on the quartz	cm^{-2}
m_e	free-electron mass	$9.109 \cdot 10^{-31}\ kg$
Δm_a	average surface density of the adsorbed atoms	$g \cdot cm^{-2}$
Δm_f	surface mass density	$g \cdot cm^{-2}$
μ_i	chemical potential of species i	$J \cdot mol^{-1}$
μ_i^0	standard chemical potential of species i	$J \cdot mol^{-1}$
μ_q	shear modulus of the quartz	$2.947 \cdot 10^{11}\ g \cdot cm^{-1} \cdot s^{-2}$
n	number of transmitted electrons	$1, 2, 3, \ldots$
	overtone number (EQCM)	$1, 3, 5, \ldots$
	number of intermediate tunneling states (STM)	$1, 2, 3, \ldots$
	diffraction order (XRD)	$1, 2, 3, \ldots$
N_A	Avogadro constant	$6.022 \cdot 10^{23}\ mol^{-1}$
n_i	Particle number of species i	
	molar quantity	mol
ν	potential sweep rate	$mV \cdot s^{-1}$
ν_i	stoichiometric coefficient of species i	

ν_{ox}	stoichiometric coefficient of oxidized species	
ν_{red}	stoichiometric coefficient of reduced species	
η	overpotential	V
	viscosity of a liquid	$mPa \cdot s$
p	pressure	Pa
P	probability density	
ϕ	electric potential	V
ϕ_0	potential drop across diffuse layer	V
ϕ'	work function	eV
ϕ'_{sample}	work function of the STM sample	eV
ϕ'_{tip}	work function of the STM tip	eV
$\phi(z)$	potential of the energy barrier in the tunneling gap in STM	eV
$\psi_n(z)$	wave function of a quantum mechanical particle	
$\Phi(l/\delta)$	scaling factor of surface roughness	
q	relative surface coverage	
q_0	$\sqrt{i\omega_0\rho/\eta}$	nm^{-1}
q_1	$\sqrt{q_0^2 + \xi_H^{-2}}$	nm^{-1}
Q	electrode capacity	$mAh \cdot g^{-1}$
ΔQ	electric charge	C
r	particle radius	μm
r_i	ionic radius of species i	Å
R	ideal gas constant	$8.314\ J \cdot mol^{-1} \cdot K^{-1}$
ρ	density of a liquid	$g \cdot cm^{-3}$
$\rho(z, E)$	1D local density of states	$eV^{-1}cm^{-1}$
ρ_b	mass-density of particles	$g \cdot cm^{-3}$
ρ_q	density of the quartz	$2.648\ g \cdot cm^{-3}$
S	entropy	$J \cdot K^{-1}$
t	time	s

T	temperature	K
θ_{hkl}	Bragg reflection angle of the (hkl)-plane	°
U	electrode potential	V
U^0	equilibrium electrode potential	V
U_l^0	equilibrium electrode potential left half cell	V
U_r^0	equilibrium electrode potential right half cell	V
ΔU^0	equilibrium cell voltage	V
U^{00}	standard equilibrium electrode potential	V
$U^{00'}$	formal electrode potential	V
ΔU^{00}	Standard equilibrium cell voltage	V
V	volume	m^3
	voltage	V
V_a	acceleration voltage	V
V_{bias}	bias voltage	V
v_D	diffusion rate	$nm \cdot s^{-1}$
V_{EDL}	double layer voltage	V
Δw	resonance broadening	Hz
Δw_{film}	surface film-induced resonance broadening	Hz
Δw_l	liquid-induced resonance broadening	Hz
W	$q_1 \cosh(q_1 L) + q_0 \sinh(q_1 L)$	nm^{-1}
x	staging number (XRD)	$1, 2, 3, \ldots$
	cartesian coordinate	
$\bar{x}$	Mean displacement in *x*-direction	nm
ξ	reaction coordinate	
$\xi(x)$	surface profile	
ξ_H	permeability of interfacial layer	nm^{-1}
χ	coefficient of sliding friction	$g \cdot cm^{-2} \cdot s^{-1}$
y	coordination number	
z	ion charge	

9.4 Scientific Contributions

9.4.1 Publications

2014 J. Ma, **L. Seidl**, W. Ju, E. Mostafa, L. Asen, S. Martens, U. Stimming, O. Schneider, *Applications of Ionic Liquids in Electrochemical Energy Conversion and Storage*, ECS Trans. 64 (2014) 407–423

2016 **L. Seidl**, S. Martens, J. Ma, U. Stimming, O. Schneider, *In-Situ Scanning Tunneling Microscopy Studies of the SEI Formation on Graphite Electrodes for Li^+-Ion Batteries*, Nanoscale. 8 (2016) 14004–14014

S. Martens, A. Ispas, L. Asen, **L. Seidl**, U. Stimming, O. Schneider, A. Bund, *Influence of Fluid Dynamics on the Electrochemical Deposition of Tantalum,* ECS Trans. 75 (2016) 287–295

2017 **L. Seidl**, N. Bucher, E. Chu, S. Hartung, S. Martens, O. Schneider, U. Stimming, *Intercalation of Solvated Na-ions into Graphite*, Energy Environ. Sci. 10 (2017) 1631 – 1642

L. Seidl, L. Asen, S. Martens, O. Schneider, *Elektrochemische Abscheidung von Refraktärmetallen aus ionischen Flüssigkeiten*, Galvanotechnik 11 (2017) 2201 – 2214

2018 **L. Seidl**, H. Si, E. Chu, S. Martens, J. Ma, X. Qiu, U. Stimming, O. Schneider, *Impact of the Morphology of V_2O_5 Electrodes on the Electrochemical Na^+-Ion Intercalation*, submitted manuscript

9.4.2 Articles in preparation

L. Seidl, S. Martens, E. Chu, U. Stimming, O. Schneider, *A Graphite | V_2O_5 Full Cell Sodium-Ion Battery*

M. Herpich, **L. Seidl**, J. Gu, Y. Liang, O. Schneider, U. Stimming, *Atomically Resolved Potential Surface of a Graphite Model Electrode Measured by the Novel Technique of Scanning Electrochemical Potential Microscopy*

L. Seidl, G. Yesilbas, P. Fischer, O. Schneider, *The Electrochemical Reduction of $NbCl_5$ in Ionic Liquds*

9.4.3 Conference talks and posters

2014 J. Ma, **L. Seidl**, E. Mostafa, O. Schneider, U. Heiz, U. Stimming, *V_2O_5-based composite as Mg-ion battery electrode material studied by electrochemical SPM at the nanoscale*, Conference Poster, The 17th International Meeting on Lithium Batteries (ILMB), Como, Italy

L. Seidl, J. Ma, O. Schneider, and U. Stimming, *Scanning probe microscopy studies of intercalation mechanisms in battery electrode materials*, Conference Talk, 16th International Scanning Probe Microscopy Conference (ISPM), Seoul, South Korea

L. Seidl, J. Ma, O. Schneider, U. Stimming, *Scanning probe microscopy studies of intercalation mechanisms in battery electrode materials*, Conference Poster, Bunsentagung 2014, Hamburg, Germany

2015 **L. Seidl**, L. Flacke, S. Martens, U. Stimming, O. Schneider, *In-Situ EC-STM Studies of interfacial processes in Na ion battery electrolytes*, Conference Poster, 66th Annual Meeting of the International Society of Electrochemistry, Taipei, Taiwan

S. Martens, **L. Seidl**, J. Ma, E. Mostafa, H. Si, X. Qiu, U. Stimming, O. Schneider, *V_2O_5 as the*

cathode for Mg^{2+}-ion batteries, preparation and characterization, Conference Poster, 66th Annual Meeting of the International Society of Electrochemistry, Taipei, Taiwan

L. Seidl, J. Ma, S. Martens, E. Mostafa, O. Schneider, U. Stimming, *In-Situ Scanning Tunneling Microscopy and Electrochemical Quartz Crystal Microbalance Studies of the SEI formation on graphite electrodes*, Conference Talk, 227th ECS Meeting, Chicago, United States of America

L. Seidl, H. Si, J. Ma, S. Martens, E. Mostafa, O. Schneider, U. Stimming, X. Qiu, *Synthesis, Tailoring and Characterization of V_2O_5-Cathodes for High Performance Li^+-, Na^+- and Mg^{2+}-Ion Batteries*, Conference Poster, 227th ECS Meeting, Chicago, United States of America

L. Seidl, J. Ma, S. Martens, E. Mostafa, O. Schneider, U. Stimming, *Insights into the SEI formation mechanism by In-Situ Scanning Tunneling Microscopy and Electrochemical Quartz Crystal Microbalance Studies*, Conference Talk, ECS Conference on Electrochemical Energy Conversion & Storage with SOFC-XIV, Glasgow, Scottland

S. Martens, **L. Seidl**, J. Ma, E. Mostafa, H. Si, X. Qiu, U. Stimming, O. Schneider, *V_2O_5 as the cathode for Mg^{2+}-ion batteries, preparation and characterization*, Conference Poster, ECS Conference on Electrochemical Energy Conversion & Storage with SOFC-XIV, Glasgow, Scottland

L. Spanier, V. Čolić, M. D. Pohl, Y. Liang, **L. Seidl**, O. Schneider, A. S. Bandarenka, *Water splitting in energy provision: Resolving the origin of the unprecedentedly high activity of non-noble nanostructured oxide systems*, Conference Poster, Green Challenge Conference – DTU, Copenhagen, Denmark

2016 **L. Seidl**, H. Si, J. Ma, S. Martens, E. Mostafa, O. Schneider, U. Stimming, X. Qiu, *Synthesis, Tailoring and Characterization of V_2O_5-Cathodes for High Performance Li^+- and Na^+-Ion Batteries*, Conference Poster, International Conference on Advanced Lithium Batteries for Automobile Applications (ABAA-9), Huzhou, China

L. Seidl, N. Bucher, E. Chu, S. Hartung, S. Martens, U. Stimming, O. Schneider, *In-operando EC-STM, XRD and EQCM studies on the formation of ternary Na graphite-intercalation-compounds*, Conference Talk, PRiME 2016 (ECS), Honolulu, United States of America

L. Seidl, S. Martens, E. Chu, U. Stimming, O. Schneider, *The effect of the V_2O_5 morphology on the intercalation behavior of Na^+-ions*, Conference Poster, PRiME 2016 (ECS), Honolulu, United States of America

2017 **L. Seidl**, N. Bucher, E. Chu, S. Hartung, S. Martens, U. Stimming, O. Schneider, *Intercalation of Solvated Na-Ions into Graphite*, Conference Poster, 68th Annual Meeting of the International Society of Electrochemistry, Rhode Island, United States of America

S. Martens, **L. Seidl**, L. Asen, O. Schneider, *Electrochemical Deposition of Niobium from Ionic Liquids*, Conference Poster, 68th Annual Meeting of the International Society of Electrochemistry, Rhode Island, United States of America

9.4.4 Paper Reviews

H. Che, J. Liu, H.Wang, X. Wang, S. S. Zhang, X.-Z. Liao, Z.-F. Ma, *Rubidium and cesium ions as the electrolyte additive for improving performance of hard carbon anode in sodium-ion battery*, Electrochemistry Communications

Acknowledgements

First and foremost I would like to thank Oliver Schneider for all his support throughout my bachelor thesis, master thesis and finally my time as a PhD student. His scientific support is unsurpassed. He always had an open ear to discuss scientific questions, experimental issues, new ideas, etc. Through his electrochemical expertise, I could explore many different topics like fuel cells, batteries or different aspects of electroplating. Moreover, I received the chance to present my research on numerous international conferences at many interesting places in different countries. I could explore the world, different cultures and connect to many people from around the world. I would also like to thank Oliver Schneider for giving me the responsibility, trust and free rein to shape my research on the battery project and for all his appreciation of my work. Thank you!

In the same way, I thank Ulrich Stimming. By him, I discovered electrochemistry in my bachelor work about direct ethanol fuel cells. Later, he always gave me the chance to continue my studies, first on Pt-nanoparticle electro-catalysts during my master thesis and finally on batteries. I am also glad that I was introduced to STM and SECPM by him. Both techniques are fascinating and I wish that Ulrich Stimming can bring forward the SECPM technology, which buries a huge scientific potential. I would also like to thank Ulrich Stimming for all the very fruitful discussions I had with him, for all his advices and for all his appreciations I could feel from him. I will never forget the delicious dinner at his home in Newcastle: It was a splendid gesture!

I would also gratefully like to acknowledge Sladjana Martens for the good scientific collaborations, especially for her great help for synthesizing the V_2O_5 battery electrodes. Moreover, she always could cheer up my mood, inspired and encouraged me in my research and supplied us with many delicious cakes and Serbian specialties. I also keep our common conference visits in a nice memory, where we could explore the Asian culture in Taipeh, or experience the fascinating islands of Hawaii. I am also happy that I could encourage her for bicycle riding.

A big appreciation goes to Ludwig Asen, my closest lab mate during my master and PhD studies. With him we solved many difficulties in the lab, we supported each other for any kind of problem and we shared many happy moments together. Here, I should mention all our common trips to Chicago, where we ate delicious burgers, supersized ice cream and explored the American culture between the skyscrapers in downtown Chicago, to the rainy but very nice Scottland, to the amazing Taipeh, and the breath taking Hawaii with all its wonderful nature.

I am happy that I had the chance to learn about battery research from Jiwei Ma and to get insights into Chinese culture from all my colleagues Wenbo Ju, Yunchang Liang and Hongjiao Li. It always was a great pleasure to exchange about cultural experiences. Here, I would also like to thank Han-Yi Chen for her cheerful character, plenty of common trips to Chiemsee, Glasgow, Edinburgh, Newcastle, Taipeh, Singapore and for fruitful collaborations.

I am also grateful to Huinan Si, who contributed a lot to the success of our collaboration and the resulting publication, who created a very cheerful atmosphere in lab and who introduced me to the Chinese culture. Our trips to the Forbidden City in Beijing will always remain in my memory, as well as our exciting Mahjongg match. Huinan Si and the Chemistry Department of Tsinghua University are acknowledged for conducting the XPS and EDS measurements.

Another thank goes to my former bachelor student Eileen Chu. Not only that she helped me with many advises to work and live in Singapore, but also that she created many nice data, which we published in numerous articles. Also Luis Flacke is acknowledged for his lab work during his bachelor thesis.

Toshinari Koketsu shall also be appreciated for his collaboration on Mg-ion batteries and for his cheerful and friendly company during numerous common trips. I learned many new aspects about battery research from him.

A very special thanks goes to Roudabeh Valiollahi, who is much more than just a lab mate. In lab we shared some wonderful and memorable moments together - the magic backpack, which even had a banana inside; a lot of delicious sweets and nuts; a lot of teasing moments and a lot of fun during lab and office work and an introduction to the Persian language: دوست دارم، رودابه عزیزم!

Hany El Sayed and Luisa Kneer are also appreciated. They helped to solve the chaos in the beginning of my PhD work, when our chair E19 was quit. I am specially grateful to Hany El Sayed for his guidance during my master and early PhD studies and for later support in Hubert Gasteiger´s lab.

Another thank goes to Ehab Mostafa, who partially helped and supported the battery project and with whom I share some funny memories about American culture and who shared Egyptian sweets with us – one of the best I ever tried.

I am also happy that I had the chance to meet Xinping Qiu. He always appreciated my work, gave valuable input and discussions with him were always fruitful. Moreover, by him I had the chance to explore Chinese cuisine during several project meetings in China. I would also like to thank his group, which was an excellent host during my stays in Beijing.

I would also like to thank Ulrich Heiz, Hubert Gasteiger and Alois Knoll for use of their facilities and their groups for different occasions, like common Christmas celebrations, group seminars, and collaborations.

A special thank also goes to Aliaksandr Bandarenka for many nice scientific discussions, different collaborations, many common conference visits, his invitation to Reitenhaslach and our numerous soccer matches. At the same time I would also like to thank his group for inviting me to the soccer matches and for our trip to Reitenhaslach.

In connection with my scientific stay in the TUM CREATE labs in Singapore, I would also like to thank different people: Nicolas Bucher for the excellent collaboration during and after my Singapore stay, for all our discussions and for introducing me to Maria-Elisabeth Michel-Beyerle, who is appreciated for her interest in my work, Steffen Hartung for his help to organize my Singapore trip and his valuable input for our common paper, Iulius Markovits for his fruitful discussions in lab, his guidance through Singapore and the common soccer matches there, Arun Nagasubramanian for his assistance in the lab and his guidance for XRD measurements. A special thanks also goes to Max Herpich, who was a great lab mate in Singapore and who showed me many nice places in Singapore and with whom I had a lot of fun when playing soccer, or when surrounding Singapore in an exhausting bicycle tour. We also had a great time on Tioman, a place that I will never forget.

Together with Max Herpich, Jinying Gu, Jochen Friedl, Yunchang Liang, Oliver Schneider and Ulrich Stimming, we also had great discussions about SECPM, which hopefully will find its way into a nice publication soon.

The ‘Bundesministerium für Bildung und Forschung’ (BMBF) is acknowledged for funding the Sino-German Network on Electromobility (reference no. 16N11930) and the IAPS project (reference no. 01DO12001).

At last, I would like to thank my family for all their support: not only for always being around, but also for covering my back from daily sorrows and for encouraging me to go the way I chose. A significant part of this work is also your merit: Thank you!